New trends in the physics of spinor exciton-polariton condensates : topological defects and low dimensional structures

Hugo Flayac

N° d'Ordre: D.U. 2262

UNIVERSITE BLAISE PASCAL
U.F.R. Sciences et Technologies

ECOLE DOCTORALE DES SCIENCES FONDAMENTALES
N° 722

THESE

Présentée pour obtenir le grade de

DOCTEUR D'UNIVERSITE

Specialité : Science des matériaux

Défendue par:

FLAYAC Hugo

Master

New trends in the physics of Spinor exciton-polariton condensates

Topological defects and Low dimensional structures

Préparée à l'Institut Pascal - Clermont-Ferrand,
au sein de l'équipe:
Optoélectronique Quantique et Nanophotonique

Soutenue publiquement le 13 Septembre 2012

Devant la commission d'examen:

Rapporteurs :	Pr. Anatoly Kamchatnov
	Pr. Cristiano Ciuti
Examinateurs :	Pr. Alberto Bramati (Président)
	Dr. Jacqueline Bloch
	Dr. Dmitry Solnyshkov
Directeur de thèse :	Dr. Guillaume Malpuech

Acknowledgments

The required involvement, intellectual and creative skills to succeed in, and to take the most of a three years PhD thesis appear actually not to be enough. As many students would testify, the working framework and interactions with the supervising team are key ingredients. Not only from the scientific point of view but also from the social side, nothing being more motivating than working with people that trust you. This statement not so surprising to Bose-Einstein condensation people knowing well that: While a condensate having negative interactions between its collective constituent will desperately collapse, the positive counterpart however, allows a positive energy renormalization that infers the superfluid property and in that case no disorder is able to block the flow. After this three years period, I definitely feel myself in the second situation. And for this reason I'm really grateful to my colleagues.

I can hardly find the words to thank Dmitry Solnyshkov for all the things I learnt from him, its involvement at all the stages of my thesis and his pragmatism at critical moments. He really showed me how to aim in the right direction. I've been sharing the office as well with my thesis supervisor Guillaume during three years and the simple fact that we almost didn't argue definitely means that the working atmosphere was extremely pleasant. I admire him for its ability to take the right decision at the right time and to reduce complex concepts to their simplest representation. Because nobody can understand better a PhD student than another PhD student, I would like to thank some of them that crossed my road namely Robert Johne, Goran Pavlovic and Dmitry Visnevskii and all the students I met during conferences and with whom I really had good times. I address a special thank to Professor Ivan Shelykh which gave me the opportunity to collaborate with both the university of Iceland and the Brazilian university of Natal and for so many other reasons. I also thank Nikolay Gippius for stimulating scientific discussions.

Out of the working circle I'm really indebted to Anne-Laure Teissèdre, she cannot imagine how much she indirectly contributed to the present manuscript, supporting me all with all her strength during hard times. I'm obviously grateful to my family that believed in me (at some point) when I announced my escape from engineering curriculum towards an academic formation, I believe that I couldn't have made a better choice in my life. To all my friends: thank you from helping me to forget about science from time to time since for a researcher thinking is working.

Finally I would like to thank my new Postdoc supervising team, that is yet unknown (edit: I'm going to the EPFL in Switzerland), for choosing me. Reading the previous paragraphs you know what I expect from you now.

To all of those that have been omitted I would like to say thanks as well, it costs nothing. Actually I have voluntarily omitted the nasty/lazy/subjective/objective Physical Review Letter referees that wrote one day the lethal sentence: "This paper will certainly be of interest for people working in the field" that seems to embody the magic words to safely a reject a paper... I'm just kidding I don't blame them, since, I might be using this weapon myself one day.

Contents

Chapter 1

Introduction to the exciton-polariton physics

Contents

The exciton-polariton research field has undoubtedly passed a threshold during the last decades since the first observation of strong coupling in semiconductor microcavities in 1992 [1], the technological progresses in the sample growth, semiconductor physics, optical technics and the theoretical development have led to the demonstration of fascinating original phenomena and to revisit several classics

as well. It appears that, at the time I'm writing this thesis, anything looks expectable from these hybrid quasiparticles. I guess that C. Weisbuch and its coworkers wouldn't have expected in the early 1990's that exciton-polaritons could offer the possibility to explore for instance the black hole [2] or magnetic monopole physics [3, 4] that shall be discussed in this thesis manuscript. Indeed, the facility to create almost any sample design allows now to look further than the classical planar microcavities, with the appearance e.g. of microwires [5], confining the polariton field in two directions or quantum dots/micropillars, providing zero dimensional states [6, 7, 8]. In this context, I really had the opportunity to let my imagination drive me at some stages. The imagination appears now to be the only limitation to people working in the field. For the previous reasons, the interplay between experimentalists and theoreticians has probably never been so strong. It led non-exhaustively to the observation of nothing less than the Bose-Einstein condensation [9], a superfluid behavior [10, 11], numerous nonlinear effects [12, 13], spin sensitive phenomena [14, 15, 16, 17, 18] and topological excitations [19, 20, 21, 22] during the years 2000. The present work fits in the continuity and is built on the basis of these fascinating results.

The manuscript will be presented as follows: In the chapter 1, I shall introduce the main mathematical tools and physical concepts that were the raw material for the descriptions of the systems we considered. Then we will turn to the topics that have been treated during my three years thesis. In more details, I shall start with a voluntarily short introduction on the now well-known formation of exciton-polaritons in semiconductors, to rather linger on describing the models that are used to analyze their behavior depending on the regime of interest. Then I will specifically discuss the Bose-Einstein condensation and related superfluidity and topological defects which constitute the main topic of this manuscript. Eventually we will introduce the spin of polariton and the related features. During the chapter 2 I concentrate on the spinor exciton-polariton condensate highlighting on how my very first work on the stability of half-vortices has led later on to their interpretation in terms of magnetic monopoles along with our recent understanding of these so-called half-integer topological defects. I will propose several realistic configurations for the nucleation of these objects and, on this road we will make stops at the physics of solitons and black hole analogues that we have put into interplay. In chapter 3, I will concentrate on the physics of exciton-polaritons in even lower dimensional systems, describing the formation of nonlinear gap states and Bloch-oscillations in periodically patterned quasi-1D microwire samples and the Josephson oscillations in pairs of quasi-0D micropillars.

1.1 Exciton-polaritons

1.1.1 The basics

Bulk semiconductors or even dielectrics are known to accommodate conduction electron-hole pairs, interacting via the Coulomb force. The dipole can be treated as a quasi-particle called *exciton* [23], which can be of the Wannier-Mott or Frenkel type depending on the relative size (Bohr radius) with respect to the crystal unit cell. Such electronic excitations are known to interact with the electromagnetic field carried by photons as first described independently by Pekar [24], Hopfield [25], and Agranovich [26] in the 1950's. However, such events remain rare in the bulk medium (apart from GaN and ZnO semiconductors) where excitons are allowed to move freely. Later on, in order to obtain a significant interaction strength between the excitons and photons towards the so-called strong light-matter coupling, artificial hybrid structures were required. Indeed, the input photonic electromagnetic field (e.g. from a coherent source) can be confined in a well controlled manner using a pair of distributed Bragg reflectors having the proper periodicity (DBRs), with a cavity between them (a Perot-Fabry resonator), while the excitons can be trapped in quantum wells as described in semiconductor textbooks [27]. The optimal configuration involves quantum wells embedded in between the DBRs at the antinodes of the photonic wavefunction so that the overlap integral becomes maximized. In the so-called planar microcavities the photonic and excitonic fields are confined along the growth axis of the sample and are allowed to evolve freely in the two remaining directions said to be in-plane. Fig.1.1 shows a scheme of a typical microcavity. One crucial point is that due to the confinement, the photons gain a parabolic dispersion for in-plane propagation and are therefore attributed an effective mass, their dynamics can be consequently described by means of the Schrödinger equation rather than standard Maxwell equations simplifying considerably the description of their coupling to the excitonic field.

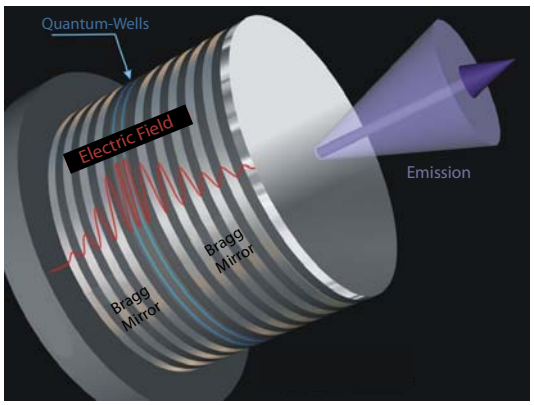

Figure 1.1: Scheme of a microcavity having here two quantum wells in the optical cavity placed at the antinodes of the electric field.

The simplest mean of describing the exciton-photon mixing is to treat the system as two coupled oscillators writing the Hamiltonian of the system the following way:

$$H = \sum_{\mathbf{k}} E_\phi(\mathbf{k})\,\phi^\dagger_{\mathbf{k}}\phi_{\mathbf{k}} + \sum_{\mathbf{k}} E_\chi(\mathbf{k})\,\chi^\dagger_{\mathbf{k}}\chi_{\mathbf{k}} + \hbar\Omega_R \sum_{\mathbf{k}} E_\phi(\mathbf{k})\left(\phi^\dagger_{\mathbf{k}}\chi_{\mathbf{k}} + \chi^\dagger_{\mathbf{k}}\phi_{\mathbf{k}}\right) \quad (1.1)$$

Here $\phi^\dagger_{\mathbf{k}}$ and $\phi_{\mathbf{k}}$ ($\chi^\dagger_{\mathbf{k}}$ and $\chi_{\mathbf{k}}$) are the second quantization bosonic operators that describe the creation and destruction of a photon (exciton) with in plane momentum $\mathbf{k} = (k_x, k_y)^T$ respectively. $E_\phi(\mathbf{k}) = \hbar^2k^2/2m_\phi + \delta$ (δ is the detuning between the photonic and excitonic modes at $\mathbf{k} = \mathbf{0}$) and $E_\chi(\mathbf{k}) = \hbar^2k^2/2m_\chi$ are the parabolic dispersions relations of the uncoupled fields. Ω_R is the Rabi frequency which describes the strength of the light matter coupling. The diagonalization is straightforwardly obtained finding the eigenvalues of the matrix:

$$M = \begin{pmatrix} E_\phi(\mathbf{k}) & \hbar\Omega_R \\ \hbar\Omega_R & E_\chi(\mathbf{k}) \end{pmatrix} \quad (1.2)$$

that give two hybrid dispersion branches describing the so-called *exciton-polariton* modes [30]

$$E_L(\mathbf{k}) = \frac{1}{2}\left(E_\phi(\mathbf{k}) + E_\chi(\mathbf{k}) - \sqrt{[E_\phi(\mathbf{k}) - E_\chi(\mathbf{k})]^2 + 4\hbar\Omega_R^2}\right) \quad (1.3)$$

$$E_U(\mathbf{k}) = \frac{1}{2}\left(E_\phi(\mathbf{k}) + E_\chi(\mathbf{k}) + \sqrt{[E_\phi(\mathbf{k}) - E_\chi(\mathbf{k})]^2 + 4\hbar\Omega_R^2}\right) \quad (1.4)$$

The corresponding eigen vectors give the $\mathbf{k}$-dependent excitonic $\chi_{L,U}$ and photonic $\phi_{L,U}$ fractions of the polaritons for both branches

$$\phi_L(\mathbf{k}) = \frac{\sqrt{4\hbar^2\Omega_R^2 - [E_\phi - E_X]\left(E_\chi - E_\phi + \sqrt{[E_\phi - E_\chi]^2 + 4\hbar^2\Omega_R^2}\right)}}{\sqrt{2[E_\phi - E_\chi]^2 + 8\hbar^2\Omega_R^2}} \quad (1.5)$$

$$\phi_U(\mathbf{k}) = \frac{\sqrt{4\hbar^2\Omega_R^2 + [E_\phi - E_X]\left(E_\phi - E_\chi + \sqrt{[E_\phi - E_\chi]^2 + 4\hbar^2\Omega_R^2}\right)}}{\sqrt{2[E_\phi - E_\chi]^2 + 8\hbar^2\Omega_R^2}} \quad (1.6)$$

$$\chi_L(\mathbf{k}) = \frac{-\hbar\Omega_R\sqrt{2}}{\sqrt{4\hbar^2\Omega_R^2 - [E_\phi - E_X]\left(E_\chi - E_\phi + \sqrt{[E_\phi - E_\chi]^2 + 4\hbar^2\Omega_R^2}\right)}} \quad (1.7)$$

$$\chi_U(\mathbf{k}) = \frac{\hbar\Omega_R\sqrt{2}}{\sqrt{4\hbar^2\Omega_R^2 + [E_\phi - E_X]\left(E_\phi - E_\chi + \sqrt{[E_\phi - E_\chi]^2 + 4\hbar^2\Omega_R^2}\right)}} \quad (1.8)$$

We note that we have imposed $\phi_L(\mathbf{k})^2 + \chi_L(\mathbf{k})^2 = 1$ and $\phi_U(\mathbf{k})^2 + \chi_U(\mathbf{k})^2 = 1$. The new polariton creation and annihilation operators are linear combination of the

exciton and photon operators following

$$p_{L\mathbf{k}} = \chi_L(\mathbf{k})b_{\mathbf{k}} + \phi_L(\mathbf{k})a^\dagger_{\mathbf{k}} \quad (1.9)$$
$$p^\dagger_{L\mathbf{k}} = \chi_L(\mathbf{k})b^\dagger_{\mathbf{k}} + \phi_L(\mathbf{k})a_{\mathbf{k}} \quad (1.10)$$
$$p_{U\mathbf{k}} = \chi_U(\mathbf{k})b_{\mathbf{k}} + \phi_U(\mathbf{k})a^\dagger_{\mathbf{k}} \quad (1.11)$$
$$p^\dagger_{U\mathbf{k}} = \chi_U(\mathbf{k})b^\dagger_{\mathbf{k}} + \phi_U(\mathbf{k})a_{\mathbf{k}} \quad (1.12)$$

The Hamiltonian of the system written on the basis of polariton operators is diagonal

$$H_P = \sum_{\mathbf{k}} E_L(\mathbf{k})p^\dagger_{L\mathbf{k}}p_{L\mathbf{k}} + \sum_{\mathbf{k}} E_U(\mathbf{k})p^\dagger_{U\mathbf{k}}p_{U\mathbf{k}} \quad (1.13)$$

The exciton-polariton is therefore a quasi-particle oscillating between a photonic state and an excitonic state at the frequency $\Omega_R/\hbar$ at least at $\mathbf{k} = \mathbf{0}$ and for zero detuning. The two dispersions branches are shown in the Fig.1.2(a) together with the fractions in the panel (b). It is seen that static polaritons of the lower branch are strongly photonic while their excitonic fraction increases with their momentum.

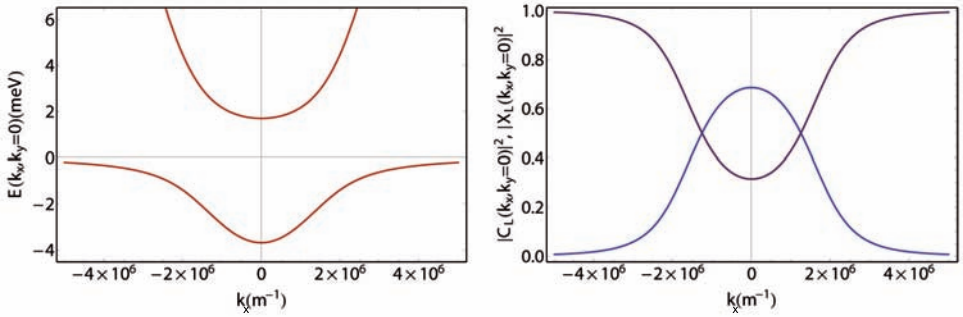

Figure 1.2: (Left panel) Polariton branches with the parameters $\Omega_R = 5$ meV, $\delta = -2$ meV, $m_\phi = 5 \times 10^{-5} m_0$ and $m_\chi = 0.4 m_0$ (m_0 is the free electron mass). (Right Panel) Associated photonic (blue curve) and excitonic (purple line) fractions for the lower polariton branch.

1.1.2 Exciton-polariton interactions

Although photons are obviously able to interfere in any medium, they cannot interact directly in the sense that they cannot scatter on each other (unless very high energies are involved). In other words, no energy exchange is possible and the quantum state is left unchanged after the crossing of two photons. There is no doubt that photonic systems can demonstrate nonlinearities, as it would be confirmed by the large community of people working in the field of nonlinear optics however, they result from the media itself, leading for instance to second harmonic generation, birefringence, or self-focusing [28]. While excitons can attract each others in the high density regimes to form biexcitons or even an electron-hole liquid, in the *low density*

regime they behave as bosonic particles, repelling each other like neutral atoms. Besides, excitons can interact with the surrounding lattice excitations (phonons) as well. Indeed, the excitons can absorb phonons to reach higher energy levels, or emit phonons demonstrating energy relaxation. These interactions are dissipative and they can be treated by means of the Lindblad formalism [29] that will be discussed in the section (3.4). The exciton-polariton consequently inherits the bosonic properties from its excitonic part, together with the capacity to interact, which is especially strong for high momenta, where the particles are strongly excitonic. The polariton-polariton interaction has a crucial impact on their dynamics and has lead to the demonstration of numerous fascinating nonlinear phenomena such as the optical parametric oscillations [12], bistability [13], or Bose-Einstein condensation [9] (here, however, phonon scattering should dominate) and its counterparts. The latter effect will be discussed in the next section.

Exciton-exciton effective interactions are included in the Hamiltonian via the density-density term:

$$H_{\chi\chi} = \frac{1}{2}\sum_{\mathbf{k},\mathbf{k}',\mathbf{q}} V_{\mathbf{q}}{}^{\chi\chi} b^{\dagger}_{\mathbf{k}+\mathbf{q}} b^{\dagger}_{\mathbf{k}'-\mathbf{q}} b_{\mathbf{k}} b_{\mathbf{k}'} \tag{1.14}$$

The interaction of photon-like polaritons in the upper dispersion branch can be neglected, provided that this branch is not significantly occupied. Transformation of the interaction Hamiltonian in the polariton basis yields

$$H_{PP} = \frac{1}{2}\sum_{\mathbf{k},\mathbf{k}',\mathbf{q}} V^{PP}_{\mathbf{q},\mathbf{k},\mathbf{k}'} p^{\dagger}_{\mathbf{k}+\mathbf{q}} p^{\dagger}_{\mathbf{k}'-\mathbf{q}} p_{\mathbf{k}} p_{\mathbf{k}'}, \tag{1.15}$$

with the interaction strength

$$V^{PP}_{\mathbf{q},\mathbf{k},\mathbf{k}'} = V^{\chi\chi}_{\mathbf{q}} \chi_L\left(\mathbf{k}+\mathbf{q}\right) \chi_L\left(\mathbf{k}'-\mathbf{q}\right) \chi_L\left(\mathbf{k}\right) \chi_L\left(\mathbf{k}'\right) \tag{1.16}$$

The Hamiltonian for the interacting polaritonic system reads

$$H = H_P + H_{PP}. \tag{1.17}$$

This retains only the energy conserving polariton-polariton interactions that lead to a density-dependent blueshift of the polariton modes. An extra term taking into account the anharmonic exciton-photon coupling saturation could be added as discussed e.g. in Ref.[31] in order to account for the exciton density-dependent Rabi splitting.

1.2 Bose-Einstein condensation

In this section we introduce first the concept of Bose-Einstein condensation in its mathematical formulation as it was originally proposed by Einstein [Sec.(1.2.1)] and then extend the concept to the two dimensional polaritonic system. At the time I'm writing this manuscript, the Bose-Einstein condensation of exciton-polaritons and their superfluidity are still under debate [see e.g. [32, 33]], which means by the way that the subject is definitely interesting. The impressive number of recent experimental reports based on the polariton condensation argument demonstrate at least that the effect in question cannot be something completely different. Along this document, the condensate terminology will be associated with the notions of accumulation of particles in their ground state and the build-up of macroscopic coherence. We will discuss here the polariton condensate forming naturally, thanks to relaxation processes, under non-resonant pumping scheme [Sec.(1.2.2)]. The artificial quasi-resonant injection of particles in well defined states leading to macroscopically occupied modes will be discussed later in Sec.(1.3). We will then describe the superfluid properties [Sec.(1.2.4)] of the condensate and introduce the concept of topological excitations [Sec.(1.2.5)].

1.2.1 Original concepts

Thanks to the symmetry of their wavefunction, bosons are allowed to accumulate in a single degenerate quantum state. In 1925, extending the work of S. Bose [34] on photon statistics, A. Einstein proposed that a new phase transition should occur for noninteracting bosons at low temperature [35]. The fact that at zero Kelvins all particles should remain in their ground state is not very surprising, as it follows from Boltzmann theory corrected for the statistics, however the description of the finite temperature counterpart was clearly a breakthrough. Until the early 1990's, the ultracold temperatures required to observe the phase transition for atomic gases were technologically unreachable and only the year 1995 brought the first experimental observation of a Bose-Einstein condensate awarded by the Nobel prize [36].

Let us consider N noninteracting bosons at the temperature T confined in a volume R^d, where R is the system size and d is the dimensionality. Their distribution is given by the function:

$$f_B\left(\mathbf{k}, T, \mu\right) = \frac{1}{\exp\left(\frac{E(\mathbf{k})-\mu}{k_B T}\right) - 1}, \tag{1.18}$$

where $\mathbf{k}$ is the d-dimensional wavevector, $E(\mathbf{k})$ is the dispersion relation of the particles, k_B is the Boltzmann constant and μ is the chemical potential, which is actually negative if $E(0) = 0$.

Adding a particle to the system requires an energy $-\mu$. The value of μ is given by the normalization condition for the fixed total number of particles N,

$$N\left(T, \mu\right) = \sum_{\mathbf{k}} f_B\left(\mathbf{k}, T, \mu\right) \tag{1.19}$$

The ground state can be separated from the others

$$N(T,\mu) = \frac{1}{\exp\left(-\frac{\mu}{k_B T}\right) - 1} + \sum_{\mathbf{k}\neq 0} f_B\left(\mathbf{k}, T, \mu\right) \tag{1.20}$$

In the thermodynamic limit, the total particle density is obtained replacing the sum by an integral over the reciprocal space:

$$n\left(T,\mu\right) = \lim_{R\to+\infty} \frac{N\left(T,\mu\right)}{R^d} = n_0 + \frac{1}{(2\pi)^d} \int_0^{+\infty} f_B\left(\mathbf{k}, T, \mu\right) d^d\mathbf{k}, \tag{1.21}$$

where

$$n_0\left(T,\mu\right) = \lim_{R\to+\infty} \frac{1}{R^d} \frac{1}{\exp\left(\frac{-\mu}{k_B T}\right) - 1} \tag{1.22}$$

If μ is nonzero, the ground state density vanishes. On the other hand, the integral on the right hand side is an increasing function of μ. So, if one increases the particle density n in the system, the chemical potential also increases. The maximum particle density that can be accommodated following the Bose-Einstein distribution is therefore:

$$n_c(T) = \lim_{\mu\to 0} \frac{1}{(2\pi)^d} \int_0^{+\infty} f_B\left(\mathbf{k}, T\right) d^d\mathbf{k} \tag{1.23}$$

This function can be calculated analytically in the case of a parabolic dispersion relation $E(\mathbf{k}) = \hbar^2 k^2/2m$. It converges for $d > 2$ and it diverges for $d \leq 2$. This means that an infinite number of bosons can always be accommodated in the system following a Bose-Einstein distribution, the chemical potential is never zero and there is no phase transition in 2 or less dimensions. In higher dimensions, n_c is a critical density above which it would seem that no more particles can be added. Einstein proposed that at such high densities the extra particles collapse into the ground-state, whose density (not accounted for in 1.23) is therefore given by

$$n_c(T) = n(T) - n_c(T). \tag{1.24}$$

The Bose-Einstein condensation is a phase transition characterized by the accumulation of a macroscopic number of particles in their ground state. The chemical potential embodies an order parameter which becomes zero at the transition.

For the 1D or 2D systems we will consider in this manuscript, the Bose-Einstein condensation is forbidden strictly speaking for the reason of divergency mentioned above. However, in 2D the transition to a superfluid state can occur, the so-called Kosterlitz-Thouless [37] transition. This effect will be described in the section (1.2.5.3). Moreover, in a finite 1D or 2D system the quasi-condensation of bosons is possible, because in that case the integral in Eq.(1.23) converges, since the system is quantized and the summation excludes the divergent region close to the ground state.

A few years after the observation of the phenomenon in ultracold atomic vapors, condensates of excitons [38], magnons [39] and exciton-polaritons [9] were claimed.

In the latter case, the experiment was performed at 5K in a CdTe/CdMgTe microcavity with 16 quantum wells. Later on, other evidences of the polariton condensation emerged [40, 41, 42]. Fig.1.3 shows the results extracted from the now famous paper of Kasprzak et al. displaying the angular distribution of the spectrally integrated emission. Below threshold (left), the emission exhibits a smooth distribution centered around an emission angle of zero degrees, that is, around $\mathbf{k} = \mathbf{0}$. When the excitation intensity is increased, the emission from the zero momentum state becomes predominant at threshold (center) and a sharp peak forms at $\mathbf{k} = \mathbf{0}$ above threshold (right). (b) shows the energy and angle-resolved emission intensities. The width of the momentum distribution shrinks with increasing excitation intensity, and above threshold, the emission mainly comes from the lowest energy state.

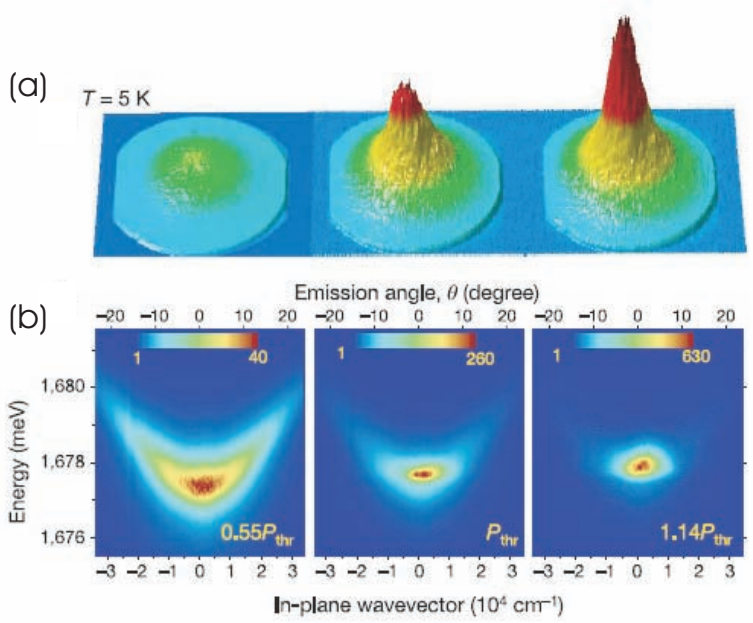

Figure 1.3: Condensation of cavity polaritons from Ref.[9]. (a) Far field emission pattern for three different excitation powers at 5K. (b) Energy resolved spectra showing the typical narrowing of the particle distribution around $k = 0$ above threshold.

Several ingredients of a true Bose-Einstein condensate have now been observed: above a critical density, condensation takes place in the ground state. The degenerate Bose gas appears fully thermalized at 19 K, supporting the interpretation of a thermodynamic phase transition - a transition between different equilibrium states. It has been shown later that, despite the finite polariton lifetime, the resulting bosonic gas can indeed reach a thermal equilibrium at an effective temperature, determined by the interactions with the phonon bath [43]. Spontaneous symmetry breaking (associated with the emergence of an order parameter) has also been demonstrated by measuring random (from pulse to pulse) polarization of the con-

densate and studying its statistics in bulk GaN sample [42], where the polarization of the condensate is not pinned.

More recently, quasi-one dimensional condensation of polaritons was reported in wire shaped microcavities by Wertz et al. [5]. In this experiment, the condensate was injected locally and formed at finite momentum due to the repulsion from the excitonic reservoir and therefore was allowed to propagate ballistically on large distances with respect to the de Broglie wavelength. The spatial coherence of the polariton cloud was shown in that experiment to extend over the whole 200 μm long wire which was an outstanding result, opening new fundamental and applied perspectives.

1.2.2 Semiclassical Boltzmann equations

The general procedure to populate the polaritonic ground state at low temperature is the following: a nonresonant (far blue detuned from the polariton branches) laser pump excites the high energy region of hot free carriers. The latter relax, forming excitons that subsequently interact dissipatively with the surrounding phonon bath to eventually reach the polariton part of the dispersion and its ground state [see Fig.1.4]. These relaxation processes can be accurately described by means of simple semi-classical rate equations: the Boltzmann equations.

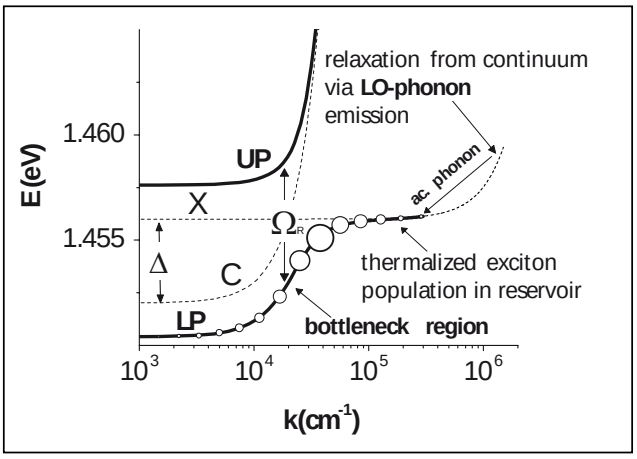

Figure 1.4: Scheme of the formation of a polariton condensate under non-resonant pumping scheme. The high energy exciton relax down the dispersion emitting phonons towards the ground state at $k = 0$.

It was first proposed by Uhlenbeck and Gropper [44] to include the quantum nature of the particles into the Boltzmann equation, taking into account their fermionic or bosonic character. In this section we describe the derivation of the kinetic Boltzmann equations and present briefly the semiclassical approach for bosons and fermions. Finally, the main scattering mechanisms in semiconductor microcavities will be discussed.

Our starting point is the usual Liouville-von Neumann equation for a quantum system:

$$i\hbar\frac{d\rho}{dt} = \left[\hat{H}(t), \rho\right], \tag{1.25}$$

where ρ is the density operator of the system in the interaction representation and $\hat{H}(t)$ is the time dependent Hamiltonian describing the interaction of polaritons and phonons given by

$$\hat{H}(t) = \sum_{\mathbf{k},\mathbf{k}'} V_{\mathbf{k},\mathbf{k}'} e^{i\left(\Omega_{\mathbf{k}'} - \Omega_{\mathbf{k}} - \omega_{\mathbf{k}'-\mathbf{k}}\right)t} b_{\mathbf{k}'-\mathbf{k}} a_{\mathbf{k}} a^{\dagger}_{\mathbf{k}'} + h.c. \tag{1.26}$$

a and b are the polariton and phonon operators respectively. These terms describe the excitation of a polariton, assisted by the absorption a phonon carrying the energy difference between the initial and final state. The hermitian conjugate stands for the reversed processes. The strength of these processes is governed by the matrix element $V_{\mathbf{k},\mathbf{k}'}$. The Liouville equation can be transformed by time integration of Eq.(1.25) and resubstitution in Eq.(1.26):

$$\frac{d\rho}{dt} = -\frac{1}{\hbar^2}\int_{-\infty}^{t}\left[\hat{H}(t), \left[\hat{H}(\tau), \rho(\tau)\right]\right] d\tau \tag{1.27}$$

After the application of the Markov approximation which consequently forbids the description of any coherent processes, Eq.(1.27) can be integrated yielding

$$\begin{aligned}\frac{d\rho}{dt} &= \frac{1}{2}\sum_{\mathbf{k}}\sum_{\mathbf{k}\neq\mathbf{k}'} W_{\mathbf{k}\to\mathbf{k}'}\left(2a^{\dagger}_{\mathbf{k}}a_{\mathbf{k}'}\rho a^{\dagger}_{\mathbf{k}'}a_{\mathbf{k}} - a_{\mathbf{k}}a^{\dagger}_{\mathbf{k}}a^{\dagger}_{\mathbf{k}'}a_{\mathbf{k}'}\rho - \rho a_{\mathbf{k}}a^{\dagger}_{\mathbf{k}}a^{\dagger}_{\mathbf{k}'}a_{\mathbf{k}'}\right) \\ &+ \frac{1}{2}\sum_{k}\sum_{k\neq k'} W_{\mathbf{k}'\to\mathbf{k}}\left(2a^{\dagger}_{\mathbf{k}'}a_{\mathbf{k}}\rho a_{\mathbf{k}'}a^{\dagger}_{\mathbf{k}} - a_{\mathbf{k}'}a^{\dagger}_{\mathbf{k}'}a^{\dagger}_{\mathbf{k}}a_{\mathbf{k}}\rho - \rho a_{\mathbf{k}'}a^{\dagger}_{\mathbf{k}'}a^{\dagger}_{\mathbf{k}}a_{\mathbf{k}}\right)\end{aligned} \tag{1.28}$$

where

$$W_{\mathbf{k}\to\mathbf{k}'} = \frac{2\pi}{\hbar}\sum_{\mathbf{k}-\mathbf{k}'}|V_{\mathbf{k},\mathbf{k}'}|^2\begin{pmatrix}0\\1+n_{\mathbf{k}-\mathbf{k}'}\end{pmatrix}\delta\left(E\left(\mathbf{k}'\right) - E(\mathbf{k}) \mp \hbar\omega_{\mathbf{k}-\mathbf{k}'}\right) \tag{1.29}$$

The Born approximation allows the density matrix to be factorized into the product of phonon ρ_{ph} and boson contributions ρ corresponding to the different states in the reciprocal space.

$$\rho = \rho_{ph} \otimes \prod_{\mathbf{k}} \rho_{\mathbf{k}} \tag{1.30}$$

The populations of polariton states with wavevector $\mathbf{k}$ lie on the diagonal elements of the density matrix ρ_k: $n_{\mathbf{k}} = \mathrm{Tr}\left(a^{\dagger}_{\mathbf{k}}a_{\mathbf{k}}\rho_{\mathbf{k}}\right)$. The same can be applied to the phonon density matrix. Both populations are assumed to be given by an equilibrium distribution. The densities dynamics are nothing but the semi-classical Boltzmann equations and read

$$\frac{dn_{\mathbf{k}}}{dt} = -n_{\mathbf{k}}\sum_{k'} W_{\mathbf{k}\to\mathbf{k}'}\left(1+n_{\mathbf{k}'}\right) + \left(1+n_{\mathbf{k}}\right)\sum_{\mathbf{k}'} W_{\mathbf{k}'\to\mathbf{k}}n_{\mathbf{k}'} \tag{1.31}$$

Taking into account pump and lifetime-induced polariton decay , one can rewrite Eq.(1.31) the following way

$$\frac{dn_{\mathbf{k}}}{dt} = P_{\mathbf{k}} - \Gamma_{\mathbf{k}} n_{\mathbf{k}} - n_{\mathbf{k}} \sum_{\mathbf{k}'} W_{\mathbf{k}\to\mathbf{k}'} (1 + n_{\mathbf{k}'}) + (1 + n_{\mathbf{k}}) \sum_{\mathbf{k}'} W_{\mathbf{k}'\to\mathbf{k}} n_{\mathbf{k}'}, \tag{1.32}$$

where $P_{\mathbf{k}}$ is the pump source term, $\Gamma_{\mathbf{k}}$ is the particle decay rate and $W_{\mathbf{k}\to\mathbf{k}'}$ is the total scattering rate between states $\mathbf{k}$ and $\mathbf{k}'$. This total scattering rate can describe various physical process, including the interaction between phonons and polaritons described above. The fermionic counterpart of Eq.(1.32) reads:

$$\frac{dn_{\mathbf{k}}}{dt} = -n_{\mathbf{k}} \sum_{\mathbf{k}'} W_{\mathbf{k}\to\mathbf{k}'} (1 - n_{\mathbf{k}'}) + (1 - n_{\mathbf{k}}) \sum_{\mathbf{k}'} W_{\mathbf{k}'\to\mathbf{k}} n_{\mathbf{k}'}, \tag{1.33}$$

A similar, but mathematically heavier procedure, can be used to describe the polariton-polariton scattering process [45]. Given the Boltzmann dynamics, the main task to be performed in order to describe the relaxation kinetics of particles in this framework is to compute the scattering rates. One should first identify the physical processes involved, and the rates follow from the Fermi golden rule. This procedure is correct only if the scattering processes are weak and treatable in a perturbative fashion. Interactions should provoke the scattering of particles within their dispersion relation and should not lead to any energy renormalization. In general, this can be not assumed for a strongly coupled microcavity. One should first treat non-perturbatively the exciton-photon coupling giving rise to a polariton basis, then, the polaritons can be said to weakly interact with their environment, which provokes the scattering of polaritons within their dispersion along with Boltzmann equations. The scattering rates are treated perturbatively, being induced by weak interactions. The interaction-induced blueshift of the polariton dispersion requires further theoretical treatment [46, 47].

In a semiconductor microcavity the main scattering mechanisms identified are: Polariton decay (mainly radiative), polariton-phonon interaction, polariton-free-carrier interaction, polariton-polariton interaction, polariton-structural-disorder interactions. These scattering rates have been carefully analyzed in Refs.[48, 49, 50, 45, 51], where the main tools were developed towards the simulation of the polariton relaxation dynamics.

In order to obtain condensation, polariton relaxation should be faster than their decay. Indeed, one well-known issue is the so-called bottleneck effect, discussed by Tassone et al. (1997) [49], observed experimentally by Tartakovskii et al. (2000) [52] and by Müller et al. (2000) [53]. In the excitonic part (large wavevectors) of the dispersion, the exciton-polaritons relax towards the ground state via scattering with phonons. This relaxation mechanism is faster than the particle decay, thanks to the strong excitonic fraction. Once the edge of the strongly coupled part of the dispersion is reached, the polaritons still need to dissipate a certain amount of energy (in the meV range) to reach the ground state of the trap. Depending on the steepness of the dispersion (that is, on the detuning and Rabi splitting), this

process, if assisted only by acoustic phonons, may take a long time, longer than the polariton lifetime in this region. Therefore, polaritons can not strongly populate the states of the dispersion minimum and they accumulate at the edge of the polariton trap where the density of states is large. Fig.(1.5) shows the observation of the bottleneck effect extracted from Ref.[53]. This effect manifests as a strong photoluminescence intensity at the inflection point of the lower polariton branch. To overcome this problem, experimentalists are used to invoke larger pump powers or positive photonic detuning that imposes a smoother polariton dispersion favoring larger lifetimes and faster relaxation due to larger excitonic fractions.

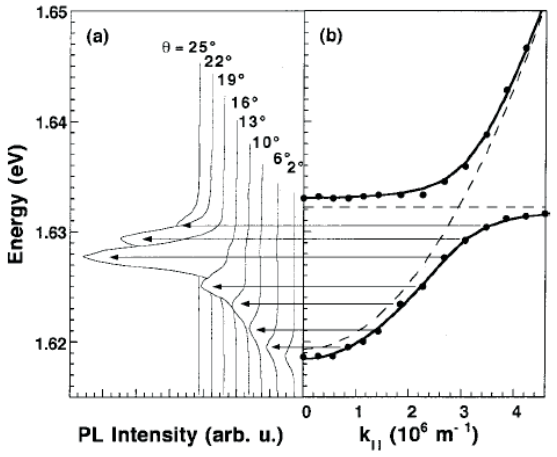

Figure 1.5: Bottleneck effect in a CdTe based microcavity at 9K with negative detunings from Ref.[53]: (a) Photoluminescence spectra and (b) corresponding theoretical polariton dispersion.

We have given the basic tools required for the description of the polariton relaxation occurring under non-resonant injection schemes. We underline that no phase coherence of the resulting condensate can be describe within this formalism. The Gross-Pitaevskii equation takes the relay in that case as we will see in the following section.

1.2.3 The Gross-Pitaevskii equation

Once the relaxation processes have successfully populated the ground state forming a condensate, the Boltzmann equations are no longer suitable to the description of the spontaneous coherence that emerges. The Gross-Pitaevskii formalism is an extension of the famous Bogoliubov theory [54], the latter treating the case of a uniform Bose gas. The Gross-Pitaevskii theory considers a non-uniform (in the general case) and dilute interacting Bose gas for which collective properties become predominant. We will follow in this section the standard description of Ref.[55]. The

starting point is the Hamiltonian of weakly interacting bosons. A Bose condensate corresponds to a macroscopically occupied state, the corresponding field operator $\hat{\Psi}(\mathbf{r})$ can be written on the basis of single particle wavefunctions ϕ_i

$$\hat{\Psi}(\mathbf{r}) = \sum_i \phi_i \hat{a}_i, \tag{1.34}$$

where $\hat{a}_i(\hat{a}_i^\dagger)$ are the annihilation (creation) operators of a particle in the state ϕ_i and they obey the commutation relations

$$\left[\hat{a}_1, \hat{a}_j^\dagger\right] = \delta_{ij}, [\hat{a}_1, \hat{a}_j] = 0. \tag{1.35}$$

The wave function ψ_0 relative to the macroscopic eigenvalue N_0, which is nothing but the population of the ground state or the number of particles in the condensate, plays a crucial role and characterizes the so-called condensates order parameter. It is useful to separate in the field operator the *condensate* term (for $i = 0$) from the other ones:

$$\hat{\Psi}(\mathbf{r}) = \phi_0(\mathbf{r})\hat{a}_0 + \sum_i \phi_{i\neq 0}(\mathbf{r})\hat{a}_i. \tag{1.36}$$

This is the natural starting point for the Bogoliubov approximation, which consists in substituting the operators $\hat{a}_0$ and $\hat{a}_0^\dagger$ with the c-number $\sqrt{N_0}$. It is equivalent to ignoring the non-commutativity of the operators $\hat{a}_0$ and $\hat{a}_0^\dagger$ and is a good approximation for the description of the macroscopic phenomena associated with the BEC, here $N_0 = \left\langle a_0^\dagger a_0 \right\rangle \gg 1$. In fact, the commutator between the operators $\hat{a}_0$ and $\hat{a}_0^\dagger$ is equal to one, while the operators themselves are of the order of $\sqrt{N_0}$. The Bogoliubov approximation is equivalent to treating the macroscopic component of $\phi_0\hat{a}_0$ of the field operator Eq.(1.36) as a classical field, so that Eq.(1.36) can be written as

$$\hat{\Psi}(\mathbf{r}) = \Psi_0(\mathbf{r}) + \delta\hat{\Psi}(\mathbf{r}), \tag{1.37}$$

where we have defined $\Psi_0(\mathbf{r}) = \sqrt{N_0}\phi_0(\mathbf{r})$ and $\delta\hat{\Psi}(\mathbf{r}) = \sum_{i\neq 0}\phi_i(\mathbf{r})a_i$. If one can neglect the non-condensate component $\delta\hat{\Psi}(\mathbf{r})$, as it should be at very low temperatures, then the field operator coincides exactly with the classical field Ψ_0. The validity of the Bogoliubov approximation is guaranteed by the occurrence of a macroscopic occupation of a single particle state $N_0 \gg 1$.

The function Ψ_0 is called condensate wavefunction and plays the role of an order parameter, which is a complex quantity, characterized by a modulus $|\Psi_0(\mathbf{r})| = \sqrt{n_0(\mathbf{r})}$ ($n_0 = N_0/V$ is the condensate's density) and a phase $\theta(\mathbf{r})$:

$$\hat{\Psi}_0(\mathbf{r}) = \sqrt{n_0(\mathbf{r})}e^{i\theta(\mathbf{r})}. \tag{1.38}$$

The order parameter characterizes the Bose-Einstein condensate's phase and vanishes above the critical temperature.

In order to study the interacting nonuniform Bose gases it is necessary to extend the previous theory. We will use the Bogoliubov field operator in its general

form Eq.(1.36). This implies that the operator $\hat{\Psi}(\mathbf{r},t)$ is replaced by its classical counterpart $\Psi_0(\mathbf{r},t)$ (the order parameter). The starting point is the many-body Hamiltonian:

$$\hat{H}=\int d\mathbf{r}\hat{\Psi}^{\dagger}\left(\mathbf{r}\right)\left[-\frac{\hbar}{2m}\Delta+V_{ext}\left(\mathbf{r}\right)+\frac{1}{2}\int d\mathbf{r}'\hat{\Psi}^{\dagger}\left(\mathbf{r}'\right)V\left(\mathbf{r}-\mathbf{r}'\right)\hat{\Psi}\left(\mathbf{r}'\right)\right]\hat{\Psi}(\mathbf{r}) \tag{1.39}$$

The next step is to obtain an equation, which governs the field $\Psi_0(\mathbf{r},t)$. For this purpose one should remember that the field operator $\hat{\Psi}(\mathbf{r},t)$, in the Heisenberg representation, fulfills the exact equation

$$\begin{aligned} i\hbar\frac{\partial}{\partial t}\hat{\Psi}(\mathbf{r},t) &= \left[\hat{\Psi}(\mathbf{r},t),\hat{H}\right] \\ &= \left[-\frac{\hbar^2\nabla^2}{2m}+V_{ext}(\mathbf{r},t)+\int\hat{\Psi}^{\dagger}\left(\mathbf{r}',t\right)V\left(\mathbf{r}'-\mathbf{r}\right)\hat{\Psi}(\mathbf{r}',t)d\mathbf{r}'\right]\hat{\Psi}(\mathbf{r},t). \end{aligned} \tag{1.40}$$

It would be a mistake to replace $\hat{\Psi}(r,t)$ with $\Psi_0(r,t)$ for a realistic interaction potential. The replacement is however accurate using an effective potential $V_{eff}=\alpha\delta(\mathbf{r}'-\mathbf{r})$, for which the Born approximation is applicable. This potential should reproduce the same low energy scattering properties as the bare potential V. Assuming that the function $\Psi_0(\mathbf{r},t)$ varies slowly over distances of the order of the range of the interaction force, one can substitute $\mathbf{r}'$ with $\mathbf{r}$ in the arguments of Ψ_0, leading to the famous Gross-Pitaevskii equation (GPE) written for the (non-zero) mean field $\langle\Psi(\mathbf{r},t)\rangle=\Psi(\mathbf{r},t)$:

$$i\hbar\frac{\partial}{\partial t}\Psi\left(\mathbf{r},t\right)=\left(-\frac{\hbar^2\nabla^2}{2m}+V_{ext}\left(\mathbf{r},t\right)+\alpha|\Psi_0\left(\mathbf{r},t\right)|^2\right)\Psi_0\left(\mathbf{r},t\right) \tag{1.41}$$

As one can immediately see, this equation coincides with the Schrödinger equation, apart from the extra nonlinear term of strength α, the latter describes the effective particle interactions that introduce an extra density-dependent potential $\alpha|\Psi_0\left(\mathbf{r},t\right)|^2$. One interesting thing to note is that the mass m that enters the equation in the kinetic energy part, is that of the particles composing the condensate and not the mass of the condensate as a whole. It originates from the fact that the GP equation is local and therefore the mass shouldn't depend on the size of the system. The validity of Eq.(1.41) is not restricted to soft potentials, but holds, in general, for arbitrary forces, the s-wave scattering amplitude providing the relevant interaction parameter. Eq.(1.41) was derived independently by Gross [56] and Pitaevskii [57] and is now the main theoretical tool for investigating nonuniform dilute Bose gases at low temperatures. For the exciton-polariton case, the interaction constant has been determined numerically [50, 58] to be

$$\alpha=\frac{6E_bX_L^2a_B^2}{S}, \tag{1.42}$$

where E_b is the exciton binding energy, a_B is the 2D exciton Bohr radius, X_C is the excitonic fraction and S is a normalization area corresponding e.g. to the pump spot extension or the size of the sample for an homogeneous pump.

The mean field approximation encompassed in the previous formalism forbids to take into account any decoherent or dephasing processes. This equation stands for the condensed states solely and any quantum fluctuations or scattering with the environment requires to develop extensions. The complementarity with the semi-classical Boltzmann equations becomes especially clear. Several attempts were performed in order to bridge the two theories [59, 47, 60, 61, 62, 63]. Each of them being accurate up to some limits, so far none of them has been able to describe the formation of a condensate via relaxation processes, that is, the formation of spontaneous coherence. Therefore, depending on the system under study, theoreticians have to switch between the different available models.

1.2.4 Elementary excitations and superfluidity

Armed with an efficient means of describing the condensate, let us discuss the textbook problem of finding its elementary excitations [55]. We shall consider weak perturbation propagating (at wavevector k) on top of the condensate, the latter being initially defined by the wave function ψ_0 associated with the density n_0. We will restrain ourselves to the one dimensional case ($\mathbf{k} \to k$), the two dimensional case being straightforwardly obtained substituting k with its radial counterpart $k_r = \sqrt{k_x^2 + k_y^2}$ the dispersion being isotropic provided that the condensate forms at $k = 0$. The perturbed order parameter reads:

$$\psi(r,t) = \sqrt{n_0} + Ae^{i(kx-\omega t)} + B^* e^{-i(kx-\omega^* t)} \tag{1.43}$$

where we assume the energy zero reference to coincide with the energy of the ground state (condensate) at $k = 0$. Here A and B are the *weak* amplitudes of the counter propagating modes having the *complex* frequency ω. The injection of this expression into the Gross-Pitaevskii equation 1.41, and linearization of the corresponding expression yields the following system:

$$+\hbar\omega A = \frac{\hbar^2 k^2}{2m} A + \alpha n_0 (A + B) \tag{1.44}$$

$$-\hbar\omega B = \frac{\hbar^2 k^2}{2m} B + \alpha n_0 (A + B) \tag{1.45}$$

Nontrivial solutions of this system exists if its determinant is zero, which gives the Bogoliubov dispersion law of elementary excitations (consequently called bogolons). The dispersion is linear for small k and tends to the dispersion of a free particle in case of large k:

$$\hbar\omega_\pm = \pm\sqrt{\left(\frac{\hbar^2 k^2}{2m}\right)^2 + \frac{\hbar^2 k^2}{m}\alpha n} \tag{1.46}$$

The first thing to notice is the negative frequency branch defined by $\hbar\omega_-$, the latter has recently been evidenced in a polaritonic system [64, 65] under the stimulation of a probe beam. The second thing is that in the limit of small wavevectors the dispersion becomes linear, which means that one can define a speed $c = \sqrt{\alpha n/m}$ for

the Bogolons called *speed of sound*. Indeed, these excitations being density waves propagating on top of a (quantum) fluid, they can be associated with sound waves. In the opposite limit of large k, the spectrum recovers a parabolic dispersive shape. The amplitudes $A_{\pm}(k)$ and $B_{\pm}(k)$ associated with each branch are found solving the system with the previously found $\omega_{\pm}$ under the normalization condition $A_{\pm}^2 + B_{\pm}^2 = 1$ yielding:

$$|A_{\pm}|^2 = \frac{\left(\omega_{\pm} + \alpha|\psi_0|^2\right)^2}{\left(\omega_{\pm} - \omega_0 - \alpha|\psi_0|^2\right)^2 + \left(\alpha|\psi_0|^2\right)} \tag{1.47}$$

$$|B_{\pm}|^2 = \frac{\left(\omega_{\pm} - \alpha|\psi_0|^2\right)^2}{\left(\omega_{\pm} - \omega_0 - \alpha|\psi_0|^2\right)^2 + \left(\alpha|\psi_0|^2\right)} \tag{1.48}$$

which gives nothing but the amplitudes of the states with wavevector k. One of the most fascinating properties of a Bose-Einstein condensate is its capability to flow without any dissipation (friction) and to exhibit an infinite thermal conductivity. The so-called superfluidity discovered by Kapitza [66] and independently by Allen and Missener [67] with liquid Helium has obviously attracted much interest. L. Laudau proposed in 1947 [68] a criterion which allows a propagating BEC to remain superfluid at subsonic velocities $0 < v < c$. The BEC would therefore ignore any defect crossing its flow. For $v > c$, the BEC is said to be supersonic, and the superfluidity is lost as we will see.

Previously, we have described a static BEC and its excitations formed at $k = 0$ which for sufficient density (which gives the extension of the linear part) will obviously be superfluid. However, it is possible for the condensate to form at finite k owing to some external potential. In that case, the dispersion of elementary excitations is no more isotropic and one should modify the ansatz, introducing the condensate wavevector $\mathbf{k}_0$ and energy $\omega_0(\mathbf{k}_0)$:

$$\psi(\mathbf{r}, t) = e^{i(\mathbf{k}_0 \cdot \mathbf{r} - \omega_0 t)} \left(\sqrt{n_0} + A e^{i(\mathbf{k}\cdot\mathbf{r} - \omega t)} + B^* e^{-i(\mathbf{k}\cdot\mathbf{r} - \omega^* t)}\right) \tag{1.49}$$

The new dispersions branches on a slice along the direction of $\mathbf{k}_0$ are found from the transformation $k \to k - k_0$ and $\omega(k) \to \omega(k - k_0) + \omega(k_0)$, and consequently the symmetry between ω_+ and ω_- is lost. Two regimes to be distinguished are shown in the Fig.1.6, where Bogoliubov dispersions are plotted. When the condensate forms with a wavevector corresponding to a subsonic velocity namely $v = d\omega/dk < c$, there is no final state for the Rayleigh scattering (which conserves the energy of the system) of the propagating BEC. In that case the condensate is said to be superfluid. On the contrary, for a supersonic regime, namely for $v > c$, the dispersion shape is modified in such a way that the backscattering becomes possible again within a single branch.

Another simple way to define the superfluidity criterion is to consider a uniform fluid at zero temperature flowing along a capillary with a constant velocity v. In that

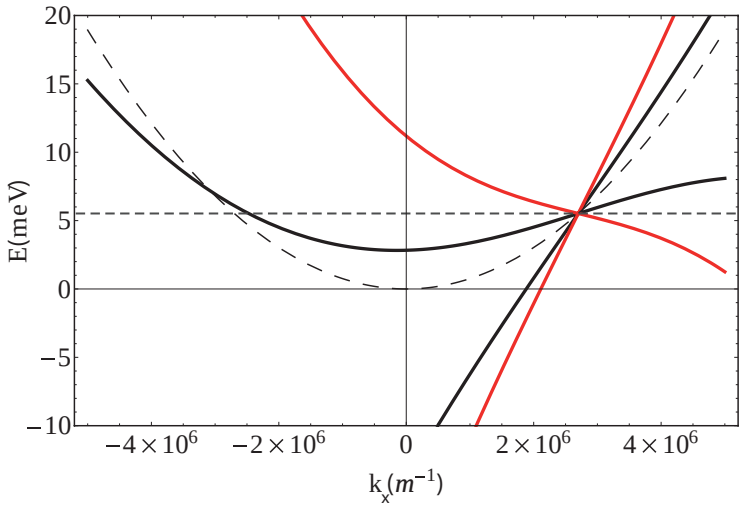

Figure 1.6: Dispersions of elementary excitations of a condensate forming at finite momentum. The dashed line is the bare dispersion. The solid red (black) line shows a superfluid $v < c$ (supersonic $v > c$) spectrum, the dotted black line is the bare parabolic dispersion of the particles involved in a linear regime and the dashed horizontal black line guides the eye to available backscattering points. As one can see, no Rayleigh scattering is possible in the superfluid regime.

case, dissipation may only come from the scattering with the walls from the capillary. The basic idea of the derivation is to calculate the energy and the momentum in the reference frame moving with the fluid and in the static one. The link between the two frames is obviously given by a Galilean transformation. If a single excitation with momentum $\hbar k$ appears, the total energy in the moving frame is $E = E_0 + \varepsilon(k)$, where E_0 is the energy of the ground state and $\varepsilon(k)$ is the dispersion of the fluid excitations. In the static frame however, the energy and momentum of the fluid read:

$$E' = E_0 + \varepsilon(k) + \hbar k v + \frac{1}{2} M v^2 \tag{1.50}$$

$$P' = p - Mv, \tag{1.51}$$

where M is here the *total* mass of the fluid. The energy of the elementary excitations in the static case is $\varepsilon(k) + \hbar k v$. Dissipation is possible only if the creation of elementary excitations is profitable energetically, which means:

$$\varepsilon(k) + \hbar k v < 0. \tag{1.52}$$

Therefore, the dissipation can take place only if $v > \frac{\varepsilon(k)}{\hbar k}$. In other words, the flow stays superfluid if the velocity is smaller than the critical velocity v_c. This is the Landau criterion:

$$v_c = \min\left(\frac{\varepsilon(k)}{\hbar k}\right). \tag{1.53}$$

The link between Bose-Einstein condensation and superfluidity becomes especially clear noting that given $\Psi(r,t)$ – a solution of the equation for the field operator in Heisenberg representation – then:

$$\Psi'(r,t) = \Psi(r - vt)\, e^{\frac{i}{\hbar}\left(mvr - \frac{1}{2}mv^2 t\right)} \tag{1.54}$$

where v is a constant vector, is also a solution of the same equation. This follows directly from the Galilean invariance of the field operator. In the moving coordinate system the condensate wavefunction of a uniform fluid is defined by $\Psi_0 = \sqrt{n_0}e^{-i\mu t/\hbar}$ where μ is the chemical potential (the energy of the condensate). In the static coordinate system, the order parameter takes the form $\Psi = \sqrt{n_0}e^{i\theta}$, where

$$\theta(r,t) = \frac{1}{\hbar}\left[mvr - \left(\frac{1}{2}mv^2 + \mu\right)t\right] \tag{1.55}$$

is the new phase, while the amplitude n_0 has obviously not changed. It follows that the velocity is proportional to the gradient of the phase:

$$\mathbf{v} = \frac{\hbar}{m}\boldsymbol{\nabla}\theta. \tag{1.56}$$

This velocity is the so-called superfluid velocity. The phase of the order parameter is playing the role of a velocity potential. Another way of establishing the relation (1.56) is to calculate directly the velocity field from:

$$\Psi(\mathbf{r},t) = \sqrt{n(\mathbf{r},t)}e^{i\theta(\mathbf{r},t)} \tag{1.57}$$

$$\mathbf{v}(\mathbf{r},t) = -\frac{i\hbar}{2mn(\mathbf{r},t)}\left[\Psi^*(\mathbf{r},t)\,\boldsymbol{\nabla}\Psi(\mathbf{r},t) - \Psi(\mathbf{r},t)\,\boldsymbol{\nabla}\Psi^*(\mathbf{r},t)\right] \tag{1.58}$$

Eq.(1.56) infers a very important property to the ensuing flow. Indeed, looking at how the latter responds to a rotation by calculating rot($\mathbf{v}$), one immediately finds that it is zero. Which means that the flow is irrotational and would therefore completely ignore any imposed rotation. Keeping this in mind, we will turn back to this statement in the section (1.2.5.2).

The very first observation of quasi-Bose-Einstein condensation of exciton-polaritons [9] did not support the superfluid picture. Strong inhomogeneous spatial distributions and a flat dispersion around $k = 0$ fed much controversy. Various following works attempted to describe this effect using various models [69, 59, 70]. Later on, two groups have independently claimed the observation of the superfluidity of exciton- polaritons [11, 10, 64]. As an illustration, we show in Fig.1.7 a series of images of a nonlinear resonantly injected polariton wavepacket colliding against a structural defect in real space [panels cI-cIII and dI-dIII] and in reciprocal space [panels cIV-cVI and dIV-dVI], extracted from Ref.[11]. The superfluid behavior is evidenced here by a suppression of backscattered waves (or Cerenkov waves) at subsonic velocities [see panel (a)]. This statement is supported by the k-space representation, where the polariton condensate does not change its momentum (no emission from backscattered states is visible), which is a signature of superfluidity,

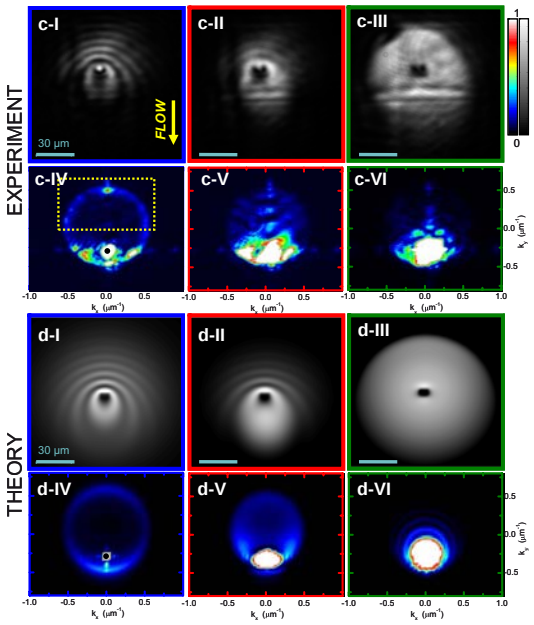

Figure 1.7: Superfluid motion of a polariton droplet and its collision with a structural defect from Ref.[11]: (c-I)-(c-III) Real space images increasing the pumping power. In the supersonics regimes (c-I) and (c-II) backscattered waves (Cerenkov waves) are clearly visible while they vanish in (c-III) evidencing the superfluid regime, the flow ignores the defect. The panels (c-IV)-(c-VI) show the associated reciprocal space revealing the suppression of backscattering in (c-VI). The panels (d-I)-(d-VI) show the corresponding numerical results.

as we have seen previously. Besides, under different conditions, Utsunomiya et al. [10] have reported the first observation of interaction-induced renormalization of the polariton dispersion, which was in qualitative agreement with the Bogoliubov theory [54], demonstrating a low momentum linear part. The sound velocity deduced from their experiments was of the order of 10^8 cm $\cdot$ s^{-1}. This value is eight orders of magnitude larger than that of atomic BECs, resulting from the very light polariton mass and the seven orders of magnitude stronger interactions. According to the Landau criterion Eq.(1.53), the observation of this linear dispersion in the low-momentum regime is an indication of superfluidity in the exciton-polariton system. A lot of efforts have been performed to understand, if the Landau criterion can be applied to the polariton system, which is characterized by a finite lifetime [71, 72, 73, 74, 75, 76]. In addition, polariton condensates have recently demonstrated at numerous occurrences the formation of topological defects which are tightly connected to the notion of superfluidity or especially to its breakdown, as we will see.

1.2.5 Topological defects

Apart from the small-amplitude excitations (Bogolons) described in the previous section, a significant perturbation of the BEC allows the appearance of nontrivial modifications of its wavefunction, including topological defects [77]. Depending on the dimensionality of the system and on the nature of the interactions between particles, these defects can be of various types. In one-dimensional systems they manifest themselves as solitons that are density dips/humps (dark/bright solitons) for the case of repulsive/attractive interactions correspondingly, accompanied with a maximum phase shift of π. Such objects are stable thanks to the interplay between nonlinear interactions and the dispersion that compensate each other. However, since a 1D soliton can be continuously unfolded into a homogeneous solution, it should rather be called a pseudo-topological defect. A vortex, the soliton's counterpart in two-dimensional (2D) systems, carries a quantum of angular momentum. Such objects cannot be continuously transformed (at least in scalar condensates) into a vortex-less solution and are said to be topologically stable. Soliton excitations can also occur in 2D in the form of oblique solitons, as we will see later [78].

We remind that a BEC is a system of bosonic particles occupying at low temperature the same lowest energy (ground) state. These particles have the property to share the same single-particle wave function. One consequently talks about a macroscopic wavefunction or order parameter of the condensate which reads:

$$\Psi(\mathbf{r},t) = \sqrt{n(\mathbf{r},t)}e^{i\theta(\mathbf{r},t)} \tag{1.59}$$

This wavefunction is in the general case complex-valued and thus possesses a phase θ which can possibly contain a propagation term $\mathbf{k}\cdot\mathbf{r}$, while its amplitude is governed by the density $n = |\Psi|^2$ of particles of mass m in the BEC. The evolution of the wave function in the mean-field approximation is well described by the Gross-Pitaevskii equation (GPE):

$$i\hbar\frac{\partial\Psi}{\partial t} = -\frac{\hbar^2}{2m}\Delta\Psi + \alpha_1|\Psi|^2\Psi \tag{1.60}$$

It what follows, we will concentrate on the case $\alpha_1 > 0$ which corresponds to repulsive interaction between particles. The GPE assumes the normalization condition: $\int |\Psi|^2 d\mathbf{r} = N$ where N is the total number of particles in the system. Stationary solutions are found upon writing $\Psi(\mathbf{r},t) = \psi(\mathbf{r})\, e^{-i\mu t}$ where μ is the chemical potential yielding the stationary Gross-Pitaevskii equation:

$$\mu\psi = -\frac{\hbar^2}{2m}\Delta\psi + \alpha_1|\psi|^2\psi \tag{1.61}$$

1.2.5.1 Dark solitons in 1D Bose-Einstein condensates

In a 1D system ($\mathbf{r} \to x$), the GPE, which remains valid according to the so-called multiple-scale expansion [79], allows special solutions to occur: the gray solitons, namely dips in the density that remain stable (do not spread with time) even if they

propagate, provided that the interactions are repulsive. This dip is associated with a local shift of the condensate's phase. The gray soliton solution reads:

$$\Psi_S(x,t) = \sqrt{n_\infty}\left[\sqrt{1-\frac{{v_s}^2}{c^2}}\tanh\left(\frac{x-v_s t}{\xi\sqrt{2}}\sqrt{1-\frac{{v_s}^2}{c^2}}\right)+i\frac{v_s}{c}\right] \tag{1.62}$$

Here n_∞ is the density far away from the soliton's core, v_s is the speed of the soliton related to its depth via $v_s = c\sqrt{n(0)/n_\infty}$ and $\xi = \hbar/\sqrt{2m\mu}$ is the healing length of the BEC which defines the size of the soliton's core, the latter being modulated by the relativistic Lorentz factor $1/\gamma = \sqrt{1-v^2/c^2}$. The faster a soliton moves, the shallower and the larger it becomes, behaving as a relativistic particle with respect to the speed of sound. The energy of a gray soliton is obtained injecting Eq.(1.62) into the condensate's energy to obtain:

$$E_s = \frac{4}{3}\hbar c n_\infty\left(1-\frac{v^2}{c^2}\right)^{\frac{3}{2}} \tag{1.63}$$

which coincides with a relativistic equation as well. One interesting feature is that assuming $v \ll c$ the effective mass of the soliton is given by

$$m_s = -\frac{4\hbar n_\infty}{c} \tag{1.64}$$

being therefore *negative*. This is actually not so surprising since we are considering a particle-like density dip, in semiconductors for example, holes have also a negative effective mass. A direct consequence is that a gray soliton will minimize its energy moving to higher density regions, and consequently two gray solitons (forming local density minima) see each other as potential barriers and *repel* on a short range. The phase shift through the soliton is given by $\Delta\theta = \arccos(v_s/c)$ varying between 0 and π. For $v_s = 0$, the wavefunction is real valued, the density at the soliton's core is exactly zero and the phase is the discontinuous Heaviside function of amplitude π, undefined at $x = 0$. This solution is called "dark soliton". Gray solitons remain stable in the system, because interactions are present to compensate the dispersion that would show a wave packet evolving in the linear Schrödinger equation. The figure 1.8 shows normalized density profile $n_s(x) = |\Psi_s(x)|^2$ [panel (a)] of several gray solitons together with their phase [panel (b)]. Noteworthy, the phase being discontinuous at the dark soliton's core (Heaviside function) it is undefined (singular) at this point, this is an important feature of topological defects that governs their stability.

1.2.5.2 Vortices and oblique solitons in 2D Bose-Einstein condensates

Let us now turn to the two dimensional case. At the very end of Sec.(1.2.4) we have seen that the superfluid is irrotational due to the link between its velocity field and the spatial variations of its phase: $\mathbf{v} = \hbar/m\boldsymbol{\nabla}\theta$, and therefore $\mathrm{rot}(\mathbf{v}) = \mathbf{0}$. So one would at first sight conclude that the fluid would not respond to an imposed

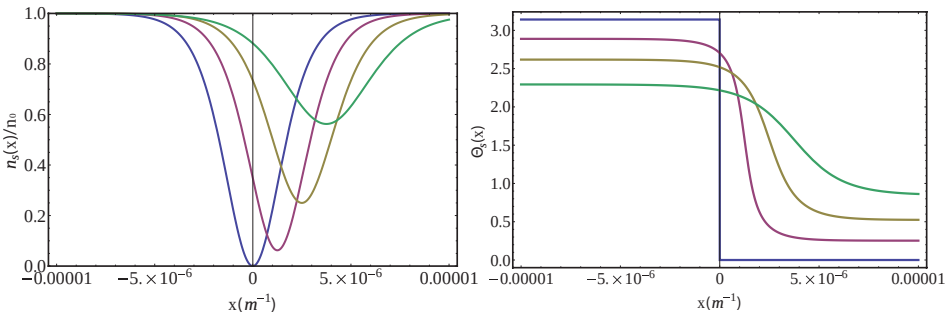

Figure 1.8: Gray solitons solutions plotted with the polariton parameters at $t = 5$ ps for the values $v_s = \{0, 0.25, 0.5, 0.75\}c$: (a) Density profiles (b) phases profiles.

rotation. This is only partially true, indeed the phase θ of the superfluid flow is defined up to 2π which means that any spatial variation of θ around a closed path is $2l\pi$ where l is an integer:

$$\oint \boldsymbol{\nabla}\theta\left(\mathbf{r},t\right) = 2l\pi \tag{1.65}$$

The case $l = 0$ obviously corresponds to a homogeneous condensate or a slightly perturbed one with a continuous flow. However, for the cases where $l \neq 0$, the situation is more intriguing. The only way of having a phase changing e.g. by 2π on a closed loop is to make it wind around a central point, where it will subsequently be singular. This phase winding defines the so-called quantized vortex introduced by Onsager in the context of liquid Helium [80], the quanta corresponding to the integer l. One direct consequence is that the circulation of the velocity on a closed loop quantized in units of h/m:

$$\oint \mathbf{v}\cdot d\mathbf{l} = \frac{\hbar}{m}\oint \boldsymbol{\nabla}\theta\left(\mathbf{r},t\right)\cdot d\mathbf{l} = l\frac{h}{m} \tag{1.66}$$

The central point where the phase is singular corresponds to a vanishing density of the fluid $n(0) = 0$ just like in the dark soliton case. The velocity field around the vortex core, given that $\theta(\phi) = l\phi$ in polar coordinates, reads

$$\mathbf{v} = \frac{\hbar}{m}\boldsymbol{\nabla}\theta\left(\mathbf{r},t\right) = l\frac{\hbar}{mr}\mathbf{u}_\theta \tag{1.67}$$

As one can see, the particles rotate faster and faster while approaching the density minimum (the vortex core) like in classical whirlpools [see right panel of Fig.1.9 (arrows)]. But their nucleation within the fluid is radically different. The quantization of the velocity field means that vortices would appear in a superfluid put in rotation in a step-like manner above some critical velocity below which the rotation is ignored by the flow. This is a strongly counterintuitive property of quantum fluids.

In the thermodynamic limit the wavefunction of a condensate carrying a vortex is [55]:

$$\psi_V\left(r,\phi\right) = f_l\left(r\right)e^{il\phi} \tag{1.68}$$

The radial part $f_l(r)$ has to be evaluated variationally to find e.g. for $l = 1$:

$$f_1(r) = \sqrt{n_\infty} \frac{r/\xi}{\sqrt{(r/\xi)^2 + 2}} \tag{1.69}$$

where n_∞ is the density at infinity and $\xi = \hbar/\sqrt{2m\mu}$ is the healing length of the condensate, determining the density-dependent vortex (core) size. The corresponding density profile $n_V = |\psi_V|^2$ is plotted in Fig.1.68 [left panel] together with the velocity field, and the associated phase [right panel].

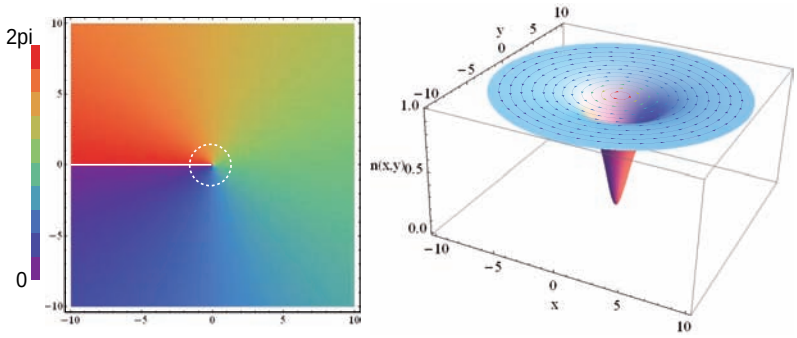

Figure 1.9: Left panel: Phase of the wavefunction (1.68), the singularity is marked with a white/dashed circle and the phase jump with solid white line. Right panel: Vortex density profile together with its velocity field (arrows).

In the Born approximation, the free energy of the condensate for the stationary solution $\psi(\mathbf{r})$ reads:

$$E = \int \left\{ \frac{\hbar^2}{2m} |\boldsymbol{\nabla}\psi(\mathbf{r})|^2 + \frac{\alpha}{2} |\psi(\mathbf{r})|^4 \right\} d\mathbf{r} \tag{1.70}$$

Injecting Eq.(1.68) into the Gross-Pitaevskii equation (1.70) gives the energy of the condensate containing a single vortex. To find the vortex energy, one should substract the energy of the uniform state $\int \frac{\alpha}{2} |\psi(\mathbf{r})|^2 d\mathbf{r}$ containing the same number of particles N. Following this procedure, the energy of a vortex is separated in a core energy part that should be evaluated numerically and a kinetic energy part E_k which dominates for large system sizes. The latter is given by

$$E_k = \frac{l^2 \pi n_\infty \hbar^2}{m} \ln\left(\frac{R}{\xi}\right) \tag{1.71}$$

where R is the radial size of the system which has to be finite, otherwise the vortex energy growing logarithmically would become infinite. We note first, that obviously the single quantized vortex ($l = 1$) is the lowest energy (vortex) state and second, that the vortex, whose energy is proportional to the condensate density, will therefore move along density gradients to minimize its energy. This latter statement will be determinant in the section (2.5) where we will discuss vortices generation and propagation.

Now, dealing with multiple vortices, the corresponding kinetic energy is found from:

$$E_k = \frac{\hbar^2}{2m} \int \left[\sum_i \boldsymbol{\nabla} \theta_i \left(\mathbf{r}_i \right) \right]^2 d\mathbf{r} \tag{1.72}$$

where $\theta_i(\mathbf{r}_i)$ is the phase of the vortex i at the position $\mathbf{r}_i$. In the simplest case of a vortex pair, the energy is found to be:

$$E_k = E_{k1} + E_{k2} + E_{int} \tag{1.73}$$

$$E_{int} = \frac{2 l_1 l_2 \pi n_\infty \hbar^2}{m} \ln \left(\frac{R}{d} \right) \tag{1.74}$$

l_1 and l_2 being the winding number associated to each vortex and d the distance between them. The interaction energy E_{int} is negative (positive) for vortices having a winding number with an opposite (the same) sign which means that they attract (repel) each others. Furthermore, it is easily seen that forming e.g. a vortex having a winding number $l = \pm 2$ is more energetically costly than forming a pair of vortices with $(l_1, l_2) = (\pm 1, \pm 1)$. Therefore, a vortex with a large winding number will decay into a corresponding number of singly-charged vortices. Another different configuration is the vortex-antivortex pair.

1.2.5.3 The Berezinskii-Kosterlitz-Thouless transition

In two dimensions, vortices behave differently from other excitations (non-topological ones), indeed, their energy grows logarithmically with the size of the system. They can consequently be activated thermally, but only above a critical temperature T_{BKT} [81, 37]. In order for the vortex solution to be profitable, it has to lower the free energy F_V of the system. Taking into account the vortex entropy S_V induced by the thermal fluctuation at the temperature T, the free energy reads

$$F_V = E_V - T S_V \tag{1.75}$$

Here E_V is the energy of a vortex at zero temperature as established previously. The vortex entropy depends on the logarithm of accessible positions for the vortex

$$S_V = k_B \ln \left(\frac{R^2}{\xi^2} \right) \tag{1.76}$$

where k_B is the Boltzmann constant and we assume a size ξ^2 for the vortex. Finally we obtain:

$$F_V = \left(\frac{l^2 \pi n_\infty \hbar^2}{m^2} - 2 k_B T \right) \ln \left(\frac{R}{\xi} \right) \tag{1.77}$$

We can immediately derive a critical temperature

$$T_{BKT} = \frac{l^2 \pi n_\infty \hbar^2}{2 k_B m^2} \tag{1.78}$$

above which the energy of vortices become smaller than the thermal energy $k_B T$. In that case we easily understand that single vortices can be thermally activated. Below T_{BKT} they are bound in vortex-antivortex pairs that only perturb the fluid locally [see Fig.1.10]. The appearance of vortices manifests a breakdown of the superfluidity as they lead to a friction force between the normal and superfluid fraction of the fluid. The temperature T_{BKT} therefore defines the frontier to be crossed to enter a superfluid regime in two dimensions: defining the so-called Berezinskii-Kosterlitz-Thouless transition that was evidenced in 2006 with a 2D gas of Rubidium atoms [82]. It is especially clear from the Eq.(1.78) that singly quantized vortices ($|l| = 1$), which are favored energetically anyway, give the lowest critical temperature with respect to other winding numbers and we will see that the so-called half-quantum vortices having half-integer winding numbers will define a twice smaller T_{BKT} in spinor condensates.

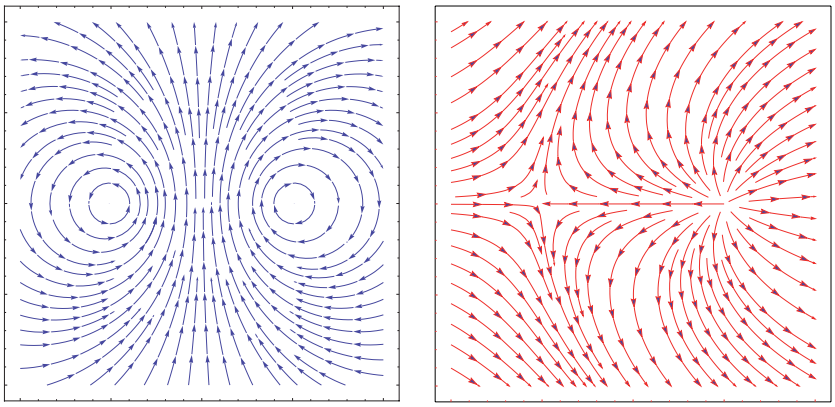

Figure 1.10: Vortex-antivortex pair ($l = \pm 1$). Left panel: velocity field. Right panel: phase field $(\cos(\theta), \sin(\theta))$.

Vortices are the elementary *topological* excitations of superfluids and are well-known in the context of superconductors [83]. Vortices and vortex lattices were first nucleated putting an atomic BEC into rotation [84, 86] with a stirring laser, following the prediction of Williams and Holland [85]. In polariton condensates, the spontaneous formation of vortices has been first observed at deterministic positions pinned to disorder [19] [see Fig.1.11]. Next, an artificial phase-imprinting method was proposed, based on a Gauss-Laguerre probe in the optical parametric oscillator regime [87, 88, 89]. More recently, vortices have been detected in turbulences in a polariton fluid propagating past an obstacle [21, 90, 91, 92]. We will focus on this kind of configuration for the discussion on oblique (half) solitons later on. Such a large number of experimental observations reflects the convenience offered by the polaritonic system for the investigation of hydrodynamic-related effects. One of the advantages is that the vortices are much larger in spatial size than in atomic condensates ($\xi \sim 1\mu$m for polaritons) and therefore more easily observable. The other advantage is that using the techniques of classical optics it is possible to reconstruct the entire wavefunction of the condensate, namely its density, from the

intensity of light escaping from the microcavity, and its phase (mod. 2π), from interferograms. Furthermore, the control of the condensate parameters such as its density or its wave vector can be performed by simply changing the pumping intensity, for example.

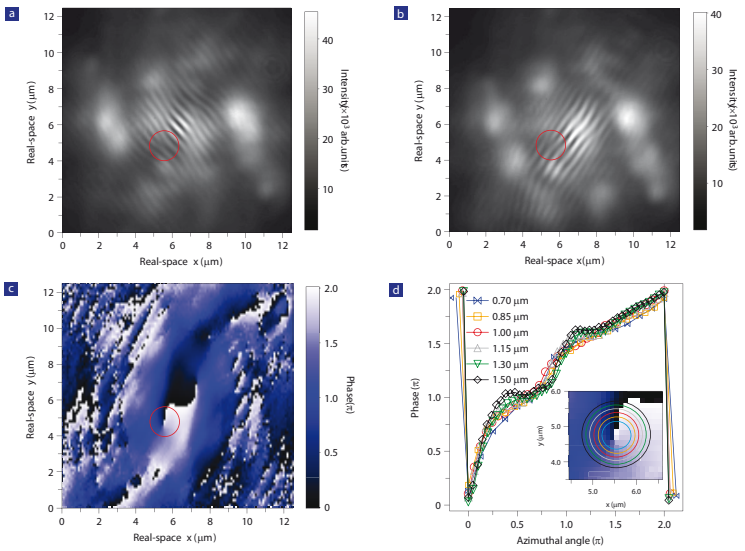

Figure 1.11: Observation of vortices in a polariton condensate from Ref.[19]. (a) Interferogram evidencing a vortex: the typical fork-like dislocation (phase singularity) is visible inside the red circle. (b) Same information, but this time the vortex is overlapped with a different region of the condensate. (c) Real-space phase profile extracted from the interferogram of panel (a). The red circle highlights the vortex (same real-space area as in (a) and (b). (d) Phase as a function of the azimuthal angle for different radii as shown in the inset of (d) (magnification of (c)).

1.2.5.4 Oblique dark solitons

In addition to vortices, various types of solitonic wavefunctions are realizable in two-dimensional BECs. Excitations, such as rarefaction pulses [93], ring solitons [94], and oblique solitons [78], are known to occur depending on the excitation conditions. Especially, in 2006, G. A. El et al. proposed to analyze theoretically the impact of a defect (potential barrier) crossing the flow of a *supersonic* BEC [78]. This experiment, quantum analogue of the one involving e.g. a jet aircraft flying at supersonic velocity in a classical fluid (air), revealed considerable differences between the two systems. Under the assumption that the defect is large enough with respect to the healing length ξ of the condensate to perturb the fluid on length scales comparable to ξ, (pseudo)-topological defects can be nucleated in a quantum fluid. The prediction of Ref.[78] was that a pair of oblique solitons would be generated in the wake of the obstacle and that they would extend without deformation [see Fig.1.12]. One can expect that this kind of solitonic solution in 2D should become

unstable against perturbations. While the stability analysis performed later showed that the soliton is indeed unstable [95], the instability is only convective, which means that the latter is damped while being dragged away downstream from the defect. The oblique solitons are nucleated from the shock waves because of the dispersion of the excitations (which is not linear), and because of the interactions between the particles, which favor the formation of solitons as stable structures. Another way to describe the generation of solitons is the following: The fluid tends to accelerate locally close to the defect [96], and since the velocity field and the phase of the fluid are related via $\mathbf{v} = \hbar/m\boldsymbol{\nabla}\theta$, an important local phase shift is acquired, giving birth to negative interference producing density dips which are nothing but solitons. Increasing the size of the defect leads to larger phase shifts and then more than one pair of solitons can appear to accommodate these phase shifts, leading to *multiplets* of oblique solitons [see Fig.3 of Ref.[78] or Fig.4 of Ref.[21]].

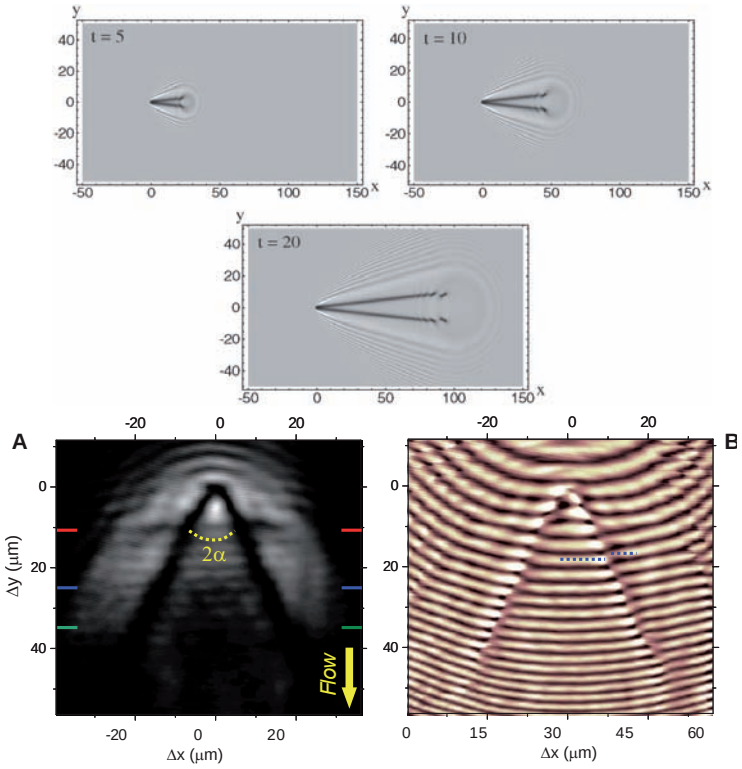

Figure 1.12: Oblique dark soliton. Top (grey) panels: theoretical prediction of their formation past an obstacle from Ref.[78] at 3 different times. The extremities of the soliton exhibit vortex pairs. Bottom panels: experimental observation in a polariton fluid from Ref.[21]. (A) Emission out of the microcavity revealing the solitons accompanied with the expected phase shift along their trajectory (B).

The stationary BEC flow containing a soliton is described by a following solution:

$$v_x = \frac{M\left(1+a^2 n\right)}{\left(1+a^2\right)n} \tag{1.79}$$

$$v_y = -\frac{aM\left(1-n\right)}{\left(1+a^2\right)n} \tag{1.80}$$

$$n\left(\chi\right) = 1-\left(1-p\right)\operatorname{sech}\left[\frac{\sqrt{1-p}}{\sqrt{1+a^2}}\chi\right]^2 \tag{1.81}$$

where $\chi = x - ay$ is a tilted coordinate perpendicular to the oblique soliton (with a the slope of the soliton with respect to the y-axis), $M = v/c$ is the so-called Mach number and $p = M^2/(1+a^2)$. In 1D systems we have seen that the speed of a soliton is related to its depth and it is still true in 2D. Indeed, at fixed value of M, increasing a increases the depth of the soliton and thus reduces its speed. In other words, the more the soliton is tilted with respect to the x-axis, the faster it moves with respect to the condensate, and the shallower and larger it becomes. The phase of the wavefunction can be recovered writing:

$$\theta\left(\mathbf{r}\right) = \frac{m}{\hbar}\int \mathbf{v}\left(\mathbf{r}\right)d\mathbf{r} \tag{1.82}$$

and as in the one dimensional case, the presence of the soliton (and the related density dip) is accompanied with a local phase shift lying between 0 and π. Indeed, the oblique soliton is nothing but 1D soliton for which the second spatial coordinate plays the role of the time. However the strict analogue of the 1D dark soliton doesn't exist in 2D since an oblique soliton cannot have zero velocity ($p = 0$) with respect to the flow. We will see in the section (2.3) how such objects become even more interesting in polariton condensates taking the spin degree of freedom of the particles into account.

1.2.5.5 Quantum hydrodynamic picture

It is often useful to operate not with the wavefunction and the Gross-Pitaevskii equation, but with the equations for density and superfluid velocity, similar to classical hydrodynamics. The Gross-Pitaevskii equation can indeed be rewritten (neglecting quantum pressure) in a set of dynamical equations for the density n and the superfluid velocity $\mathbf{v}$:

$$\frac{\partial n}{\partial t} + \operatorname{div}\left(\mathrm{n}\mathbf{v}\right) = 0 \tag{1.83}$$

$$m\frac{\partial \mathbf{v}}{\partial t} + \boldsymbol{\nabla}\left[m\mathbf{v}^2 + \mu\left(n\right)\right] = 0 \tag{1.84}$$

The first one is nothing but the continuity equation for the flow and the second one an Euler-like equation for a potential flow and zero viscosity fluid. In the presence of some external potential $V(\mathbf{r})$ where the total potential energy of the system becomes

$\mu(n(\mathbf{r})) + V(\mathbf{r})$, and in the simplest case where $\mathbf{v}(\mathbf{r}) = \mathbf{0}$, the density landscape has to satisfy the simple equation:

$$\mu_0 = \mu\left[n\left(\mathbf{r}\right)\right] + V\left(\mathbf{r}\right) \tag{1.85}$$

which embody the ground state profile having a chemical potential μ_0 of the so-called Thomas-Fermi approximation [55] which corresponds to density profiles varying slowly in space. For dilute gases the previously defined hydrodynamics equations can be recovered starting from the Gross-Pitaevskii equation neglecting the quantum pressure (kinetic energy) terms that depend on the spatial derivative. In that regime, the chemical potential grows linearly with n and the equation for the dynamics of $\mathbf{v}$ reads

$$m\frac{\partial \mathbf{v}}{\partial t} + \nabla\left(m\mathbf{v}^2 + \alpha n + V\right) = 0 \tag{1.86}$$

1.3 Quasi-resonant injection

One of the strong assets of the polaritonic system is that it offers the possibility to perform quasi-resonant excitation with a laser pump at any energy, momentum and density, with a well defined spin [see Sec.1.4] (imposed by the polarization of the laser) to form macroscopically occupied and coherent states having a controllable spatial extension. Resonant excitation setups have allowed to shine the light on extremely rich physics: e.g. the bistability [13] and the multistability effect [97], the optical parametric oscillator [12] regime, or the formation of solitons and vortices [21, 98].

1.3.1 Modeling the quasi-resonant injection

1.3.1.1 Driven dissipative Gross-Pitaevskii equation

How does one create-exciton-polaritons? Photons are injected through the Bragg mirrors of the microcavity which have a voluntarily unperfect reflection coefficient $R < 1$, so that the photons are allowed to escape, after interacting with the quantum well excitons, producing a detectable signal for the experimentalist. This photonic leaking determines the polariton radiative lifetime which typically lies in the range from picoseconds to tens of picoseconds. Recently, samples possessing very high quality factors have demonstrated an outstanding polariton lifetime of the order of 30 ps, allowing to analyze the long range ballistic propagation of the quasiparticles [5]. Besides, while the energy of excitation is fixed by the pump laser wavelength, the in-plane momentum of polaritons $\mathbf{k}$ is inherited from the angle γ at which the microcavity is pumped simply following $\mathbf{k} = \omega_P/c \sin(\gamma)\mathbf{u}$, where ω_P is the frequency of the pump.

The simplest quasi-resonant experiment to describe involves a spatially homogeneous and continuous wave (cw) pump. Under such conditions, after a steady state is established, the balance between gains and losses allows to maintain a constant polariton population within the microcavity, fixing the energy of the system associated with a chemical potential μ. Furthermore, exciting the lower polariton branch at (close to) $\mathbf{k} = \mathbf{0}$ makes possible to appy the parabolic dispersion approximation for the dispersion of polaritons. The polariton is therefore associated with an effective mass m^* defined by

$$\frac{1}{m^*} = \frac{1}{m_\phi} + \frac{1}{m_\chi} \tag{1.87}$$

at zero detuning, where m_ϕ and m_χ are the photon and exciton mass respectively. In this framework, the regular time independent Gross-Pitaevskii equation for the polariton mean field $\psi(\mathbf{r}) = \psi_0$ would seem to be a good approximation to describe the macroscopically occupied ground state, just like in the non-resonant case far above the condensation threshold [see Sec.(1.2)].

$$-\frac{\hbar^2}{2m}\Delta\psi_0 + \alpha|\psi_0|^2\psi_0 = \mu\psi_0 \tag{1.88}$$

As we have seen in the section (1.1.2), [see also Eq.(1.42)] the interactions are provided by the excitonic part and depend on the detuning between the photonic and excitonic modes that impacts the excitonic fraction X_L.

However, in the previous description a key ingredient has been omitted. Indeed, in experiments, the frequency ω_P of the pump is obviously fixed and the stationary Gross-Pitaevskii equation would remain valid only assuming a perfect resonance, which would be plausible only in the low pump intensity (low density) regimes. One should keep in mind that the repulsive interactions introduce an extra density dependent and positive energy term $\alpha|\psi_0|^2 = \alpha n_0$, which consequently tends to blueshift the pumped state. As soon as the interactions become significant, keeping a perfect resonance becomes elusive and, at this point, taking into account the injection and lifetime of the particles becomes unavoidable. The first thing is to go back to a time dependent equation. The pump term is accounted for with a plane wave source term $P(\mathbf{r},t) = A_P \exp[i(\mathbf{k}_P \cdot \mathbf{r} - \omega_P t)]$ and the radiative lifetime is phenomenologically introduced via the decay term $-i\hbar\psi(\mathbf{r},t)/2\tau$, τ being the polariton lifetime. These terms can be properly derived using a dissipative Lindblad formalism [30] [see also Sec.3.4]. The modified time dependent Gross-Pitaevskii equation reads:

$$i\hbar\frac{\partial\psi}{\partial t} = -\frac{\hbar^2}{2m}\Delta\psi + \alpha|\psi|^2\psi - \frac{i\hbar}{2\tau}\psi + P \tag{1.89}$$

In this description, the pump spot can have any spatial extension provided that large wavevectors, out of the parabolic approximation, remain unpopulated.

1.3.1.2 Elementary excitations

Due to the presence of a detuning δ_P between the pump frequency and the polariton mode at $\mathbf{k} = \mathbf{0}$ and of the lifetime, the spectrum of elementary excitations strongly differs from the equilibrium one [59, 99]. The spectrum of the homogeneous condensate can be found upon injecting the ansatz

$$\psi(\mathbf{r},t) = e^{i(\mathbf{k}_p\cdot\mathbf{r}-\omega_p t)}\left(\psi_0 + Ae^{+i(\mathbf{k}\cdot\mathbf{r}-\omega t)} + B^* e^{-i(\mathbf{k}\cdot\mathbf{r}-\omega^* t)}\right) \tag{1.90}$$

into Eq.(1.89) and following the same linearization procedure as in the section (1.2.4). It gives the following set of coupled equations

$$\left[E(k_p) - \hbar\omega_p + \alpha|\psi_0|^2 - \frac{i\hbar}{\tau}\right]\psi_0 + A_P = 0 \tag{1.91}$$

$$\left[E(\mathbf{k}_p+\mathbf{k}) - \hbar\omega_p - \hbar\omega + 2\alpha|\psi_0|^2 - \frac{i\hbar}{\tau}\right]A + \alpha\psi_0^2 B = 0 \tag{1.92}$$

$$\alpha\left(\psi_0^2\right)^* A + \left[E(\mathbf{k}_p-\mathbf{k}) - \hbar\omega_p + \hbar\omega + 2\alpha|\psi_0|^2 - \frac{i\hbar}{\tau}\right]B = 0 \tag{1.93}$$

and the corresponding four dispersion branches are found to be

$$\hbar\omega_+(\mathbf{k}) = \hbar\omega_P(\mathbf{k}_P) + \sqrt{\left[E_{LPB}(\mathbf{k}) - \hbar\omega_P + 2\alpha n\right]^2 - [\alpha n]^2} \tag{1.94}$$

$$\hbar\omega_-(\mathbf{k}) = \hbar\omega_P(\mathbf{k}_P) - \sqrt{\left[E_{LPB}(\mathbf{k}) - \hbar\omega_P + 2\alpha n\right]^2 - [\alpha n]^2} \tag{1.95}$$

Here $E_{LPB}(\mathbf{k})$ is the bare dispersion relation of the lower polariton modes. The main difference between the macroscopic occupation of a mode driven by an external pump and the usual equilibrium situation is that the dispersion of elementary excitations can exhibit diffusive flat parts for $\delta_P > \mu_0$ or a gap for $\delta_P < \mu$, and the linear Bogoliubov spectrum is recovered only when the detuning is exactly compensated by the interaction energy which means that $\hbar\delta_P = \alpha n_0 = \mu_0$ as shown in Fig.1.13. Besides, the imaginary parts of the dispersion branches, which can have positive for large values of δ_P, leads to possible instabilities.

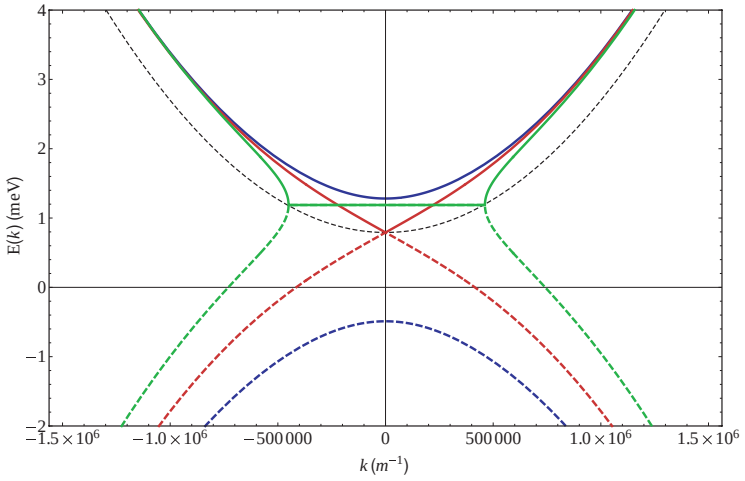

Figure 1.13: Dispersion of elementary excitations of a driven mode at $k = 0$ for 3 values of the detuning: $\delta = 0.5\mu_0$ (blue lines), $\delta = \mu_0$ (red lines) and $\delta = 1.5\mu_0$ (green lines). The dashed parts are the negative energy branches. The dashed black line stands for the bare dispersion of the particles E_{LPB} assumed to be parabolic here.

1.3.1.3 Exciton/photon representation

Now, to model accurately the polaritonic system fully taking into account its non-parabolic dispersion, it is convenient to separate the excitonic field $\chi(\mathbf{r}, \mathbf{t})$ from the photonic one $\phi(\mathbf{r}, \mathbf{t})$ coupled by the strong light matter interaction described by the Rabi frequency Ω_R. Each field is associated with a particle mass $m_{\phi,\chi}$. Forgetting first about the pumping and decay terms, analogically to the previous single-field description, the energy of the system reads

$$E = \int \left\{ \frac{\hbar^2}{2m_\phi} |\boldsymbol{\nabla}\phi|^2 + \frac{\hbar^2}{2m_\chi} |\boldsymbol{\nabla}\chi|^2 + \frac{\alpha}{2}|\chi|^4 + \frac{\hbar\Omega_R}{2}\left(\chi^*\phi + \chi\phi^*\right) \right\} d\mathbf{r} \qquad (1.96)$$

The dynamics of the photonic and excitonic fields can be found from the following Lagrange equations:

$$i\hbar\frac{\partial\phi}{\partial t} = \frac{\partial E}{\partial\phi^*} \tag{1.97}$$

$$i\hbar\frac{\partial\chi}{\partial t} = \frac{\partial E}{\partial\chi^*} \tag{1.98}$$

to obtain the following coupled set of modified Schrödinger and Gross-Pitaevskii equations

$$i\hbar\frac{\partial\phi}{\partial t} = -\frac{\hbar^2}{2m_\phi}\Delta\phi - \frac{i\hbar}{2\tau_\phi}\phi + \frac{\hbar\Omega_R}{2}\chi + P \tag{1.99}$$

$$i\hbar\frac{\partial\chi}{\partial t} = -\frac{\hbar^2}{2m_\chi}\Delta\chi + \alpha|\chi|^2\chi - \frac{i\hbar}{2\tau_\chi}\chi + \frac{\hbar\Omega_R}{2}\phi \tag{1.100}$$

Here, we have added the phenomenological lifetimes $\tau_{\phi,\chi}$ of the particles and the pumping term P that obviously enters the photonic dynamics solely, while the interactions are restricted to the excitonic part. Their strength given by $\alpha = 6E_b a_B^2/S$ doesn't depend on the excitonic fraction anymore the latter being self consistently taken into account in the field separation. The set of equations (1.99) and (1.100) is especially accurate describing the resonant polariton injection and will be used many times to describe various effects along this manuscript.

1.3.2 Optical parametric oscillator

One of the most striking results demonstrating the bosonic character of polaritons was reported first by Savvidis et al. in 2000 [12]. The authors have observed the stimulated scattering of polaritons within a pump-probe experiment. They basically varied the angle of the resonant excitation to tune the in plane wavevector of the injected polaritons. A sketch of the experimental setup is shown in Fig.1.14(b). The cavity had a variable thicknesses around the average value of $3\lambda/2$ which allowed to access different detunings. In the zero detuning case, the lower polariton branch was excited at variable the angle of the pump beam. A weak probe was used to excite the $k = 0$ state providing an initial population. In weak pumping regime, the reflected spectrum showed the two polariton peaks separated by the Rabi splitting, which was about 7 meV. When the pump is switched on and for small pump-probe delays τ, an enhancement of the emission of the lower polariton branch was observed. For a specific angle of $\theta = 16.5$, the so-called magic angle, the emission rises up to a gain of 70. The measured intensity is shown in Fig.1.14(c).

This process can be understood as the scattering of two polaritons from the pump, having a wavevector $\mathbf{k}_P$, to a signal polariton at $\mathbf{k} = \mathbf{0}$ and an idler polariton at $2\mathbf{k}_P$. This is possible close to the magic angle, which fulfills the energy and momentum conservation $E(2k_P) + E(0) = 2E(k_P)$. The process is sketched on Fig.1.14(a). This experiment brought a strong support to the polariton picture and offered three new features: First, polaritons can scatter strongly on each other,

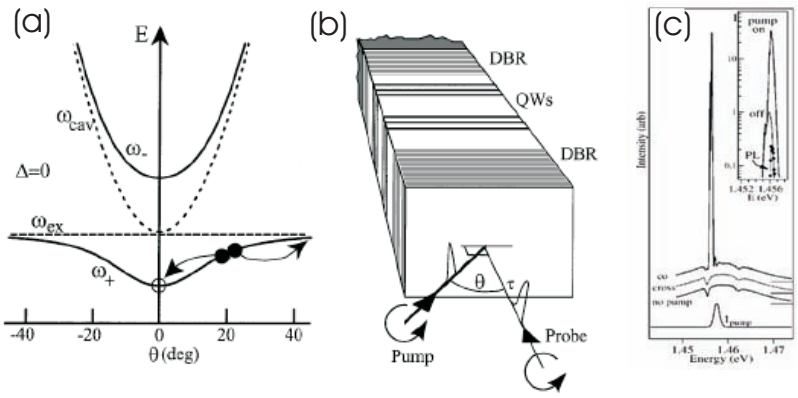

Figure 1.14: Savvidis et al. experiment [12]: (a) Scheme of the parametric scattering, (b) experimental setup and (c) Reflected probe spectra at $\tau = 0$ ps for pump off, co-, and cross-circularly polarized to the probe. Pump spectrum on lower trace. Inset: Reflected narrow band probe spectra at $\tau = 0$ ps, with pump pulse on/off, together with pump photoluminescence without probe pulse (black dots).

provided that both energy and momentum conservations are simultaneously satisfied in the two-particle collision. This effect requires a nonparabolic dispersion. Second, polariton scattering can be enhanced by the occupation of the final state. In other words, polariton scattering can be stimulated, as it is expected for bosons. Third, polaritons can be present in relatively large numbers at the bottom of the polariton trap in spite of their short lifetime governed by photon decay.

There are different ways to describe the parametric scattering effect. We will briefly present the *semiclassical* description and the three-level quantum model developed by Ciuti et al. (2000) [100].

1.3.2.1 Semiclassical description

The parametric scattering can be described using simple rate equations. These rate equations for occupation numbers are closely linked to the Boltzmann equations. The advantage of the description is that it allows to account easily for all interaction processes affecting the polariton relaxation. The important disadvantage is that the description of the polariton dispersion can not be easily included in this model. In the resonant configuration one can single out the states, where the energy-momentum transfer is very efficient and dominates the system, neglecting all other states. This leads in the simplest case to a three-level model containing the ground or *signal* state, the *pump* state and the *idler* state. The losses, such as the dominant radiative decay and the scattering processes driven by disorder, can be taken into account by phenomenological decay rates. The disorder effects are neglected in this

model, but scattering with phonons can be included.

The system can be written as a set of three equations

$$\partial_t n_0 = P_0 - \Gamma n_0 - \alpha n_0 n_i (n_p+1)^2 + \alpha\,(n_0+1)\,(N_i+1)\,n_p^2 \quad (1.101)$$

$$\partial_t n_p = P_p - \Gamma n_p + 2\alpha n_0 n_i (n_p+1)^2 - 2\alpha\,(n_0+1)\,(N_i+1)\,n_p^2 \quad (1.102)$$

$$\partial_t n_i = P_i - \Gamma n_i - \alpha n_0 n_i (n_p+1)^2 + \alpha\,(n_0+1)\,(N_i+1)\,n_p^2 \quad (1.103)$$

The corresponding linewidth broadening can be written as

$$\frac{1}{\Gamma} = \frac{|\chi_k|^2}{\Delta + \Gamma_{ph}} + \frac{|\phi_k|^2}{\gamma_\phi}, \quad (1.104)$$

where χ_k and ϕ_k are the exciton and photon Hopfield coefficients, respectively, Δ is the so-called exciton inhomogeneous broadening, Γ_{ph} is the phonon-induced broadening and γ_ϕ is the cavity-photon broadening. At low temperatures $\Gamma_{ph} \ll \Delta$ and in most of the cavity samples $\Delta \approx \gamma_C$. We will use Γ as a decay constant. Here

$$\alpha = \frac{2\pi}{\hbar^2}\frac{|M|^2}{\pi\Gamma/2}. \quad (1.105)$$

M is the polariton-polariton matrix element of interaction, which is here approximately equal to one fourth of the exciton-exciton matrix element of interaction. This system can be easily solved numerically. In the *cw* excitation case $P_0 = P_i = 0$, it gives $n_0 = n_i$ and the system can be reduced to two equations. Using the evolution equation for the ground state population

$$\partial_t n_0 = n_0\,(W_{in} - W_{out}) + W_{in}, \quad (1.106)$$

where W_{in} and W_{out} include all channels for incoming and outgoing polaritons, respectively. The threshold of parametric scattering is given by the condition $W_{in} - W_{out} = 0$ which implies:

$$n_0 = \frac{\alpha n_p^2 - \Gamma}{\alpha(2n_p+1)}. \quad (1.107)$$

The population n_0 should be positive or zero which is given by $n_p = \sqrt{\Gamma/\alpha}$ and using $n_p \approx P/\Gamma$ yields

$$P_{thres} = \Gamma\sqrt{\frac{\Gamma}{\alpha}} = \gamma\frac{\hbar\Gamma}{2|M|} \quad (1.108)$$

for the threshold of parametric scattering.

1.3.2.2 Quantum model

A quantum model has been developed by Ciuti et al. [100] and is similar to the Gross-Pitaevskii approach discussed previously, but considering three modes. The starting point is the Hamiltonian, where interactions with phonons and free carriers

are neglected. To obtain the equation of motion for polariton operators a_k and $a_k^\dagger$ we write the Heisenberg equation:

$$i\hbar\frac{da_k}{dt} = [a_k, H] = E_{LP}(k)\,a_k + \sum_{k,k''} E^{int}_{k,k',k''} a^\dagger_{k'+k''-k} a_{k'} a_{k''} + P(k) \quad (1.109)$$

$$i\hbar\frac{da_k^\dagger}{dt} = \left[a_k^\dagger, H\right] = E^*_{LP}(k)\,a_k^\dagger - \sum_{k,k''} E^{int}_{k,k',k''} a_{k''} a_{k'} a^\dagger_{k'+k''-k} + P(k) \quad (1.110)$$

where E_{LP} is the lower polariton branch dispersion relation. The interaction energy reads

$$E^{int}_{k,k',k''} = \frac{1}{2}(V_{k',k'',k-k'} + V_{k',k'',k''-k}), \quad (1.111)$$

and $P(k)$ is a source term induced by an external pumping field. Once again, only the signal, pump, and idler states are considered, and it is assumed that all states are macroscopically and coherently occupied. In other words, the states are assumed to behave as classical coherent fields and one can replace them by there c-numbers as first proposed by Bogoliubov [54]. Ciuti et al. used the same approximations but assuming three macroscopically occupied states. Keeping the signal and idler state operators and replacing the pump state by a complex number, one can consequently describe the system by the following set:

$$i\hbar a_0 = \tilde{E}_{LP}(0)\,a_0 + E_{int} a^\dagger_{2k_p} P^2_{k_p} + P_{probe}(t) \quad (1.112)$$

$$i\hbar P_{k_p} = \tilde{E}_{LP}(k_p)\,P_{k_p} + E_{int} P^*_{k_p} a_0 a_{2k_p} + P_{pump}(t) \quad (1.113)$$

$$i\hbar P_{2k_p} = \tilde{E}_{LP}(2k_p)\,a^\dagger_{2k_p} + E^*_{int} a_0 P^{*2}_{k_p}, \quad (1.114)$$

where

$$\tilde{E}_{LP}(0) = E_{LP}(0) + 2V_{0,k_p,0}|P_{k_p}|^2 \quad (1.115)$$

$$\tilde{E}_{LP}(k_p) = E_{LP}(k_p) + 2V_{k_p,k_p,k_p}|P_{k_p}|^2 \quad (1.116)$$

$$\tilde{E}_{LP}(2k_p) = E_{LP}(2k_p) + 2V_{2k_p,k_p,0}|P_{k_p}|^2 \quad (1.117)$$

and

$$\tilde{E}_{int} = \frac{1}{2}\left(V_{k_p,k_p,k_p} + V_{k_p,k_p,-k_p}\right) \quad (1.118)$$

The advantage of this formalism with respect to the one presented in the previous section is that it allows one to account for the energy renormalization processes driven by the inter-particle interaction. Here, a blueshift of the three states considered is induced by the pump intensity. The blueshift itself can result in another nonlinear effect, which will be discussed in the next section namely the bistability. On the other hand, spontaneous scattering processes and the phonon scattering cannot be described in this framework. This system of equations can be solved numerically replacing all operators by complex numbers. Finally, further treatments given in detail e.g. in Ref.[30] result in a similar equation for the parametric scattering threshold. This illustrates the equivalence of the semi-classical and quantum models in this context.

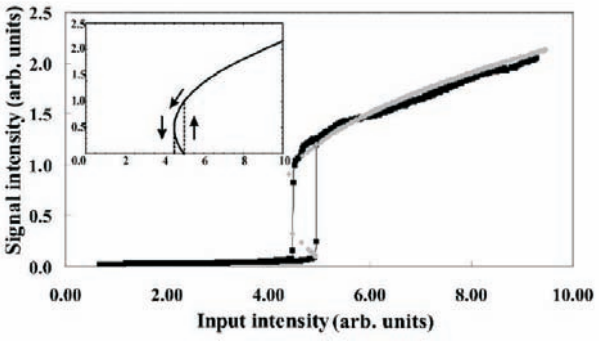

Figure 1.15: Experimental observation of the bistability cavity polaritons from Ref.[102]: Variations of the signal output power (in transmission) as a function of the pump power for a pump detuning $\delta = -0.42$ meV. The gray curve is the result of a theoretical fit. The inset shows more clearly the unstable branch and the series of intermediate states that are obtained when varying the input intensity in both directions.

1.3.3 Bistability

An important feature of the resonant excitation scheme is the renormalization of the polariton energies. This renormalization is observed in the polariton emission, but it plays also a key role in the absorption of the light from the pump. Two situations can be distinguished: First, if the laser energy (frequency) is *below* the bare polariton energy (negative detuning), the absorption is simply reduced by the pump-induced blue shift, which drives the mode out of the resonance. Second, if the laser energy lies *above* the bare polariton energy (positive detuning), the polariton energy gets closer to the pump energy owing to the blueshift, which in turn increases the blueshift, that enhances the absorption and so on.

In the case of positive detuning, two different regimes can be distinguished in that case. Indeed, while at low pump intensities the polariton energy remains below the pump energy, at higher pump intensities the polariton gets over the pump energy and stabilizes above it. It results in a dramatic increase in the population of the pump state, and the absorption becomes maximum. The threshold is called bistable threshold, since two polariton populations are possible for the same pump intensity. Besides, this effect can result as well from the saturation of the exciton oscillator strength [101]. The bistability phenomenon was first observed experimentally in 2004 by Baas et al. [102]. Also the interplay between the two nonlinear effects (parametric amplification and bistability) opened a wide field of research [103, 104].

In order to theoretically analyze the bistability, the dynamics of the pump state can be written as follows

$$\partial t \bar{P}_{k_p} = i\left(\omega_{k_p} - \omega_p + i\Gamma_{k_p}\right)\bar{P}_{k_p} + \frac{2}{\hbar}V_{k_p,k_p,k_p}\left|\bar{P}_{k_p}\right|^2\bar{P}_{k_p} + P_{pump}\left(t\right) \qquad (1.119)$$

Then multiplying Eq.(1.119) by its complex conjugate and replacing $\bar{P}_{k_p}$ by the

population of the pump state and $|\bar{P}_{k_p}|^2$ by the pump intensity I_p, one gets:

$$I_p = \left[\left((\omega_{k_p} - \omega_p) + \frac{2}{\hbar} V_{k_p,k_p,k_p} N_p \right)^2 + \Gamma_{k_p}^2 \right] N_p \tag{1.120}$$

The experimental observation of the bistability of cavity polaritons [102] is shown in Fig.(1.15). The emission versus the pump intensity shows the typical s-shape. Increasing the pump intensity from the lower branch results in a clear jump of the population at the turning point 1 (higher pumping power). Starting now from the upper branch and decreasing the pump intensity, the population drops down at the turning point 2 (lower pumping power). It basically corresponds to a hysteresis cycle, when the pump intensity is stepwise increased and decreased. The part of the curve, which connects the two turning points is unstable, which can be found from stability analysis using Lyapunov exponents and adding a small perturbation to the model. The turning points can be found under the condition $dI_p/dN_p = 0$, yelding:

$$3\left(\frac{2}{\hbar} V_{k_p,k_p,k_p}\right)^2 N_p^2 + 4\left(\omega_{k_p} - \omega_p\right)^2 + \Gamma_{k_p}^2 = 0 \tag{1.121}$$

The bistability region is defined by the existence of two distinct positive solutions for this quadratic equation leading to

$$\omega_p > \omega_{k_p} + \sqrt{3}\Gamma_{k_p}. \tag{1.122}$$

It follows directly from this condition, that it is necessary to pump at least one linewidth above the bare polariton state to observe the bistability. Consequently the solution for the turning points reads

$$N_p = \frac{2\hbar\left(\omega_{k_p} - \omega_p\right) \pm \sqrt{\left(\omega_{k_p} - \omega_p\right)^2 - 3\Gamma_{k_p}^2}}{6V_{k_p,k_p,k_p}} \tag{1.123}$$

The solution with the minus sign corresponds to the turning point with the higher pumping intensity. Plugging Eq.(1.123)into Eq.(1.120) defines the threshold for the pumping intensity.

1.4 Spin sensitive phenomena

So far we have been neglecting any spin-dependent phenomena and we have seen that this simplified vision was sufficient to describe the fundamental features of the exciton-polaritons. However, as we will see in this section, taking into account the two possible spin projections of polaritons allows to shine the light on a bestiary of fascinating effects that merge both fundamental and applied concepts. Under resonant pumping, the spin of the particles is under complete control from the polarization of the input laser (except the multistable case), that has to be right (left) circularly polarized in order to excite spin-up (down) polaritons. On the contrary, under non-resonant pumping conditions, above the condensation threshold, the polariton condensate forms with a well-defined linear polarization which corresponds to a linear combination of spin-up and spin-down polaritons due to the spin anisotropy of the polariton interactions [9] and to built-in splitting between linear polarizations. We discuss in this section the spin dependent phenomena, focusing especially on the spinor polariton condensate and its topological excitations. We refer to the exhaustive review by Shelykh et al. [14] for further details.

1.4.1 The spin of exciton-polaritons

In the domain of the mesoscopic physics, spintronics [105] is currently one of the most promising areas. The main idea of this discipline, based on the quantum properties of the electrons and/or holes, is to achieve the control of the spins of individual carriers which would potentially have a huge impact on future information technologies. Although currently, the applications of spintronics rely on giant magneto-resistance effect in metals only, there are good perspectives that in the future, semiconductor spintronic devices, which now still remain at the stage of the theoretical modeling, will find their way to practical implementations.

One of the most serious obstacles to the realization of spintronic components is a dramatic role played by the processes of spin relaxation. In this context, it was proposed that the optical counterpart of spintronics, namely spin-optronics [106] would represent a valuable alternative, since characteristic decoherence times of exciton-polaritons are orders of magnitude longer than decoherence times of electrons and holes [107]. Let us introduce here the spin structure of exciton-polaritons.

An exciton is formed by an electron and hole, namely by two fermions having a projections of their angular momenta equal to $J_z^e = S_z^e = \pm 1/2$ for an electron in the conduction band with S-symmetry and $J_z^h = S_z^e + M_z^h = \pm 1/2, \pm 3/2$ for a hole in the valence band with P-symmetry. The states having $J_z^h = \pm 1/2$ appear if the spin projection of the hole S_z^h is antiparallel to the projection of its mechanical momentum M_z^h, these states are called light holes. On the contrary, if the spin and the mechanical momentum are parallel, the heavy holes with $J_z^h = \pm 3/2$ are formed.

In the bulk samples, at $\mathbf{k} = \mathbf{0}$ the light and heavy hole states are degenerate. However, in quantum wells the confinement in the direction of the structure growth axis lifts this degeneracy so that energy levels of the heavy holes lie closer to the

bottom of the well than the light-hole levels. The ground state exciton is thus formed by an electron and a heavy-hole. The total exciton angular momentum J (in the following it will be referred to as the exciton's spin) has the allowed projections ± 1 and ± 2 on the structure's growth axis. Bearing in mind that the photon's spin is ± 1 and that the spin is conserved in the processes of photoabsorption, the excitons with spin projections equal ± 2 cannot be optically excited. These are the so-called *dark states*. In microcavities they are not coupled with the photonic mode so we can safely neglect them in the following considerations. We note, however, that in some cases the dark states come into play: they can be mixed with the bright states by an in-plane magnetic field or, despite the fact that they are optically inactive, their presence can obviously modify the scattering processes. The bright excitons having ± 1 spin projections couple efficiently to light to form exciton-polaritons with the same spin. It follows that exciton-polaritons behave as a two-level spin system similar to electrons, but they are bosonic particles (with integer spin) in the low density limit.

The conservation of the spin during photoabsorption allows to orient the spins of excitons by polarized light beams: the optical orientation, an effect that impacts also the polarization of associated photoluminescence. A σ_+ (σ_-) circularly polarized light excites states with angular momenta $J = +1$ ($J = -1$). Besides, linearly polarized light excites a linear combination of $J = +1$ and $J = -1$ exciton states, so that the total exciton spin projection on the structure axis is exactly zero in this case. Optical orientation of carrier's spins in bulk semiconductors was discovered by a Georges Lampel in 1968 [108]. In quantum wells, it has been extensively studied since the 1980s. This mechanism is especially useful in resonant pumping experiments, where the polarization of the pump laser allows a complete control of the spin of polaritons.

1.4.2 Pseudospin representation

We introduce here the pseudospin vector [109] extensively used for electrons, applied to the polaritonic system. This representation is very convenient to describe the spin dynamics of the particles and will be used at many occurrences in the next chapters. Exciton-polaritons with a given in-plane wavevector $\mathbf{k}$ can be treated as a two level system described by the density matrix ρ_k, completely analogous to the spin density matrix of electrons. ρ_k can be decomposed on a set consisting in the density matrix $\mathbf{I}$ and the three Pauli matrices $\sigma_{x,y,z}$

$$\rho_k = \frac{N_k}{2}\mathbf{I} + \mathbf{S}_k \cdot \boldsymbol{\sigma} \tag{1.124}$$

Here $\mathbf{S}_k$, giving the coefficient of the decomposition, is the pseudospin vector of the state with wavevector $\mathbf{k}$, namely a three dimensional vector lying on a Poincaré sphere. Its components $(S_x, S_y, S_z)^T$ completely determine the spin states (and the polarization of the corresponding emission). In particular, the in-plane components, lying on the equator of the sphere, define the linear polarization states: S_x

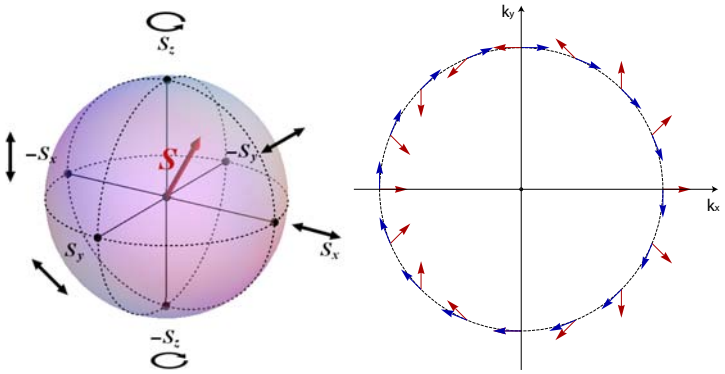

Figure 1.16: Left panel: a pseudospin vector (red arrow) on the Poincaré sphere, the black arrows illustrate the corresponding polarization of light. Right panel: effective magnetic field induced by the TE-TM splitting (red arrows) versus the Rashba spin-orbit field (blue arrows) on an elastic ring (dashed black circle).

and S_y are the degrees of linear polarization in the horizontal/vertical and diagonal/antidiagonal directions respectively (which means that the pseudospin makes a double angle with respect to the polarization direction) while the S_z projection gives the degree of circular polarization of the emission corresponding to the spin state +1 ($\mathbf{S} = S_z \mathbf{u}_z$) and -1 ($\mathbf{S} = -S_z \mathbf{u}_z$) [see left panel of Fig.1.16].

Considering first noninteracting polaritons, the dynamics of the density matrix is governed by the Liouville-von Neumann equation

$$i\hbar \frac{\partial \rho_k}{\partial t} = [H_k, \rho_k] \tag{1.125}$$

The corresponding Hamiltonian reads

$$H_k = E(k) - \mathbf{H}_{eff,k} \cdot \mathbf{S}_k \tag{1.126}$$

where $E(k)$ is the polariton dispersion branch under consideration (the lower one in the following) and the second term is the magnetic energy term, H_{eff} being an effective magnetic field. The latter term minimizes the total energy of the system when $\mathbf{H}_{eff,k}$ and $\mathbf{S}_k$ are aligned and have the same orientation. The word "effective" means that we are not dealing with real magnetic fields involving the exciton's g factor that would mix the dark and bright states – H_{eff} applies to the bright states only. For the noninteracting case we consider, the effective field lies in the plane of the microcavity. It is called effective, since mathematically it enters the equation the same way as a real magnetic field would do.

1.4.3 TE-TM splitting and linear spin dynamics

In 1993 Maialle et al. [110] have shown that the Bir-Aronov-Pikus spin relaxation mechanism [111] involving the spin-flip exchange interaction of electrons and holes is predominant for the confined quantum-well excitons. The long-range electron-hole

interaction leads to the longitudinal-transverse splitting of exciton states (or TE-TM splitting), i.e. the energy splitting between excitons having a dipole moment parallel (TM) and perpendicular (TE) to the wave-vector. This splitting is responsible for rapid spin relaxation of excitons in quantum wells. The difference between spin relaxation dynamics of exciton polaritons and spin relaxation of pure excitons is expected to come from the different shape of dispersion curves and, consequently, different energy relaxation dynamics. The Maialle mechanism of spin relaxation is strongly enhanced because of an additional splitting of the TE and TM polarized photonic modes in the cavities. It is also essential that the final state bosonic stimulation is much more efficient for polaritons than for pure excitons, which makes collective effects in their spin dynamics extremely important. The TE-TM splitting (or LT splitting) can be mapped to the effective in plane magnetic field $\mathbf{H}_{eff} = \mathbf{H}_{LT}$ acting on the polariton pseudospin. $\mathbf{H}_{LT}$ being an analogue of the Rashba spin orbit field acting on electron, possesses however some very peculiar properties as we will see now.

Indeed, the polariton eigen modes within the microcavity are TE and TM linearly polarized and these states are by definition dependent on the direction (given by $\mathbf{k}$) of propagation of the particles. On an elastic circle ($\|\mathbf{k}\|$ kept constant) around the origin in reciprocal space, the TM state having polarization direction parallel to $\mathbf{k}$ therefore corresponds to a pseudospin vector $\mathbf{S}$ making a double angle with respect to $\mathbf{k}$. The consequence is that the orientation of $\mathbf{H}_{LT}$ makes a double angle with respect to the wavevector as well, while the Rashba field is always aligned with $\mathbf{k}$ [112] [see right panel of Fig.1.16].

The strength of $\mathbf{H}_{LT}$ is defined by the energy splitting between the polaritonic TE and TM modes. The degeneracy of the TE-TM photonic and excitonic eigen modes is lifted, considering that they demonstrate different effective masses. The direct consequence is that the TE-TM splitting for the bare modes grows quadratically with k and is exactly zero at $\mathbf{k} = \mathbf{0}$. The corresponding bare photonic (ϕ) and excitonic (χ) dispersion branches are defined by

$$E_{\phi}^{TE}(\mathbf{k}) = \frac{\hbar^2 k^2}{2m_{\phi}^{TE}} + \delta,\ E_{\chi}^{TE}(k) = \frac{\hbar^2 k^2}{2m_{\chi}^{TE}} \tag{1.127}$$

$$E_{\phi}^{TM}(\mathbf{k}) = \frac{\hbar^2 k^2}{2m_{\phi}^{TM}} + \delta,\ E_{\chi}^{TM}(k) = \frac{\hbar^2 k^2}{2m_{\chi}^{TM}} \tag{1.128}$$

where we have allowed for a detuning δ between the excitonic and photonic modes at $\mathbf{k} = \mathbf{0}$. The associated TE and TM polariton branches are uncoupled being (orthogonal) eigen modes and are found from the eigen values of the matrices [see Sec.1.1.1 for the spinless two oscillators model]

$$M_{TE}(\mathbf{k}) = \begin{pmatrix} E_{\phi}^{TE}(\mathbf{k}) & \hbar\Omega_R \\ \hbar\Omega_R & E_{\chi}^{TE}(\mathbf{k}) \end{pmatrix} \tag{1.129}$$

$$M_{TM}(\mathbf{k}) = \begin{pmatrix} E_{\phi}^{TM}(\mathbf{k}) & \hbar\Omega_R \\ \hbar\Omega_R & E_{\chi}^{TM}(\mathbf{k}) \end{pmatrix} \tag{1.130}$$

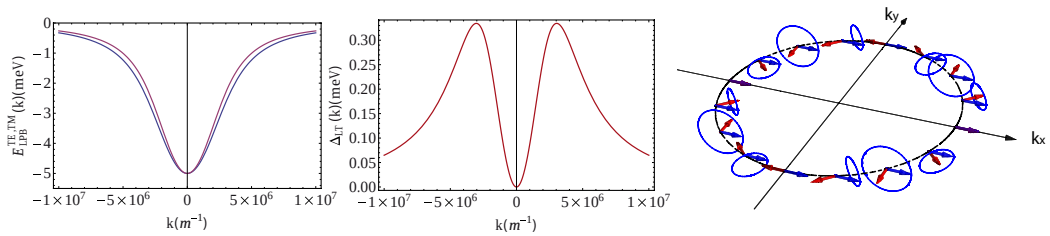

Figure 1.17: TETM splitting and pseudospin precession. Left panel: lower TE (blue line) and TM (purple line) branches, central panel: TETM splitting and right panel: pseudospin (blue arrows) precession (blue circle) around $\mathbf{H}_{LT}$ (red arrows) on an elastic circle (dashed black line) in reciprocal space.

giving the lower $E_L^{TE,TM}(\mathbf{k})$ and upper $E_U^{TE,TM}(\mathbf{k})$ dispersion branches:

$$E_L^{TE} = \frac{E_\phi^{TE}+E_\chi^{TE}}{2} - \frac{1}{2}\sqrt{\left(E_\phi^{TE}-E_\chi^{TE}\right)^2+4\hbar^2\Omega_R^2} \tag{1.131}$$

$$E_L^{TM} = \frac{E_\phi^{TM}+E_\chi^{TM}}{2} - \frac{1}{2}\sqrt{\left(E_\phi^{TM}-E_\chi^{TM}\right)^2+4\hbar^2\Omega_R^2} \tag{1.132}$$

$$E_U^{TE} = \frac{E_\phi^{TE}+E_\chi^{TE}}{2} + \frac{1}{2}\sqrt{\left(E_\phi^{TE}-E_\chi^{TE}\right)^2+4\hbar^2\Omega_R^2} \tag{1.133}$$

$$E_U^{TM} = \frac{E_\phi^{TM}+E_\chi^{TM}}{2} + \frac{1}{2}\sqrt{\left(E_\phi^{TM}-E_\chi^{TM}\right)^2+4\hbar^2\Omega_R^2} \tag{1.134}$$

Focusing on the lower branch, where the condensation usually takes place and that will be under consideration in the following, the strength of the TE-TM splitting is simply defined by

$$\Delta_{LT}(\mathbf{k}) = E_L^{TE}(\mathbf{k}) - E_L^{TM}(\mathbf{k}) \tag{1.135}$$

The values of the TE and TM masses are dependent on the structure under consideration, and both $m_{\phi,\chi}^{TE} > m_{\phi,\chi}^{TM}$ and $m_{\phi,\chi}^{TE} < m_{\phi,\chi}^{TM}$ situation are possible, which basically changes only the sign of Δ_{LT}. This interrelation depends on the detuning of the frequency of the cavity photon mode from the center of the stop-band of the distributed Bragg mirrors [113]. Besides, while the TE-TM splitting grows quadratically with $\mathbf{k}$ for the bare modes, the exciton-photon mixing modifies this dependence and it demonstrates a maximum value at finite $\mathbf{k}$ as it was observed experimentally in Ref.[107]. We also point out that an energy splitting at $\mathbf{k}=\mathbf{0}$ is possible and has been e.g. reported in a CdTe microcavities, leading to a pinning of the linear polarization along a crystallographic axis [114]. The latter effect actually induces a $\mathbf{k}$-independent effective magnetic field pointing in a well defined direction determined by the crystallographic axis. Finally, we note that the excitonic TE-TM splitting is usually orders of magnitude lower than its photonic counterpart and can be safely neglected. The left panel of Fig.1.17 shows the split lower TE-TM dispersion branches while the central panel gives the k-dependance of the splitting Δ_{LT}.

The global expression for TE-TM effective magnetic field reads

$$\mathbf{H}_{LT}(\mathbf{k}) = \Delta_{LT}(\mathbf{k}) \begin{pmatrix} \cos(2\phi) \\ \sin(2\phi) \end{pmatrix} \tag{1.136}$$

where ϕ is the polar angle in reciprocal space. The specific orientation of $\mathbf{H}_{LT}$ can now be better understood. Indeed, for particles propagating along the x-direction the TM state corresponds to x-polarized particles while for the y-direction it corresponds to y polarized particles and reciprocally for TE states. The dispersions of the x and y polarized particles are consequently anisotropic and H_{LT} has an opposite orientation with respect to x and y propagation directions and by extension the same applies for any orthogonal directions. The field therefore makes a double angle with respect to the propagation direction of the particles defined by their wavevector $\mathbf{k}$ as previously mentioned.

The Eq.(1.125) allows to derive the dynamical equation for the pseudospin

$$\frac{\partial \mathbf{S}_k}{\partial t} = \frac{\mathbf{H}_{eff}}{\hbar} \times \mathbf{S}_k \tag{1.137}$$

which is nothing but a regular precession equation of $\mathbf{S}$ around $\mathbf{H}_{eff}$. In particular, no evolution of $\mathbf{S}$ is obtained when the vectors have the same direction, while the precession demonstrates a maximum amplitude when $\mathbf{S} \perp \mathbf{H}_{eff}$. This description is accurate, provided that the kinetic energy term is negligible with respect to the (effective) magnetic term which means that $-\mathbf{H}_{eff,k} \cdot \mathbf{S}_k \gg E(k)$. The right panel of Fig.1.17 shows the pseudospin (blue arrows) precession (blue circles) around $\mathbf{H}_{LT}$ (red arrows) on an elastic circle (dashed black line). The initial pseudospin is assumed to lie along the x-axis (linear horizontal polarization).

The full picture can be obtained writing the energy of the system on the exciton-photon basis [see Eq.(1.96)], which allows to avoid the complicated expression for the nonparabolic dispersions defined above, introducing the spin and the effective field. First, the two allowed polariton spin projections are included considering vectorial fields $\boldsymbol{\phi} = (\phi_+, \phi_-)^T$ and $\boldsymbol{\chi} = (\chi_+, \chi_-)^T$ where the indices $\pm$ means that we will work here on the natural circular polarization basis corresponding to polaritons states with spin ± 1. Second, the link between the fields and the pseudospin representation is made via the density matrix ρ of the system. Considering only the photonic field which is the measurable quantity from the emission escaping the microcavity, one can write the density matrix in both the pseudospin and the field representations

$$\rho = \frac{n}{2}\mathbf{I} + \mathbf{S} \cdot \boldsymbol{\sigma} \tag{1.138}$$

$$\rho = \begin{pmatrix} |\phi_+|^2 & \phi_+ \phi_-^* \\ \phi_- \phi_+^* & |\phi_-|^2 \end{pmatrix} \tag{1.139}$$

where $\mathbf{S} = (S_x, S_y, S_z)^T$ and $\boldsymbol{\sigma} = (\sigma_x, \sigma_y, \sigma_z)^T$ and n is the total density of particles in the system. We obtain the equality

$$\begin{pmatrix} n/2 + S_z & S_x - iS_y \\ S_x + iS_y & n/2 - S_z \end{pmatrix} = \begin{pmatrix} |\phi_+|^2 & \phi_+ \phi_-^* \\ \phi_- \phi_+^* & |\phi_-|^2 \end{pmatrix} \tag{1.140}$$

that allows us to express the pseudospin projections in terms of the photonic wave functions

$$S_x = \frac{1}{2}\left(\phi_+^*\phi_- + \phi_+\phi_-^*\right) \tag{1.141}$$

$$S_y = \frac{i}{2}\left(\phi_+^*\phi_- - \phi_+\phi_-^*\right) \tag{1.142}$$

$$S_z = \frac{|\phi_+|^2 + |\phi_-|^2}{2} \tag{1.143}$$

The energy of the noninteracting system, neglecting the excitonic TE-TM splitting, reads

$$E = \int \left\{ \sum_{\substack{\psi=\{\phi,\chi\} \\ \sigma=\{+,-\}}} \left[\frac{\hbar^2}{2m_\psi}|\boldsymbol{\nabla}\psi_\sigma|^2\right] + \sum_{\sigma=\{+,-\}} \left[\frac{\Omega_R}{2}\left(\phi_\sigma\chi_\sigma^* + \phi_\sigma^*\chi_\sigma\right)\right] - \mathbf{S}\cdot\mathbf{H}_{LT} \right\} d\mathbf{r} \tag{1.144}$$

Using the identities (1.141-1.143) and the Lagrange equations of the Eqs.(1.97,1.98) kind we obtain the dynamics of the photonic and excitonic fields

$$\begin{aligned} i\hbar\frac{\partial\phi_\pm}{\partial t} &= -\frac{\hbar^2}{2m_\phi}\Delta\phi_\pm + \frac{\hbar\Omega_R}{2}\chi_\pm - \frac{i\hbar}{2\tau_\phi}\phi_\pm + P_\pm \\ &- \left(H_{LT,x} \mp iH_{LT,y}\right)\phi_\mp \end{aligned} \tag{1.145}$$

$$i\hbar\frac{\partial\chi_\pm}{\partial t} = -\frac{\hbar^2}{2m_\chi}\Delta\chi_\pm + \frac{\hbar\Omega_R}{2}\phi_\pm - \frac{i\hbar}{2\tau_\chi}\chi_\pm \tag{1.146}$$

where we have included the lifetime and pumping terms. We note here that in the most general case, the term associated with an arbitrary (not necessarily in-plane) effective magnetic field $\mathbf{H} = (H_x, H_y, H_z)^T$, reads $-\mathbf{H}\cdot\boldsymbol{\sigma}(\phi_+, \phi_-)^T$.

The explicit expressions of the components of $\mathbf{H}_{LT}$ are found keeping in mind that here the photonic and excitonic part are separated. It means that the *photonic* dispersion being parabolic, the corresponding splitting is growing quadratically with k. Then, the coupling with the excitonic field self-consistently modifies the splitting seen by the *polaritons*. Consequently in reciprocal space one has

$$H_{LT}^x = \frac{\hbar^2k^2}{4}\left(\frac{1}{m_\phi^{TM}} - \frac{1}{m_\phi^{TE}}\right)\cos(2\phi) = \beta\left(k_x^2 + k_y^2\right) \tag{1.147}$$

$$H_{LT}^y = \frac{\hbar^2k^2}{4}\left(\frac{1}{m_\phi^{TM}} - \frac{1}{m_\phi^{TE}}\right)\sin(2\phi) = 2\beta k_x k_y \tag{1.148}$$

where $\beta = \hbar^2/4(1/m_\phi^{TM} - 1/m_\phi^{TE})$. Finally, in the dynamical equations for $\phi_\pm$ the terms can be rewritten as

$$H_{LT}^\pm = H_{LT}^x \mp iH_{LT}^y = \beta(k_x \pm ik_y)^2 \tag{1.149}$$

or equivalently in real space given that $k_{x,y} \to -i\partial_{x,y}$:

$$H_{LT}^\pm = \beta(\partial_y \mp i\partial_x)^2 \tag{1.150}$$

1.4.4 Optical spin-Hall effect

The spin-Hall effect, proposed by Dyakonov and Perel in 1971 [115], is one of the key concept of spintronics which aims at replacing electric currents by spin currents for the information transport. The concept of the spin-Hall effect is that an electric current induces a spin current without any applied magnetic field. It was revisited and has attracted a lot of attention [116, 117] after its rediscovery by Hirsch in 1999 [118]. Due to the spin-orbit interaction, the scattering probability of an electron over an impurity in two opposite directions is spin dependent.

The optical counterpart called optical spin-Hall effect [119, 17, 120, 121] is the most clear evidence of the peculiar spin dynamics of polaritons: When polariton wave packet, injected resonantly at finite momentum with a linear polarization, scatters on the structural disorder of the microcavity, it exhibits Rayleigh scattering in every direction of the plane. The **k**-dependent precession of **S** around $\mathbf{H}_{LT}$ results in the appearance, in both real and reciprocal space, of circular polarization domains in the four quarters of the plane [see Fig.1.18].

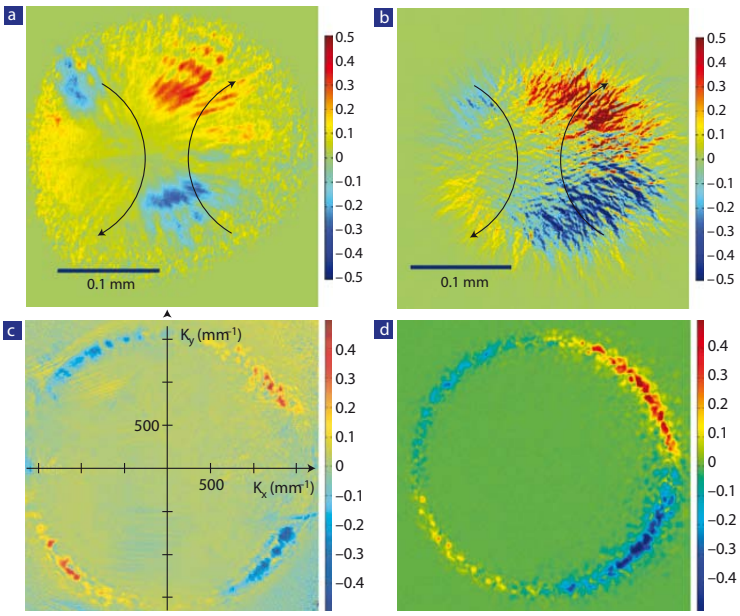

Figure 1.18: Optical spin-Hall effect from Ref.[17] starting from a TM polarized pulsed pump with wavevector $k_P = 1.5\ \mu\text{m}^{-1}$ that Rayleigh scatters on the disorder landscape of the planar microcavity. (a,c) Experimental results and (b,d) simulation. (a,b) Real space degree of circular polarization ρ_c (colormap) and (c,d) reciprocal space counterpart. We clearly see the circular polarization domains: red is σ_+, blue is σ_- and green stands for the linearly polarized regions and regions absent of particles in (c,d).

The OSHE is a linear effect that is especially well described by the pseudospin formalism, however one should keep in mind that the phase of the particles is lost in this framework. The precession equation (1.137) can be extended to include

pumping and lifetime (τ) terms following:

$$\frac{\partial \mathbf{S}}{\partial t} = \mathrm{H}_{LT,\mathbf{k}} \times \mathbf{S} + \mathbf{f} - \frac{\mathbf{S}}{\tau} \tag{1.151}$$

Here the source term $\mathbf{f}(t)$ describes the particles injected by a pulse into the state having a pseudospin $\mathbf{S}$ and reads

$$\mathbf{f}\left(t\right) = \frac{\mathbf{S}_0}{\tau_R} e^{-t/\tau_R} \tag{1.152}$$

where τ_R is the characteristic Rayleigh scattering time and $\mathbf{S}_0$ is the initial pseudospin vector imposed by the polarization of the pump. The population dynamics is governed by the following rate equation

$$\frac{\partial N}{\partial t} = 2\frac{\mathbf{S}_0}{\tau_R} e^{-t/\tau} - \frac{N}{\tau} \tag{1.153}$$

Assuming that the pump is linearly polarized along the x-axis, which means $\mathbf{S}_0 = (S_{x,0}, 0, 0)^T$, yields the important result

$$S_z\left(\phi, t\right) = S_0 \frac{\Omega_{LT,y}\left(\phi\right)}{\tau_R \Omega_{LT}^2} \left[1 - \cos\left(\Omega t\right)\right] e^{-t/\tau} \tag{1.154}$$

$$N_z = 2\frac{S_{z,0}}{\tau_R} t e^{-t/\tau} \tag{1.155}$$

Here ϕ is the polar angle. The degree of circular polarization reads

$$\rho_c\left(\phi, t\right) = \frac{2S_z\left(\phi, t\right)}{N} = \frac{\Omega_{LT,y}\left(\phi\right)\left[1 - \cos\left(\Omega t\right)\right]}{2\Omega_{LT}^2 t} \tag{1.156}$$

Its time averaged value is found to be

$$\rho_c\left(\phi\right) = \frac{\Omega\tau \sin\left(2\phi\right)}{1 + \Omega^2\tau^2} \tag{1.157}$$

and therefore the maximum value of ρ_c is achieved for diagonal directions for which $\phi = p\pi/4$. This is not so surprising since for these specific directions, $\mathbf{H}_{LT}$ and the initial pseudospin $\mathbf{S}_0$ are exactly perpendicular leading to a maximum precession amplitude as discussed previously. This leads to the antisymmetric polarization domains in the four quarters of the plane [see Fig.1.18]. The optical spin-Hall Effect is an analogue to the intrinsic spin-Hall effect for electrons [116, 117]. The role of the Rashba spin-orbit field in this case is played by the TE-TM splitting [112], but the associated field has a different symmetry since the Rashba field is aligned with $\mathbf{k}$. We note that in the case where a polarization pinning is present along a crystallographic axis, induced by a splitting at $\mathbf{k} = \mathbf{0}$ (static effective magnetic field), the geometry $\mathbf{H}_{LT}$ is modified leading to the so-called anisotropic optical spin-Hall effect reported in Ref.[122].

1.5 Spinor polariton condensate

In this section we discuss the nonlinear spin dynamics of polaritons brought by the particles self-interactions. We shall introduce first the spin anisotropy of polariton interactions and review briefly the most famous related effects and then we will turn to the theory of spinor polariton condensates and their topological defects. Previously [see Sec.(1.1.2)] we have described the polariton-polariton interactions whose strength α is dependent on the excitons properties. We have also described several nonlinear effect such as the condensation, the optical parametric oscillator or the bistability. Now taking into account both the spin degree of freedom of polaritons and their interactions will lead to several very interesting new results.

1.5.1 Spin anisotropy of polaritons

Polariton-polariton interactions are known to be *spin-anisotropic*. Indeed, the interaction of polaritons having the same spin projection is much stronger than that of polaritons with opposite spin as described in the reference [123]. Basically, the interaction of two polaritons with antiparallel spins is a second order process that involves an intermediate scattering event with a dark exciton lying at higher energy which is consequently less probable. Furthermore, the second order process (involving the product of two matrix elements) produces a correction to the ground state which is known to be always negative. In summary, the interaction constant α_2 between particles having opposite spin projections is much weaker than the parallel spin interaction constant α_1, the typical ratio is $\alpha_2 = -0.1, -0.2\alpha_1$ but is variable depending on the number of quantum well in the structure, their separation and the detuning between the cavity and exciton modes [124].

The polariton spin anisotropy is responsible for several interesting nonlinear effect, among which is found: the inversion of the linear polarization during parametric processes [125] as it was observed under resonant excitations, the self-induced Larmor precession [109] [see Sec.1.5.2.3], the multistability [97], the spin Meissner effect [126], or condensation related phenomena [14] that shall be discussed in the following.

1.5.2 The spinor condensate

In the section (1.2), we have introduced the mean field treatment of the macroscopically occupied ground state via the Gross-Pitaevskii equation, here we will extend this theory including the two spin projections allowed for the polariton condensate that is consequently said to be spinor. There are two competing representations for the description of a spinor polariton condensate. The first option is to use the linear polarization basis (x, y), which can be convenient since the eigen modes are TE and TM polarized and to describe a condensate forming with a linear polarization, but since real spin states correspond to circular polarization of the emission, it is far more natural especially for writing the interaction terms to use the circular polarization basis (σ_+, σ_-). We shall anyway detail both representation in the following

which will be very useful for the chapter 2.

1.5.2.1 Linear polarization basis

The functional energy of the spin dependent polariton system reads [127]

$$E = \int (E_{kin} + E_{int} - \mu n)\, d\mathbf{r} \tag{1.158}$$

The order parameter is normalized to the polariton concentration $n = \boldsymbol{\psi}^* \cdot \boldsymbol{\psi}$. We will assume here a parabolic polariton dispersion valid around $\mathbf{k} = 0$ and for values of the interaction blueshift much smaller than the Rabi splitting. The kinetic energy term encompasses the TE-TM splitting and reads:

$$E_{kin} = \frac{\hbar^2}{2m_{TE}} \left(\boldsymbol{\nabla}_i \psi_j^* \boldsymbol{\nabla}_i \psi_j\right) + \frac{\hbar^2}{2} \left(\frac{1}{m_{TM}} - \frac{1}{m_{TE}}\right) |\boldsymbol{\nabla} \cdot \psi|^2 \tag{1.159}$$

$\boldsymbol{\psi} = (\psi_x, \psi_y)$ is the vectorial wavefunction of the condensate and we assume a summation over repeated index, $i, j = x, y$. The interaction energy part is defined by

$$E_{int} = \frac{U_0}{2}(\boldsymbol{\psi}^* \cdot \boldsymbol{\psi})^2 - \frac{U_1}{2}|\boldsymbol{\psi} \cdot \boldsymbol{\psi}|^2 \tag{1.160}$$

U_0 is the polarization independent interaction constant and is nothing but α_1. $U_1 = (\alpha_1 - \alpha_2)/2$ is the so-called linear-circular dichroism [128]. The polarization of quasi-equilibrium condensate formed under nonresonant pumping is governed by the minimization of its interaction energy [129] which can be rewritten as

$$E_{int} = \frac{(U_0 - U_1)}{2}(\boldsymbol{\psi}^* \cdot \boldsymbol{\psi})^2 + \frac{U_1}{2}|\boldsymbol{\psi}^* \times \boldsymbol{\psi}|^2 \tag{1.161}$$

Since for the typical microcavities $U_1 > U_0 - U_1$ ($\alpha_2 = -0.1\alpha_1$), E_{int} is minimized for $|\boldsymbol{\psi}^* \times \boldsymbol{\psi}|^2 = 0$ which means that $\theta_x = \theta_y = \theta$. Consequently $\boldsymbol{\psi}$ can be written as

$$\psi_x(\mathbf{r}) = \sqrt{n_0} \cos[\eta(\mathbf{r})]\, e^{i\theta} \tag{1.162}$$

$$\psi_y(\mathbf{r}) = \sqrt{n_0} \sin[\eta(\mathbf{r})]\, e^{i\theta} \tag{1.163}$$

Where η is the polarization angle and θ the is the global phase of the condensate. The polarization of the ground state is therefore linear with a direction defined by the angle $\eta(\mathbf{r})$ not necessarily uniform in space and which completely determines the order parameter. Indeed, the interaction energy is invariant under local linear polarization angle modification, however the kinetic energy, being sensitive to local fluctuation via the gradient operator, is definitely minimized by a uniform polarization angle distribution over the whole space. This prediction has been confirmed in the observations of Kasprzak et al. in 2006 [9] and of Ballili et al. next [40]. In these experiments, the orientation of the linear polarization was fixed along a crystallographic axis and imposed by a splitting at $\mathbf{k} = \mathbf{0}$ that breaks the cylindrical

symmetry of the Hamiltonian. The chemical potential of the lowest energy state is found to be $\mu = (U_0 - U_1)n$. We note here that applying an external magnetic field along the growth axis of the sample can drastically modify the polarization of the condensate as demonstrated in Ref.[130, 131]: while the condensate becomes elliptically polarized at low magnetic field, it becomes fully circularly polarized above a critical field $\mathbf{H}_c = U_1 n$ that imposes the pseudospin vector to lie along the z-axis as well.

Once again, the dynamics of the order parameter $\boldsymbol{\psi}$ can be obtained from the Lagrange equations $i\hbar\partial\boldsymbol{\psi} = \delta E/\delta\boldsymbol{\psi}^*$ yielding

$$i\hbar\frac{\partial\psi}{\partial t} = T\psi + U_0\left(\psi^*\cdot\psi\right)\psi - U_1\psi^*\left(\psi\cdot\psi\right) \tag{1.164}$$

where T is the kinetic energy tensor that includes the TE-TM splitting terms and reads:

$$T = -\frac{\hbar^2}{2m_{TE}}\begin{pmatrix} \Delta + \beta\partial_{xx}^2 & \beta\partial_{xy}^2 \\ \beta\partial_{xy}^2 & \Delta + \beta\partial_{yy}^2 \end{pmatrix} \tag{1.165}$$

and $\beta = \hbar^2/4(1/m_{TM} - 1/m_{TE})$ is the strength of the TE-TM splitting.

1.5.2.2 Circular polarization basis

The circular polarization basis $\sigma_\pm = \pm$ is more natural not only because it is the basis of the polariton spin states, but also because preserves the shape of the standard Gross-Pitaevskii equation where interaction terms are more transparent acting as density dependent potentials in each components [132]. The functional energy of the system reads

$$E = \int\left[\boldsymbol{\psi}^* T\boldsymbol{\psi} + \frac{\alpha_1}{2}\left(|\psi_+|^4 + |\psi_-|^4\right) + \alpha_2|\psi_+|^2|\psi_-|^2\right]d\mathbf{r} \tag{1.166}$$

where this time $\boldsymbol{\psi} = (\psi_+, \psi_-)^T$, the kinetic energy tensor T is defined by

$$T = \begin{pmatrix} -\frac{\hbar^2\Delta}{2m^*} & \beta(\partial_y - i\partial_x)^2 \\ \beta(\partial_y + i\partial_x)^2 & -\frac{\hbar^2\Delta}{2m^*} \end{pmatrix} \tag{1.167}$$

The effective mass of both component is the same and is taken as $m^* = m_{TE}m_{TM}/(m_{TE} + m_{TM})$. The minimization of E leads to the following coupled set of Gross-Pitaevskii equations

$$i\hbar\frac{\partial\psi_+}{\partial t} = -\frac{\hbar^2}{2m^*}\Delta\psi_+ + \alpha_1|\psi_+|^2\psi_+ + \alpha_2|\psi_-|^2\psi_+ + \beta(\partial_y - i\partial_x)^2\psi_- \tag{1.168}$$

$$i\hbar\frac{\partial\psi_-}{\partial t} = -\frac{\hbar^2}{2m^*}\Delta\psi_- + \alpha_1|\psi_-|^2\psi_- + \alpha_2|\psi_+|^2\psi_- + \beta(\partial_y + i\partial_x)^2\psi_+ \tag{1.169}$$

There are here two coupling terms the first one is the intercomponent interaction of strength α_2, the latter acts as a potential $\alpha_2|\psi_-|^2$ ($\alpha_2|\psi_+|^2$) on the ψ_+ (ψ_-) component and since α_2 is negative this potential is actually attractive. The second coupling term is the TE-TM splitting that induces an exchange of the σ_+ and σ_- populations. This circular polarization representation will be mostly favored in the chapters 2 and 3.

1.5.2.3 Intrinsic Zeeman splitting

We have already discussed the extrinsic effective magnetic field induced by the TE-TM splitting, here we present another feature that is the interaction induced intrinsic Zeeman splitting. Neglecting here the TE-TM splitting, the set of equations (1.169,1.169) can be rewritten in the following form

$$\begin{aligned} i\hbar\frac{\partial\psi_+}{\partial t} &= -\frac{\hbar^2}{2m^*}\Delta\psi_+ + \frac{\alpha_1+\alpha_2}{2}\left(|\psi_+|^2+|\psi_-|^2\right)\psi_+ \\ &+ \frac{\alpha_1-\alpha_2}{2}\left(|\psi_+|^2-|\psi_-|^2\right)\psi_+ \end{aligned} \tag{1.170}$$

$$\begin{aligned} i\hbar\frac{\partial\psi_-}{\partial t} &= -\frac{\hbar^2}{2m^*}\Delta\psi_- + \frac{\alpha_1+\alpha_2}{2}\left(|\psi_+|^2+|\psi_-|^2\right)\psi_- \\ &- \frac{\alpha_1-\alpha_2}{2}\left(|\psi_+|^2-|\psi_-|^2\right)\psi_- \end{aligned} \tag{1.171}$$

It is easily noticed that the last term enters the two equations with opposite signs, and therefore can be described by the Pauli matrix σ_z.

$$\begin{pmatrix} +\frac{\alpha_1-\alpha_2}{2}(n_+-n_-) & 0 \\ 0 & -\frac{\alpha_1-\alpha_2}{2}(n_+-n_-) \end{pmatrix}\begin{pmatrix}\psi_+\\ \psi_+\end{pmatrix} = H_z\underbrace{\begin{pmatrix}+1 & 0\\ 0 & -1\end{pmatrix}}_{\sigma_z}\begin{pmatrix}\psi_+\\ \psi_+\end{pmatrix} \tag{1.172}$$

where $n_\pm = |\psi_\pm|^2$. It can therefore be treated as an effective magnetic field along the z direction. It is very important to note here, that the direction of this field is opposite to the z-projection of the polariton pseudospin. Therefore, if the condensate is completely circularly polarized with $\psi_+ = \sqrt{n}$, $\psi_- = 0$, n being the total density, the effective magnetic field will point in the *negative* direction of the z-axis:

$$H_z = -\frac{\alpha_1-\alpha_2}{2}\left(|\psi_+|^2-|\psi_-|^2\right) \tag{1.173}$$

In the case of polaritons, where $\alpha_2 = -0.1\alpha_1$ the effective field is strengthened and tends to lock circularly polarized states (having strong density imbalance) in the system. This feature is responsible for the so-called self-induced Larmor precession of the polariton pseudospin [16] around the field. In usual spin isotropic atomic condensates $\alpha_1 \simeq \alpha_2$, and therefore $\Omega_z \simeq 0$, the field is completely absent. We note here that this intrinsic Zeeman splitting is responsible for the spin-Meissner effect [126] namely the suppression of the real Zeeman splitting induced by an *applied* magnetic field along the z-axis up to a critical value, and under resonant pumping, it gives rise to the multistability [97] of the driven polariton mode, that is the bistable jump of only one circular component while the other is locked down (from the energy point of view). This specificity will become especially important in the framework of half-integer topological defects as we will see in the Chapter 2.

1.5.3 Spectrum of elementary excitations

Let us discuss here the spin dependent dispersion of elementary excitations already introduced in Sec.(1.2.4) for the spinless case. As we know, two situations can be

distinguished, we can either consider the natural formation of the polariton condensate under nonresonant pumping thanks to relaxation mechanisms or the artificial macroscopic population of a mode via resonant injection.

In the work of Solnyshkov et al. [99] the spin dependent dispersion of elementary excitations was analyzed for a driven mode neglecting the TE-TM splitting. Similarly to Sec.(1.3.1.2), the requirement is to write a spin dependent ansatz for the perturbed vectorial wavefunction $\boldsymbol{\psi} = (\psi_+, \psi_-)^T$:

$$\boldsymbol{\psi} = e^{i(k_p x - \omega_p t)} \left(\boldsymbol{\psi}_0 + \mathbf{A} e^{+i(kx - \omega t)} + \mathbf{B}^* e^{-i(kx - \omega^* t)} \right) \tag{1.174}$$

where $\boldsymbol{\psi}_0 = (\psi_{0+}, \psi_{0-})^T$. $\mathbf{A} = (A_+, A_-)^T$ and $\mathbf{B} = (B_+, B_-)^T$ are the amplitudes of the perturbations on top of the condensate for each spin component. Injecting this ansatz (1.174) into the driven-dissipative Gross-Pitaevskii equation

$$\begin{aligned} i\hbar \frac{\partial \psi_+}{\partial t} = & - \frac{\hbar^2}{2m^*} \Delta \psi_+ + \alpha_1 |\psi_+|^2 \psi_+ + \alpha_2 |\psi_-|^2 \psi_+ - \frac{i\hbar}{2\tau} \psi_+ \\ & + P_+ e^{i(k_p x - \omega_p t)} \end{aligned} \tag{1.175}$$

$$\begin{aligned} i\hbar \frac{\partial \psi_-}{\partial t} = & - \frac{\hbar^2}{2m^*} \Delta \psi_- + \alpha_1 |\psi_-|^2 \psi_- + \alpha_2 |\psi_+|^2 \psi_- - \frac{i\hbar}{2\tau} \psi_- \\ & + P_- e^{i(k_p x - \omega_p t)} \end{aligned} \tag{1.176}$$

and linearizing the resulting set of equations yields very complex expressions for the subsequent dispersion branches in the general case. However for circularly polarized (e.g. $P_- = 0$, σ_+ polarization) and linearly polarized ($P_+ = P_-$) pumps the results are actually much simpler. In the first case one finds the following four branches for the circularly polarized excitations:

$$\begin{aligned} \hbar\omega_1^+ = & \hbar\omega_p + \sqrt{\left[E_{LP}(k) - \hbar\omega_p + 2\alpha_1 n_0\right]^2 - \left[\alpha_1 n_0\right]^2} \\ & - \frac{i\hbar}{2\tau} \end{aligned} \tag{1.177}$$

$$\begin{aligned} \hbar\omega_2^+ = & \hbar\omega_p - \sqrt{\left[E_{LP}(k) - \hbar\omega_p + 2\alpha_1 n_0\right]^2 - \left[\alpha_1 n_0\right]^2} \\ & - \frac{i\hbar}{2\tau} \end{aligned} \tag{1.178}$$

$$\hbar\omega_1^- = E_{LP}(k) + \alpha_2 n_0 - \frac{i\hbar}{2\tau} \tag{1.179}$$

$$\hbar\omega_2^- = 2\hbar\omega_0 - \alpha_2 n_0 - \frac{i\hbar}{2\tau} \tag{1.180}$$

Here $k_p = 0$ and $n_0 = |\psi_0|^2$. The renormalization of the dispersion of cross-polarized excitations (σ_- here) consists only in the concentration dependent shift with respect to the bare dispersion as follows from Eqs.(1.179,1.180). It remains parabolic with a constant imaginary part given by $i\hbar/2\tau$. This is because polariton-polariton interactions do not mix the circularly polarized components. The renormalization of the co-polarized dispersion is much more interesting: It is seen from Eq.(1.178) that the real part is dispersionless in the vicinity of the point where $E_{LP} = \hbar\omega_p + 2\alpha_1 n_0$.

Physically, it means that the renormalized mode is diffusive: the excitations cannot propagate, because their group velocity is zero. As in the spinless case the renormalization of the co-polarized excitations depends on the detuning $\delta = \hbar\omega_p - E_{LP}$ [see Sec(1.3.1.2)]. One can assist to a parabolic, flat or linear spectrum. And especially for the larger values of δ the diffusive flat parts form at $k \neq 0$ [see Fig.1.19].

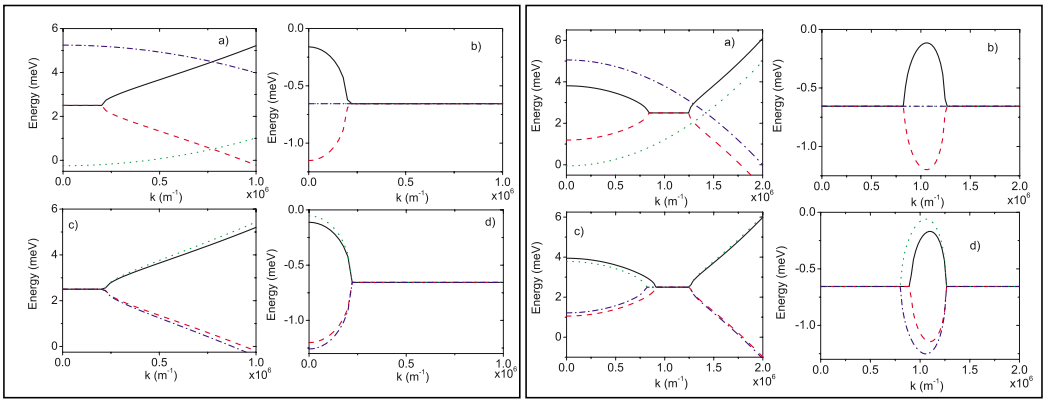

Figure 1.19: Dispersion of the elementary excitations of a driven polariton mode. (a) and (c) real parts and (b) and (d) imaginary parts. Upper panels: circularly polarized pump and lower panels: linearly polarized pump. Left panels: flat part forming at $k = 0$ for $\delta > (\alpha_1 - \alpha_2)n_0$ and right panel: flat parts forming at $k \neq 0$ for larger values of δ.

In the second case of a linearly polarized driven mode, the elementary excitations are also linearly polarized with dispersions given by the following expressions

$$\hbar\omega_1^+ = \hbar\omega_p + \sqrt{\left[E_{LP}(k) - \hbar\omega_p + \alpha_1 n_0 + \alpha_2 n_0\right]^2 - \frac{1}{4}\left[\alpha_1 n_0 + \alpha_2 n_0\right]^2} - \frac{i\hbar}{2\tau} \tag{1.181}$$

$$\hbar\omega_2^+ = \hbar\omega_p + \sqrt{\left[E_{LP}(k) - \hbar\omega_p + \alpha_1 n_0 + \alpha_2 n_0\right]^2 - \frac{1}{4}\left[\alpha_1 n_0 + \alpha_2 n_0\right]^2} - \frac{i\hbar}{2\tau} \tag{1.182}$$

$$\hbar\omega_1^- = \hbar\omega_p + \sqrt{\left[E_{LP}(k) - \hbar\omega_p + \alpha_1 n_0 - \alpha_2 n_0\right]^2 - \frac{1}{4}\left[\alpha_1 n_0 - \alpha_2 n_0\right]^2} - \frac{i\hbar}{2\tau} \tag{1.183}$$

$$\hbar\omega_1^- = \hbar\omega_p - \sqrt{\left[E_{LP}(k) - \hbar\omega_p + \alpha_1 n_0 - \alpha_2 n_0\right]^2 - \frac{1}{4}\left[\alpha_1 n_0 - \alpha_2 n_0\right]^2} - \frac{i\hbar}{2\tau} \tag{1.184}$$

As the linear polarizations are mixed by the anisotropic polariton-polariton interactions ($\alpha_2 \neq \alpha_1$), the dispersions of both co- and cross-polarized modes can exhibit flat parts [see Fig.1.19].

An important result emerges, when the detuning δ is exactly compensated by the interaction-induced blueshift $\mu_0 = (\alpha_1 - \alpha_2)n_0$. In that case the linear Bogoliubov spectrum is recovered and we see comparing Eq.(1.181) and Eq.(1.183) that if $\alpha_2 \neq 0$, the corresponding branches are shifted with respect to each other. The consequence is that the speed of sound is polarization dependent: The linearly polarized spinor polariton condensate is characterized by two speed of sounds. This result is also valid for the condensate under non-resonant pumping [see left panel of Fig.1.20].

Additionally, the case of a quasi-equilibrium condensate in the presence of the TE-TM splitting was analyzed by Shelykh et al. [127]. The main result was that the linear polarization splitting induces an anisotropic dispersion of elementary excitations, depending on the relative condensate and excitation polarizations [see right panel of Fig.1.20].

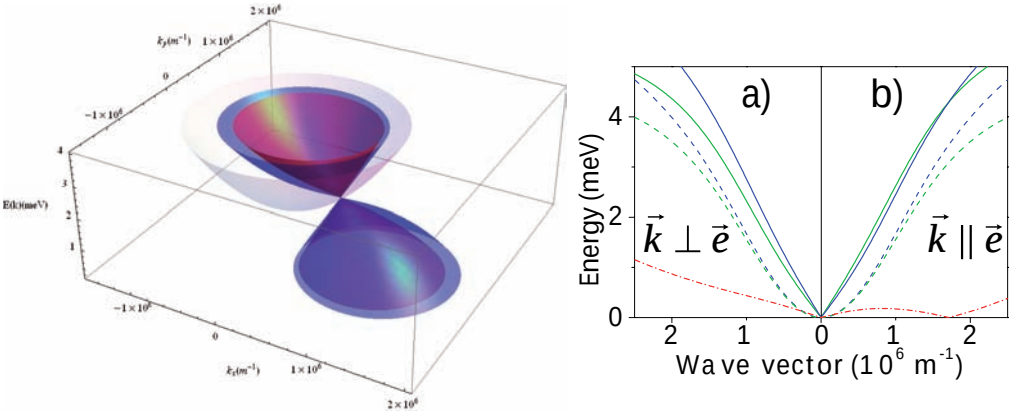

Figure 1.20: Left panel: 2D Linear dispersions of the elementary excitations of a driven mode pumped with a linear polarization at $k \neq 0$. The co- and cross-polarized excitations (blue and purple) define two different speeds of sound. The bare dispersion appears as a white/transparent parabola. Right panel: anisotropic dispersion of elementary excitations induced by the TE-TM splitting from Ref.[127]. Dashed lines: bare dispersion branches and solid lines: renormalized lower-polariton branches. The splitting is shown in a dashed/dotted red line. The excitation's wave vector is perpendicular to the condensate polarization in panel (a) and collinear with it in panel (b).

Bibliography

[1] C. Weisbuch, M. Nishioka, A. Ishikawa, and Y. Arakawa, Observation of the coupled exciton-photon mode splitting in a semiconductor quantum microcavity, *Phys. Rev. Lett.* **69**, 3314 (1992). (Cited on page 1.)

[2] D. D. Solnyshkov, H. Flayac, and G. Malpuech, Black Holes and Wormholes in spinor polariton condensates, *Phys. Rev. B* **84**, 233405 (2012). (Cited on page 2.)

[3] D. D. Solnyshkov, H. Flayac, and G. Malpuech, Stable magnetic monopoles in spinor polariton condensates, *Phys. Rev. B* **85**, 073105 (2012). (Cited on pages 2 and 84.)

[4] H. Flayac, D. D. Solnyshkov, and G. Malpuech, Separation and propagation of monopole analogues in semiconductor microcavities, to appear in *New J. Phys*, *arXiv*:1203.0885 (2012). (Cited on page 2.)

[5] E. Wertz, L. Ferrier, D. D. Solnyshkov, R. Johne, D. Sanvitto, A. Lemaître, I. Sagnes, R. Grousson, A. V. Kavokin, P. Senellart, G. Malpuech, and J. Bloch, Spontaneous formation and optical manipulation of extended polariton condensates, *Nature Physics* **6**, 860 (2010). (Cited on pages 2, 10 and 31.)

[6] J. P. Reithmaier, G. Sek, A. Löffler, C. Hofmann, S. Kuhn, S. Reitzenstein, L. V. Keldysh, V. D. Kulakovskii, T. L. Reinecke, and A. Forchel, Strong coupling in a single quantum dot-semiconductor microcavity system, *Nature* **432**, 197 (2004). (Cited on page 2.)

[7] L. Ferrier, E. Wertz, R. Johne, D. D. Solnyshkov, P. Senellart, I. Sagnes, A. Lemaître, G. Malpuech, and J. Bloch, Interactions in Confined Polariton Condensates, *Phys. Rev. Lett.* **106**, 126401 (2011). (Cited on page 2.)

[8] M. Galbiati, L. Ferrier, D. D. Solnyshkov, D. Tanese, E. Wertz, A. Amo, M. Abbarchi, P. Senellart, I. Sagnes, A. Lemaître, E. Galopin, G. Malpuech, and J. Bloch, Polariton Condensation in Photonic Molecules, *Phys. Rev. Lett.* **108**, 126403 (2012). (Cited on page 2.)

[9] , J. Kasprzak, M. Richard, S. Kundermann, A. Baas, P. Jeambrun, J. M. J. Keeling, F. M. Marchetti, M. H. Szymaska, R. André, J. L. Staehli, V. Savona, P. B. Littlewood, B. Deveaud, and Le Si Dang, Bose-Einstein condensation of exciton polaritons, *Nature* **443**, 409 (2006). (Cited on pages 2, 6, 8, 9, 19, 40 and 50.)

[10] S. Utsunomiya, L. Tian, G. Roumpos, C. W. Lai, N. Kumada, T. Fujisawa, M. Kuwata-Gonokami, A. Löffler, S. Höfling, A. Forchel and Y. Yamamoto, Observation of Bogoliubov excitations in exciton-polariton condensates, *Nature Physics* **4**, 700 (2008). (Cited on pages 2, 19 and 20.)

[11] A. Amo, J. Lefrère, S. Pigeon, C. Adrados, C. Ciuti, I. Carusotto, R. Houdré, E. Giacobino, and A. Bramati, Superfluidity of polaritons in semiconductor microcavities, *Nat. Phys.* **5**, 805 (2009). (Cited on pages 2, 19 and 20.)

[12] P. G. Savvidis, J. J. Baumberg, R. M. Stevenson, M. S. Skolnick, D. M. Whittaker, and J. S. Roberts, Angle-resonant stimulated polariton amplifier *Phys. Rev. Lett.* **84**, 1547 (2000). (Cited on pages 2, 6, 31, 34 and 35.)

[13] A. Baas, J.-Ph. Karr, M. Romanelli, A. Bramati, and E. Giacobino, Optical bistability in semiconductor microcavities in the nondegenerate parametric oscillation regime: Analogy with the optical parametric oscillator, *Phys. Rev. B* **70**, 161307(R) (2004). (Cited on pages 2, 6 and 31.)

[14] I. A. Shelykh, A. V. Kavokin, Y. G. Rubo, T. C. H. Liew, and G Malpuech, Polariton polarization-sensitive phenomena in planar semiconductor microcavities, *Semic. Sci. Techn.* **25**, 013001 (2010). (Cited on pages 2, 40 and 49.)

[15] G. Dasbach, C. Diederichs, J. Tignon, C. Ciuti, Ph. Roussignol, C. Delalande, M. Bayer, and A. Forchel, Polarization inversion via parametric scattering in quasi-one-dimensional microcavities, *Phys. Rev. B* **71**, 161308(R) (2005). (Cited on page 2.)

[16] D. N. Krizhanovskii, D. Sanvitto, I. A. Shelykh, M. M. Glazov, G. Malpuech, D. D. Solnyshkov, A. Kavokin, S. Ceccarelli, M. S. Skolnick, and J. S. Roberts, Rotation of the plane of polarization of light in a semiconductor microcavity *Phys. Rev. B* **73**, 073303 (2006). (Cited on pages 2 and 52.)

[17] C. Leyder, M. Romanelli, J.-Ph. Karr, E. Giacobino, T. C. H. Liew, M. M. Glazov, A. V. Kavokin, G. Malpuech and A. Bramati, Observation of the optical spin-Hall effect, *Nature Phys.* **3**, 628 (2007). (Cited on pages 2 and 47.)

[18] T. K. Paraïso, M. Wouters, Y. Léger, F. Morier-Genoud, and B. Deveaud-Plédran, Multistability of a coherent spin ensemble in a semiconductor microcavity, *Nature Materials* **9**, 655-660 (2010). (Cited on page 2.)

[19] K. G. Lagoudakis, M. Wouters, M. Richard, A. Baas, I. Carusotto, R. André, Le Si Dang, and B. Deveaud-Plédran, Quantized vortices in an exciton-polariton condensate, *Nature Physic*, **4**, 706 (2008). (Cited on pages 2, 26 and 27.)

[20] K. G. Lagoudakis, T. Ostatnický, A. V. Kavokin, Y. G. Rubo, R. André, and B. Deveaud-Plédran, Observation of half-quantum vortices in an exciton-polariton condensate, *Science* **326**, 974 (2009). (Cited on pages 2, 70 and 71.)

[21] A. Amo, S. Pigeon, D. Sanvitto, V. G. Sala, R. Hivet, I. Carusotto, F. Pisanello, G. Leménager, R. Houdré, E Giacobino, C. Ciuti, and A. Bramati, Polariton Superfluids Reveal Quantum Hydrodynamic Solitons, *Science* **3**, 1167 (2011). (Cited on pages 2, 26, 28 and 31.)

[22] R. Hivet, H. Flayac, D. D. Solnyshkov, D. Tanese, T. Boulier, D. Andreoli, E. Giacobino, J. Bloch, A. Bramati, G. Malpuech, A. Amo, Half-solitons in a polariton quantum fluid behave like magnetic monopoles, *arXiv*:1204.3564 (2012). (Cited on page 2.)

[23] N. W. Ashcroft and N. David Mermin, Solid State Physics, Harcourt, Orlando (1976). (Cited on page 3.)

[24] S. I. Pekar, The theory of electromagnetic waves in a crystal in which excitons are produced, *Zh. Eksp. Teor. Fiz.* **33**, 1022 (1957). (Cited on page 3.)

[25] J. Hopfield, Theory of the contribution of excitons to the complex dielectric constants of crystals, *Phys. Rev.* **112**, 1555 (1958). (Cited on page 3.)

[26] V. Agranovich, Dispersion of electromagnetic waves in crystals, *JEPT Lett.* **37**, 430 (1959). (Cited on page 3.)

[27] E. Rosencher, and B. Vinter, Optoelectronics, Cambridge University Press, (2002). (Cited on page 3.)

[28] M. O. Scully and M. Suhail Zubairy, Quantum Optics, Cambridge University Press, Cambridge (1997). (Cited on page 5.)

[29] H. Carmichael, Quantum Optics 1: Master Equations And Fokker-Planck Equations, Springer, New York (2007). (Cited on page 6.)

[30] A. V. Kavokin, J. J. Baumberg, G. Malpuech, and F. P. Laussy, Microcavities, Oxford University Press, Oxford (2007). (Cited on pages 4, 32 and 37.)

[31] C. Ciuti, P. Schwendimann, B. Deveaud, and A. Quattropani, *Phys Rev B* **62**, 4825 (2000). (Cited on page 6.)

[32] L. V. Butov, and A. V. Kavokin, The behaviour of exciton-polaritons, *Nature Photonics* **6**, 2 (2012). (Cited on page 7.)

[33] Reply to "The behaviour of exciton-polaritons", *Nature Photonics* 6, 205 (2012). (Cited on page 7.)

[34] S. N. Bose, Plancks Gesetz Lichtquantenhypothese, *Z. Phys* **26**, 178, (1924). (Cited on page 7.)

[35] A. Einstein, Quantentheorie des einatomigen idealen Gases, *Zweite Abhandlung, Sitzber Klg. Preuss. Akad. Wiss.* **1**, 3 (1925). (Cited on page 7.)

[36] M. H. Anderson, J. R. Ensher, M. R. Matthews, C. E. Wieman, and E. A. Cornell, Observation of Bose-Einstein Condensation in a Dilute Atomic Vapor, *Science* **269**, 5221 (1995). (Cited on page 7.)

[37] J. M. Kosterlitz, D. J. Thouless, Ordering, metastability and phase transitions in two-dimensional systems, *Journal of Physics C: Solid State Physics* **6**: 1181 (1973). (Cited on pages 8 and 25.)

[38] L. V. Butov, A. Zrenner, G. Abstreiter, G. Böhm, and G. Weimann, Condensation of Indirect Excitons in Coupled AlAs/GaAs Quantum Wells *Phys. Rev. Lett.* **73**, 304 (1994). (Cited on page 8.)

[39] S. O. Demokritov, V. E. Demidov, O. Dzyapko, G. A. Melkov, A. A. Serga, B. Hillebrands, and A. N. Slavin, Bose-Einstein condensation of quasi-equilibrium magnons at room temperature under pumping, *Nature* **443**, 430 (2006). (Cited on page 8.)

[40] R. Balili, V. Hartwell, D. Snoke, L. Pfeiffer, and K. West, Bose-Einstein Condensation of Microcavity Polaritons in a Trap, *Science* **316**, 5827 1007 (2007). (Cited on pages 9 and 50.)

[41] C. W. Lai, N. Y. Kim, S. Utsunomiya, G. Roumpos, H. Deng, M. D. Fraser, T. Byrnes, P. Recher, N. Kumada, T. Fujisawa, Y. Yamamoto, Coherent zero-state and π-state in an exciton-polariton condensate array, *Nature* **450**, 529-532 (2007). (Cited on page 9.)

[42] S. Christopoulos, G. Baldassarri Höger von Högersthal, A. J. D. Grundy, P. G. Lagoudakis, A. V. Kavokin, J. J. Baumberg, G. Christmann, R. Butté, E. Feltin, J.-F. Carlin, and N. Grandjean, Room-Temperature Polariton Lasing in Semiconductor Microcavities, *Phys. Rev. Lett.* **98**, 126405 (2007). (Cited on pages 9 and 10.)

[43] J. Kasprzak, D. D. Solnyshkov, R. André, Le Si Dang, and G. Malpuech, Formation of an Exciton Polariton Condensate: Thermodynamic versus Kinetic Regimes, *Phys. Rev. Lett.* **101**, 146404 (2008). (Cited on page 9.)

[44] G. E. Uhlenbeck, and L. Gropper, The equation of state of a non-ideal Einstein-Bose or Fermi-Dirac gas, *Phys. Rev.* **1**, 79 (1932). (Cited on page 10.)

[45] D. Porras, C. Ciuti, J. J. Baumberg, and C. Tejedor, Polariton dynamics and Bose-Einstein condensation in semiconductor microcavities *Phys. Rev. B* **8**, 085304 (2002). (Cited on page 12.)

[46] I. A. Shelykh, G. Malpuech, R. Johne and A. V. Kavokin, The system of interacting polaritons: Classical versus quantum kinetic equation, *Solid State Communications* **144** 9, 378 (2007). (Cited on page 12.)

[47] M. Wouters and V. Savona, Stochastic classical field model for polariton condensates, *Phys. Rev. B* **79**, 165302 (2009). (Cited on pages 12 and 16.)

[48] G. Malpuech, A. V. Kavokin, A. Di Carlo, J. J. Baumberg, Polariton lasing by exciton-electron scattering in semiconductor microcavities, *Phys. Rev. B* **65** 153310 (2002). (Cited on page 12.)

[49] F. Tassone, C. Piermarocchia, V. Savona, A. Quattropani, and P. Schwendimann, Bottleneck effects in the relaxation and photoluminescence of microcavity polaritons, *Phys. Rev. B* **56**, 7554 (1997). (Cited on page 12.)

[50] F. Tassone, and Y. Yamamoto, Exciton-exciton scattering dynamics in a semiconductor microcavity and stimulated scattering into polaritons, *Phys. Rev. B* **59**, 10830 (1999). (Cited on pages 12 and 15.)

[51] D. Porras, C. and Tejedor, Linewidth of a polariton laser: Theoretical analysis of self-interaction effects, *Phys. Rev. B* **67**, 161310 (2003). (Cited on page 12.)

[52] A.I. Tartakovskii, M. Emam-Ismail, R. M. Stevenson, M. S. Skolnick, V. N. Astratov, D. M. Whittaker, J. J. Baumberg, and J. S. Roberts, Relaxation bottleneck and its suppression in semiconductor microcavities, *Phys. Rev. B* **62**, 2283(R)(2000). (Cited on page 12.)

[53] M. Müller, J. Markus, and A. Bleuse, Dynamics of the cavity polariton in CdTe-based semiconductor microcavities: Evidence for a relaxation edge, *Phys. Rev. B* **62** 16886 (2000). (Cited on pages 12 and 13.)

[54] N. N. Bogoliubov, On the theory of superfluidity, *J. Phys. USSR* **11**, 23 (1947). (Cited on pages 13, 20 and 37.)

[55] L. Pitaevskii and S. Stringari, Bose-Einstein Condensation, *Oxford Science Publications - International Series of Monographs on Physics 116* (2002). (Cited on pages 13, 16, 23, 30, 102, 122 and 123.)

[56] E. P. Gross, Structure of a quantized vortex in boson systems, *Novo Cimento* **20**, 454 (1961). (Cited on page 15.)

[57] L. P. Pitaevskii, Vortex Lines in an Imperfect Bose Gas, *Soviet Physics JETP* **13**, 451 (1961). (Cited on page 15.)

[58] C. Ciuti, V. Savona, C. Piermarocchi, A. Quattropani, P. Schwendimann, Role of the exchange of carriers in elastic exciton-exciton scattering in quantum wells, *Phys. Rev. B* **58**, 7926 (1998). (Cited on page 15.)

[59] M. Wouters and I. Carusotto, Excitations in a Nonequilibrium Bose-Einstein Condensate of Exciton Polaritons, *Phys. Rev. Lett.* **99**, 140402 (2007). (Cited on pages 16, 19 and 32.)

[60] G. Malpuech and D. D. Solnyshkov, Bose Einstein condensation and superfluidity in an open system: theory, *arXiv*:0911.0807 (2009). (Cited on page 16.)

[61] M. Wouters and V. Savona, Energy Relaxation in the Gross-Pitaevskii equation, *arXiv*:1007.5453 (2011). (Cited on page 16.)

[62] I. G. Savenko, E. B. Magnusson, and I. A. Shelykh, Density-matrix approach for an interacting polariton system, *Phys. Rev. B* **83**, 165316 (2011). (Cited on page 16.)

[63] M. Wouters, Wave function Monte Carlo method for polariton condensates, *Phys. Rev. B* **85**, 165303 (2012). (Cited on page 16.)

[64] V. Kohnle, Y. Léger, M. Wouters, M. Richard, M. T. Portella-Oberli, and B. Deveaud-Plédran, From Single Particle to Superfluid Excitations in a Dissipative Polariton Gas, *Phys. Rev. Lett.* **106**, 255302 (2011). (Cited on pages 16 and 19.)

[65] T. Byrnes, T. Horikiri, N. Ishida, M. Fraser, and Y. Yamamoto, Negative Bogoliubov dispersion in exciton-polariton condensates, *Phys. Rev. B* **85**, 075130 (2012). (Cited on page 16.)

[66] P. L. Kapitza, Viscosity of Liquid Helium below the λ-point, *Nature* **141**, 74 (1938). (Cited on page 17.)

[67] J. F. Allen and A. D. Misener, Flow of Liquid Helium II, *Nature* **142**, 643 (1938). (Cited on page 17.)

[68] L. D. Landau, The theory of superfluidity of helium II, *J. Phys. USSR* **5**, 71 (1941). (Cited on page 17.)

[69] G. Malpuech, D. D. Solnyshkov, H. Ouerdane, M. M. Glazov, and I. Shelykh, Bose Glass and Superfluid Phases of Cavity Polaritons, *Phys. Rev. Lett.* **98**, 206402 (2007). (Cited on page 19.)

[70] F. M. Marchetti, J. Keeling, M. H. Szymanska, and P. B. Littlewood, Thermodynamics and Excitations of Condensed Polaritons in Disordered Microcavities, *Phys. Rev. Lett.* **96**, 066405 (2006). (Cited on page 19.)

[71] I. Carusotto, C. Ciuti, Probing Microcavity Polariton Superfluidity through Resonant Rayleigh Scattering, *Phys. Rev. Lett.* **93**, 166401 (2004). (Cited on page 20.)

[72] M. Wouters and I. Carusotto, Superfluidity and Critical Velocities in Nonequilibrium Bose-Einstein Condensates, *Phys. Rev. Lett.* **105**, 020602 (2010). (Cited on page 20.)

[73] M. Wouters and V. Savona, Superfluidity of a nonequilibrium Bose-Einstein condensate of polaritons, *Phys. Rev. B* **81**, 054508 (2010). (Cited on page 20.)

[74] D. Sanvitto, F. M. Marchetti, M. H. Szymanska, G. Tosi, M. Baudisch, F. P. Laussy, D. N. Krizhanovskii, M. S. Skolnick, L. Marrucci, A. Lemaître, J. Bloch, C. Tejedor, and L. Vina, Persistent currents and quantized vortices in a polariton superfluid, *Nature Physics* **6**, 527 (2010). (Cited on page 20.)

[75] J. Keeling, Superfluid Density of an Open Dissipative Condensate, *Phys. Rev. Lett.* **107**, 080402 (2011). (Cited on page 20.)

[76] J. Keeling, Response functions and superfluid density in a weakly interacting Bose gas with nonquadratic dispersion, *Phys. Rev. B* **74**, 155325 (2006). (Cited on page 20.)

[77] P. G. Kevrekidis, D. J. Frantzeskakis, and R. Carretero-González, Emergent Nonlinear Phenomena in Bose-Einstein Condensates, Springer, (2008). (Cited on page 21.)

[78] G.A. El, A. Gammal, and A.M. Kamchatnov, *Phys. Rev. Lett.* **97**, 180405 (2006). (Cited on pages 21, 27 and 28.)

[79] V. V. Konotop and M. Salerno, Small amplitude excitations in a deformable discrete nonlinear Schrödinger equation, *Phys. Rev. E* **55**, 4706 (1997). (Cited on page 21.)

[80] L. Onsager, Statistical hydrodynamics, *Nuovo Cimento* **6**, 249 (1949). (Cited on page 23.)

[81] V. L. Berezinskii, Violation of long range order in one-dimensional and two-dimensional systems with a continuous symmetry group, *Sov. Phys. JETP* **32**, 493 (1971). (Cited on page 25.)

[82] Z. Hadzibabic, P. Krüger, M. Cheneau, B. Battelier and J. Dalibard, Berezinskii-Kosterlitz-Thouless crossover in a trapped atomic gas, *Nature* **441**, 1118 (2006). (Cited on page 26.)

[83] A. A. Abrikosov, On the magnetic properties of superconductors of the second group, *Zh. Exp. Teor. Phz.* **32**, 1442 (1957). (Cited on page 26.)

[84] M. R. Matthews, B. P. Anderson, P. C. Haljan, D. S. Hall, C. E. Wieman, and E. A. Cornell, Vortices in a Bose-Einstein Condensate, *Phys. Rev. Lett.*, **83**, 2498 (1999). (Cited on page 26.)

[85] J. Williams and M. Holland, Preparing topological states of a Bose-Einstein condensate, *Nature* **401**, 568 (1999). (Cited on page 26.)

[86] K. W. Madison, F. Chevy, W. Wohlleben, and J. Dalibard, Vortex Formation in a Stirred Bose-Einstein Condensate, *Phys. Rev. Lett.* **84**, 806 (2000). (Cited on page 26.)

[87] F. M. Marchetti, M. H. Szymanska, C. Tejedor, and D. M. Whittaker, Spontaneous and Triggered Vortices in Polariton Optical-Parametric-Oscillator Superfluids, *Phys. Rev. Lett.* **105**, 063902 (2010). (Cited on page 26.)

[88] G. Tosi, F. M. Marchetti, D. Sanvitto, C. Antón, M. H. Szymanska, A. Berceanu, C. Tejedor, L. Marrucci, A. Lemaître, J. Bloch, and L. Vina, Onset and Dynamics of Vortex-Antivortex Pairs in Polariton Optical Parametric Oscillator Superfluids, *Phys. Rev. Lett.* **107**, 036401 (2011). (Cited on page 26.)

[89] G. Roumpos, M. D. Fraser, A. Löffler, Sven Höfling, A Forchel, and Y. Yamamoto, Single vortex-antivortex pair in an exciton-polariton condensate, *Nature Physics* **7**, 129 (2011). (Cited on page 26.)

[90] G. Nardin, G. Grosso, Y. Léger, B. Pietka, F. Morier-Genoud, and B. Deveaud-Plédran, Hydrodynamic nucleation of quantized vortex pairs in a polariton quantum fluid, *Nature Phys.* **7**, 635 (2011). (Cited on page 26.)

[91] D. Sanvitto, S. Pigeon, A. Amo, D. Ballarini, M. De Giorgi, I. Carusotto, R. Hivet, F. Pisanello, V. G. Sala, P. S. S. Guimaraes, R. Houdré, E. Giacobino, C. Ciuti, A. Bramati and G. Gigli, *Nature Photonics* **5**, 610 (2011). (Cited on page 26.)

[92] G. Grosso, G. Nardin, F. Morier-Genoud, Y. Léger, and B. Deveaud-Plédran, Soliton Instabilities and Vortex Street Formation in a Polariton Quantum Fluid, *Phys. Rev. Lett.* **107**, 245301 (2011). (Cited on page 26.)

[93] C. A. Jones and P. H. Roberts, Motions in a Bose condensate - Axisymmetric solitary waves, *J. Phys. A* **15**, 2599, (1982). (Cited on page 27.)

[94] G. Theocharis, D. J. Frantzeskakis, P. G. Kevrekidis, B. A. Malomed, and Y. S. Kivshar, Ring Dark Solitons and Vortex Necklaces in Bose-Einstein Condensates, *Phys. Rev. Lett.* **90**, 120403 (2003). (Cited on page 27.)

[95] A. M. Kamchatnov, L. P. Pitaevskii, Stabilization of Solitons Generated by a Supersonic Flow of Bose-Einstein Condensate Past an Obstacle, *Phys. Rev. Lett.* **100**, 160402 (2008). (Cited on page 28.)

[96] T. Frisch, Y. Pomeau, and S. Rica, Transition to dissipation in a model of superflow, *Phys. Rev. Lett.* **69**, 1644 (1992). (Cited on page 28.)

[97] N. A. Gippius, I. A. Shelykh, D. D. Solnyshkov, S. S. Gavrilov, Yuri G. Rubo, A. V. Kavokin, S. G. Tikhodeev, and G. Malpuech, Polarization Multistability of Cavity Polaritons, *Phys. Rev. Lett.* **98**, 236401 (2007). (Cited on pages 31, 49 and 52.)

[98] M. Sich, D. N. Krizhanovskii, M. S. Skolnick, A. V. Gorbach, R. Hartley, D. V. Skryabin, E. A. Cerda-Méndez, K. Biermann, R. Hey, and P. V. Santos, Observation of bright polariton solitons in a semiconductor microcavity, *Nature Photonics* **6**, 50 (2012). (Cited on page 31.)

[99] D. D. Solnyshkov, I. A. Shelykh, N. A. Gippius, A. V. Kavokin, and G. Malpuech, Dispersion of interacting spinor cavity polaritons out of thermal equilibrium, *Phys. Rev. B* **77**, 045314 (2008). (Cited on pages 32 and 53.)

[100] C. Ciuti, P. Schwendimann, B. Deveaud, and A. Quattropani, Theory of the angle-resonant polariton amplifier, *Phys. Rev. B* **62**, 4825(R)-4828(R) (2000). (Cited on pages 35 and 36.)

[101] A. Tredicucci, Y. Chen, V. Pellegrini, M. Börger, and F. Bassani, Optical bistability of semiconductor microcavities in the strong-coupling regime, *Phys. Rev. A* **54**, 3493 (1996). (Cited on page 38.)

[102] A. Baas, J.-Ph. Karr, M. Romanelli, A. Bramati, and E. Giacobino, Optical bistability in semiconductor microcavities in the nondegenerate parametric oscillation regime: Analogy with the optical parametric oscillator, *Phys. Rev. B* **70**, 161307(R) (2004). (Cited on pages 38 and 39.)

[103] N. A. Gippius, S. G. Tikhodeev, V. D. Kulakovskii, D. N. Krizhanovskii and A. I. Tartakovskii, Nonlinear dynamics of polariton scattering in semiconductor microcavity: Bistability vs. stimulated scattering, *Europhys. Lett.* **67** 997 (2004). (Cited on page 38.)

[104] D. M. Whittaker, Effects of polariton-energy renormalization in the microcavity optical parametric oscillator, *Phys. Rev. B* **71**, 115301 (2005). (Cited on page 38.)

[105] T. Dieti, D. D. Awschalom, M. Kaminska and H. Ohno, *Spintronics*, Elsevier (2008). (Cited on page 40.)

[106] I. A. Shelykh, K. V. Kavokin, A. V. Kavokin, G. Malpuech, P. Bigenwald, H. Deng, G. Weihs, and Y. Yamamoto, Semiconductor microcavity as a spin-dependent optoelectronic device, *Phys. Rev. B* **70**, 035320 (2004). (Cited on page 40.)

[107] W. Langbein, I. A. Shelykh, D. D. Solnyshkov, G. Malpuech, Y. G. Rubo, and A. Kavokin, Polarization beats in ballistic propagation of exciton-polaritons in microcavities, *Phys. Rev. B* **75**, 075323 (2007). (Cited on pages 40 and 44.)

[108] G. Lampel, Nuclear dynamic polarization by optical electronic saturation and optical pumping in semiconductors, *Phys. Rev. Lett.* **20**, 491 (1968). (Cited on page 41.)

[109] D. D. Solnyshkov, I. A. Shelykh, M. M. Glazov, G. Malpuech, T. Amand, P. Renucci, X. Marie, and A. V. Kavokin, Nonlinear effects in spin relaxation of cavity polaritons, *Semiconductors* **41**, 9 (2007). (Cited on pages 41 and 49.)

[110] M. Z. Maialle, E. A. de Andrada e Silva, and L. J. Sham, Exciton spin dynamics in quantum wells, *Phys. Rev. B* **47**, 15776 (1993). (Cited on page 42.)

[111] L. Bir, A. G. Aronov, and G. E. Pikus, *Zh. Eksp. Teor. Fiz.*, **69**, 1382 (1975). (Cited on page 42.)

[112] I. A. Shelykh, G. Pavlovic, D. D. Solnyshkov, and G. Malpuech, Proposal for a Mesoscopic Optical Berry-Phase Interferometer, *Phys. Rev. Lett.* **102**, 046407 (2009). (Cited on pages 43 and 48.)

[113] G. Panzarini L. C. Andreani, A. Armitage, D. Baxter, M. S. Skolnick, V. N. Astratov, J. S. Roberts, A. V. Kavokin, M. R. Vladimirova, and M. A. Kaliteevski, Exciton-light coupling in single and coupled semiconductor microcavities: Polariton dispersion and polarization splitting, *Phys. Rev. B* **59**, 5082 (1999). (Cited on page 44.)

[114] L. Klopotowski, M. D. Martin, A. Amo, L. Vina, I. A. Shelykh, M. M. Glazov, G. Malpuech, A. V. Kavokin, and R. André, Optical anisotropy and pinning of the linear polarization of light in semiconductor microcavities, *Solid State Communications* **139** 10, 511 (2006). (Cited on page 44.)

[115] M. I. Dyakonov and V. I. Perel', Possibility of orientating electron spins with current, *Sov. Phys. JETP Lett.* **13**, 467 (1971). (Cited on page 47.)

[116] S. Murakami, N. Nagaosa, and S. C. Zhang, Dissipationless Quantum Spin Current at Room Temperature, *Science* **301**, 1348 (2003). (Cited on pages 47 and 48.)

[117] Y. K. Kato, R. C. Myers, A. C. Gossard and D. D. Awschalom, Observation of the Spin Hall Effect in Semiconductors, *Science* **306**, 1910 (2004). (Cited on pages 47 and 48.)

[118] J. E. Hirsch, Spin Hall Effect, *Phys. Rev. Lett.* **83**, 1834 (1999). (Cited on page 47.)

[119] A. Kavokin, G. Malpuech, and M. Glazov, Optical spin-Hall effect, *Phys. Rev. Lett.* **95**, 136601 (2005). (Cited on page 47.)

[120] M. Maragkou, C. E. Richards, T. Ostatnicky, A. J. D. Grundy, J. Zajac, M. Hugues, W. Langbein, and P. G. Lagoudakis, Optical analogue of the spin Hall effect in a photonic cavity, *Opt. Lett.* **36**, 1095 (2011). (Cited on page 47.)

[121] N. Shitrit, I. Bretner, Y. Gorodetski, V. Kleiner, and E. Hasman, Optical spin Hall effects in plasmonic chains, *Nano Lett.* **11** 5, 2038 (2011). (Cited on page 47.)

[122] A. Amo, T. C. H. Liew, C. Adrados, E. Giacobino, A. V. Kavokin, and A. Bramati, Anisotropic optical spin Hall effect in semiconductor microcavities *Phys. Rev. B* **80**, 165325 (2009). (Cited on page 48.)

[123] M. Combescot and O. Betbeder-Matibet, Faraday rotation in photoexcited semiconductors: A composite-exciton many-body effect, *Phys. Rev. B* **74**, 125316 (2006). (Cited on page 49.)

[124] M. Vladimirova, S. Cronenberger, D. Scalbert, K. V. Kavokin, A. Miard, A. Lemaitre, J. Bloch, D. Solnyshkov, G. Malpuech, and A. V. Kavokin, Polariton-polariton interaction constants in microcavities, *Phys. Rev. B* **82**, 075301 (2010). (Cited on page 49.)

[125] P. Renucci, T. Amand, X. Marie, P. Senellart, J. Bloch, B. Sermage, and K. V. Kavokin, Microcavity polariton spin quantum beats without a magnetic field: A manifestation of Coulomb exchange in dense and polarized polariton systems, *Phys. Rev. B* **72**, 075317 (2005). (Cited on page 49.)

[126] A. V. Larionov, V. D. Kulakovskii, S. Höfling, C. Schneider, L. Worschech, and A. Forchel, Polarized Nonequilibrium Bose-Einstein Condensates of Spinor Exciton Polaritons in a Magnetic Field, *Phys. Rev. Lett.* **105**, 256401 (2010). (Cited on pages 49 and 52.)

[127] I. A. Shelykh, Y. G. Rubo, G. Malpuech, D. D. Solnyshkov, and A. Kavokin, Polarization and Propagation of Polariton Condensates, *Phys. Rev. Lett.* **97**, 066402 (2006). (Cited on pages 50 and 55.)

[128] P. D. Maker, R. W. Terhune, and C. M. Savage, Intensity-Dependent Changes in the Refractive Index of Liquids, *Phys. Rev. Lett.* **12**, 507 (1964). (Cited on page 50.)

[129] J. Kasprzak, R. André, Le Si Dang, I. A. Shelykh, A. V. Kavokin, Yuri G. Rubo, K. V. Kavokin and G. Malpuech, Build up and pinning of linear polarization in the Bose condensates of exciton polaritons, *Phys. Rev. B* **75**, 045326 (2007). (Cited on page 50.)

[130] Y. G. Rubo, A. V. Kavokin, and I. A. Shelykh, Suppression of superfluidity of exciton-polaritons by magnetic field, *Physics Letters A* **358** 3, 227 (2006). (Cited on page 51.)

[131] T. C. H. Liew, Y. G. Rubo, I. A. Shelykh, and A. V. Kavokin, Suppression of Zeeman splitting and polarization steps in localized exciton-polariton condensates, *Phys. Rev. B* **77**, 125339 (2008). (Cited on page 51.)

[132] H. Flayac, I. A. Shelykh, D. D. Solnyshkov, and G. Malpuech, Topological stability of the half-vortices in spinor exciton-polariton condensates, *Phys. Rev. B* **81**, 045318 (2010). (Cited on pages 51, 70 and 74.)

Chapter 2

Half-integer topological defects in spinor polariton condensates

Contents

Multicomponent (spinor) condensates allow more complex topological excitations than scalar ones, which mix both the phase and the spin topologies [1]. One can cite solitons in spinor one dimensional condensates [2, 3] (vector solitons) and oblique solitons in spinor two dimensional systems, that have already been considered theoretically [4]. In one dimension, many possible configurations were described, depending on the strength and type of the particle interactions (repulsive or attractive). In particular, a solution where the kink lies in only one component was reported: The dark-antidark soliton or half-soliton (HS) [5]. The counterpart of such a defect in 2D systems is the so-called half-vortex or Skyrmion [6, 7] depending on the intercomponent interactions type.

Half-integer topological defects were originally predicted by Volovik and Mineev [8] in 1976 the context of superfluid Helium 3 and their experimental observation was reported at the intersection of three grain boundaries of cuprate superconductors by Kirtley et al. (1996) [9] in the form of half-vortices. Along with the first reports of polariton condensation it appeared quite natural to investigate the possibility of having quantized vortices in the systems. Rubo predicted in 2006 [10], that due to the spontaneous formation of the polariton condensate with a well defined linear polarization as we have seen previously, the elementary topological excitations are not regular but half-integer vortices. This discovery being first quite mysterious to the polariton community, has next attracted much attention. The first experimental observation of vortices in a polariton condensate by the group of Lausanne [11] followed in 2008 with a non-resonantly populated condensate with a pulsed pump. In that work, the sample used had strong enough structural imperfections to induce a significant disorder landscape. The separated condensate islands forming (due to the disorder) at the early times have different phases, and their reconnection at higher densities induces phase dislocations at their interface in the form of vortices, as it was understood later [12]. Therefore, the vortices were observed pinned to defects at deterministic positions. Since this very first experiment was not polarization resolved, there was no chance of evidencing half-vortices. The next year, the same group revisited their own experiment [20] [see Fig.2.1] separating the two circular polarization components to discover that regular vortices actually coexisted with the expected half-quantum vortices, which was quite an exciting result. These experiments have then paved the way to an impressive number of proposals [14, 15, 16, 17, 18, 19] and experimental reports [20, 21, 22, 23, 24, 25, 26, 27] on vortices in semiconductor microcavities. And this, thanks to the high degree of control that is now possible on the optically generated polariton fluid. The generation of half-vortices has so far been much less studied [10, 132, 29], and observed only once [20].

In this chapter we will introduce these half-integer topological defects. We will first analyze the stability of half-vortices in the TE-TM effective magnetic field and their interactions [Sec.2.1]. Next, we will introduce their one dimensional counterpart namely half-soliton and show that half-integer topological defects behave as

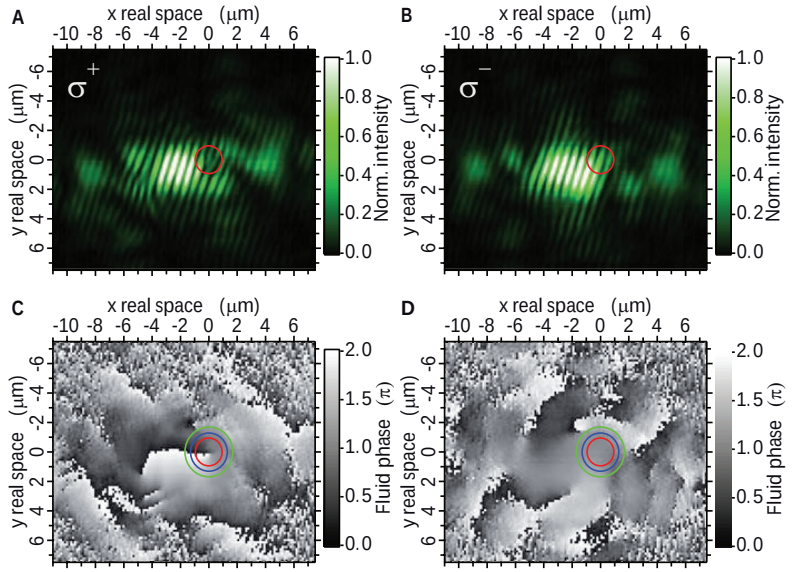

Figure 2.1: Observation of half-quantum vortices in a polariton condensate from Ref.[20]. (A,B) Reconstructed interferograms for σ_+ and σ_- polarizations at the energy of the condensate. We see the typical forklike dislocation appearing in only one component, highlighted by the circles, evidencing the half-vortex. (C,D) Associated real space phase map extracted from the interferograms.

magnetic charges accelerated by effective magnetic fields. We shall then propose means of exciting such fascinating objects towards the formation of real magnetic currents [Sec.2.2]. We will then switch to the hydrodynamic generation of oblique half-solitons in a propagating polariton quantum fluid, see that they behave as magnetic charges as well, and present their recent experimental observation [Sec.2.3]. We will make a stop at the physics of Black holes demonstrating that the polariton fluid is a valuable candidate for the formation of sonic holes and we will see that half-integer topological defects can embody seed signals propagating through these gravitational analogues [2.4]. Eventually, we will propose another means of exciting integer and half-integer topological defects using electric currents [2.5].

2.1 Stability of the half-vortices

2.1.1 Half-vortices

The original description of half-vortices proposed by Rubo [10] was performed on the linear polarization basis neglecting the TE-TM splitting. The stationary vectorial order parameter $\boldsymbol{\psi}(\mathbf{r})$ of the two component spinor condensate reads

$$\boldsymbol{\psi} = \begin{pmatrix} \psi_x \\ \psi_y \end{pmatrix} = \begin{pmatrix} \sqrt{n_x} e^{i\theta_x} \\ \sqrt{n_y} e^{i\theta_y} \end{pmatrix} \tag{2.1}$$

Indeed, for an arbitrary polarization of the condensate, the phases $\theta_{x,y}(\mathbf{r})$ and the densities $n_{x,y}(\mathbf{r})$ are defined independently for each component. However, since the condensate forms with a well defined polarization, the previous expression can be rewritten as

$$\boldsymbol{\psi}_{lin} = \begin{pmatrix} \psi_x \\ \psi_y \end{pmatrix} = \sqrt{n_0} \begin{pmatrix} \cos(\eta)\, e^{i\theta} \\ \sin(\eta)\, e^{i\theta} \end{pmatrix} \tag{2.2}$$

Which means that $\theta_x = \theta_y = \theta$, $\sqrt{n_x} = \sqrt{n_0}\cos\eta$ and $\sqrt{n_y} = \sqrt{n_0}\sin\eta$. n_0 is the total density, $\eta(\mathbf{r})$ is the linear polarization angle and $\theta(\mathbf{r})$ is a global phase of the spinor condensate, namely the phase that would be measured in an experiment where the polarization is not resolved. This representation, where the phase and polarization angle are separated means that we consider the particles being part of a global fluid, each particle having a linear polarization defined by η. It is possible here to define a global velocity for the spinor condensate $\mathbf{v} = \hbar/m\boldsymbol{\nabla}\theta$. We insist on the fact that this representation is valid only for linear polarization states, indeed no global phase can be correctly defined for elliptic condensates (i.e. forming under applied magnetic field [30]).

We see that for the two component spinor condensate, we are dealing with two phases η and θ. Following the argumentation of the section 1.2.5.2 devoted to vortices, we can easily understand that $\theta(\mathbf{r})$ being defined modulus 2π is allowed to wind around a central point to form a global phase vortex which actually coincides with a usual integer vortex provided that the orientation of η remains homogeneous in space. As well, nothing prevents η from winding, in its turn keeping θ constant to form the so-called polarization vortex. To describe a vortex state we therefore need two winding numbers denoted as k and m for the polarization an phase respectively. The latter cases correspond to an integer value of one winding number while the other one is zero. One thing to note is that since a linear polarization direction (corresponding to the oscillation direction of the electric field) is defined only up to π, it should therefore be possible for η to wind e.g. by only π around the vortex core preserving the continuity of the polarization texture. However, the whole order parameter defined by Eq.(2.2) is not invariant under the transformation $\eta \to \eta + p\pi$ ($p \in \mathbb{Z}$) so we need something more and anyway the orientation of η is oscillating with time, breaking the continuity. Indeed, on the other hand, we have

$$\begin{pmatrix} \psi_x \\ \psi_y \end{pmatrix} = \begin{pmatrix} \cos(\eta + p\pi)\, e^{i(\theta + q\pi)} \\ \sin(\eta + p\pi)\, e^{i(\theta + q\pi)} \end{pmatrix} = \begin{pmatrix} (-1)^p (-1)^q \cos(\eta)\, e^{i\theta} \\ (-1)^p (-1)^q \sin(\eta)\, e^{i\theta} \end{pmatrix} \tag{2.3}$$

which means that the order parameter is invariant under the *combined* transformations $\{\eta, \theta\} \rightarrow \{\eta + p\pi, \theta + q\pi\}$ where $\{p, q\} \in \mathbb{Z}$ provided that p and q have the same parity. In the winding number representation given that $\{k, m\} = \{p/2, q/2\}$ we immediately obtain that k and m are allowed to take both integer and *half-integer* values, defining the so-called *half-quantum vortices* in the latter case. The π winding of a quantity on a closed loop appears as strongly counterintuitive since the particles need to wind two times in order to recover the initial phase for a Möebius band. However, it is important to note that for example the $\{k, m\} = \{1/2, 0\}$ half-vortex is forbidden, since the global continuity of the order parameter is violated in that case. The half winding of one of the two phases imposes the other one to behave in a fractional fashion as well, to preserve this global continuity. A global winding number could be defined as $\kappa = k + m$ and the continuity would require κ to be an integer in order to recover physical phase windings of $2\kappa\pi$ around the vortex core.

The order parameter of the spinor polariton condensate can be seen as an infinite chessboard. A vortex is defined by a diagonal line connecting two equivalent points on this chessboard characterized by the winding numbers k and m as shown in Fig.2.2.

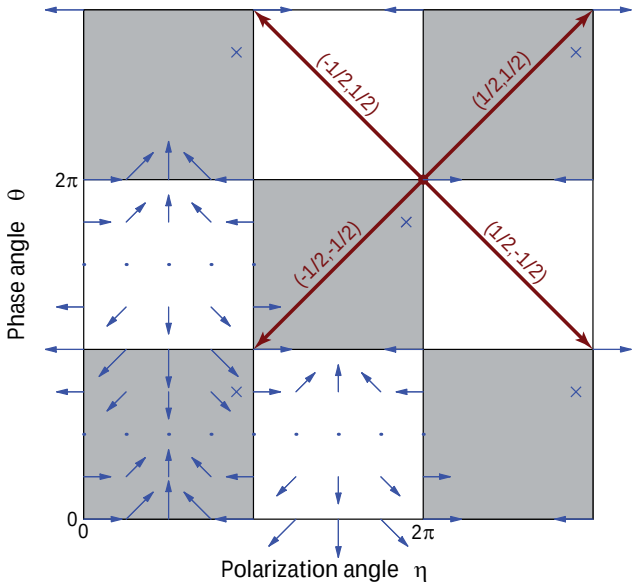

Figure 2.2: Representation of the spinor polariton condensate's order parameter. A vortex corresponds to a diagonal line connecting two points of the chessboard. This line is associated with the transformation $\eta \rightarrow \eta + 2k\pi$ and $\theta \rightarrow \theta + 2m\pi$. The blue arrows show the vector field associated with η namely $\mathrm{Re}(\psi_{\mathrm{lin}})$.

2.1.2 Energy

We know from the section (1.2.5.2) that the vortex energy is dominated by its kinetic part (or elastic part) [31] growing logarithmically with the system size and this statement has no reason to fail for half-vortices. Since for the linearly polarized condensate far from the vortex core we are allowed to separate θ and η, the kinetic energy of the condensate reads:

$$E_k = \frac{\hbar^2 n_0}{2m^*} \int \left[\nabla\eta\left(\mathbf{r}\right) + \nabla\theta\left(\mathbf{r}\right)\right]^2 d\mathbf{r} \tag{2.4}$$

having a single vortex in the system means that

$$\theta = k\phi \tag{2.5}$$

$$\eta = m\phi \tag{2.6}$$

where ϕ is the polar angle, E_k is therefore reduced to

$$E_k = \frac{\hbar^2 n_0}{2m^*}\left(k^2 + m^2\right) \ln\left(\frac{R}{\xi}\right) \tag{2.7}$$

$\xi = \hbar/\sqrt{2m^*\mu}$ is the healing length of the condensate and the chemical potential is defined by $\mu = (U_0 - U_1)n_0$. As one would have expected, the lowest energy half-vortices possess winding numbers equal to one half. The four building blocks are thus defined by

$$\{k, m\} = \begin{cases} \{+1/2, +1/2\} \\ \{-1/2, -1/2\} \\ \{+1/2, -1/2\} \\ \{-1/2, +1/2\} \end{cases} \tag{2.8}$$

Noticing moreover that if e.g. $l = 1$ and $k, m = \pm 1/2$, one has $l^2 = 2(k^2 + m^2)$ which means that the energy of an integer, phase or polarization, vortex is *twice* larger than that of a half-vortex. The latter therefore embody the *elementary topological excitation* in a polariton condensate. Importantly enough, the Berezinskii-Kosterlitz-Thouless [see Sec.1.2.5.3] is reduced by a factor 2 if half-vortices are involved.

2.1.3 Polarization texture

So far we haven't yet discussed the core structure of the half-vortex which is especially interesting. This aspect is however far more transparent on the circular polarization basis as we will see [132].

Let us rewrite the order parameter (2.2) on the circular polarization basis. Using the transformation $\psi_\pm = \left(\psi_x \mp i\psi_y\right)/\sqrt{2}$ we easily obtain

$$\boldsymbol{\psi}_{lin} = \sqrt{\frac{n_0}{2}} \begin{pmatrix} e^{i(\theta+\eta)} \\ e^{i(\theta-\eta)} \end{pmatrix} \tag{2.9}$$

Each component possesses its own phase $\theta_+ = \theta + \eta$ and $\theta_+ = \theta - \eta$. As well, the linear polarization angle is defined by the phase difference between the two

circular components $\eta = (\theta_+ - \theta_-)/2$ and the global phase is the sum of the two $\theta = (\theta_+ + \theta_-)/2$. Considering a vortex state characterized by the winding numbers k and m we can define a new set of winding numbers $(l_+, l_-) = (k+m, k-m)$ which are bound to be integer. The corresponding vortex order parameter reads

$$\boldsymbol{\psi}_{HV} = \sqrt{\frac{n_0}{2}} \begin{pmatrix} e^{il_+\phi} \\ e^{il_-\phi} \end{pmatrix} \tag{2.10}$$

Which makes the half-vortex representation much clearer and intuitive, indeed, we see that from the phase point of view, each component takes separately the form a vortex wavefunction with the winding numbers (l_+, l_-). In this representation, the four elementary half-vortices are characterized by

$$\{l_+, l_-\} = \begin{cases} \{+1, 0\} \\ \{-1, 0\} \\ \{0, +1\} \\ \{0, -1\} \end{cases} \tag{2.11}$$

Meaning that a half-vortex solution corresponds to having a vortex in one component while the other one remains unperturbed at least if $\alpha_2 = 0$, which makes their interpretation far more natural.

Let us now discuss the half-vortex as a whole, including its core structure. To do so, we need to rewrite the order parameter out of the linear polarization approximation, which was found by an asymptotic analysis far away from the vortex core, including the radial profiles $f_+(r) = \sqrt{n_+(r)}$ and $f_-(r) = \sqrt{n_-(r)}$.

$$\psi_{HV}(r, \phi) = \begin{pmatrix} f_+(r)\, e^{il_+\phi} \\ f_-(r)\, e^{il_-\phi} \end{pmatrix} \tag{2.12}$$

The stationary ($\partial_t \to -i\mu$) spinor Gross-Pitaevskii equations (1.169,1.169) can be rewritten in the following dimensionless form

$$\begin{pmatrix} -\frac{\Delta}{2} - 1 + A_1|\psi_+|^2 + A_2|\psi_-|^2 & \chi(\partial_y + i\partial_x)^2 \\ \chi(\partial_y - i\partial_x)^2 & -\frac{\Delta}{2} - 1 + A_1|\psi_-|^2 + A_2|\psi_-|^2 \end{pmatrix} \begin{pmatrix} \psi_+ \\ \psi_- \end{pmatrix} = \begin{pmatrix} 0 \\ 0 \end{pmatrix} \tag{2.13}$$

We have used here the scaling relations: $\psi_\pm \to (\mu/(\alpha_1+\alpha_2))^{1/2}\psi_\pm$, $\mathbf{r} \to \left(\hbar^2/(m^*\mu)\right)^{1/2}\mathbf{r}$ and $t \to (\hbar/\mu)\, t$. Here, $\mu = (\alpha_1+\alpha_2)\, n_\infty/2$ with $n_\infty = |\psi_+(\infty)|^2 + |\psi_-(\infty)|^2$ being the condensate density far away from the vortex core, $A_{1,2} = \alpha_{1,2}/(\alpha_1+\alpha_2)$ and $\chi = \beta m^*/\hbar^2$. Injecting the ansatz (2.12) in the equations (2.13) neglecting first the TE-TM splitting ($\chi = 0$) yields the equations for the radial functions.

$$f_+'' + f_+' + \left(2 - 2A_1 f_+^2 - 2A_2 f_-^2 - \frac{l_+^2}{r^2}\right) f_+ = 0 \tag{2.14}$$

$$f_-'' + f_-' + \left(2 - 2A_1 f_-^2 - 2A_2 f_+^2 - \frac{l_-^2}{r^2}\right) f_- = 0 \tag{2.15}$$

In the simplest case, where the circular polarized components do not interact ($A_2 = 0$), the half-vortex with e.g. $l_+ = +1$, $l_- = 0$ corresponds to a homogeneous distribution of σ_+ component and a simple vortex in σ_-. Clear enough, in the center of such a half-vortex the density is non-zero (due to the σ_+ component) and the polarization is circular, since the density of the σ_- component is zero in the center of the vortex. Such kind of vortices is referred to as a coreless vortex [1] in atomic condensates but in that case, the spin isotropy of the interactions gives rather birth to skyrmion [6, 7] that are asymptotically circularly polarized. In our case, moving from the center of the vortex, the polarization of the half-vortex changes from circular to linear in a continuous manner [see Fig.2.3].

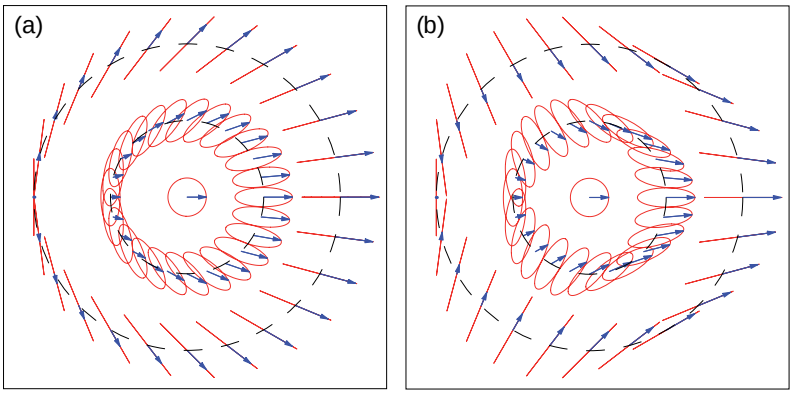

Figure 2.3: Two half-vortex polarization textures from Ref.[10]. (a) (+1/2,+1/2) or (+1/2,-1/2) and (b) (-1/2,+1/2) or (-1/2,-1/2) half-vortices. The red arrows show the orientation of the linear polarization at a specific time and the red circles show the trajectories of the arrows displaying the degree of circular polarization.

It is interesting to note that at the core position neither the σ_+ nor the σ_- particles contribute to the condensate's motion since one component is completely static and the other one is absent. As well, far away from the vortex core the particles of the component carrying the vortex are almost immobile since $v(r) \sim 1/r$. It is therefore very tempting to define a global hydrodynamic velocity $\mathbf{v}_g$ for the spinor condensate

$$\mathbf{v}_g = \frac{n_+}{n_0}\mathbf{v}_+ + \frac{n_-}{n_0}\mathbf{v}_- \tag{2.16}$$

that describes well this behavior. However, apart from a linear polarization case (which is definitely not the case of the vortex core) for which $\mathbf{v}_g = \hbar/m^*\theta$ (θ the global phase defined above), this velocity cannot be linked with any phase in the system and its circulation is in the general case not quantized.

The set of equations (2.14,2.15) can only be solved numerically and the results are shown in the Fig.2.4 in the case $(l_+, l_-) = (+1, 0)$ for $A_2 = 0$ [panel(a)] and $A_2 = -0.1A_1$ [panel (b)]. In the first case, the normalized radial function in the σ_+ component is obviously that of a regular vortex and can be well approximated by the function $f_+(r) = r/\sqrt{r^2+2}$, while $f_-(r) = 1/2$. In the second case the intercomponent interactions being attractive ($A_2 < 0$) the presence of the dip in

the σ_+ density is seen as a weak potential barrier by the σ_- component, which therefore exhibits a shallow density minimum at the vortex position as well [see Fig.2.4]. Additionally, the vortex size is slightly reduced: the healing length ξ is renormalized in the σ_+ component.

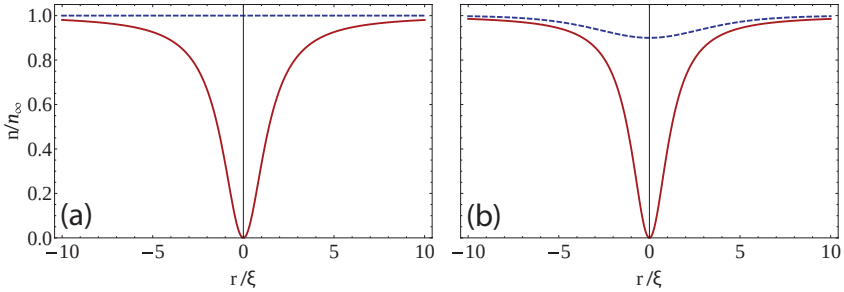

Figure 2.4: Half-vortex normalized density slice $n_\pm(r) = f_\pm^2(r)$. (a) $A_2 = 0$ and (b) $A_2 = -0.1A_1$. The solid red (dashed/blue) curve shows the σ_+ (σ_-) component. The vortex therefore lies here in the σ_+ component here: $(\pm 1, 0)$ half-vortex.

2.1.4 Impact of the TE-TM effective magnetic field

Now, let us consider a more interesting case where $\chi \neq 0$. The terms associated with the TE-TM splitting [see Sec.1.4.3] have to be rewritten in polar coordinates:

$$(\partial_y \pm i\partial_x)^2 = e^{\mp 2i\phi}\left(\frac{\partial_r}{r} \mp 2i\frac{\partial_\phi}{r^2} \pm 2i\frac{\partial_r\partial_\phi}{r} - \partial_r^2 + \frac{\partial_\phi^2}{r^2}\right) \tag{2.17}$$

The non-zero exchange between the two components leads to the mutual dependence of their winding numbers. The only *cylindrically symmetric* solutions of Eqs.(2.13) have the following form:

$$\begin{pmatrix} \psi_+(r,\phi) \\ \psi_-(r,\phi) \end{pmatrix} = e^{il\phi}\begin{pmatrix} f_+(r) \\ e^{2i\phi} f_-(r) \end{pmatrix} \tag{2.18}$$

which means that necessarily

$$l = l_+ = l_- - 2 \tag{2.19}$$

In terms of Ref.[10] this state corresponds $k = -1$ and $m = 0$, namely, a polarization vortex. Which means that in the thermodynamic limit we consider here, the half-vortex is not allowed to be a *stationary* solution keeping the symmetry of the Hamiltonian anymore. In a comment [32] on our paper [28], an asymptotic non-cylindrical half-vortex solution was proposed for which the polarization and phase become warped and the stream lines are no more concentric but warped as well. However, we explained in our reply [33] that this asymptotic analysis is definitely not sufficient to prove the existence of this solution since this is the core region, which was neglected in the comment, that is actually the most affected by the TE-TM splitting. Later on, we have been performing numerical simulations

to see the impact of the TE-TM splitting on a single half-vortex. What we found was that while for realistic values of the field the half-vortex was not destroyed, we observed that its core was oscillating being squeezed periodically demonstrating its non-stationarity.

Back to our cylindrically symmetric solution, the elastic energy of a vortex can be rewritten on the circular polarization basis as

$$E_{kin} = \frac{\hbar^2 n_\infty}{2m^*} \int \left[|\boldsymbol{\nabla}\theta_+|^2 + |\boldsymbol{\nabla}\theta_-|^2 \right] d\mathbf{r} = \frac{\pi\hbar^2 n_\infty}{2m^*} \left(l_+^2 + l_-^2 \right) \ln\left(\frac{R}{\xi}\right) \tag{2.20}$$

From the above formula and under the condition $l_+ = l_- - 2$, it follows that the kinetic energy is minimized for $(l_+, l_-) = (-1, +1)$. However, one shouldn't forget that under the action of an effective magnetic field (induced here by the TE-TM splitting), the condensate acquires the magnetic energy

$$E_{mag} = -\int d\mathbf{r} \left(\mathbf{H}_{LT} \cdot \mathbf{S} \right) \tag{2.21}$$

whose contribution to the total energy can be significant, depending on the pseudospin texture. Let us therefore calculate the pseudospin associated with our vortex solution. Since we have $|l_+| = |l_-| = 1$ we will use the standard approximated radial functions for scalar vortices to write the following (dimensionless) order parameter

$$\begin{pmatrix} \psi_+ \\ \psi_- \end{pmatrix} = \frac{r}{\sqrt{r^2+2}} \begin{pmatrix} e^{-\phi} \\ e^{+\phi} \end{pmatrix} \tag{2.22}$$

The pseudospin follows from Eqs.(1.141-1.143) and we obtain

$$\begin{pmatrix} S_x \\ S_y \\ S_z \end{pmatrix} = \frac{r^2}{r^2+2} \begin{pmatrix} \cos(2\phi) \\ \sin(2\phi) \\ 0 \end{pmatrix} \tag{2.23}$$

The corresponding texture is shown in the right panel of Fig.2.5. We note that a similar object was refereed to as a wavefunction monopole (by its spin texture) in Ref.[34] in atomic Bose-Einstein condensates. Two things are remarkable: first, the pseudospin is in-plane ($S_z = 0$), and thus the polarization is linear everywhere, defining a polarization vortex, second, $\mathbf{S}$ makes an angle 2ϕ with the x-direction (the polarization of the emitted light is radial everywhere). Consequently, our solution corresponds to a pseudospin aligned with H_{LT} all over the plane. The condensate is fully TE or TM polarized depending on which of these two states has the lower energy, and the magnetic energy is strongly negative. One extra thing to note is that since the polarization is linear everywhere, the global phase θ of the condensate can be defined and is constant. At the vortex core, the total density is zero, while the σ_+ and σ_- particles rotating in opposite directions (at the same speed) impose a globally "static" condensate as follows from $\mathbf{v}_g \sim \boldsymbol{\nabla}\theta$ which appears quite counterintuitive. Of course, it does not mean that the corresponding kinetic energy is zero.

To compare, the $(l_+, l_-) = (0, +1)$ half-vortex pseudospin texture in the absence of the TE-TM splitting is found as

$$\begin{pmatrix} S_x \\ S_y \\ S_z \end{pmatrix} = \frac{r^2}{r^2+2} \begin{pmatrix} \cos(\phi) \\ \sin(\phi) \\ 0 \end{pmatrix} \tag{2.24}$$

and it is shown in the left panel of Fig.2.5. In that case, the pseudospin is divergent and makes an angle ϕ with $\mathbf{H}_{LT}$ bringing a significant positive contribution to the magnetic energy where the TE-TM splitting is strong in the core region. Of course, this solution is not stationary in such field, which can be easily checked by numerical simulations.

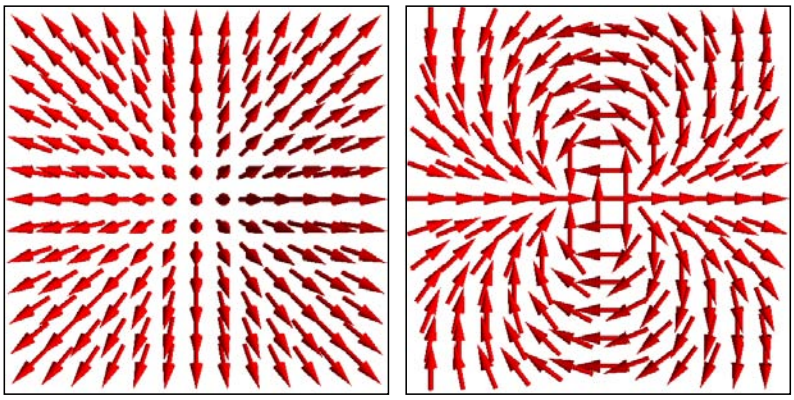

Figure 2.5: Left panel: (+1,0) half-vortex pseudospin texture. Right panel: (-1,+1) polarization vortex pseudospin texture aligned with the TE-TM splitting induced effective magnetic field.

In summary, the polarization vortex strongly minimizes the magnetic energy while its kinetic energy is twice larger than in the half-vortex case, as we know. However, the half-vortex carries much larger magnetic energy, which is significant near its core where the TE-TM splitting is strong. The kinetic energy is dependent on the system size, so there is necessarily a crossing between the total energy carried by the polarization vortex and the one carried by the half-vortex increasing R from zero to infinity.

2.1.5 Interactions

Now let us consider half-vortex pairs. As we have seen in Sec.1.2.5.2, the kinetic energy can be reduced by the vortex-antivortex interaction. Indeed, the presence of a vortex pair heals the large scale perturbation of the phase and velocity field to keep it only local, the interaction term removes the system size dependent divergence in the kinetic energy. This is the reason why a condensate perturbed locally would favor the nucleation of vortex anti-vortex pairs [see Sec.2.5]. Topologically speaking, the uniform state and the vortex pair state are equivalent [31]. This argument stands for

a large number of vortices where an equal number of vortex and antivortex should be excited. For the spinor condensate, and from the point of view of the magnetic energy, it is necessary to excite an equal quantity of σ_+ and σ_- vortices. In the absence of the TE-TM splitting, in addition to their individual energy, a half-vortex pair separated by the distance d adds the following interaction term to the kinetic energy of the condensate

$$E_{int} = \frac{\pi\hbar^2 n_\infty}{2m^*}\left(l_{1+}l_{2+} + l_{1-}l_{2-}\right)\ln\left(\frac{\xi}{d}\right) \tag{2.25}$$

It is clear intuitively and from the above formula (2.25) that half-vortices sharing the same component interact, within this component, like scalar vortices, while the half-vortices lying in different components cannot interact. However, in the presence of the TE-TM splitting the particle exchange between the two components should modify the situation. The polarization vortex $(-1,+1)$ appears to be the linear combination of the $(-1,0)$ and the $(0,+1)$ half-vortex. Let us separate these two elementary half-vortices by a distance d between them (e.g. along x-axis). In view of the induced symmetry breaking, it is necessary to rewrite the associated order parameter in cartesian coordinates

$$\begin{pmatrix} \psi_+\left(r_+,\phi_+,d\right) \\ \psi_-\left(r_-,\phi_-,d\right) \end{pmatrix} = \begin{pmatrix} f_+\left(r_+\right)e^{il_+\phi_+} \\ f_-\left(r_-\right)e^{il_-\phi_-} \end{pmatrix} \tag{2.26}$$

where $r_\pm = \sqrt{(x \mp d/2)^2 + y^2}$, $\phi_\pm = \arctan[y/(x \mp d/2)]$ and $f_\pm(r_\pm) = r\pm/\sqrt{r_\pm^2 + 2}$ are the approximate radial functions that we take as in the unperturbed case for simplicity. The corresponding pseudospin texture is shown Fig.2.6(b). The separation of the half-vortices impacts on the magnetic energy of the system

$$E_{mag} = \int \left[\psi_+^*(\partial_y + i\partial_x)^2\psi_- + \psi_-^*(\partial_y + i\partial_x)^2\psi_+\right]d\mathbf{r} \tag{2.27}$$

that increases with d. The numerical evaluation of E_{mag} is shown in Fig.2.6(a) as a function of d. One can see that as expected the energy grows logarithmically with d. It follows that the TE-TM splitting makes $(-1,0)$ and $(0,+1)$ vortices interact and collapse on each other to form the $(-1,+1)$ vortex.

2.1.6 Conclusion

In conclusion, we have seen that in the absence of the TE-TM splitting, half-vortices are the elementary topological excitations of the spinor polariton condensate. Taking into account the TE-TM splitting, that is always present in planar microcavities, shows that the single half-vortex is no more a solution preserving the symmetry of the Hamiltonian, meaning that it is no more a stationary solution. The integer polarization vortex, being the bound state of two half-vortices, preserves the symmetry of the Hamiltonian and its pseudospin geometry is the same as the TE-TM effective field geometry which minimizes both the magnetic and interaction energy of the

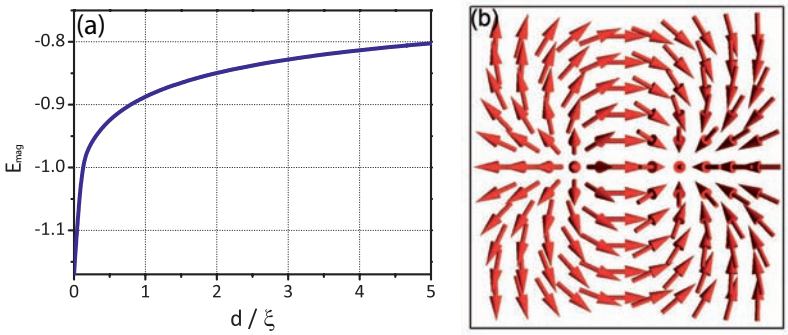

Figure 2.6: (a) Growing of the magnetic energy E_{mag} with the increase of separation d between the $(-1, 0)$ and $(0, +1)$ half-vortices. The associated pseudospin texture is shown in the panel (b).

condensate. This solution is consequently stable and stationary and will definitely not decay into a pair of half-vortices. On the contrary, half-vortices merge to form the polarization vortex.

2.2 Half-integer topological defects as magnetic monopoles analogues

Abstraction is a common tool in physics, serving the better comprehension of complex phenomena. The most evident example is the atom, encompassing an intricate underlying structure of electrons and hadrons, the latter themselves composed of quarks and gluons. This internal structure can of course be completely neglected while discussing the properties of gases in statistical physics. Such multilevel abstraction is especially common for solid-state physics, where excitons are formed from electrons and holes, themselves being complicated elementary excitations formed from several electronic levels of atoms constituting the solid. The excitons can be described as massive quantum particles, which can couple with photons and form new particles of an even higher level of abstraction: exciton-polaritons.

When a Bose condensate is formed, one can consider its weak excitations as elementary particles (Bogolons) [see Sec.1.2.4], forgetting the nature of the underlying bosons. But the weak elementary excitations are not the only type of interesting perturbations which can occur in a Bose condensate. The topological defects [35] are currently (and since quite a long time) in the focus of intense theoretical and experimental research and will be the main topic of the present work. We shall see how the behavior of half-quantum topological defects can be described in terms of relativistic "material points" and "point charges" (an easy way) or in terms of underlying local spin dynamics (a harder way). The importance of such analogies as "magnetic charges" or magnetic monopoles [36] will thus become especially clear.

We shall start in this section introducing the 1D half-soliton that is the simplest candidate for the magnetic monopole analogy and analyze their behavior in the presence of an in-plane magnetic field. We shall extend the theory to the case of half-vortices. We will discuss how to realistically excite such objects in a semiconductor microwire and how they will naturally decay into their half-integer constituents, serving as a source for magnetic currents. Finally, we will concentrate on a new type of topological excitation in a 2D system: the oblique half-soliton, that has led to the very first experimental observation of the acceleration of a half-integer topological defect behaving as a magnetic charge.

2.2.1 Half-solitons as magnetic charges

2.2.1.1 Half-solitons

So far, we have introduced the half-vortex solution in a two dimensional system, we have analyzed its one dimensional counterpart that we have called a half-soliton in the Refs.[37, 38, 39, 40] as a continuation of the works of Salomaa and Volovik [5]. Analogously to the half-vortex discussion, the half-soliton corresponds to its integer counterpart in one component while the other component remains homogeneous (at least for α_2=0). Therefore, the polarization of the condensate is circular (elliptic if the soliton is moving) at the half-soliton core and linear at $\pm\infty$. Since the scalar

dark soliton solution [see 1.2.5.1] is simply given by $\psi_S(x) = \sqrt{n_0}\tanh(x)$ and its phase is a Heaviside function of amplitude π, on the circular polarization basis and, in the simplest case where $\alpha_2 = 0$, the dark half-soliton order parameter reads

$$\begin{pmatrix} \psi_+(x) \\ \psi_-(x) \end{pmatrix} = \sqrt{\frac{n_0}{2}} \begin{pmatrix} 1 \\ \tanh(x) \end{pmatrix} \tag{2.28}$$

Where the dark soliton lies here in the σ_- component. Obviously the σ_- phase displays a π phase shift while it remains constant in the σ_+ component. Rewriting Eq.(2.28) on the linear polarization basis yields

$$\begin{pmatrix} \psi_x(x) \\ \psi_y(x) \end{pmatrix} = \frac{\sqrt{n_0}}{2} \begin{pmatrix} 1+\tanh(x) \\ i - i\tanh(x) \end{pmatrix} \tag{2.29}$$

Looking at asymptotic forms, one can easily obtain:

$$\psi_x^{HS}(+\infty) = \sqrt{n_0}e^{2ih\pi}\cos(2s\pi) \tag{2.30}$$
$$\psi_y^{HS}(+\infty) = \sqrt{n_0}e^{2ih\pi}\sin(2s\pi) \tag{2.31}$$
$$\psi_x^{HS}(-\infty) = \sqrt{n_0}e^{ih\pi}\cos(s\pi) \tag{2.32}$$
$$\psi_y^{HS}(-\infty) = \sqrt{n_0}e^{ih\pi}\sin(s\pi) \tag{2.33}$$

where h and s are half-integer numbers which can be seen as topological charges. Elementary dark half-solitons appear for $\{h, s\} = \{\pm 1/2, \pm 1/2)\}$ and their phase and polarization angle are shifted from 0 to $\pi/2$ going through their circularly polarized core. This topological defect can also be seen as a domain wall with respect to x- and y-polarized particles. A plot of the HS density profiles ($n_j = \left|\psi_j^{HS}\right|^2$, $j = \pm, x, y$) is proposed in Fig.2.7(a). The corresponding pseudospin projections are found as

$$\begin{pmatrix} S_x \\ S_y \\ S_z \end{pmatrix} = \frac{n_0}{4} \begin{pmatrix} 2\tanh(x) \\ 0 \\ 1-\tanh(x)^2 \end{pmatrix} \tag{2.34}$$

and its not surprising that the pseudospin points in opposite directions at the opposite sides sides of the soliton, as shown in Fig.2.7 (red arrows), since it is a domain wall between x and y polarizations. It is possible to tune the global orientation of the linear polarization introducing a constant relative phase between the σ_+ and σ_- components appearing as an $\exp(i\phi_0)$ factor in one of the two wavefunctions $\psi_\pm$. Four configurations are shown in the Fig.2.7(b) changing ϕ_0 from 0 to 2π with a $\pi/2$ step. Remarkably, the pseudospin field of the half-soliton is similar to the field created by a point charge being either divergent or convergent for $\phi_0 = 0$ or $\phi_0 = \pi$ respectively.

2.2.1.2 Half-solitons acceleration

We know well now that the pseudospin interacts with effective magnetic fields. Let us first try to understand from "microscopic" considerations what will happen to

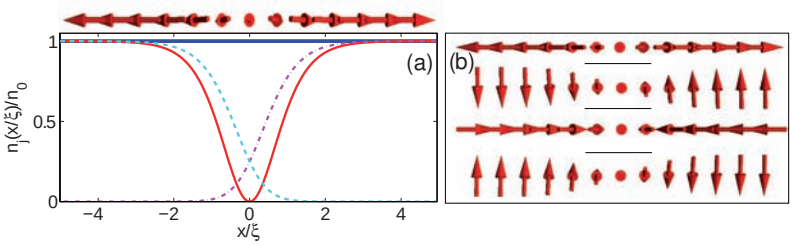

Figure 2.7: (a) Half-soliton density profiles scaled to n_0 and ξ. The solid (blue) and (red) curves represent the σ_+ (σ_-) density profiles, while the dashed-dotted purple and dashed cyan curves show the x and y components respectively. The red arrows show the pseudospin vector field. (b) ϕ_0 dependent half-soliton pseudospin textures. From the top to the bottom: $\phi_0 = 0, \pi/2, \pi, 3\pi/2$.

this object, when an in-plane effective magnetic field $\mathbf{H}_{LT} = H_x \mathbf{u}_x$ is applied along the x-direction. We have already discussed the presence of a splitting at $\mathbf{k} = \mathbf{0}$ in planar microcavities in the context of the optical spin-Hall effect (leading to the anisotropic OSHE) [see Sec.1.4.4]. This splitting is especially well resolved above the condensation threshold thanks to the sharpening of the emission lines, and induces an in-plane effective magnetic field pointing in a well defined direction, determined by the orientation of the crystallographic axes of a planar cavity or the orientation of the microwire [41] [see also Sec.3.3.2.1 for more details]. Its interpretation in terms of a constant effective in-plane magnetic field is even more direct than in the case of the interaction-induced field in the z direction: if the x and y polarizations have different energies when the Gross-Pitaevskii equation is written on the xy basis, this splitting transforms into a term $-H_x\psi_\mp/2$ in the circular polarization basis with the usual coordinate transformation rules $\psi_\pm = (\psi_x \mp i\psi_y)/\sqrt{2}$.

Since the existence of a soliton requires a significant interaction energy and therefore a significant condensate density, the intrinsic Zeeman splitting [see Sec.1.5.2.3] behaving as an effective magnetic field $\mathbf{H}_Z = H_z \mathbf{u}_z$ is expected to play an important role in circularly polarized regions such as a half-soliton (or a half-vortex) core. Indeed, due to the spin anisotropy of polariton interactions [see Sec.1.5.1] the effective field is amplified and tends to lock circularly polarized states (strong density imbalance) in the system. It provides the natural stability of half-integer topological defects against an effective magnetic field preventing the precession of the polarization at their core up to the critical value [3]

$$H_c = \frac{(\alpha_1 - \alpha_2)\, n}{4}, \tag{2.35}$$

that would lead to their destruction.

Assuming here $\phi_0 = 0$, let us consider the pseudospin dynamics at each point, since the other terms in the Gross-Pitaevskii equation (the kinetic energy and the interaction energy) compensate each other at $t = 0$. For the linearly polarized regions far from the soliton's core $|x| \gg \xi$, the pseudospin is aligned or anti-aligned with

the magnetic field (which contains only a x component) and there is no evolution: $\partial \mathbf{S}/\partial t = \mathbf{0}$. For the core region, there is a non-zero pseudospin projection on the z axis, and therefore the pseudospin will rotate (precess) around the magnetic field (which now contains both x and z components). Let us consider the initial moments of this rotation for the pseudospin in the center of the soliton: $\mathbf{S}(x = 0, t = 0) = \mathbf{u}_z$, while the total magnetic field is

$$\mathbf{H}\left(x = 0, t = 0\right) = H_x \mathbf{u}_x - \frac{\alpha_1 - \alpha_2}{2}\left(-\frac{n}{2}\right)\mathbf{u}_z, \tag{2.36}$$

Rotating around the (positive) H_x component, the pseudospin (initially negative along z) gains a positive S_y projection and starts to precess around the positive H_z field, turning towards the negative direction of the x-axis. This is the main result of our qualitative vectorial consideration of the polarization dynamics: the pseudospin in the center of the soliton gains a *negative* x-projection. Therefore, the domain of negative x pseudospin projection becomes larger, the domain of positive x-projection smaller, and the wall between these domains is moving to the right. However, once the soliton core starts to propagate, the kinetic and interaction energy terms are no more compensated everywhere, and one cannot discuss the evolution of the system using the qualitative arguments based on polarization dynamics. At first sight, one may even think that the nonlinear system in question can be solved only numerically.

However, an important insight into the behavior of the system can be gained by "changing the zoom". Forgetting about the internal structure, a vectorial grey soliton in a Bose-Einstein condensate can be considered as a particle [42] with a negative effective mass (at least at low velocities). Moreover, the pseudospin pattern of this particle is the same as the field of a point magnetic charge in 1D. The magnetic energy of the system can be found from the Hamiltonian as the usual scalar product of the field and the spin, and this magnetic energy depends on the position of the soliton because of the finite system size. Thus, one can evaluate the force acting on the magnetic charge from the magnetic field as a gradient of the magnetic energy with respect to the position of the soliton. This force will consequently accelerate the soliton.

Considering the soliton as an elementary particle without internal structure means passing to the limit $L \gg \xi$, where L is the system size (for example, the length of a wire-shaped cavity, which is usually of the order of 100μm). The healing length of a polariton condensate for a reasonable blue shift of 1 meV expected for GaAs or CdTe cavities and a polariton mass of 5×10^{-5} of a free electron mass is $\xi \sim 1\mu$m. In this limit, the wavefunction of the soliton at $t = 0$ becomes simply $\psi_+ = \sqrt{n/2}\mathrm{sign}(x - x_0)$, $\psi_- = \sqrt{n/2}$, where x_0 is the position of the soliton. In general, the *tanh* function is replaced by the *sign* function. The magnetic energy of a condensate containing a half-soliton in an external in-plane magnetic field is

$$E_{mag} = -\int \mathbf{H} \cdot \mathbf{S} dx \tag{2.37}$$

Here $\mathbf{S}(x-x_0) = n\text{sign}(x-x_0)\mathbf{u}_x$ (x_0 is the soliton position) in the limit we consider, giving

$$E_{mag}(x_0) = H_x n(x_0) \tag{2.38}$$

$$F_{mag} = -\frac{dE_{mag}}{dx_0} = -nH_x \tag{2.39}$$

The force in Eq.(2.39) is therefore acting opposite to the direction of the magnetic field, but the acceleration will occur in the direction opposite to the force, because the effective mass of the soliton is negative, at least at low velocities.

For a grey soliton propagating at the speed v, the phase shift induced by the soliton in the σ_+ component is $\Delta\theta = 2\arccos(v/c) < \pi$ and the pseudospin projection S_x is reduced, which can be expressed as a renormalization of the magnetic charge. The correction to the charge is found as

$$q = q_0\left(1 - \frac{v^2}{c^2}\right) \tag{2.40}$$

where $q_0 = \alpha n/2$ is the charge at rest for a dark half-soliton. The total correction for the mass of the soliton and its charge gives the equation of motion

$$a = q_0\frac{nH_x}{m_0}\left(1 - \frac{v^2}{c^2}\right)^{3/2} \tag{2.41}$$

the same as in relativistic physics, integrating which one obtains

$$v(t) = c\tanh\left(\frac{q_0 H_x n}{c}t\right), \tag{2.42}$$

assuming zero initial velocity. This trajectory is perfectly confirmed by numerical simulations as shown in Fig.2.8 [see captions]. In the panel (b), the soliton is introduced as an initial condition and no lifetime is accounted for. In the configuration of the panel (c) we have included the polariton lifetime and the pumping term, the half-solitons are created with a pulsed potential acting on only one condensate's components (σ_+ here). We see that, using the abstraction of a point magnetic charge appears particularly useful, since it allows solving the nonlinear spinor Gross-Pitaevskii equation analytically and gives a good qualitative understanding of observed phenomena.

The relative phase ϕ_0 between the two components impacts strongly the soliton acceleration, indeed, as we have noticed previously, the continuous variation of ϕ_0 leads to a continuous rotation of the linear polarization around the soliton's core [see Fig.2.7]. Since the force acting on the half-soliton is dependent on the scalar product $\mathbf{H}_{LT}\cdot\mathbf{S}$, the relative orientation of S and $\mathbf{H}_{LT}$ becomes determinant. In the cases where $\phi_0 = (2p+1)\pi/2$ ($p\in\mathbb{Z}$), away from the soliton's core $\mathbf{S}$ lies along the y direction, thus $\mathbf{H}_{LT}\cdot\mathbf{S} = 0$ and no soliton motion can minimize the magnetic energy of the system which is zero initially. The charge of such a soliton is zero. On the contrary, for $\phi_0 = 2p\pi$ ($\phi_0 = (2p+1)\pi$), the soliton is bound to move along

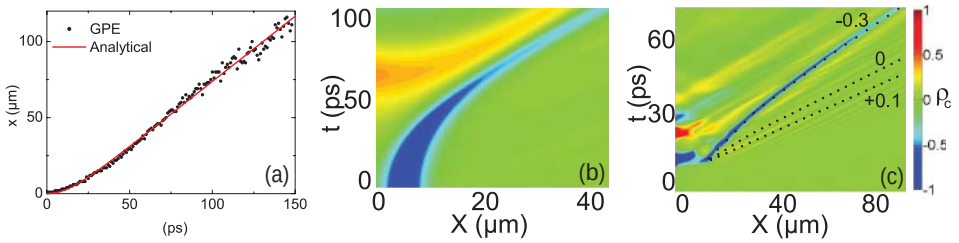

Figure 2.8: Half-soliton acceleration. (a) Trajectory of a half soliton accelerated in a constant in-plane effective magnetic field calculated analytically (red solid line) and numerically (black dots). (b,c) Circular polarization degree ρ_c as a function of coordinate and time calculated using the spinor Gross-Pitaevskii equation, including the constant in-plane effective magnetic field. The half-soliton trajectory is visible as the deep blue minimum (the core is filled with σ_- particles). (b) Half-soliton as an initial condition, no lifetime. (c) Pumping and lifetime the half-soliton is created here by a pulsed potential. The black/dotted lines are guides for the eyes showing trajectories for the splitting values indicated on the figure (in meV).

(against) the field and is attributed a positive (negative) charge. Consequently, in addition to its velocity-dependent charge renormalization, the soliton charge is ϕ_0 dependent:

$$q = q_0\left(1-\frac{v^2}{c^2}\right) \tag{2.43}$$

$$q_0 = \frac{\alpha n}{2}\cos(\phi_0) \tag{2.44}$$

The figure 2.9 showing numerical simulations using the spinor Gross-Pitaevskii equations (2.13) (the TE-TM splitting has to be replaced by a k-independent field along the x-axis) illustrates the ϕ_0 dependent motion of the half-soliton. The visible displacements (oscillations at larger time scales) in the cases $\phi_0 = \pi/2, 3\pi/2$ [Fig.2.9(b,d)] originate from the precession of the pseudospin away from the soliton's core visible in the colormap.

We conclude this section with the following remark. First, the ϕ_0-dependent renormalization of the charge is given in Eqs.(2.43,2.44) for a well defined orientation of the effective field $\mathbf{H}_{LT}$ namely along the x-direction as in a real microwire. Allowing for an arbitrary orientation of $\mathbf{H}_{LT}$ associated with an angle ϕ_{LT} the renormalization would read $q_0 = \alpha n/2\cos(\phi_0 - \phi_{LT})$. Second, this charge renormalization seems at first sight to go against a complete magnetic monopole analogy as the charge is not conserved with ϕ_0. However, changing the referential in order to compensate for ϕ_0 namely working in the basis where the field is divergent allows to recover a fixed charge and in that case it is the effective field itself that would be renormalized. The situation would be similar to that of an electron in a one dimensional crystal accelerated by a non longitudinal electric field when $\phi_0 \neq 0$.

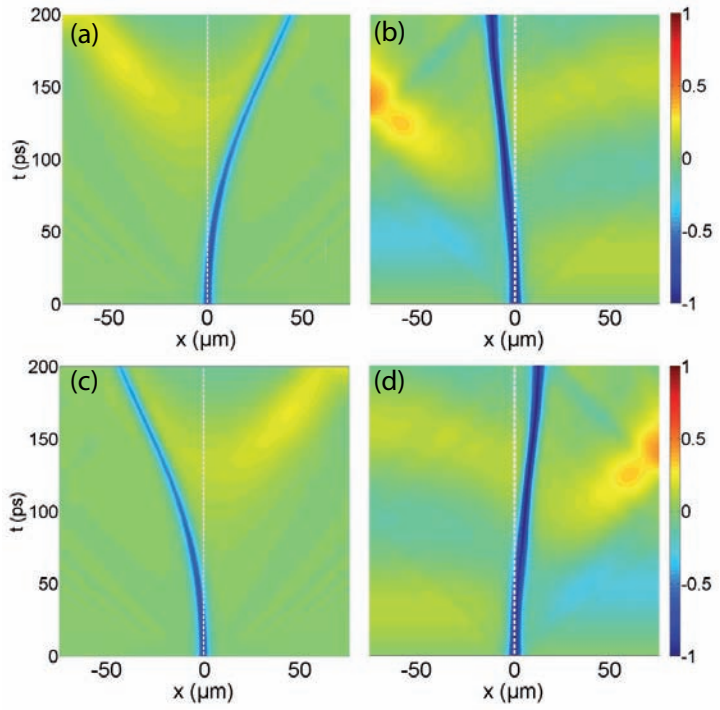

Figure 2.9: ϕ_0-dependent half-soliton acceleration. We start here from an initial condition neglecting the polariton lifetime. From (a) to (d), $\phi_0 = 0, \pi/2, \pi, 3\pi/2$.

2.2.1.3 Soliton and half-soliton interactions

Short Range Interaction

Dark (gray) solitons are the solution of the 1D Gross-Pitaevskii equation provided that the condensate is formed of particles that repel each other ($\alpha_1 > 0$). Interactions between solitons themselves have been thoroughly analyzed an it is now well known that dark solitons tend to repel each other as well [43] up to a limiting speed where they can cross each other, their kinetic energy being dominant. Such a behavior is illustrated in the Fig.2.10 showing the degree of circular polarization and where we have solved the *scalar* Gross-Pitaevskii equation with the initial condition given by two dark solitons spatially shifted by 0.5 μm [see Eq.(2.55) below]. The solitons repel at the initial moment and then demonstrate a linear trajectory, which is a clear signature of their *short range* interaction.

Now, what about the half-soliton in the two-component condensate? Let us remind that a half-soliton corresponds to a soliton occurring in only one of the two components. Additionally, if the intercomponent interaction is not neglected, the presence of a half-soliton in one component obviously perturbs the other one in a fashion depending on the type of interactions, given by the sign of α_2. Indeed, for $\alpha_2 > 0$ ($\alpha_2 < 0$), the presence of a density minimum in the component carrying the soliton is seen as a potential well (barrier) of amplitude $\alpha_2 n_\infty/2$, where n_∞ is the

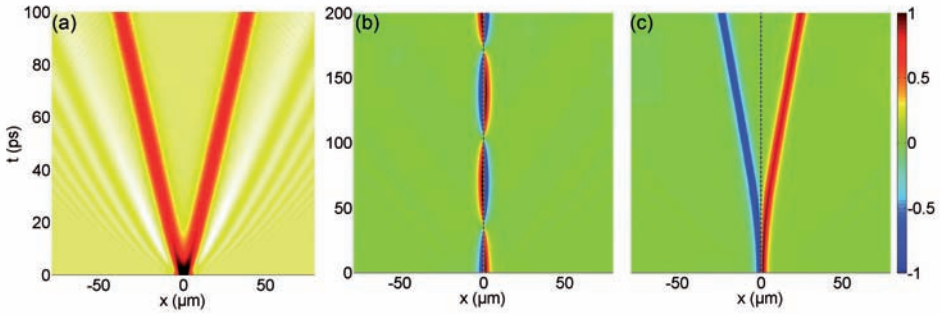

Figure 2.10: Short range interaction between solitons initially separated by 0.5 μm. (a) Integer soliton repulsion the colormap shows the density $n = |\psi|^2$ of the single component of a scalar condensate. (b) Half-solitons attraction, which shows dipolar oscillations for $\alpha_2 = +0.2\alpha_1$ (c) half-solitons repulsion for $\alpha_2 = -0.2\alpha_1$, the colormap in (b) and (c) shows the degree of circular polarization of the spinor condensate: $\rho_c = (n_+ - n_-)/(n_+ + n_-)$.

total density far away from the soliton, by the other component and consequently a density maximum (minimum) appears at the position of the soliton [see Sec.2.3.1]. Putting two half-solitons lying in different components next to each other induces a short range interaction within each component, between a soliton and the density maximum (minimum) induced indirectly by the other soliton. The half-solitons having a negative effective mass are repelled (attracted) by the potential wells (barriers) they encounter, which, from their point of view, are barriers (or wells). This argumentation leads to the following statement: For $\alpha_2 > 0$ ($\alpha_2 < 0$), half-soliton attract (repel) each other while they obviously don't interact for $\alpha_2 = 0$. This trend is shown in Fig.2.10(b) and (c). We note, that in the repulsive case, dipolar oscillations occur between the solitons, this is due to the effect of their mutual attraction and the slight initial displacement (the system can be described by a simple pendulum in this case). In the framework of polariton condensates where $\alpha_2 < 0$, the repulsion of half-solitons is therefore a strong asset for the separation of an integer soliton into a pair of half-solitons of opposite charges.

Long Range Interaction

The solution of Maxwell's equations for a point electric charge in 1D is a constant electric field pointing in opposite directions on each side of the charge. Such field would produce a force of constant magnitude on a second charge independent of its position, according to the Coulomb's law. Another way of tracking this interaction is by looking at the fields generated by the ensemble of the two charges. In 1D, in the case of two identical charges with opposite signs separated by a distance d, the sum of the fields they generate in the region outside of the charges cancels out exactly and is equal to zero. Between the two charges the fields add and it becomes twice as large as the field created by each individual charge. When the two electric charges have the same sign, the situation is opposite (zero field in between and

double field outside). This is the manifestation of the Coulomb behavior of point electric charges in 1D.

One would expect magnetic monopoles to interact in a similar way. In our monopole analogues, the role of the field created by each magnetic charge is played by the pseudospin vector field **S** emanating from the half-soliton. For instance, the wave functions describing two individual half-solitons of opposite charges are:

$$\boldsymbol{\psi}_1 = \begin{pmatrix} +\sqrt{n/2}\tanh\left[(x-x_1)/\xi\sqrt{2}\right] \\ \sqrt{n/2} \end{pmatrix} \tag{2.45}$$

$$\boldsymbol{\psi}_2 = \begin{pmatrix} -\sqrt{n/2}\tanh\left[(x-x_2)/\xi\sqrt{2}\right] \\ \sqrt{n/2} \end{pmatrix} \tag{2.46}$$

In that case, the solitons occur in the σ_+ component, located at the positions x_1 and x_2 for ψ_1 and ψ_2 wavefunctions respectively, as sketched in the two upper images of Fig.2.11, showing their densities (solid red lines). The σ_- density remains constant, and equal to the asymptotic value of the σ_+ density (linear polarization). The direction of the pseudospin **S** vector field can be directly calculated from $\psi_{1,2}$ [see Eqs.(1.141-1.143)] and is illustrated by the red arrows in Fig.2.11 lying along the (x,z) plane since $S_y = 0$. We remind that the charge of the half-solitons is given by the orientation of its divergent surrounding pseudospin [see Eq.2.44]. Looking at the first two rows in Fig.2.11(a) we see that the solitons have opposite charges, indeed while in the first row the pseudospin is divergent (ψ_1), it is convergent (ψ_2) in the the second one.

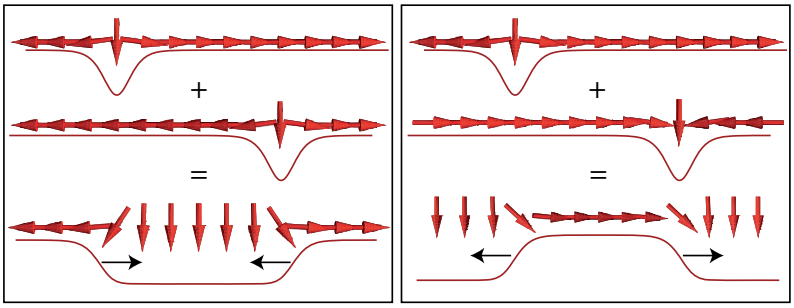

Figure 2.11: Coulomb-like interaction between two half-solitons. The red arrows show the pseudospin vector field in the (x, z) plane. The solid/red lines stand for the density profiles of the spin component that contains the solitons (σ_+ in our case), the σ_- component remains homogeneous. The black arrows give the propagation direction of each half soliton due to their interaction. The left panel illustrates the interaction between two solitons of identical charges that attract each others. The right panel shows the repulsive interaction between two solitons of opposite charge.

In order to study the magnetic interaction between the solitons, we make half the sum of the wavefunctions ψ_1 and ψ_2 to obtain:

$$\psi_{1+2} = \begin{pmatrix} \sqrt{n/2}\left(\tanh\left[(x-x_1)/\xi\sqrt{2}\right] - \tanh\left[\left((x-x_2)/\xi\sqrt{2}\right)\right]\right)/2 \\ \sqrt{n/2} \end{pmatrix} \tag{2.47}$$

If we concentrate on the σ_+ component, this total wavefunction gives a finite density between the two half-solitons and zero density far away from them, as depicted by the red solid line in the third row of the panel (b). Since in the condensate the intracomponent interactions are repulsive ($\alpha_1 > 0$), within the σ_+ component the particles will diffuse from larger density regions to the lower ones. Clearly enough, this effect is not at all dependent on the distance between the solitons and provides the solitons long range repulsion, marked with the black arrows in the panel (b). The associated pseudospin projection on the axis of the soliton (x-axis) coincides exactly with the field expected for two electric point charges under the Coulomb's interaction. Indeed, S_x is zero away from the solitons and twice the value of the field S_x^0 produced by a single charge in-between them. The behavior is the exact opposite in the case of two half-solitons having the same charge as illustrated in the panel (a).

We note that the attractive/repulsive behavior of our magnetic charges is opposite to that of electric charges because of the negative effective mass of solitons. Two half-solitons having opposite charge [panel (b)] repel each others, while they attract if they have the same charge [panel (a)].

Though the wavefunction profiles we have just described already coincide with those of the field of attracting/repulsing charges, we can also understand the origin of this Coulomb-like force looking at the energy of the system arising from the interparticle interactions. Since polariton-polariton interactions are strongly spin-anisotropic, the condensate is bound to evolve towards a linearly polarized state to minimize its free energy [see Sec.1.5.2]. In view of this, we can understand that the minimization of the energy in the case shown in Fig.2.11(a) pushes the half-solitons away from each others. This way the system evolves towards linearly polarized state and reduces its energy. The same considerations apply to the case of Fig.2.11(b) where this time the minimization imposes the soliton attraction.

We can quantify the magnitude of the Coulomb-like force acting on each half-soliton by calculating the gradient of the total energy of the system: $F_i = -\partial E/\partial x_i$, where x_i is the position of the i^{th} soliton. Assuming that the distance between the solitons is much larger than the healing length $|x_1 - x_2| \gg \xi$, we obtain (in the case where $\alpha_2 = 0$) a force:

$$|\mathbf{F}| = \frac{\alpha_1 n^2}{8} \tag{2.48}$$

which does not depend on x_i. In order to write this force as the product of a charge and a field $\mathbf{F} = q\mathbf{S}$, we use the equivalent of Maxwell's equation $\mathrm{div}(\mathbf{S}) = \rho/\alpha_1$ where ρ is the charge density and α_1 plays the role of the dielectric permittivity ε_0. Thus, in our case the field of a single charge is given by $|\mathbf{S}| = n/4$, and the divergence theorem gives the charge of the topological defect: $q = \alpha_1 n/2$.

It is impossible to observe the long-range interaction of half-solitons in the typical configuration where the condensate is linearly polarized everywhere, because in this case the pseudospin field does not correspond to the field of just 2 electric charges in 1D. In fact, a homogeneous linearly-polarized condensate corresponds to a field of a single point charge located at infinity, or to two half-charges at plus and minus

infinities. This field compensates that of the two half-solitons and screens their long-range interaction.

2.2.2 Half-vortices as magnetic charges

In the 2D case, the object possessing the spin texture close to that of a magnetic monopole is the elementary half-vortex (HV) carrying winding number ± 1 in the component where it appears. Indeed, provided that the relative phase between the $\sigma_\pm$ components is zero, the pseudospin texture is either divergent or convergent. However, there is an important difference between the field of an electric charge, which in 2D decreases as $1/r$, and the "field" of the half-vortex, which is approximatively constant at large distances. In spite of that, it is still possible to find the force acting on the HV from the magnetic field as the gradient of the energy of the system as the function of the displacement of the monopole.

A crucial peculiarity arises from the relative phase ϕ_0 of the two wavefunction components:

$$\psi_+ = \sqrt{n_+} e^{i(l_+\phi+\phi_0)} \tag{2.49}$$

$$\psi_- = \sqrt{n_-} e^{il_-\phi} \tag{2.50}$$

which gives another continuous degree of freedom for the pseudospin orientation. Several pseudospin textures are shown in Fig.2.12(a) together with the resulting sketched trajectories of the HV in the constant in-plane magnetic field H_x (black arrow). These trajectories have been calculated by solving the 2D spinor Gross-Pitaevskii equations with infinite lifetime. We have considered a cylindrical trap of radius 50 μm with impenetrable boundaries and we have found the associated half-vortex "ground state" at fixed chemical potential $\mu = \alpha_1 n \simeq 1$ meV with a given set (l_+, l_-, ϕ_0). Then, for each of the eight half-vortex configurations shown in the Fig.2.12(a), we have applied the constant magnetic field. The resulting calculated trajectories are shown in black on the Fig.2.12(b).

We see that the propagation direction is determined both by the topological charges (l_+,l_-) of the HV and by the continuous variable ϕ_0. We note that the (l_+, l_-, ϕ_0) and the $(-l_+, -l_-, \phi_0)$ HVs are symmetric with respect to the magnetic field and follow the same trajectory. The proper description for the force acting on the HV from the magnetic field is given by a charge tensor: $F_i = q_{ij} H_j$ with

$$q_{ij} = q_0 \begin{bmatrix} -\cos(\phi_0) & -\sin(\phi_0) \\ +\sin(\phi_0) & -\cos(\phi_0) \end{bmatrix} \tag{2.51}$$

In order to understand better the forces acting on the half-vortex, let us consider the (+1,0,0) one. Two effects, induced by magnetic field, are observed in the simulations. First, because of the pseudospin rotation around the magnetic field far from the vortex core, a density gradient appears at short times along the field's axis (x in our case) as shown in the [Fig.2.13(a)]. The density determines the kinetic energy, whose gradient creates an additional force acting on the half-vortex. This

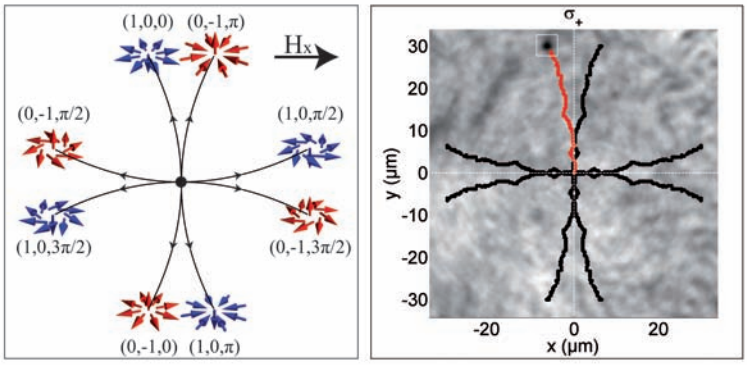

Figure 2.12: Left panel: Pseudospin textures of eight half-vortices as a function of the topological charge and the relative phase ϕ_0 (labeled as (l_+, l_-, ϕ_0)) and the resulting propagation directions in a constant magnetic field pointing along the x direction. Right panel: The σ^+ density at the end of the simulation with the Gross-Pitaevskii equation showing the trajectory (red line) of a particular HV (white square) together with the other trajectories (black lines) corresponding to the cases described on the left panel.

force is strong and well defined only in the initial moments after the application of the field, because later on the different eigenfunctions of the vessel oscillate with different frequencies and the resulting "storm in a teacup" gives zero net force for the vortex, which therefore propagates with a constant speed acquired in the initial moments. Second, the constant effect of the magnetic field on the pseudospin texture creates a constant force accelerating the vortex in the direction given by Eq.(2.41). The trajectory is parabolic, with the acceleration proportional to the strength of the magnetic field, as shown in Fig.2.13(b). It is precisely this effect, and not the previous one, which corresponds to the expected behavior of a magnetic monopole. The vortices having monopole-like pseudospin textures (divergent or convergent) are accelerated in a direction parallel to the field. However, the behavior is opposite to that of the half-solitons namely the divergent (convergent) vortex accelerates along (against) the effective magnetic field, since contrary to half-solitons, they possess a positive effective mass. The half-vortex is remarkably stable against density fluctuations, and we are able to track its trajectory for 80 ps. Relativistic effects are not observed in this case, because the speed v_x remains relatively small.

We note that the effect of a static polarization splitting on a half-vortex has been analyzed in Ref.[45] and a polarization string has been predicted to be attached to the half-vortex in the lowest energy state. This is indeed what we observe in the early times of the simulation when the magnetic field is turned on but the string tends to unbind from the half-vortex because our initial condition is calculated in the absence of the field and this initial condition is not the eigenfunction of the complete Hamiltonian, otherwise it would not evolve with time.

The half-vortex can become unstable against the magnetic field, with the stabil-

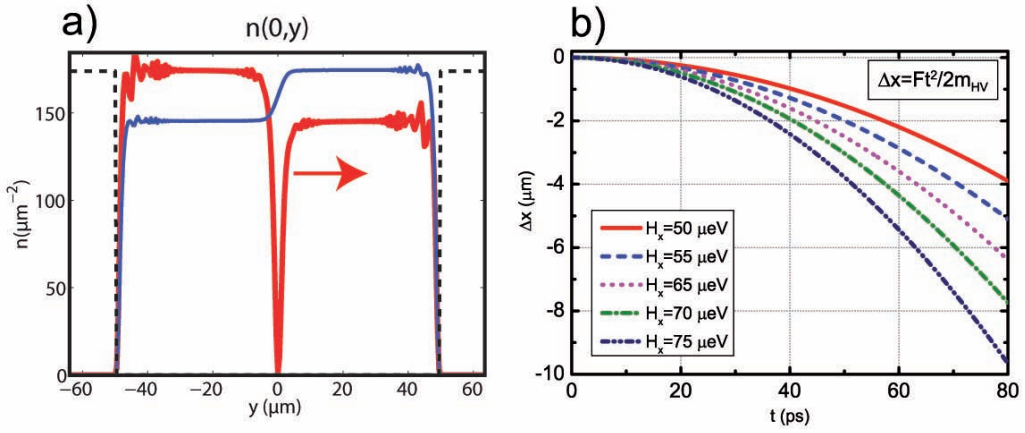

Figure 2.13: (a) The density distributions of the two components: σ^+ (red) and σ^- (blue), creating the gradient of the interaction energy accelerating the HV in the y direction. (b) The x coordinate of the HV as a function of time for several values of the magnetic field, demonstrating constant acceleration of the half-vortex, increasing with the field.

ity criterion given in our case by the same estimate as in 1D [see Eq.(2.35)]. If the magnetic field is stronger, the vortex disappears. Without spin-anisotropy of the interactions in the homogeneous magnetic field we consider, the pseudospin along the y axis would make a turn around the magnetic field H_x and become completely S_z on one side and $-S_z$ on the other side, leading to the destruction of the half-vortex: instead of having a single point with zero density of σ^+, we would have a semi-infinite string. This is the signature of the fact that in the case of a spinor condensate, the velocity circulation is not conserved topologically, because one cannot define in the general case a unique superfluid velocity [46]. Therefore, the HVs can be destroyed (unwound) by applying a certain magnetic field, as it has been demonstrated experimentally [47]. In the case of polaritons, the particular spin-dependence of interactions prevents this from happening for sufficiently low magnetic fields.

Finally, we note that the relative phase between the condensate components could be tuned applying a weak external magnetic field in the z direction, leading to a Zeeman splitting for the σ^+ and σ^- components. The relative phase would increase linearly with time and therefore the direction of the in-plane magnetic force would change as well.

2.2.3 Towards polariton magnetricity

2.2.3.1 Soliton imprinting

Vortices have already been created in polaritons condensates by several means, among which is found the artificial phase imprinting induced by a probe carrying an angular momentum: a "Gauss-Laguerre" (GL) beam [20, 21]. Such a beam is

obtained from a usual Gaussian beam scattered on a hologram containing a forklike dislocation. Mathematically, this type of pumping can be described by the following complex function

$$\begin{aligned} P_{GL}(\mathbf{r},t,l) &= A_{GL}\sqrt{(x-\Delta x)^2+(y-\Delta y)^2} \\ &\times e^{-\left(\frac{x-\Delta x}{\sigma_x}\right)^2} e^{-\left(\frac{y-\Delta y}{\sigma_y}\right)^2} e^{-\left(\frac{t-\Delta t}{\sigma_t}\right)^2} e^{il\phi} e^{-i\omega_{GL}t}, \end{aligned} \tag{2.52}$$

The exponentials give the "Gauss" part of the function, while the square root is the 1^{st} order Laguerre polynomial, giving zero density in the center of the beam. l is the integer winding number that is to be transferred to the vortex state. The laser frequency ω_{GL} should be slightly blue-detuned from the bare polariton mode, in order to make use of the bistability effect and obtain an almost flat density profile of the condensate except in the center, due to the saturation of the pumping efficiency on the upper bistability branch [48].

As one can see from the sixth factor of Eq.(2.52), where ϕ is here the polar angle, the phase is changing continuously from 0 to $2l\pi$ encircling the beam center. In a pure 1D system, the notion of angular momentum vanishes and grey solitons embody elementary topological excitations in BECs in place of vortices. The action of a Gauss-Laguerre beam is therefore to induce a local phase step of $-l\pi$ or smaller, equal to the one resulting from a cut of a vortex by a plane. It is illustrated in Fig.2.14(a) showing a density slice of the Gauss-Laguerre beam together with its phase. This technique constitutes an efficient mean for soliton engineering in 1D condensates. We note that, in order to allow the soliton to evolve freely, it is necessary to use a pulsed Gauss-Laguerre beam, which will also form the background condensate for sufficient pump intensity.

Besides, experimental creation of half-solitons with independent selection of their phase (given by l) would require to separate a linearly polarized input laser in its two circularly polarized components ($\sigma_\pm$) using polarizers, to make one component (for a single half-soliton) or both of them (for a pair of half solitons) scatter on a hologram, and to recombine them on the sample. For the case where both components carry an angular momentum it looks difficult to recover a perfect spatial overlap of the two beams, which will naturally trigger the separation of the half-solitons, especially for the normal case of $\alpha_2 < 0$. Additionally a relative phase ϕ_0 can be introduced between the two beams increasing the optical path of one component with respect to the other. ϕ_0 has a crucial impact on the pseudospin textures of the half-solitons and therefore on their interaction with effective fields. A scheme of a potential experimental setup is shown in the Fig.2.14(b).

If we consider now a more realistic system such as a microwire [see Fig.2.14], we should take into account the transverse width of the sample and treat the case of a quasi-1D condensate for which the angular momentum cannot be neglected anymore. The central position of the pump spot crucially impacts the symmetry of the imprinted flow. We have performed numerical simulations of a 2 μm wide and 100 μm long wire using polariton parameters to highlight this feature. On one hand, if the spot is transversally centered, a static and therefore dark soliton is nucleated

in the wire, almost as in the pure 1D case [see Fig.2.14(c),(d)]. On the other hand, a shift of the Gauss-Laguerre beam along the y-axis induces a uniform propagation of the resulting grey soliton in a direction depending on the transverse shift and on the sign of the imprinted winding number l as it is illustrated in the figure 2.14(c)-(f). A positive (negative) y-shift induces a soliton propagation to the right (left) for $l < 0$ and reciprocally for $l > 0$. This effect can be qualitatively seen as a "rolling" of the particles on the boundaries, introduced by a gradient of angular velocity in the transverse direction. Moreover, the closer is the spot center to a boundary, the faster the soliton moves along the wire. This "extrinsic" motion has to be taken into account for an experiment, in which imposing a perfectly centered spot is elusive. Even in the simulation [see Fig.2.14(d)], where the precision on the centering is about 0.1 μm, we observe a very small drift of the solitons.

For the simulations, we use the typical parameters of modern GaAs cavities, including their outstanding lifetimes of about 30 ps in modern samples [44]. We have solved the spinor Gross-Pitaevskii equations for the photonic $\phi(\mathbf{r},t)$ and excitonic fields $\chi(\mathbf{r},t)$ (coupled via the Rabi splitting $V_R = 15$ meV), fully taking into account the polarization $\sigma_\pm = \pm$, the finite lifetimes $\tau_\phi = 25$ ps and $\tau_\chi = 300$ ps and the injection of the particles via $P^\pm_{GL}(\mathbf{r},t,l_\pm,\phi_0)$:

$$i\hbar\frac{\partial\phi_\pm}{\partial t} = -\frac{\hbar^2}{2m_\phi}\Delta\phi_\pm + \frac{V_R}{2}\chi_\pm - \frac{i\hbar}{2\tau_\phi}\phi_\pm + P^\pm_{GL} + U\phi_\pm - \frac{\hbar\Omega_x}{2}\phi_\mp \quad (2.53)$$

$$i\hbar\frac{\partial\chi_\pm}{\partial t} = -\frac{\hbar^2}{2m_\chi}\Delta\chi_\pm + \frac{V_R}{2}\phi_\pm - \frac{i\hbar}{2\tau_\chi}\chi_\pm + \left(\alpha_1|\chi_\pm|^2 + \alpha_2|\chi_\mp|^2\right)\chi_\pm \quad (2.54)$$

Here $m_\phi = 3.6\times10^{-5}m_0$, $m_\chi = 0.4m_0$ and m_0 are the cavity photon, the quantum well exciton and the free electron masses respectively. $U(\mathbf{r})$ is a potential (e.g. the confinement potential for quasi-1D wires, or a wedge potential) and $\hbar\Omega_x = H_x$

2.2.3.2 Natural separation and acceleration of half-solitons in microwires

Armed with efficient means of creating half solitons, let us now argue on their potential propagation and acceleration. We shall consider the following situation: A pair of half-solitons is created by the separated Gauss-Laguerre beams. They are slightly spatially shifted either initially or naturally due to an intrinsic noise that breaks the symmetry between the two components. Several contributions will lead to the separation, evolution and acceleration of half-solitons. First, their dissociation is triggered by a negative value of α_2 as discussed previously and can be emphasized by the rolling effect imposed by the GL pump. Second, after the unbinding, half-solitons start to feel the longitudinal effective field. Let us now discuss the impact on their evolution.

The normalized condensate wavefunction carrying a dark soliton in both components reads

$$\psi = \begin{pmatrix}\psi_+\\ \psi_-\end{pmatrix} = \sqrt{\frac{n}{2}}\begin{pmatrix}\tanh\left[l_+\left(x-d/2\right)\right]e^{i\phi_0}\\ \tanh\left[l_-\left(x+d/2\right)\right]\end{pmatrix} \quad (2.55)$$

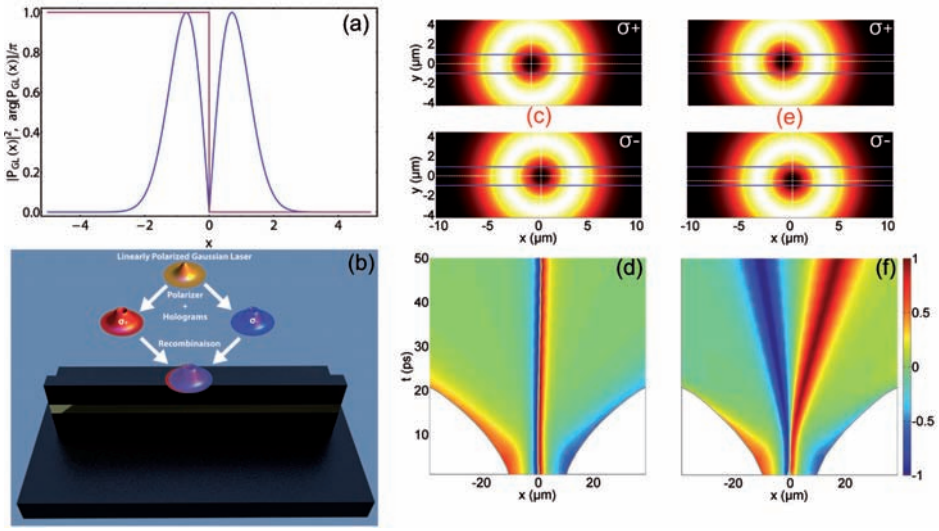

Figure 2.14: (a) Normalized slice of a Gauss-Laguerre beam together with its phase (for the case $l = +1$) as seen by a pure 1D system. (b) Scheme of the separation of a Gaussian beam into two Gauss-Laguerre beams subsequently shined on a wire shaped microcavity. (c)-(f) Impact of the traverse displacement of the spots, here $\alpha_2 = 0$ and $(l_+, l_-) = (-1, -1)$. (c)-(d) No transverse displacement leads to static dark half-solitons in each component. (e)-(f) A small y shift leads to a uniform propagation of the HS. We see that the direction and speed of propagation depends on the direction of the shift sign and on the proximity of the spot center from a boundary respectively. In (e) the σ_+ (σ_-) beam is shifted by $\Delta y_+ = +0.25$ μm ($\Delta y_- = -0.50$ μm). The blue lines in (c) and (e) stand for the wire's boundaries while the white dashed lines show the position of the spot center. In (d) and (f) the white regions are absent of particles due to the finite size of the spot.

assuming a variable spatial separation d and $\alpha_2 = 0$. ϕ_0 is a constant relative phase between the two components, and (l_+, l_-) can take independently the values ± 1 determining the sign of the π phase shift through each soliton. The pseudospin components are straightforwardly calculated using the Eqs.(1.141-1.143) giving

$$S_x = \frac{n}{2}\cos(\phi_0)\tanh\left[l_+\left(x-\frac{d}{2}\right)\right]\tanh\left[l_-\left(x+\frac{d}{2}\right)\right] \tag{2.56}$$

$$S_y = \frac{n}{2}\sin(\phi_0)\tanh\left[l_+\left(x-\frac{d}{2}\right)\right]\tanh\left[l_-\left(x+\frac{d}{2}\right)\right] \tag{2.57}$$

$$S_z = \frac{n}{4}\tanh\left[l_+\left(x-\frac{d}{2}\right)\right]^2 - \frac{n}{4}\tanh\left[l_-\left(x+\frac{d}{2}\right)\right]^2 \tag{2.58}$$

In the case where $d = 0$, it is seen that the orientation of $\mathbf{S}$ is homogeneous and fixed by the total relative phase $\Delta\theta = \phi_0 \text{sign}(l_+/l_-)$. On the other hand for $d \neq 0$, while the homogeneous pseudospin texture remains constant far from the solitons cores, it is of course modified between them. Comparing e.g. $\mathbf{S}_\parallel(\pm\infty)$ and $\mathbf{S}_\parallel(0)$, it is

easily seen that the direction of the in-plane pseudospin is always opposite between the solitons and away from them. This is a crucial point since depending on the orientation of the effective magnetic field $\mathbf{\Omega}_{LT}$, the half-soliton separation will occur in opposite directions. For example with the set $(l_+, l_-, \phi_0) = (+1, +1, 0)$, $\Delta\theta = 0$ and therefore $\mathbf{S}_\parallel(\pm\infty) = +S_x\mathbf{u}_x$ while $\mathbf{S}_\parallel(-d/2 \to d/2) = -S_x\mathbf{u}_x$. A field $\mathbf{\Omega}_{LT} = \Omega_x\mathbf{u}_x$ is parallel to $\mathbf{S}_\parallel$ far from the solitons bringing negative contribution in to E_{mag} [see Eq.(2.37)], the latter is therefore maximized increasing the spacing between the solitons, where $\mathbf{\Omega}_{LT}$ and $\mathbf{S}_\parallel$ are antiparallel, the solitons are consequently accelerated in opposite directions (because their mass is negative). In this configuration, the integer soliton is unstable against the field, the slightest symmetry breaking (e.g. some noise) between the σ_+ and σ_- components result in its decay into half-solitons. The situation is opposed for $(l_+, l_-, \phi_0) = (+1, +1, \pi)$. We finally note that $\Delta\theta = (p+1/2)\pi$ ($p \in \mathbb{Z}$) implies $\mathbf{S}_\parallel(x)\cdot\mathbf{\Omega}_{LT}=0$ giving $E_{mag}(d) = E_0$: An integer soliton or a pair of half-solitons carry the same magnetic energy whatever d. However, as soon as one of the half-solitons starts to move, the $\mathbf{S}_\parallel(x)\cdot\mathbf{\Omega}_{LT}=0$ is no longer verified, and the half-solitons become accelerated by the field. We show in the Fig.2.15 several types of soliton pair pseudospin textures depending on the value of $\Delta\theta$.

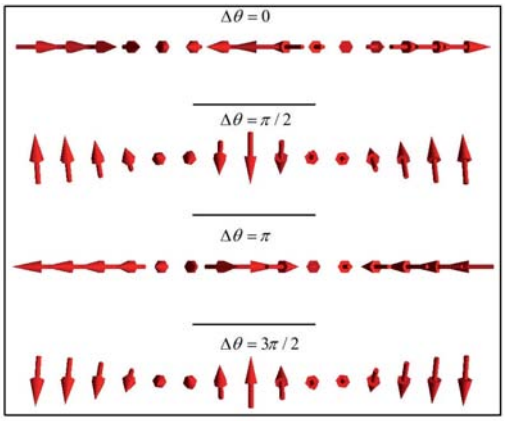

Figure 2.15: Pseudospin textures of four separated half-soliton pairs depending on the relative phase $\Delta\theta$.

To underline the contributions to the dissociation of solitons, we have numerically implemented a realistic configuration using Gauss-Laguerre beams in each component with winding numbers $(l_+, l_-) = (+1, +1)$ and $\phi_0 = 0$. We show in Fig.2.16 the half-soliton propagation, separating the different contributions in a situation where there is no rolling effect. In the panel (a), we show the α_2 impact on the separation, with $\Omega_x = 0$: we observe the linear trajectories (similarly to Fig.2.10(c)) after the HS are released from the pulsed pump spot, no acceleration is observed. In the panel (b) only $\mathbf{\Omega}_{LT} = \Omega_x\mathbf{u}_x$ is present ($\alpha_2 = 0$), trajectories become parabolic up to the limiting speed, which is a clear signature for the constant monopole acceleration (non-relativistic limit). In the panel (c), we show the combined effect of both α_2 and $\mathbf{\Omega}_{LT}$ together with the traces of the soliton trajectories (dashed lines)

from the panels (a) and (b), in that case the acceleration is emphasized by the initial repulsion. The rolling effect can either assist the separation or block it, depending on both the winding number imposed and the lateral shift direction.

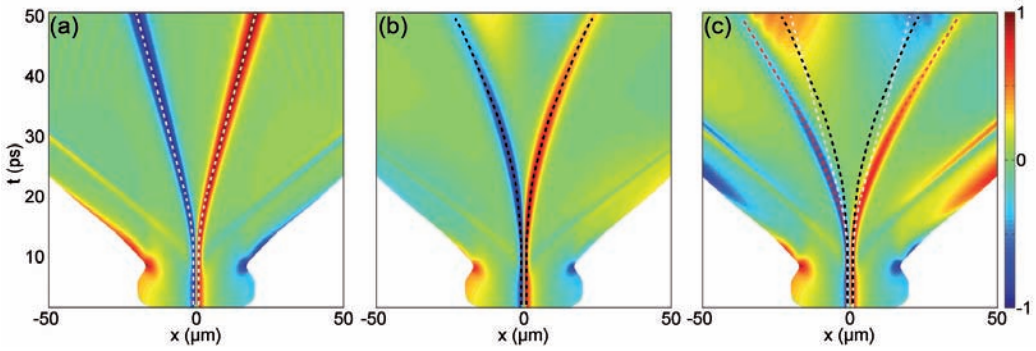

Figure 2.16: Contributions to the half-solitons motion. (a) $\alpha_2 = -0.2\alpha_1$ and $\hbar\Omega_x = 0$, (b) $\alpha_2 = 0\alpha_1$ and $\hbar\Omega_x = 100$ μeV and (c) $\alpha_2 = -0.2\alpha_1$ and $\hbar\Omega_x = 100$ μeV. The dashed lines stand for the trajectories in the configuration of the panel (a) (white) and (b) (black) to be compared with the red line.

We have seen that the splitting of a linearly polarized beam into its circularly polarized components allows an independent selection of the winding numbers of the half-solitons in each component and to fix their initial separation. However, even this step can be avoided, in order to further simplify the experimental configuration. Indeed, making the entire beam scatter on a hologram will impose the same winding number $l_+ = l_-$ to both condensate components, and the two components will this time be perfectly superimposed on the sample. In that case, the separation will not occur, unless the symmetry between the σ_+ and σ_- components is broken by some means. Although noise will always be present in the system and allow the separation to occur, it might induce (in some realizations) a symmetry breaking on time scales larger than the polariton lifetime. Moreover, the σ_+ and σ_- solitons will be separated randomly (e.g. σ_- going to left and σ_+ going to the right in one realization and the opposite behavior in the next one). These two points, that we have checked numerically (not shown), are clearly harmful to the reproducibility of the effect, and therefore, to the creation of a spin current. One should also bear in mind that a beam prepared to be linearly polarized might carry a small ellipticity. The ensuing density imbalance between the two condensate components will lead to the formation of half-solitons with slightly different healing lengths and therefore different effective masses. The rolling effect (which will occur in the same direction for both HSs) or possibly the wedge naturally present in microcavities (or the small gradient of the wire width), will induce an effective mass-dependent motion providing the separation. We have simulated this configuration with no initial separation, $(l_+, l_-) = (+1, +1)$ and a 1% ellipticity of the input beam. We show in Fig.2.17 the separation obtained from the rolling effect shifting the beam

by $\Delta y = +0.5$ μm [panel(a)] and from a wedge in the sample producing linear ramp potential of slope 10 μeV/μm [panel (b)]. In that latter case the HSs are accelerated by the force they undergo not from the side of the magnetic field, but directly from the potential ($\hbar\Omega_x = 0$ here).

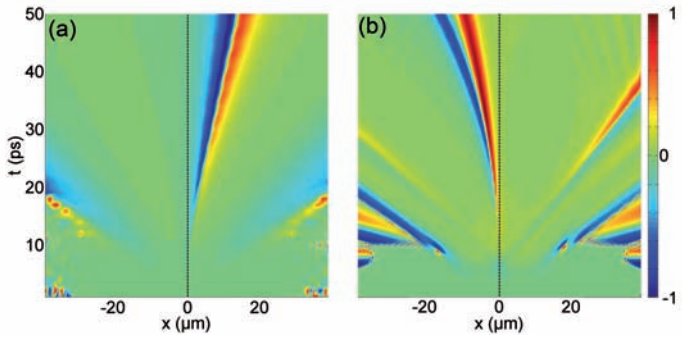

Figure 2.17: Separation of perfectly overlapping HSs thanks (a) to the rolling effect induced by a $\Delta y = 0.5$ μm shift and (b) to a wedge producing a potential ramp of slope 10 μeV/μm. For both configurations $\alpha_2 = -0.2\alpha_1$, $\hbar\Omega_x = 0$ and $l_+ = l_- = +1$.

In conclusion, polariton condensates in quasi-1D microwires constitute an ideal system for the creation of magnetic currents based on half-solitons thanks to their easy nucleation, natural separation, and acceleration. The half-light component in the polariton wavefunction allows the particles to travel at high velocities and therefore the analogues of magnetic monopoles that are half solitons can travel at the speeds close to the speed of light. They constitute extremely promising entities for the fabrication of a new class of high speed spin-optronic devices. While the propagation of these magnetic charges in wires is technologically attractive, two dimensional systems (planar microcavities) allow even more freedom and fundamental richness encompassed in the angular momentum of vortices as we will discuss in the following section.

2.2.3.3 Half-vortices separation

Integer vortices in "scalar" polariton condensates (that is, circulary polarized, without significant coupling between the two components) have already been demonstrated experimentally in the optical parametric oscillator (OPO) configuration [20, 21]. These vortices have been shown to be relatively persistent, remaining in the ground state of the OPO for long times, much longer than polariton lifetime. Another configuration, where the integer and half-integer vortices occur due to the persistent flows in the polariton condensate under non-resonant pumping, has also been studied experimentally [11, 13].

We are not particularly interested in demonstrating the self-sustained coherence of polariton condensate maintained by the OPO. We propose a configuration which seems to be the simplest from the point of view of experimental realization, in order to observe controlled separation of half-vortices. Using the Gauss-Laguerre beam we

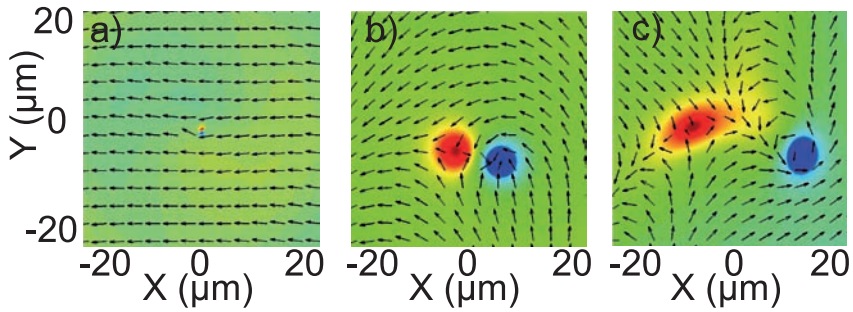

Figure 2.18: (a) Initial pseudospin configuration for an integer vortex (+1,+1). (b) Dissociation into two HVs under the effect of α_2-induced repulsion only; c) Dissociation and acceleration of the two HVs under the effect of magnetic field Ω_x. Panels (b) and (c) correspond to 50 ps after the pulse.

create an integer vortex, which then evolves freely under the effect of spin-dependent polariton-polariton interactions, constant effective in-plane magnetic field, and **k**-dependent TE-TM splitting. We demonstrate numerically the separation of a vortex $(l_+, l_-) = (+1, +1)$, with both components rotating in the same direction, in a weak static in-plane field of 10 μeV. Such integer vortex is likely to form in case of non-resonant pumping, due to persistent flows in the polariton condensate in a disorder landscape. The separation into half-vortices occurs for $\phi_0 = \pi$, while for $\phi_0 = 0$ the two vortices remain coupled with each other. Indeed, the half-vortices of opposite charges form a dipole, and the interaction between these charges induced by the field increases with the applied field. This is why, depending on the initial winding numbers and on the pseudospin texture defined by ϕ_0, one can sometimes observe the stabilization of the dipole length at an equilibrium value. Figure 2.18 shows the initial pseudospin texture (a) and the comparison between the situations without in-plane magnetic field (b) and with magnetic field (c). In the case (b) the small separation is due to the α_2-induced repulsion. In the panel (c) the half-vortices are dissociated and accelerated in opposite directions by the constant in-plane magnetic field, although its value is relatively small.

The parameters of the Gauss-Laguerre beam have to be chosen carefully, in order to minimize the non-desired effects such as the dynamic formation of solitons on the outer horizon of the density profile. At the same time, the size of the minimum in the center should be in agreement with the expected healing length. In a word, one should be as close to the perfect initial condition of a flat infinite condensate with a vortex in the center, as possible.

However, peculiar undesired effects can arise if a half-vortex becomes trapped in the spatial density inhomogeneity created by the rotation of the pseudospin of the other half-vortex, which is not cylindrically symmetric: in some directions the pseudospin is initially aligned with the field and does not rotate, while in the other directions the pseudospin is not aligned with the field and is bound to gain a nonzero Z-projection, which can be a barrier or a trap for the other half-vortex.

When the half-vortices are sufficiently far from each other (that is, when the distance between the vortices $d \gg \xi$), each of them can be considered separately, as a half-vortex composed of a vortex in one component and a homogeneous background in the other component. Each of them is therefore subject to a force acting from the effective magnetic field, and we can expect them to accelerate freely. The pseudospin texture of a half-integer vortex can be either convergent or divergent, looking similar to that of a point charge, as it is the case in 1D, but there are two important differences between the 1D and the 2D case. Indeed, in 1D the constant pseudospin field far from the vortex core is exactly the solution of the Maxwell's equation $\boldsymbol{\nabla}\cdot\mathbf{S} = \delta(x)$, whereas in 2D the pseudospin texture does not depend on the distance from the core (as well as in 1D), while the solution of the Maxwell's equation in this case should be decaying: the field of a charge depends on the distance from it. The second important difference resides in the presence of the relative phase ϕ_0, which influences the more complicated texture of the half-vortex and its propagation direction. Various cases and the corresponding textures have been considered in Ref.[38]. Moreover, in the 2D case there is a long-distance interaction between the vortices lying in the same component, and even between vortices in different components, when a magnetic field is applied. The field creates a transfer of particles between the two components, and since the particles have nonzero propagation velocities even far from the vortex core, this creates a long-distance interaction force, absent in 1D. For the **k**-dependent TE-TM splitting in planar microcavities, this interaction has been considered in Ref.[45].

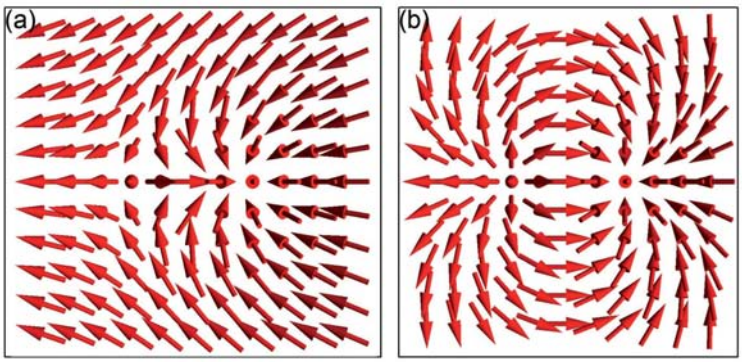

Figure 2.19: Pseudospin textures of (a) phase vortex $(l_+, l_-, \phi_0) = (+1, +1, \pi)$ and (b) a polarization vortex $(l_+, l_-, \phi_0) = (1, -1, \pi)$, dissociated in their associated half-vortices.

In the ideal case, the condensate wavefunction containing a half-vortex in both components separated by d reads

$$\psi = \begin{pmatrix} \psi_+ \\ \psi_- \end{pmatrix} = \begin{pmatrix} \sqrt{n_+}e^{il_+\phi_+}e^{i\phi_0} \\ \sqrt{n_-}e^{il_-\phi_-} \end{pmatrix} \tag{2.59}$$

The radial functions take the approximated form [55] $n_\pm(r_\pm, \phi_\pm) = r_\pm^2/(r_\pm^2 + 2)$,

where $r_\pm = \sqrt{(x \mp d/2)^2 + (y \mp d/2)^2}$ and $\phi_\pm = \arctan[(y \mp d/2)/(x \mp d/2)]$. The components of $\mathbf{S}$ are easily found using the Eqs.(1.141-1.143). To give the complete picture, we show in Fig.2.19 the pseudospin textures for two half-vortex pairs using the sets of parameters $(l_+, l_-, \phi_0) = (+1, +1, \pi)$ and $(l_+, l_-, \phi_0) = (1, -1, \pi)$ which constitute a phase and a polarization vortex respectively when the half-vortices overlap.

In conclusion, half-vortices embody the 2D candidates for the monopole analogy possessing a divergent pseudospin field (depending on ϕ_0). They accelerate under the action of the effective field and are characterized as well by a ϕ_0-dependent propagation direction [38] at fixed orientation of the effective field. They constitute the building blocks for potential 2D-magnetic circuits.

2.2.4 Conclusion

We have shown that the half-integer topological defects in spinor polariton condensates not only possess a divergent or convergent pseudospin texture similar to the textures of point charges in 1D and 2D, but also behave as magnetic charges (monopoles) in presence of effective magnetic fields, accelerating along them. They exhibit a velocity dependent renormalization of their mass, size, and charge, and produce a magnetic analogue of Coulomb's force. We have proposed a simple configuration for experimental creation, dissociation, and acceleration of half-integer topological defects – towards magnetricity. In the next section we will present another type of two dimensional topological defect behaving as a magnetic monopole, that was recently observed experimentally.

2.3 Hydrodynamic generation of oblique half-Solitons and half-vortices

In the chapter 1 we have introduced the oblique dark soliton solution of the scalar Gross-Pitaevskii equation [see Sec.1.2.5.4]. Its experimental evidence was obtained in an exciton-polariton condensate in 2011 [50] thanks to the high degree of control offered by the system [see Fig.1.12]. The experiment involved a propagating polariton fluid injected resonantly against an immobile structural defect in the microcavity following the prediction of Ref.[51] analyzed later on in Ref.[52].

2.3.1 Theory

As we know now, to generate topological excitations we need to be able to create local phase shifts. A resonant continuous wave pumping scheme imposes a specific phase at any time under the pump spot. Therefore, the latter has to be absent over some part of the sample, otherwise the phase would be imprinted everywhere. Pigeon et al. [51] proposed to use a localized pump spot with finite momentum upstream from the defect, allowing the phase to evolve freely around the defect. The counterpart is that because of the finite lifetime of the particles involved, the density is decaying with the propagation distance. They managed to obtain numerically three detuning- and thus density-dependent regimes. At larger detunings, low densities and thus in supersonic regimes, dark solitons appeared downstream from the defect. In this setup, the solitons appear as stable stationary solutions; however, one cannot say that they preserve their shape. Actually, due to the density decay, the healing length increases with the distance from the defect $\xi = \xi(x - x_D)$ and then the oblique soliton adapts to the local density, becoming larger, shallower, and curved. One extra feature of the polaritonic oblique solitons is that they are able to survive even at subsonic velocities. Namely, in the regimes, where no Ćerenkov-like radiation (ship waves) is visible upstream from the defect, the oblique solitons are stabilized by the damping associated with the decaying flow. Reducing the detuning/increasing the density, the oblique solitons tend to disappear, due to the development of snake instabilities, to the benefit of vortex dipoles (vortex streets), as predicted in Refs.[53, 54], but with a lower critical velocity than in the undamped BEC [55]. One should note here, that vortices survive in subsonic regimes thanks to the local acceleration of the fluid close to the defect [56], which does not violate Landau's criterion. Increasing the density further should allow to enter a superfluid regime, where no perturbations are induced by the presence of the defect. Nevertheless, in that case, the position of the pump spot becomes determinant. Indeed, if the latter is too much overlapping with the defect, then the phase will be imprinted, hiding potential perturbations. If the pump is too far, then the density will have decayed too much, arriving at the defect's position. The condition is $E_{int} \geq 2E_{kin}$, where $E_{int} = \mu = \alpha n$ is the interaction energy and $E_{kin} = m^* v^2/2$, with m^* an effective mass, is the kinetic energy. In summary: the polaritonic system allows the investigation of various hydrodynamic regimes ranging from generation of oblique

solitons to a superfluid flow, passing by emission of vortex streets, all observed experimentally by Amo et al. [57, 50]. In their observation, Amo et al. did not resolve the polarization of the condensate and the solitons were "scalar", since the excitation was performed with a circularly polarized pump.

In the following, we discuss the hydrodynamic generation of oblique half-solitons [37] and half-vortices in polariton condensates and their experimental observation, that was performed in collaboration with our group [40]. I refer the reader to the section [Sec.1.2.5.4] devoted to scalar oblique solitons.

Let us now focus on the possibility of creating 2D *oblique* half-solitons. First of all, it is clear that in the case, where the two components of a spinor BEC do not interact ($\alpha_2 = 0$), if they are initially equally populated, a significant perturbation in only *one* of the components will lead to the formation of half-integer topological excitations. Next, what happens if the interaction between the two components is no longer negligible? To answer this question following Ref.[4], we turn back to the spinor Gross-Pitaevskii, rescale them like in Eqs.(2.13), and look for stationary solutions, where the phase of each component is expressed by means of their stationary and irrotational velocity fields via $\mathbf{v}_\pm(\mathbf{r}) = \hbar/m^* \boldsymbol{\nabla}\theta_\pm(\mathbf{r})$, with $\mathbf{r} = (x, y)$. We look for oblique solutions that depend only on the tilted coordinate $\chi = (x - ay)/\sqrt{1+a^2}$, which leads to the following set of equations

$$\left(n_+'^2/4 - n_+ n_+''/2\right) + 2n_+^2\left(\Lambda_1 n_+ + 2\Lambda_2 n_-\right) = (q+2\mu)\, n_+^2 - q n_0^2 \quad (2.60)$$

$$\left(n_-'^2/4 - n_- n_-''/2\right) + 2n_-^2\left(\Lambda_1 n_- + 2\Lambda_2 n_+\right) = (q+2\mu)\, n_-^2 - q n_0^2 \quad (2.61)$$

where $\Lambda_{1,2} = \alpha_{1,2}/(\alpha_1 + \alpha_2)$ and $q = U^2/(1+a^2)$ (U is the velocity of the flow). This system has to be solved numerically, but we can first consider some simple arguments. The density profile of an integer oblique soliton in a spinor fluid is given by $n_{ODS} = 1 - (1 - q/\mu)\,\mathrm{sech}[\chi\sqrt{\mu - q}]^2$ with $\mu = (\Lambda_1 + \Lambda_2)n_0/2 = \Lambda n_0/2$. Now, for the case of the OHS, the density notch in the σ_- component, that contains the defect, is seen as an external potential by the initially unperturbed σ_+ component, because of the interactions between the particles of different spins. We suppose that the σ_+ component fits the shape of this potential which is nothing but $\Lambda_2 n_-$. Then, this perturbation creates in turn a potential for the σ_- component given by $-\Lambda_2 n_+ = -\Lambda_2^2 n_-$. Therefore, the density profile is modified as $\widetilde{n}_- \leftarrow \left(\Lambda n_- - \Lambda_2^2 n_-\right)/\Lambda$. Iterating this procedure leads to a geometric series and to a renormalization of the interaction constant seen by the component containing the soliton $\widetilde{\Lambda} \leftarrow \Lambda - \Lambda_2^2/(\Lambda - \Lambda_2)$. Consequently, the OHS solution is approximated by

$$n_{OHS} = 1 - (1 - q/\widetilde{\mu})\,\mathrm{sech}\left[\chi\sqrt{\widetilde{\mu} - q}\right]^2 \quad (2.62)$$

with $\widetilde{\mu} = \widetilde{\Lambda} n_0$. In this description, the sound velocity is changed like $c_s \to \widetilde{c}_s = \sqrt{\widetilde{\mu}/m^*}$ and the healing length like $\xi \to \widetilde{\xi} = \hbar/\sqrt{2m^*\widetilde{\mu}}$. In the case where $\Lambda_2 < 0 (> 0)$, which corresponds to an attractive (repulsive) interaction, c_s is slightly increased (decreased) and inversely for ξ. The component without a soliton obviously presents a minimum (maximum). This argumentation is compared to direct

numerical solutions of Eqs.(2.60,2.61) in the Fig.2.20 showing a remarkable accuracy provided that Λ_2 remains small.

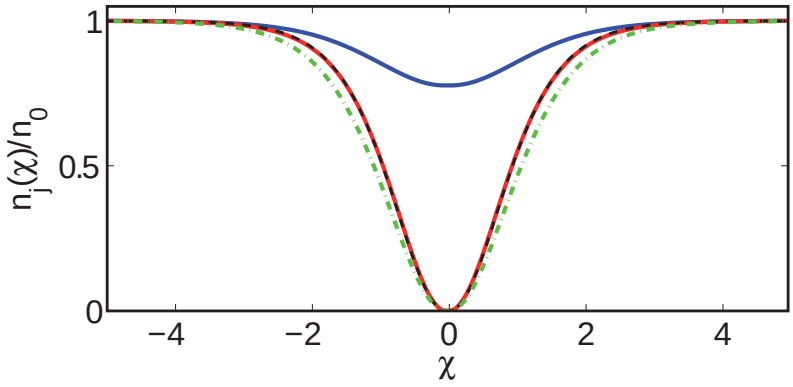

Figure 2.20: An oblique half-soliton density slice normal to its axis. The solid blue and red curves show numerical profiles, the dashed black curve is the perturbative solution described in the text and the dashed/dotted green curve show the scalar soliton solution.

Now let us see how half-vortices [see Sec.(2.1)] and oblique half-solitons can be generated in a propagating exciton-polariton fluid. The setup we propose is basically the same as the one required to generate the integer oblique solitons described previously [51, 50, 52], namely a continuous and resonant pumping scheme locally upstream from a defect, imposing a supersonic flow. However, we will now focus on the spin degree of freedom of the condensate, namely the polarization of the pump and the polarization of the emission along the propagation. To describe more accurately the spinor polariton BEC, we take into account the real non-parabolic dispersion of the particles, their decay and injection, via the set of four coupled spin-dependent equations

$$\begin{aligned} i\hbar\frac{\partial\phi_\pm}{\partial t} = & -\frac{\hbar^2}{2m_\phi}\Delta\phi_\pm + \Omega_R\chi_\pm + D_\pm\phi_\pm + \beta\left(\frac{\partial}{\partial x} \mp i\frac{\partial}{\partial y}\right)^2\phi_\mp \\ & + P_\pm e^{i(\mathbf{k}_P\cdot\mathbf{r}-\omega_P t)} - \frac{i\hbar}{2\tau_\phi}\phi_\pm \end{aligned} \tag{2.63}$$

$$i\hbar\frac{\partial\chi_\pm}{\partial t} = -\frac{\hbar^2}{2m_\chi}\Delta\chi_\pm + \Omega_R\phi_\pm + \left(\alpha_1|\chi_\pm|^2 + \alpha_2|\chi_\mp|^2\right)\chi_\pm - \frac{i\hbar}{2\tau_\chi} \tag{2.64}$$

The pump terms of amplitudes $P_\pm$ allow to select the polarization of injected photons and thus of polaritons. $D_\pm$ is the impenetrable potential barrier, that can affect independently each component. We have chosen a bar-shaped pump spot upstream from the defect. The effective mass m_ϕ is therefore approximated by $m_\phi = m_\phi^{TM}m_\phi^{TE}/(m_\phi^{TM} + m_\phi^{TE})$. To generate half-integer topological defects past the obstacle we need to be able to break the symmetry of the flow not only with respect to the density (integer topological defects) but also with respect to its polarization. In what follows, we present 2 different schemes for the generation of oblique half-solitons.

The first alternative is to find a way to perturb only one of the two components. This could be done experimentally if the defect is created optically by a circularly polarized pulse [58, 21]. This scheme is however far from being ideal since it would bring of lot of unwanted perturbations to the system and it should rather be seen as a model experiment. In this framework, one needs to impose $D_- = 0$ and to inject *linearly polarized* photons upstream from the defect which requires $P_+ = P_-$ and creates equal population of polaritons with spin $+1$ and -1. In that case oblique half-solitons pairs (or HV at higher densities) obviously appear in the component containing the defect (see Fig.2 of Ref.[37]) and a weak density minimum is imposed in the other component due to the fact that $a_2 < 0$.

The second alternative, that we will discuss in more details is, on the other hand, completely realistic, as it will be confirmed in the next section. The impenetrable defect is restored in both components and we will benefit from the polarization separation brought by the TE-TM splitting. We need to carefully select the polarization of the pump laser to avoid pseudospin rotation before the fluid reaches the defect. We choose the latter to be linear in a TM state which corresponds to a polarization along the direction of propagation (x-axis) and to $\mathbf{S}$ pointing along $\mathbf{H}_{LT}$.

Arriving at the obstacle, the supersonic fluid is split into two parts, propagating in opposite oblique directions around the obstacle. Before the defect, the pseudospin was aligned with the effective field, but when the propagation direction changes, the angle between the pseudospin and the field starts to increase. It induces an antisymmetric rotation of the pseudospin: the particles going up (down) will gain a σ_+ (σ_-) component, providing the seed for the OHS/HV generation. The mechanism of nucleation of the oblique half-solitons, however, is not as trivial as in the case of the polarized defect. If no TE-TM splitting was present, our experiment would lead to the nucleation of a pair of integer oblique solitons, and each of them can be seen as a superposition of two perfectly overlapping oblique-half solitons. With the splitting turned on, the oblique-half solitons do not overlap perfectly anymore, becoming slightly shifted because of the antisymmetry of the flow with respect to circular polarizations, σ_+ and σ_- providing the seed for their separation. However, this initial separation is weak for a small defect and seems to be insufficient to separate them significantly away from the defect, and we definitely need something more.

Downstream from the defect the flows are complex, but globally the fluid is moving along the x-axis. Since the half-solitons have been separated, they start to behave as magnetic monopoles having opposite charges, just like in the 1D case, because their pseudospin texture is divergent. They start to feel the TE-TM induced effective magnetic field $\mathbf{H}_{LT}$ that is pointing along the flow. Since the solitons are oblique, the scalar product $\mathbf{H}_{LT} \cdot \mathbf{S}$ is not zero, providing their separation and acceleration, increasing with the distance from the defect. One of them is bent slightly towards the axis of symmetry of the flow, becoming deeper, while the other one is moved in the opposite direction, becoming shallower and larger and possibly hardly visible for larger values of H_{LT} (larger $\mathbf{k}_P$). The situation is obviously totally antisymmetric for the lower oblique soliton. Moreover, this separation effect is

emphasized for large density regions (close to the defect) if α_2 is negative as it induces the half-soliton repulsion [see Fig.2.21].

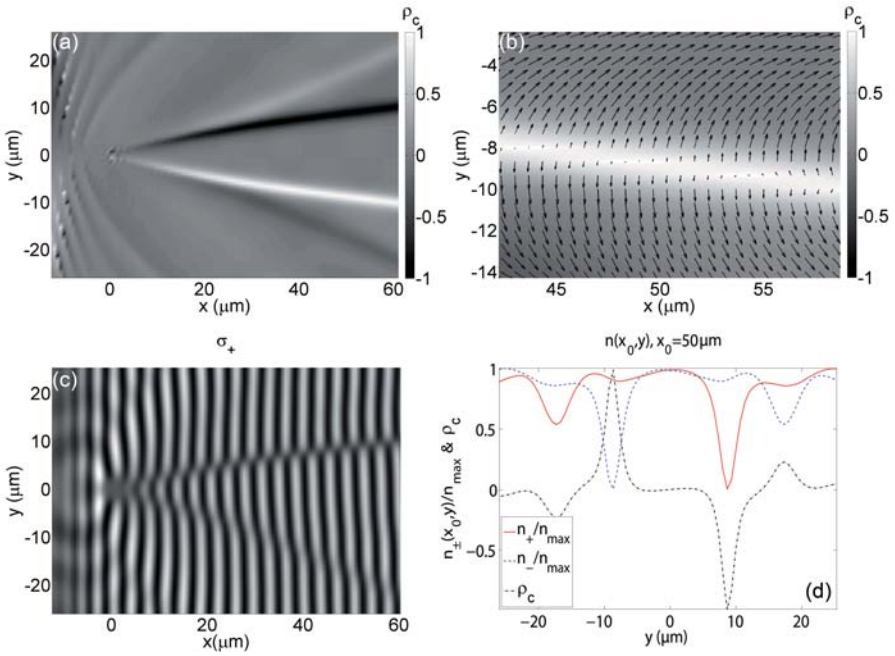

Figure 2.21: Stationary 2D oblique half-soliton, the flow is going from left to the right. (a) Degree of circular polarization ρ_c: one clearly sees the antisymmetric pattern imposed by the effective field's geometry and the OHS separation. (b) Zoom on the lower σ_- soliton (white one in (a)) with the in-plane pseudospin component $\mathbf{S}_{\|} = (S_x, S_y)^T$ (black arrows) exhibiting a rotation of almost π through the OHS ($\pi/2$ rotation of η). (c) Interference pattern in the σ_+ component showing the phase shifts at the soliton position the situation is obviously antisymmetric in the other component (not shown). The repelled soliton is shallower which corresponds to smaller phase shifts. (d) Density slices 50 μm downstream from the defect together with a ρ_c slice.

Once again, the intrinsic Zeeman splitting arising from the polariton spin-anisotropy protects the half-soliton up to the critical magnetic field H_c [see eq.(2.35)]. One should keep in mind however, that due to the finite polariton lifetime, the total density is decaying away from the defect and the Zeeman splitting is decaying as well. At some point, it is unavoidable, that the effective magnetic field felt by the half-solitons gets over the critical value. At this point, they start to be converted in the other component, and thus their extension is finite [see e.g Fig.3(c) of our theoretical paper [37]].

Let us remember that 1D half-solitons are the domain walls between linear polarizations, which means that the polarization angle η rotates by $\pi/2$ and the in-plane projection of $\mathbf{S}\| = (S_x, S_y)^T$ by π going through the HS. This rotation of η is also expected for a the 2D system, nevertheless, the *oblique* half-solitons possess a non-

zero velocity with respect to the flow, and therefore have nonzero density in the component where the soliton lies. Thus, the rotation of η as well as the shift of the global phase θ are bound to be smaller than $\pi/2$.

We know now that in the scalar condensate increasing the fluid density (or reducing its speed) leads to the dissociation of oblique solitons into vortex streets [53] and eventually to the onset of superfluidity [see Sec.1.2.5.4 and Ref.[51]]. We obviously expect the same behavior to occur for the spinor system. The half-vortex generation at higher densities can be understood similarly to the half-soliton nucleation: integer vortices are split into HVs by the effective magnetic field around the defect and they become accelerated. The difference is that vortices cannot be more or less shallow like solitons, they can only appear or not, being real topological defects, which explains why only one species of half-vortices appears in each half-plane in our simulation but the situation can be different depending on the strength of the field. We show the corresponding numerical stationary solutions in Fig.2.22, demonstrating the three density dependent hydrodynamic regimes: Oblique Half-Solitons [Fig.2.21], streets of half-vortex dipoles [Fig.2.22(a),(b)], and finally a superfluid regime [Fig.2.22(c),(d)].

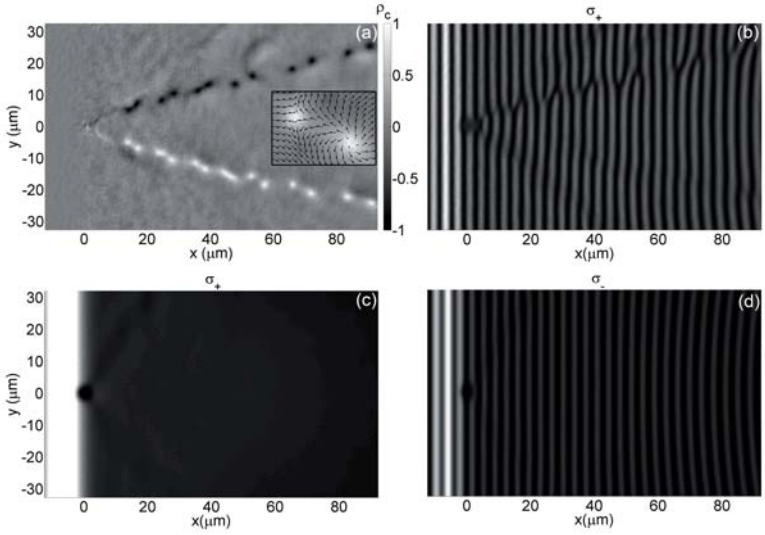

Figure 2.22: (a) Degree of circular polarization: HV trains generation increasing the pump intensity with respect to Fig.2.21. The inset displays $\mathbf{S}\|$ for a σ_- HV pair (black arrows) and shows the opposite winding of the polarization around the HVs core. (b) The interference pattern in the σ_+ component shows the typical forklike dislocations at the HV position. The positions corresponding to σ_- vortices show no phase modification. (c) Superfluid regime: The flow ignores the presence of the obstacle and shows no phase perturbation as one can see in the panel (d) showing the complementary antisymmetric σ_- component.

2.3.2 Experiment

Our oblique half-soliton prediction as well as their monopole-like behavior was recently confirmed experimentally in the framework of a collaboration with the L.K.B. and L.P.N. laboratories in Paris [40]. The setup that was retained was the one involving the quasi-resonant injection of linearly polarized particles and resolving the polarization. The experiment was performed at 10K within a GaAs microcavity characterized by a 5.1 meV Rabi splitting, the required defect (potential barrier) originated naturally from the microcavity structure. The shape of the pump spot was chosen to be half-Gaussian upstream from the defect [see Fig.2.23 for a scheme]. The polarization of the beam was chosen to be in a TM state (parallel to the flow direction) and the wavevector was imposed to be $k_P = 1.3\ \mu\text{m}^{-1}$ – large enough to impose a supersonic flow at the chosen pumping power. The value of the TE-TM splitting for this wavevector was estimated to be 20 μeV, which is large enough to separate the half-solitons and low enough not to destroy them on the distance of observation.

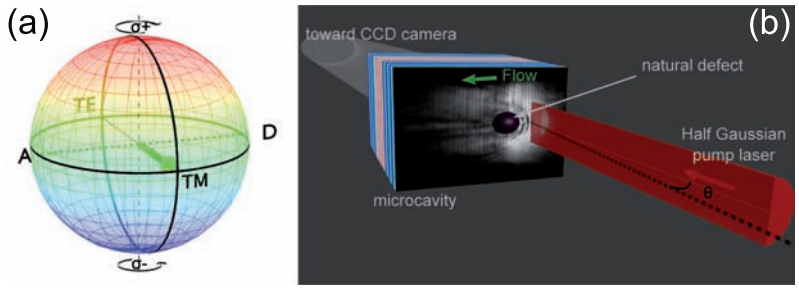

Figure 2.23: (a) Polariton pseudospin **S** (green arrow) on the Poincaré sphere representing all the possible spin configuration of the polariton gas and the associated polarizations. Initially **S** points along the y direction followed by the flow (TM state). (b) Scheme of the resonant injection of the polariton gas above a round potential barrier (defect) in the sample.

The first thing to note is that since the natural defect was large (around 10 μm) and the speed of the flow was high (to have sufficiently large splitting), multiplets of solitons were nucleated and four pairs of oblique half-solitons are visible, which slightly reduces their separation due to their short range repulsion where the density is large. Now that we know the generation mechanism, we know that close to the defect the solitons are almost integer, namely the half-solitons are only slightly spatially shifted due to the combined effect of the defect and the TE-TM splitting. Farther away, they start to be accelerated in opposite directions by the TE-TM field, behaving as magnetic monopoles. This is visible in the degree of circular polarization of the emission. In the experiment, the half-solitons could be evidenced as domain walls the most clearly on the diagonal polarization basis (simply due to their oblique behavior), providing an efficient way of tracking their trajectories. Experimentally, the pseudospin components cannot be extracted from the order

parameter of the condensate, they have to be reconstructed from the circular (S_z, indices $\pm$), horizontal/vertical (S_x, indices H/V) and diagonal/antidiagonal (S_y, indices D/A) polarization components of the emission following

$$S_x = (I_H - I_V)\,/\,(I_H + I_V) \tag{2.65}$$
$$S_y = (I_D - I_A)\,/\,(I_D + I_A) \tag{2.66}$$
$$S_z = (I_+ - I_-)\,/\,(I_+ + I_-) \tag{2.67}$$

where I_j are the measured intensities with the correspondence $I_j = |\psi_j|^2$.

The figure 2.24(a)-I shows the formation of two oblique dark solitons to the right of the barrier's wake in the σ_+ component of the emission. They can be identified as the dark straight notches in the polariton density. These solitons are almost absent in the σ_- component [Fig.2.24(a)-II]. In turn, in the σ_- emission, a deep soliton (S1) clearly appears to the left of the barrier's wake (blue arrow), where only a very shallow one is present in σ_+ [see the profiles in Fig.2.24(c)]. The absence of mirror symmetry between Figs.2.24(a)-I and 2.24(a)-II arises from the specific and uncontrolled form of the natural potential barrier. The individual dark solitons in each $\sigma_\pm$ component of the fluid appear as long spatial traces with a high degree of circular polarization $\rho_c = (I_+ - I_-)/(I_+ + I_-)$, as shown in Fig.2.25(a). Interferometry images obtained by combining the real space emission field with a reference beam of homogeneous phase [Fig. 2.24(b)-I and 2.24(b)-II] give access to the phase jump across each soliton. For instance, for the soliton S1 observed in σ_-, we measure a phase jump $\Delta\theta_- = 0.85\pi$ as shown in Fig.2.24(e), note that it would be π for a strict dark soliton with zero density at its center, while in the same region the phase in the σ_+ component is almost unaffected $\Delta\theta_+ \simeq 0$. As we know, a dark soliton lying in only one spin component of the fluid *is* the half-soliton. The mixed spin-phase character of these topological excitations is further evidenced when analyzing them in the linear polarization basis.

In the regions where the two circular polarizations are of equal intensity (i.e., the fluid surrounding the half-solitons) the linear polarization angle $\eta = (\theta_+ - \theta_-)/2$ and the global phase $\theta = (\theta_+ - \theta_-)/2$ can be defined. In our experiments we directly access $\Delta\Theta$ and the change in η across the solitons by looking at the linearly polarized emission, for instance, in the diagonal and anti-diagonal directions (polarization plane rotated by $+45$ and -45 with respect to the TM direction). The figure 2.24(d) and 2.24(f) show that the half-soliton S1 is also present in these polarizations with a phase jump $\Delta\theta = 0.4\pi$. This confirms that across the half-solitons, θ undergoes a jump $\Delta\theta \simeq 0.85\pi/2 \simeq (\Delta\theta_+ + \Delta\theta_-)/2$, that is, one half the phase jump observed in the circularly polarized component in which the soliton is present. We also expect a similar jump $\Delta\eta$ of the polarization angle [see Fig.2.26(c)]. This is illustrated in Fig.2.25(b), where all the half-solitons present in our fluid [dashed lines extracted from Figs.2.24(a)-I and 2.24(a)-II] appear as walls between domains of diagonal (magenta) and antidiagonal (green) polarizations. Mapping the linear polarization vector in the vicinity of the soliton S1 [Fig.2.26(a)], we deduce a jump $\Delta\eta = 0.32\pi$ (Fig.2.26c], close to the ideal expected value of 0.4π.

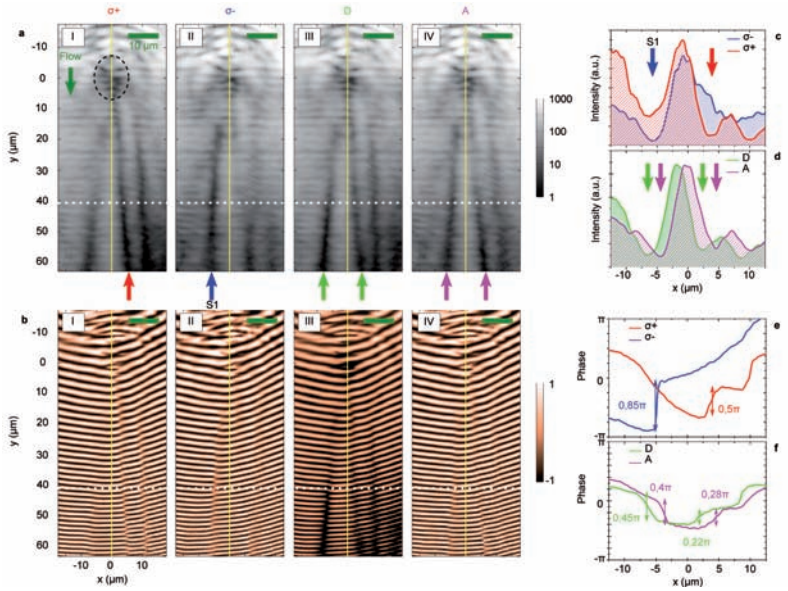

Figure 2.24: Density and phase tomography of the half-solitons. (a) Emission of the polariton gas in σ_+/σ_- components and in diagonal/antidiagonal linearly polarized components with respect to the TM polarization of injection. Half-solitons nucleate in the wake of the potential barrier [circle in (a)-I] and are evidenced as dark traces present in only one circular component (arrows). S1 is the half-soliton discussed in the text. (b) Interferometric images obtained from the interference with a beam of homogeneous phase. (c) Density profiles of σ_+/σ_- emission along the dotted line in (a)-I and (a)-II. The arrows indicate the position of the inner half-solitons, only present in a given circular polarization, with an associated phase jump shown in (e) [obtained from (b)-I and (b)-II]. Half-solitons appear in the density profiles of both diagonal and antidiagonal polarizations (d) (extracted from the dashed line in (a)-III and (a)- IV), with phase jumps of half the value measured in circular polarization (f) (obtained from (b)-III and (b)-IV).

Analyzing the half-soliton trajectory from polarization-resolved real-space measurements, we study their acceleration within the effective magnetic field $\mathbf{H}_{LT}$ pointing in the direction of the flow [y, red arrow in Fig.2.23(b)]. The acceleration arises from the interaction between this magnetic field, and the pseudospin texture of the half-soliton, shown in Fig.2.26(b) for the half-soliton S1. In the direction perpendicular to the soliton (dotted line), the in-plane pseudospin $\mathbf{S}_{\parallel}$ is divergent, since it points away from S1 on both sides, as expected for a magnetic charge. Once again, we are able to evaluate the force acting on the half-soliton as the gradient of the magnetic energy with respect to the half-soliton position x_0. We know from Sec.(2.2.1.2) that the magnetic energy per unit length is

$$E_{mag}(x_0) = -\int \mathbf{S}(x - x_0) \cdot \mathbf{H}_{LT} dx \tag{2.68}$$

where the integral is performed here along the x' transverse direction, perpendicular to the half-soliton located at x_0. The energy has a positive contribution from the left of the half-soliton ($\mathbf{S}$ and $\mathbf{H}_{LT}$ pointing in opposite directions), and a negative one from the right ($\mathbf{S}$ and $\mathbf{H}_{LT}$ having the same direction). In order for the magnetic energy to be minimized, a magnetic force appears pushing the half-soliton towards the left, increasing the negative contribution. The negative mass of the solitons imposes the acceleration in the direction opposite to the force. Thus, the half-soliton S1 that appears in the σ_- component of the fluid accelerates towards the right, as sketched in Fig.2.26(b). The direction of the acceleration is opposite for the soliton present in the σ_+ component [see arrows in Fig.2.26(b)]. Moreover, the simple fact that we observe half-solitons in the system means that they have been accelerated in opposite directions.

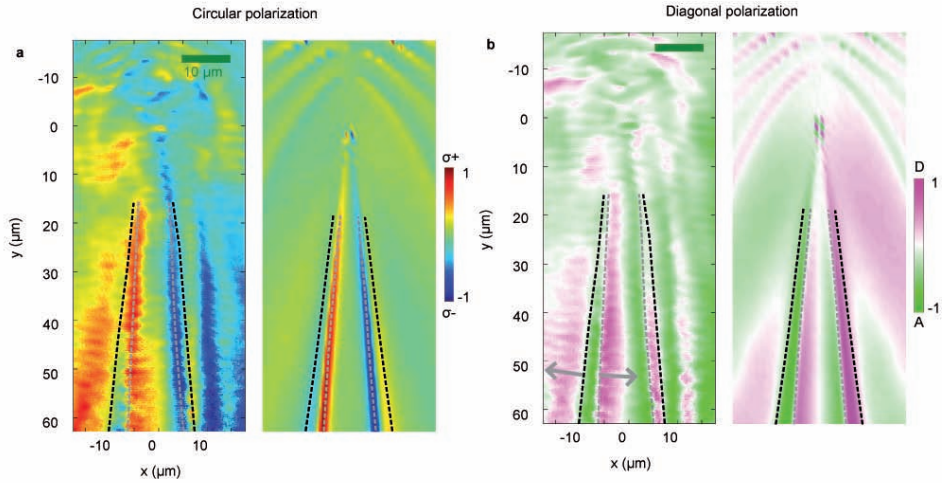

Figure 2.25: Polarization texture of half-solitons. Left panels in (a) and (b) show the measured degree of circular and diagonal polarizations, respectively. The right panels show the calculated patterns from the solution of the spin dependent Gross-Pitaevskii equation describing the system in the conditions of the experiment. The dashed lines show the trajectory of the half-solitons extracted from Fig.1(a)-I and 1(a)-II. The trajectories of the half-solitons appear as extrema of circular polarization and domain walls in diagonal polarization.

The monopole dynamics allows understanding the mechanisms of formation of the half-solitons in our experiments. An integer soliton nucleated right behind the obstacle is a superposition of two overlapping half-solitons of opposite magnetic charges. The presence of the TE-TM splitting induced effective magnetic field makes them experience opposite magnetic forces, leading to their separation and their trajectories become curved, as depicted by dashed lines in Fig.2.25, a behavior similar to the monopole separation in spin ices [49] under magnetic field. The half-solitons pushed towards the center are slowed down with respect to the flow as the trajectory becomes parallel to the field. Simultaneously, they gain stability and

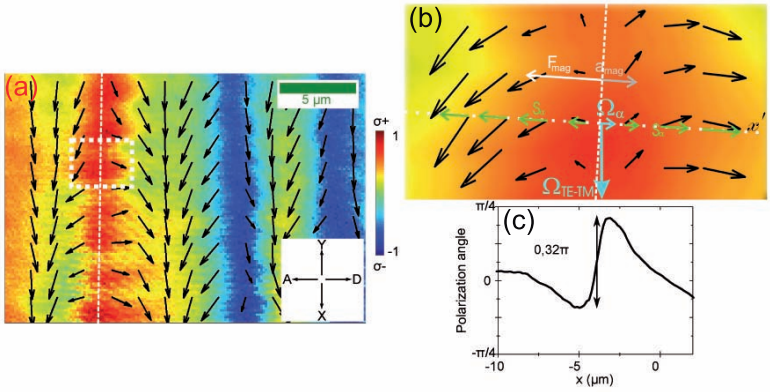

Figure 2.26: Magnetic force acting on the half-solitons. (a) Complete spin texture of the polariton fluid in the region between 30 and 50 μm downstream from the barrier. The color scale indicates the degree of circular polarization (latitude in the Bloch sphere), and the black arrows the direction of the linear polarization as defined in the equator of the Bloch sphere. The half- soliton S1 presents a pseudospin field analogue to that of a point charge in the direction perpendicular to its trajectory, as depicted in (b) for the dash-boxed area of (a). The polarization angle jumps from the antidiagonal to the diagonal direction when crossing the soliton, as shown in (c). The TE-TM effective magnetic field schematized in b has a component perpendicular to the half-soliton resulting in its acceleration.

become darker. Those pushed outwards gain velocity and become shallower, until they eventually disappear. The trajectories of the external shallow half-solitons are clearly visible in our experiments as domain walls in the diagonal basis, and as maxima of polarization degree on the circular basis [black dashed lines in Fig.2.25]. One should however notice that the trajectories of these expelled secondary half-solitons are perturbed far from the obstacle axis by the presence of additional solitons nucleated by the large barrier, particularly on the right side of the images. The figure 2.27 show a theoretical fit of all the panels of the experimental Fig.2.24 and 2.26. In these simulations we solve Eqs.(2.63,2.64) and we have deliberately chosen a smaller defect in order to get rid of the soliton multiplets to emphasize on the monopole acceleration.

Additionally, we have made a comparison with the original setup for the observation of integer solitons [50] involving a right circularly polarized beam (σ_+ and pseudospin along the z-direction). But this time, the polarization was resolved. In such a situation, under the pump spot upstream from the defect the strong density imbalance induces a significant effective field $\mathbf{H}_z$ that prevents the pseudospin from precessing around the in-plane $\mathbf{H}_{LT}$ field. Such a behavior is clearly visible in the Fig.2.28, where the degree of circular polarization remains close to 1 and almost unperturbed close to the barrier. The strength of $\mathbf{H}_z$ is however reduced far away from the defect where the density of polaritons decays due to their finite lifetime which allows here the conversion from spin up to spin down polaritons (yellow regions).

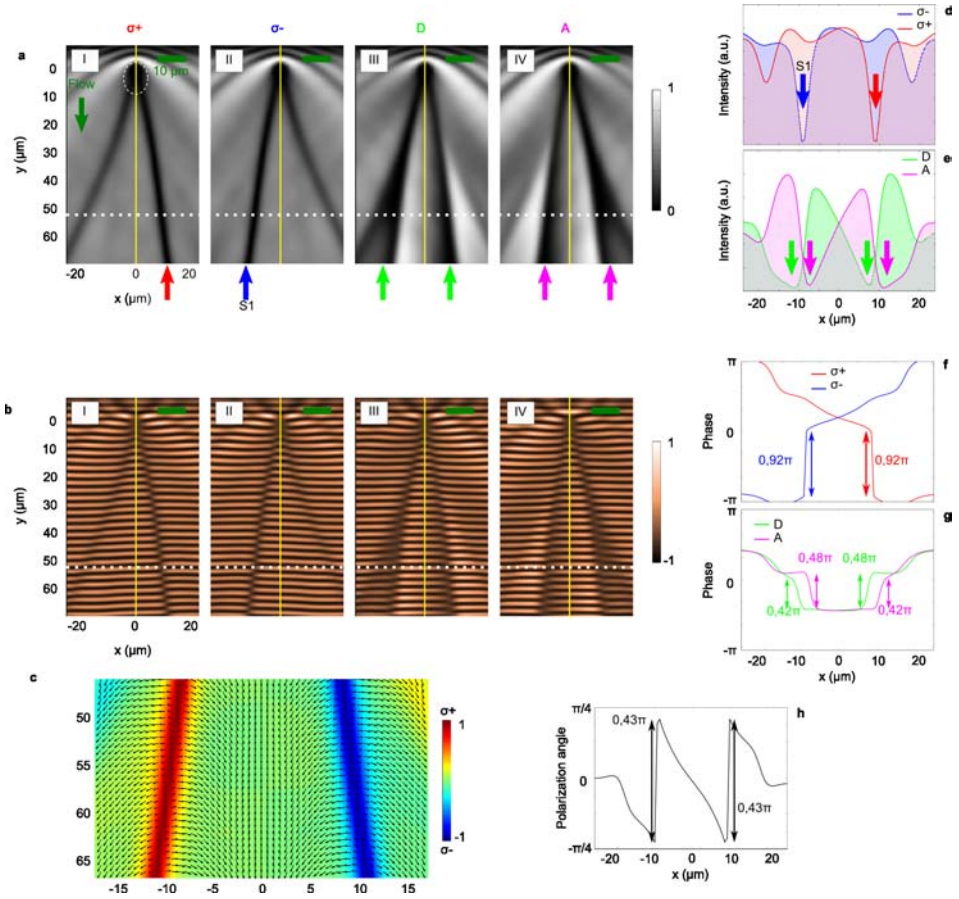

Figure 2.27: Results from Gross-Pitaevskii simulations. The defect is small (4 μm large) to get rid of the secondary solitons to emphasize on the half-soliton acceleration.

Therefore, under strong σ_+ pumping, the σ_- population remains weak everywhere, being completely determined by the transfer of particles from the other component. This is seen in Figs.2.28(a) and 2.28(b), where one can observe integer (scalar) solitons in the σ_+ component, and their copy (but with a smaller density) in the other component. These integer solitons are not affected by the in-plane field $\mathbf{H}_{LT}$ and no acceleration can be observed in that case.

This experiment constitutes not only the first evidence of the analogy between half-integer topological defects and magnetic monopoles but also the first proof of the separation of an integer topological defect in its half-integer constituents and this within a stationary regime. This paves the way towards magnetic currents in semiconductor microcavities. Now that the effect has been observed in the form of half-solitons, the next step in this direction will be to implement the on-demand generation of these magnetic currents in a real device using for example our proposal based on Gauss-Laguerre beams in wires (half-solitons) or planar cavities (half-vortices).

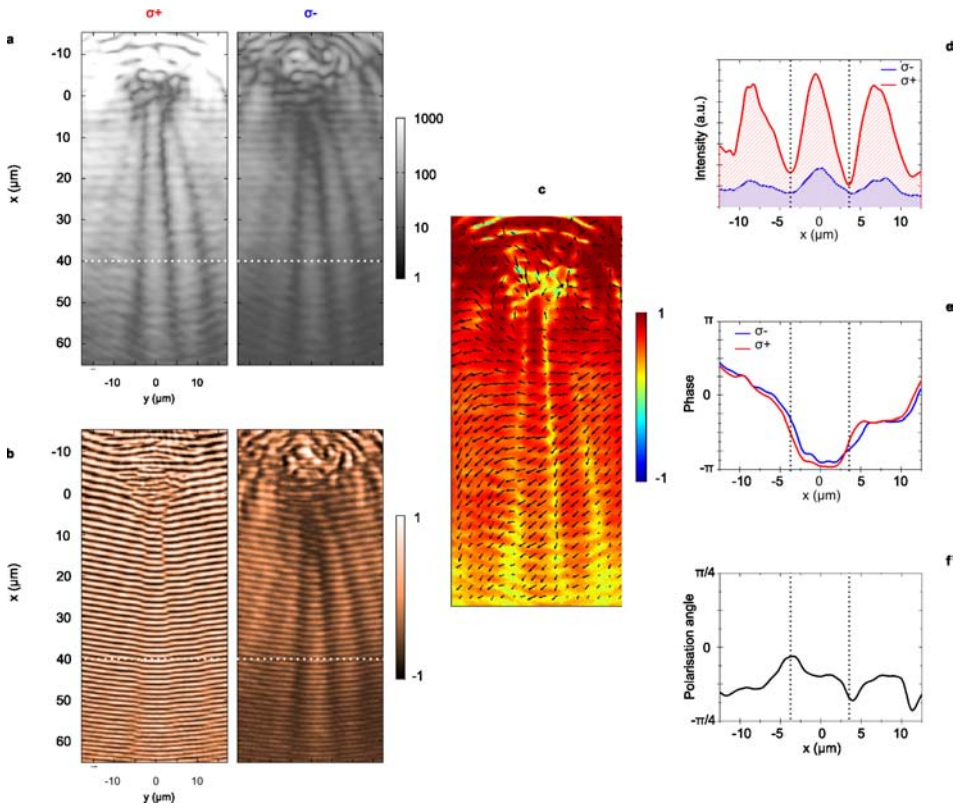

Figure 2.28: Experimental results using a right circularly polarized (σ_+) pump. No half-soliton acceleration is visible (possible) in that case.

2.4 Sonic black holes and wormholes in spinor polariton condensates

In this part we propose the polariton BEC as an excellent candidate for the construction of 1D and 2D sonic black holes thanks to the finite lifetime of the particles [59]. While this part looks at first sight to be disconnected from the previous one, it is actually based on the spinor properties of the polariton condensate and its topological excitations. Once again, the spinor nature of the BEC allows to expect even more interesting features. Indeed, mapping the two spin components to two parallel universes allows the construction of wormholes or Einstein-Rosen bridges [60] connecting these universes. To test the wormhole structure one needs to study the propagation of a signal through it. This signal has to be intrinsically stable and to initially exist in only one of the two universes. Here half-integer topological defects come into play: a half-soliton appears perfectly suitable for this task. We will describe inter- and intra-universe wormholes, the latter offering the possibility of a "faster than sound" travel.

It happens quite often in physics that striking similarities are found between systems, which from the first glance have absolutely nothing in common. Sometimes,

such similarities can be exploited to perform laboratory studies on accessible objects similar to inaccessible ones. One of the most recent examples is that of Klein tunneling in graphene [61]: The quasi-particles in a solid-state object obey the same mathematical equations as very high-energy relativistic particles. Astrophysics allows even less laboratory studies than high-energy physics: scientists are restrained to the objects in the universe proposed by the Nature, these are studied from very far and the consideration of gravitational fields requires to manipulate very large masses. Thus, having a desktop version of a supermassive black hole [62] would be even more useful. Once again, the physics of the small comes to the aid of the physics of the large. The analogy between the equations describing the excitations of a Bose-Einstein condensate and the metrics of the curved space-time has been noticed about a decade ago [63]. Since then, the scientists have managed to experimentally observe the event horizons in atomic BECs [64].

However, such atomic condensates are still a bit far from being a convenient laboratory tool, because they require ultra-low temperatures for their formation, the measurements of the distributions inside the condensates are relatively complex to carry out and the construction of the event horizon is provided by artificial external potentials. Here the solid-state physics comes into play with the exciton-polariton condensates. The finite lifetime of polaritons in the range of tens of picoseconds turns into an important advantage, simplifying all measurements, because the decay of the condensate means the emission of photons from the cavity, and the distribution of emitted photons gives direct information on the polariton distribution function, on their dispersion and spatial evolution. Finally, the spin structure of polaritons [see Sec.1.4] implies possible new effects due to the vectorial nature of the condensates. These particularities favor polaritons with respect to other systems proposed for the simulation of black holes, including the optical ones based on metamaterials [65, 66, 67].

2.4.1 Theoretical description of sonic black holes

It has been understood quite a long time ago in hydrodynamics, that an event horizon can appear if the flow speed increases and becomes larger than the speed of sound [68]. Indeed, the excitations in the flowing medium propagate with the speed of sound (in the linear approximation, that is, long-wavelength limit), and therefore in the laboratory frame they are unable to go against the flow if its speed is too high. A great research effort in this domain has recently culminated with the observation of stimulated Hawking emission in a water tank [69]. A most widespread example of a structure exhibiting an event horizon is the de Laval nozzle [see Fig.2.29] used in jet engines. In order to have the exhaust gas velocity higher than the limit allowed by the Bernoulli's principle, the gas is accelerated from subsonic to supersonic speed. No sound waves are able to propagate backwards in the supersonic part of the flow, which is therefore separated from the subsonic part by what can be called an event horizon.

The work of W. Unruh [68] has laid down the foundations for this domain of

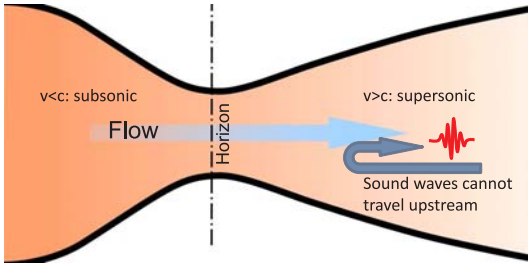

Figure 2.29: Scheme of a de Laval nozzle.

research by showing how the hydrodynamic equations can be rewritten using the metrics to obtain exactly the Schwarzschild's metric of a black hole (close to its horizon). Starting from the equations of motion for an irrotational fluid:

$$\boldsymbol{\nabla} \times \mathbf{v} = 0 \tag{2.69}$$

$$n\left(\partial \mathbf{v}/\partial t + (\mathbf{v}\cdot\boldsymbol{\nabla})\,\mathbf{v}\right) = -\boldsymbol{\nabla} p - n\boldsymbol{\nabla}\Phi \tag{2.70}$$

$$\partial n/\partial t + \boldsymbol{\nabla}\cdot(n\mathbf{v}) = 0 \tag{2.71}$$

and considering weak perturbations about a stationary solution, one can obtain the equations for a massless scalar field with a metric

$$ds^2 = \frac{n_0}{c\left(n_0\right)}\left[\left(c^2\left(n_0\right) - \mathbf{v}_0\cdot\mathbf{v}_0\right)dt^2 + 2dt\mathbf{v}_0\cdot d\mathbf{r} - d\mathbf{r}\cdot d\mathbf{r}\right] \tag{2.72}$$

where $c_0 = g'\ln\left(n_0\right)$ is the local velocity of sound. For a spherically symmetric converging flow in the region where the speed of the flow becomes equal to the sound velocity, this metric takes exactly the form of the Schwarzschild's metric of a black hole at the horizon:

$$ds^2 \approx \frac{n_0\left(R\right)}{c}\left(2c\alpha\left(r-R\right)d\tau^2 - \frac{dr^2}{2\alpha\left(r-R\right)}\right) \tag{2.73}$$

where α is the first coefficient of the development of $v(r)$ around R, that is $\alpha = \partial v_r^0/\partial r\big|_{r=R}$.

The seminal work of Unruh considered an arbitrary irrotational fluid, defined by $\mathbf{v} = \hbar/m\boldsymbol{\nabla}\theta$, without detailing its nature. An application for BEC has logically come 20 years later [63], where θ was interpreted as the phase of the order parameter of the condensate and

$$\Psi\left(\mathbf{r},t\right) = \sqrt{n\left(\mathbf{r}\right)}e^{i\theta(\mathbf{r})}e^{-i\mu t/\hbar} \tag{2.74}$$

In order to discuss the hydrodynamic approximation for BEC let us rewrite the stationary Gross-Pitaevskii equation using the phase-density representation of the wavefunction:

$$\hbar\frac{\partial\theta}{\partial t} + \left(\frac{1}{2}m\mathbf{v}_s^2 + V_{ext} + \alpha n - \frac{\hbar^2}{2m\sqrt{n}}\nabla^2\sqrt{n}\right) = 0 \tag{2.75}$$

The last term in this equation is the quantum pressure term, which scales as R^{-2} and becomes negligible if the typical density variations occur at scales much larger

than the characteristic length ξ. When quantum pressure is neglected, one obtains what is called the Thomas-Fermi limit or hydrodynamic approximation, because the equation of motion for the condensate becomes simply the Euler's equation for potential flow of a nonviscous liquid, as discussed in chapter 1.

Considering the density and phase perturbations n' and θ' for the BEC (as in the general case of Unruh [68]) and performing the linearization, one obtains the following first-order equation for the phase:

$$\partial_\mu \left(\sqrt{-g} g^{\mu\nu} \partial_\nu \theta'\right) = 0 \tag{2.76}$$

with the metric g given by

$$g_{\mu\nu} = \begin{pmatrix} -\left(c^2 - v^2\right) & -v^T \\ -v & 1 \end{pmatrix} \tag{2.77}$$

As one can see, the condition $v = c$ imposes a diagonal element to be zero, which defines the position of the event horizon.

2.4.2 Hawking emission

The most important goal of the research activity centered on the acoustic black holes has been to verify the famous S. Hawking's prediction [70], which described cosmological black holes and showed that vacuum fluctuations producing particle/antiparticle pairs would behave in a singular way at the event horizon position. The huge gravitational fields that reign past the event horizon would absorb one of the photons towards the black hole which it could not escape, while the other one would propagate away from the horizon. The consequence of such events would lead to a loss of mass or evaporation of the black hole with time until its explosion. However, no detection of such Hawking photons was reported so far, because anyway they can hardly be extracted from the warmer cosmic background. Consequently, a quantitative study of such a phenomenon required model systems [71] and among them are the very promising BECs [63, 72].

The small amplitude excitations (bogolons) in a BEC, can also exhibit linear dispersion in the long-wavelength limit, defining the speed of sound. The finite lifetime of polaritons provides a natural way of varying the speed of sound. We know that propagating condensate can be injected locally via non-resonant [73] or resonant [50] pumping. Its density is bound to decrease with the distance from the pumping spot, and c will therefore decrease as well, whereas the propagation speed will remain constant or may even increase, if the condensate is accelerated by a potential ramp (for example, by its own self-interactions). At some point the two speeds become equal, defining the position of the event horizon of the black hole.

The spinor polariton condensate is described by the set of equations (2.63,2.64). Here $D(x,t)$ becomes a total potential that can encompass: disorder in the microcavity, potential barriers, and time dependent potentials to impose excitations in the system. An extra $\mathbf{k}$-independent polarization coupling (conversion) term $i\hbar\partial_t\phi_\pm = H_0(\mathbf{r},t)\phi_\mp$ should be added to photonic parts to account for the extra

longitudinal-transverse polarization splitting that occurs in 1D wires at $\mathbf{k} = \mathbf{0}$ [41], and which can vary along the wire.

2.4.3 Sonic holes and wormholes in polariton condensates

2.4.3.1 1D sonic holes

First, let us consider a 1D configuration neglecting the spin degree of freedom. The polariton flow is resonantly and locally injected by a pumping laser located close to $x = 0$ on the figure 2.30(a). The medium is assumed to exhibit small structural disorder mainly due to the etching of the 1D wire cavities. It is modeled by a random series of delta-peaks separated by 1 μm on average. All results shown in Fig.2.30 are averaged over 100 disorder realizations. The Fig.2.30(a) shows the polariton density $n_\phi(x)$, the visible decay is mainly due to the finite lifetime of polaritons. The speed of the sound $c(x)$ decreases together with the density. On contrary, the speed of the flow $v(x)$ is increasing because of the self-interactions within the condensate. In the left part, the flow is subsonic and cannot be scattered by the disorder (superfluid). In the right part, the flow is supersonic. The exponential decay is induced not only by the life time but also because of the Anderson like-localization in the disorder. The two regions are separated by an event horizon at $v = c$. In the supersonic region no excitation can propagate towards the horizon. The generation of Hawking emission on the horizon is demonstrated in the Fig.2.30(b). Indeed, as recently proposed in Refs.[74, 75], emission of Hawking phonons means correlated density perturbations propagating on both sides of the horizon. Hawking emission can therefore be detected using the following second order density-density correlation matrix:

$$g^{(2)}\left(x, x'\right) = \frac{\overline{n\left(x\right) n\left(x'\right)}}{\overline{n}\left(x\right)\overline{n}\left(x'\right)} \tag{2.78}$$

This matrix is in averaged on many realization of disorder, and is shown at in Fig.2.30(b). Indeed, as expected, characteristic "Hawking tongues", indicating positive correlations (because the emission is stimulated by disorder in our case), are extending from the horizon position, marked by the red dotted lines. We underline that there is no need to introduce quantum fluctuations to seed Hawking emission thanks to the presence of the disorder potential, interactions and to the finite lifetime which broaden the states in momentum and frequency.

2.4.3.2 Closed 2D sonic holes

The finite lifetime of polaritons allows to organize persistent flows, as shown in Refs.[11, 50, 73] for the cases of quasi-resonant or non-resonant pumping. This particular property makes the formation of closed event horizon in 2D possible. This is much more complicated with atomic condensates, where only 1D configurations have been considered [64]. With polaritons, one needs to pump in a regime allowing the superfluidity to arise, around a large-scale defect in the microcavity mirrors, possessing a lower quality factor. Polariton-polariton repulsive interactions will

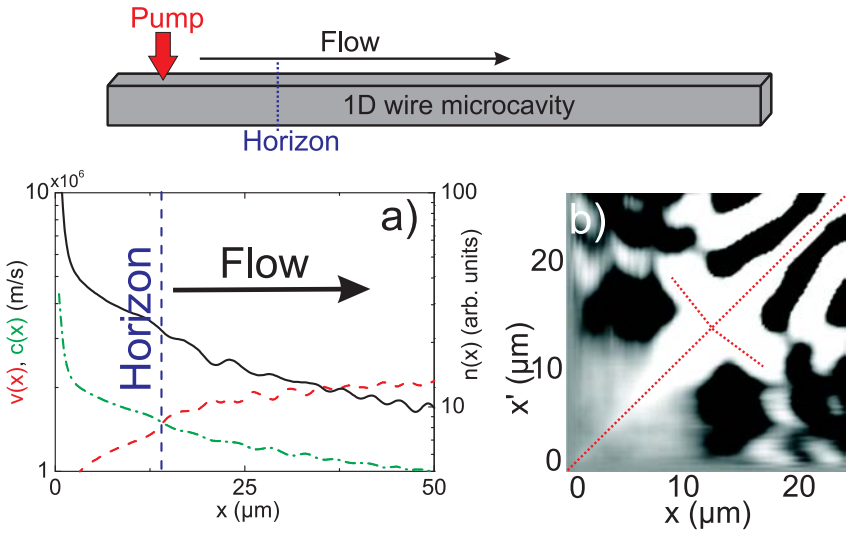

Figure 2.30: (a) Propagation of a polariton condensate in 1D: density (black solid line), flow speed (red dashed line), sound speed (green dash-dotted line). The horizon is indicated by a blue dashed vertical line. (b) Density-density correlation matrix $g^{(2)}(x, x')$ at $t = 200$ ps. Dotted red lines are a guide for the eyes, indicating the Hawking tongues (positive correlations) extending from the main diagonal.

then create a persistent flow converging into the defect region, where the density is always lower due to the shorter lifetime. The boundary between the superfluid and supersonic regions forms a circular event horizon.

The figure 2.31 shows the results of a realistic 2D simulation with pulsed spatially homogeneous pumping. The photon density n_ϕ at the time $t = 8$ ps is plotted as a function of coordinates [panel (a)]. The defect region with a shorter lifetime is located at the origin $[(x, y) = (0, 0)]$, while the disorder is neglected. The density inside the defect region decreases faster than outside, and the repulsive interactions make polaritons propagate towards the center of the figure. The event horizon at that time is marked with a dashed blue line. The Hawking radiation is in that case seeded by the non-equilibrium spatial distribution that populates excited states. It can be observed on the panel (b) as density waves propagating inwards inside and outwards outside the horizon (red arrows).

2.4.3.3 Wormholes analogue in the spinor polariton condensate

If a single scalar condensate is a model of a universe which might contain black holes, it seems natural to map two spinor components to two different universes. They can be completely decoupled from each other if there are no interactions between the particles of different spins. Adding a magnetic field can provide a coupling between these two universes, making possible simulation of wormholes [77].

In astrophysics, inter-universe wormholes are the pairs of singularities located in different universes and connected together. Using such wormhole, one could pass

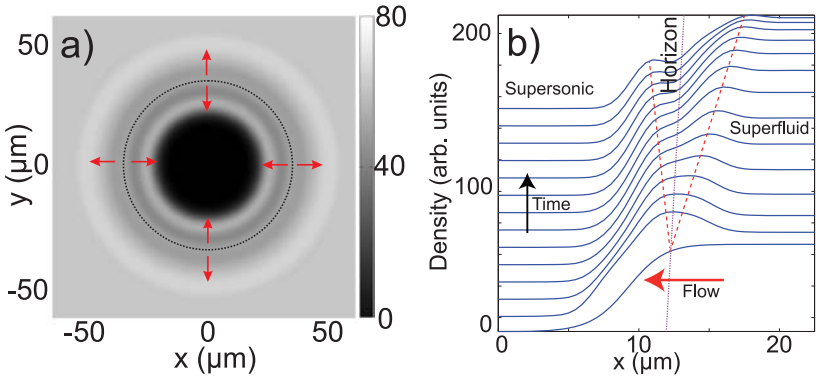

Figure 2.31: (a) 2D black hole around a defect (dark region) in a polariton condensate. The dashed red circle shows the event horizon, and red arrows point the directions of the propagation of the Hawking radiation on both sides of the horizon. (b) Waterfall density plot at different times. Propagating Hawking phonons are marked by the red dashed lines.

from one universe to the other. A more interesting situation, when both holes connected together are in the same universe, is called an intra-universe wormhole. Such wormhole can connect two distant regions of space with a tunnel much shorter than the distance between the two, which might allow faster-than-light travel [78].

Inter-universe wormhole

Let us start with the simpler case of an inter-Universe wormhole. We consider a 1D quantum wire, as in Ref.[73] and [Sec.2.2.3]. The idea is to first create a closed black hole bordered by two event horizons and to connect the latter with a white hole in the other spin component using a local effective magnetic field H_{LT}, induced by the TE-TM splitting at $\mathbf{k} = \mathbf{0}$ [see Sec.3.3.2.1]. H_{LT} can be controlled by varying the width of the wire [41], or by applying an electric field [79].

In general relativity, a key concept is the propagation of signals, whose speed can never exceed that of light in the vacuum. The propagation of phonon wavepackets across the event horizons in BECs has already been studied, for example in Refs.[74, 76]. In our model system, we need a "signal" that appears in only one spin component (e.g. σ_+, representing our universe), that is stable and able to propagate. The perfect candidate for this task appears to be the 1D half-soliton. As already mentioned in Secs.1.2.5.1,2.2, solitons have a lot of properties similar to those of relativistic particles [55, 42], except that their mass is negative (because they are actually holes rather than particles): $m_s = m_0/\sqrt{1 - v_s^2/c^2}$; their size is given by $l_s = \xi/\sqrt{1 - v_s^2/c^2}$ where v_s is their velocity. For attractive interactions, the mass can of course be positive. Pairs of half-solitons are created here thanks to a short time-dependent pulsed potential acting on a single spin component

$$U(x,t) = U_0 e^{-(x-x_0)^2/w_x^2} e^{-(t-t_0)^2/\tau^2} \tag{2.79}$$

The Gauss-Laguerre imprinting [see Sec.2.2.3.1] could be used as well. However, as the speed of a soliton is related to its depth by $v = cn(0)/n_\infty$ where $n(0)$ is

the density at its center and n_∞ in its surrounding [55], we need a weak enough perturbation to excite shallow solitons that will be able to travel at speeds close to c in both spin components (marked as c_1, c_2 below).

The figure 2.32 shows the scheme of a numerical experiment with a single wormhole [panel (a)] and the results of the simulations [panels (b), (c)]. A 1D polariton wire is *cw*-pumped by two spatially separated, quasi-resonant, σ_+ polarized lasers allowing the formation of a steady state flow and convenient density distribution sketched on the panel (a). Polaritons flow away from the pumping regions and a closed black hole is formed in the middle. A local effective magnetic field converting σ_+ to σ_- is present in the black hole region. The σ_- density therefore shows a maximum expelling excitations outside from the central region which corresponds to the formation of a white hole, in which no excitation can enter, in the σ_- universe.

After the steady state is obtained, a weak pulsed potential is applied in the σ_+-component [panel (b)] at $t = 5$ ps at the left of the left horizon, creating propagating half-solitons. The continuity of the phase imposes the creation of solitons by pairs. One of these propagates freely to the left, whereas the other enters the black hole and remains partly guided inside. The effective magnetic field converts a part of this soliton into the other spin component: σ_- [panel (c)]. The soliton is then able to cross the horizon of the white hole, propagating away together with the flowing condensate. One can also see that short-wavelength (corresponding to nonlinear parts of the spectrum) perturbations are still able to cross the horizon of the black hole in any direction. The holes possess an internal structure. The speed of the flow is zero at the center and the black hole is in fact composed by two narrower black holes surrounding a subsonic region.

Intra-universe wormhole

In this last part, we will discuss a scheme for an intra-universe wormhole allowing the transfer of a HS with an apparent velocity faster than the speed of sound of its original universe. Such intra-universe wormhole is based on two inter-universe wormholes similar to the the ones previously described, but connecting the Universes in opposite directions. The scheme in the figure 2.33(a) shows the proposed $\sigma_\pm$ density profiles with the two wormholes. Dashed line indicates the propagation of a half-soliton. A σ_+ half-soliton is generated at the left. It enters in the σ_+ black hole where it is converted in a σ_- soliton, which is ejected by the white hole part of the wormhole. Then, it travels in the σ_- component between the two wormholes with a velocity close to c_2. It then reaches the second wormhole, which is a black hole in the σ_- component, where it is captured and converted to a σ_+ soliton ejected from the white hole. The average velocity of this soliton is close to c_2 which can be larger than c_1, the speed of sound in the σ_+ universe. The results of corresponding simulations are presented in panels (b) and (c).

The pumping is *cw* quasi-resonant with inhomogeneous elliptical polarization, providing the density profiles close to Fig.2.33(a). A pair of half-solitons is created at $t = 5$ ps in the σ_+-component at $x = 0$ [panel (b)]. The "reference" half-soliton propagates to the left with the speed limited by c_1 and arrives to the edge at around $t = 30$ ps. The half-soliton falling inside the black hole converts into the

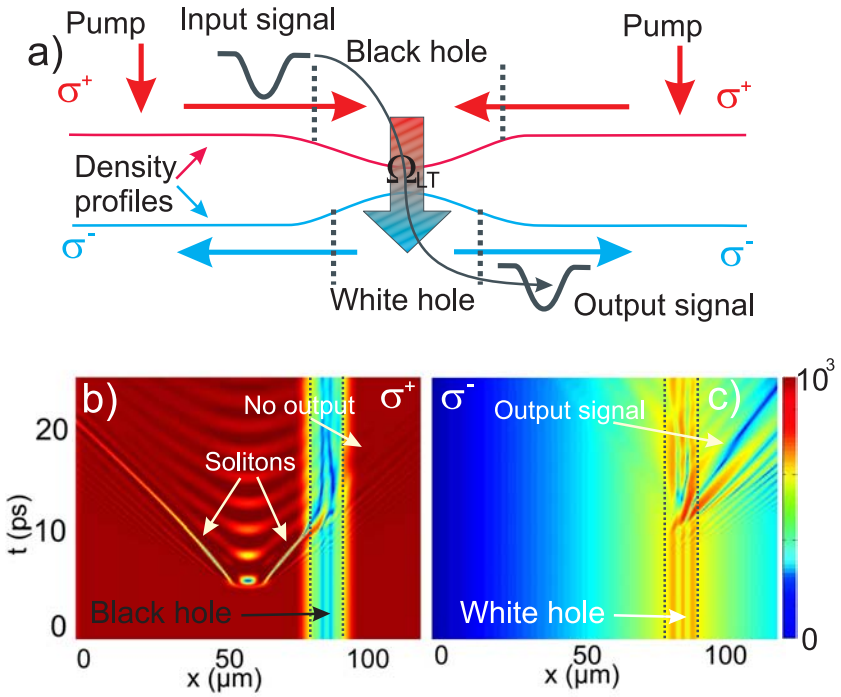

Figure 2.32: (a) Scheme of a wormhole between the σ_+ (red) and σ_- (blue) universes. Arrows show the directions of the flow in the two components. Dashed lines mark the event horizons in both components. (b) Results of numerical simulation: $n_\phi(x,t)$ for both spin components with black dotted lines showing the boundaries of the black/white holes and white arrows indicating the propagation of signals.

σ_- component, gets out of the white hole in σ_- [panel (c)] and propagates with a higher speed, limited by $c_2 > c_1$. This half-soliton arrives to the second wormhole and is converted back into the σ_+-component, appearing there at $t = 25$ ps (marked by the dashed green circle). The two events are marked with black horizontal lines, and the time difference between them is $\Delta t \approx 5$ ps.

2.4.3.4 Conclusions

Spinor polariton condensates, being relatively easy to produce and manipulate, can be used as well for the simulation of astrophysical objects, such as black holes and wormholes. A 2D black hole with a closed event horizon can be simulated. Effective magnetic fields, well known as the cause of non-trivial spin dynamics of polaritons, can be used to organize the coupling between the black holes and white holes in the two spin components. Half-integer topological defects allow to test the propagation of signals through the wormhole structures. A system of two separated and complementary wormholes allows one to organize "faster-than-sound" signal propagation. This section demonstrates the polyvalence of the polariton system and the new trends that are now opened by this fascinating research field.

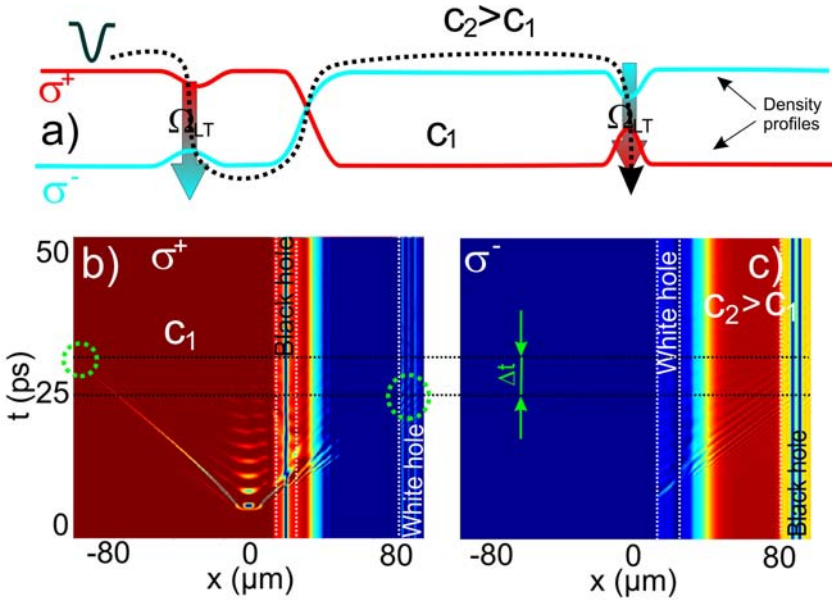

Figure 2.33: Faster-than-sound signal propagation with two wormholes. (a) Scheme with two wormholes showing density profiles; (b) σ_+ density; (c)σ_- density. Dashed horizontal lines mark the arrival of the two signals (green dashed circles), with Δt the time difference between them.

2.5 Electric generation of vortices in a polariton superfluid

At this stage, we know that vortices can be excited in a polariton fluid via phase imprinting techniques using a Gauss-Laguerre beam or in the flowing condensate past an obstacle. The first option allows the generation of almost static vortices (if only integer vortices are considered) and the second one nucleates "vortex streets" propagating along deterministic trajectories. None of these proposals consequently allows an on-demand generation of vortices combined with the possibility of controlling their trajectory. We propose here a real device devoted to study the vortex physics allowing to generate vortex-antivortex pairs at will and to control their propagation towards a real vortex circuit [81].

In more details, we propose another strategy for the generation of vortices in the polariton superfluid. Contrary to previous proposals, the vortices are not excited optically but electrically. The idea is based on the possibility of creating dynamical confining potentials for the particles, by deposition of metallic contacts on top of the sample and by the application of short voltage impulses to them. We will show that the use of a horseshoe-shaped contact [shown in Fig. 1] leads to the generation and propagation of vortex-antivortex pairs (VAPs). Such a structure acts as a "vortex gun" triggered by an applied external potential. On the basis of this main element, we will propose schemes towards the guiding and unbinding of VAPs provided by additional metallic gates. Eventually, we will discuss another simple configuration

allowing the nucleation of single vortices. Eventually, capitalizing on our previous knowledge 2.3.1, we will see how in addition to integer vortex dipoles, the device could allow the generation of half-vortices in the system.

2.5.1 The system and the model

We shall consider a microcavity, assumed to have a high quality factor and characterized by weak intrinsic disorder (e.g. GaAs based) with metallic mesas deposited on its top. A voltage can be applied to the metal via integrated electric contacts [see Fig.2.34]. We assume that the polariton condensate is non-resonantly populated by means of a far detuned *cw*-homogeneous pump over the whole sample. This is a crucial point, as a resonant injection scheme would continually impose, at any time, a well defined phase to the condensate preventing phase singularities (vortices) from appearing. The polariton population n can remain constant and fix a chemical potential for the system (since the pump is homogeneous), provided that a quasi-equilibrium regime between gains – from excitons that relax towards the ground state – and losses – from photons escaping through the Bragg mirrors – is achieved.

The role of the metallic contacts on top of the sample is twofold: First, at the interface between a metal and dielectric Bragg reflectors (DBRs), Tamm plasmon-polariton states can appear. Such states lead to a local *redshift* of the lower polariton mode and thus a time-independent potential *trap* is created in the region where the metal is deposited [82, 83]. We note that this configuration is different from the one involving surface states of a Shottky-like junction resulting in a *blueshift* of the polariton modes [84, 85]. The depth of the trap depends on the type of metal and on the thickness of the layer and values of several meVs are easily achievable. Second, the application of a voltage to the metallic contacts gives birth to an additional *redshift* of the polariton energy due to the excitonic Stark effect[86, 87]. The value of the shift depends of course on the applied voltage and values of the corresponding electric field in the range of 0-50 kV/cm result in a potential U_V lying between -2 and 0 meV. Besides, the abrupt appearance of a potential well can strongly perturb the condensate locally in the region of the contacts. Such a perturbation results in the excitation of a nonlinear density wave similar to a ring soliton [88] and possibly of dispersive shock waves in the condensate [89]. Vortices can emerge, when the solitonic wave expands above some critical velocity producing a vortex necklace [88] or when two nonlinear waves collide and interfere. This latter situation can be realized using two facing electric contacts or just a single one with the proper geometry as we will see.

For the description of the dynamics of the system, we have first used the standard Gross-Pitaevskii equation for the macroscopic wavefunction of the condensate $\psi(\mathbf{r},t)$:

$$\begin{aligned} i\hbar\frac{\partial\psi(\mathbf{r},t)}{\partial t} = & - \frac{\hbar^2}{2m^*}\Delta\psi(\mathbf{r},t) + \alpha|\psi(\mathbf{r},t)|^2\psi(\mathbf{r},t) \\ & + \left[U_0(\mathbf{r}) + U_V(\mathbf{r},t)\right]\psi(\mathbf{r},t) \end{aligned} \tag{2.80}$$

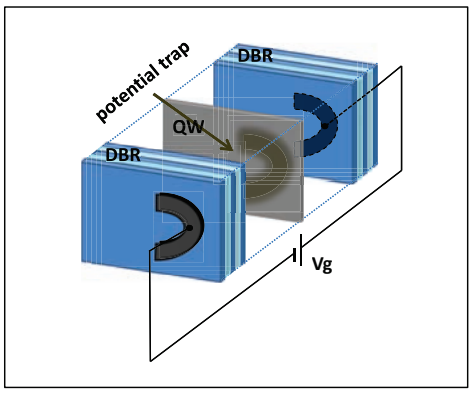

Figure 2.34: The vortex gun: A microcavity with a horseshoe-shaped metallic contact deposited on top of its DBRs. The metal creates a local potential trap for polaritons due to the formation of Tamm-polariton solitons. The application of a time-dependent voltage V_g is able to increase temporally the depth of the trap towards the generation of VAPs.

$U_0(\mathbf{r})$ is a potential well of the amplitude of 2 meV created by the metallic contacts and appearing due to the formation of Tamm plasmon-polaritons. $U_V(\mathbf{r},t)$ is an extra time dependent potential accounting for the exciton Stark shift generated by the applied voltages. $m^* = 5 \times 10^{-5} m_0$ (m_0 is the electron mass) is the polariton effective mass. α is the polariton-polariton interaction constant. We start here by neglecting the spin degree of freedom of polaritons assuming that the polariton condensate is linearly polarized and that both spin components are fully equivalent.

2.5.2 The vortex gun

We start our description with the configuration shown at Fig.2.34. A metallic contact in the form of a horseshoe (half a ring) is deposited on top of DBRs. It has an inner radius of 5 μm (roughly 2ξ) and outer radius of 10 μm. We apply to the contacts a short 5 ps long Gaussian voltage impulse, producing a time-dependent redshift of the amplitude of 1.5 meV associated with the potential well U_V. It results in a local non-adiabatic perturbation of the condensate which generates a non-cylindrically symmetric solitonic density wave propagating outwards from the contact. In the inner part of the horseshoe the breakdown of the meeting wavefronts occurs, allowing the nucleation a VAP propagating along the axis of symmetry of the system, as shown in Fig.2.35. The vortices are evidenced by: the vanishing density at their core visible in the colormap, the characteristic velocity field tangent to them in the panel (b) and the winding of the phase in anticlockwise (vortex $l = +1$) and clockwise (antivortex $l = -1$) directions around their core in the panel (c). The distance separating the vortex and antivortex in the pair related to their speed of propagation depends on the size of the contact, on the applied voltage and on the concentration of the polariton superfluid (here on average $\overline{n} = 2.5 \times 10^9 \mathrm{cm}^{-2}$).

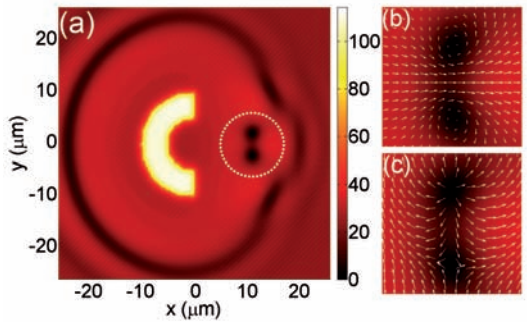

Figure 2.35: VAP nucleated by the application of a voltage impulse of amplitude -1.5 meV and duration 5 ps to the horseshoe contact. (a) Density $n(x, y)$ (μm^{-2}) of the condensate, 20 ps after the pulse. One clearly sees the solitonic density wave propagating away from the contact (dark regions) and the single VAP (dashed white circle). (b) Velocity field of the condensate and (c) phase vector field $(\cos(\theta), \sin(\theta))$.

We have therefore proposed a system able to generate VAPs on demand propagating along straight lines: a "vortex gun". Moreover, the modification of the excitation conditions allows the creation of more than a single VAP. For example if a periodic sequence of voltage impulses is applied to the horseshoe, the generation of series of VAPs is observed.

To check the validity of our model based on the equilibrium Gross-Pitaevskii equation [see eq.(2.80)], we have performed numerical simulations using a more accurate model: namely a set of modified Ginzburg-Landau equations. Indeed, to take into account the nonparabolicity of the polariton dispersion, we have separated the photonic field $\phi(\mathbf{r}, t)$ from the excitonic one $\chi(\mathbf{r}, t)$ that are coupled via the light matter interaction associated with the Rabi energy $\Omega_R = 10$ meV. We have taken into account the particles lifetime: $\tau_\phi = 15$ ps and $\tau_\chi = 400$ ps. To model the nonresonant pumping scheme, we assumed that the exciton relaxation towards the ground state is embodied by a reservoir which evolves along a simple rate equation [eq.(2.82)] similarly to the proposal of Ref.[92]. $\Gamma_R = 5/\tau_\chi$ is the scattering rate between reservoir excitons and condensate polaritons. The reservoir filling is provided by the source term (pump laser) $P_R = 50/\tau_R$ where $\tau_R = 100$ ps is the lifetime of the particles in the reservoir. The stimulation of the condensate population is seeded by a short low amplitude probe pulse tuned at the energy of the lower polariton

branch at $\mathbf{k} = \mathbf{0}$: $\omega_S = -\hbar\Omega_R/2$. The corresponding set of equations reads:

$$\begin{aligned} i\hbar\frac{\partial\phi}{\partial t} &= -\frac{\hbar^2}{2m_\phi}\Delta\phi + \frac{\Omega_R}{2}\chi \\ &+ P_S e^{-\left(\frac{t-t_S}{\Delta t_S}\right)^2} e^{-i\omega_S t} - \frac{i\hbar}{2\tau_\phi}\phi \qquad (2.81) \\ i\hbar\frac{\partial\chi}{\partial t} &= -\frac{\hbar^2}{2m_\chi}\Delta\chi + \frac{\Omega_R}{2}\phi + \alpha\left(|\chi|^2 + n_R\right)\chi \\ &+ \left(U_0 + U_V\right)\chi - \frac{i\hbar}{2\tau_\chi}\chi + i\hbar\frac{\Gamma_R}{2}n_R\chi \qquad (2.82) \\ \frac{\partial n_R}{\partial t} &= P_R - \frac{n_R}{\tau_R} - \Gamma_R|\chi|^2 n_R \qquad (2.83) \end{aligned}$$

In this framework, we present the result of a numerical simulation in the figure 2.36 showing the vortex gun configuration (see captions). As one can see, the results obtained remain very similar to the one obtained using the simplified approach [to be compared with the Fig.2.35]. The main difference is that the results are less smooth and therefore less instructive due to the instabilities, intrinsic to the model, that develop at later times [visible in the density landscape of the panel (e)]. We therefore assert that the simple model is sufficient to realistically describe the vortex nucleation and the following guiding processes.

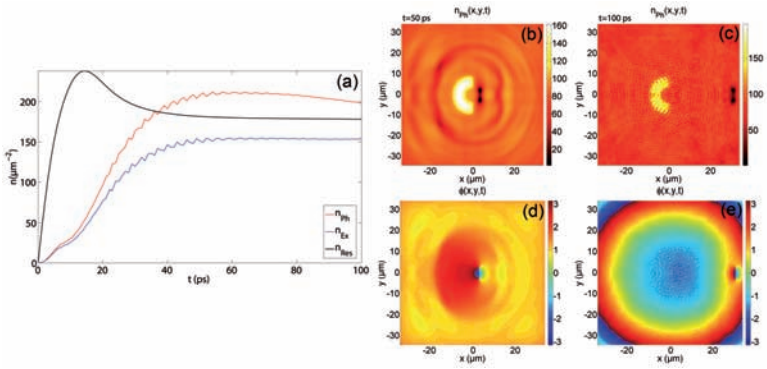

Figure 2.36: Simulations based on the modified Ginzburg Landau model. VAP nucleated by the application of a voltage impulse associated with a gaussian potential of amplitude −1.5 meV and duration 5 ps to the horseshoe contact. (a) Total densities of: the photonic component (red line), the excitonic component (blue line) and the reservoir (black line) showing the condensate being populated by the reservoir. (b) Density of the photonic component (emission out of the microcavity) 5 ps after the arrival of the impulse revealing the vortex anti-vortex pair. (c) Propagation of the VAP away from the horseshoe (gun). (d) and (e) show the phase of the photonic component associated with (b) and (c) to evidence its characteristic winding around the vortices.

2.5.3 Vortex guiding

The motion of vortices is affected by flow directions and density gradients [92]. Indeed, as the metal creates a potential well for polaritons, it makes the concentration of the condensate under the contacts greater than in the surrounding area [it is clearly visible e.g. in Fig.2.35(a)]. We note that, even if photoabsorption from the nonresonant pump laser can be blocked by the presence of the metal, the polariton-polariton repulsion would allow an efficient filling occurring much faster than the polariton lifetime. The elastic energy of singly quantized vortices ($l = 1$) is proportional to the condensate density [93]:

$$E_{el} = \pi\hbar^2 n/m^*, \tag{2.84}$$

and thus metallic layers acts as a potential barrier for vortices. This opens the way towards the control the VAPs trajectories by means of extra gates flanking the vortex gun. In this context, we propose first to add a pair of circular electrodes as shown in Fig.2.37. Owing to the symmetry of our structure, no deviation occurs until a voltage is applied to one of the two electrodes. On the other hand, if a 15 ps long Gaussian voltage pulse is imposed to one of them, the VAP deviates from its straight trajectory as it is shown at Fig.2.37 . One could of course envisage as well a configuration with a single electrode that would deviate the vortex in a constant deterministic way. No applied voltage would be obviously required in that case.

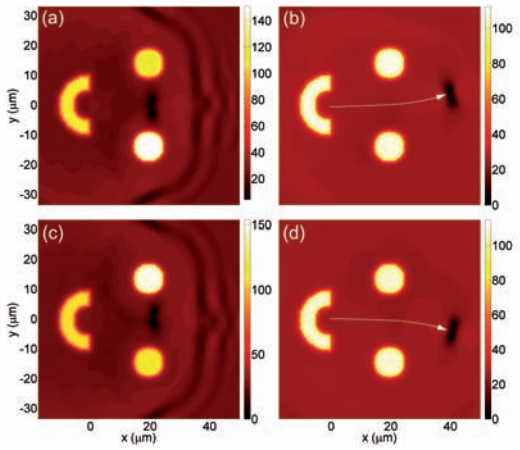

Figure 2.37: Control of the VAP trajectory by a pair of circular gates. Panels (a)-(b) and (c)-(d) show the density of the polariton superfluid in real space 30 ps and 55 ps after the VAP generation respectively. The upper (lower) panels correspond to a voltage applied to the lower (upper) mesa and thus to an upward (downward) deviation of the VAP. The corresponding trajectories are marked by the white dashed arrows.

Capitalizing on the previous results, we can now envisage a scheme for a vortex guide. Indeed, one can deposit two metallic stripes next to the vortex gun. The

application of a sinusoidal voltage to the upper and lower stripes leads to the oscillation of the VAP between them, as it is illustrated in the inset of Fig.2.38 [see also Ref.[90] for a movie]. It is important that the voltage applied to the gates are weak enough not to excite parasite vortices in the system.

Vortex guides could be connected to each other and constitute a basis for varieties of logic elements. For example we can propose a design for a vortex switch shown in Fig.2.38: VAPs are created by the vortex gun and move along the vortex guide E which splits into two outgoing leads L_1 and L_2. The metallic gates G_1 and G_2 allow a controllable redistribution of the vortices between the two paths namely: The application of the voltage impulse to the gate G_1 (G_2) sends the VAP to the outgoing lead L_1 (L_2).

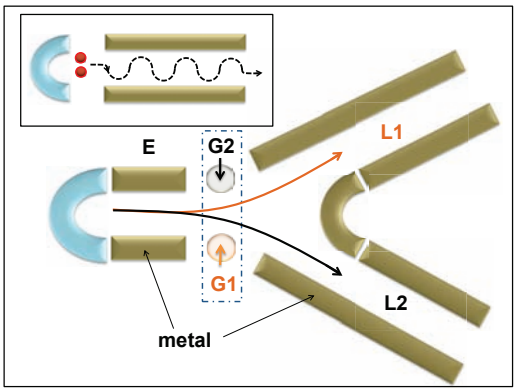

Figure 2.38: Inset: Vortex guide consisting of a vortex gun and two metallic stripes. Periodic application of voltage to upper and lower stripes makes VAP to oscillate between them. Main plot: vortex switch composed of a vortex gun, a vortex guide E, two outgoing leads L_1 and L_2 and controlling gate electrodes G_1 and G_2. The application of the electric impulse to gates G_1 or G_2 sends VAPs to leads L_1 or L_2 respectively as marked by black and orange arrows.

2.5.4 Vortex splitting

VAPs can be unbound (destroyed) by means of a wedged metallic mesa, as shown in Fig.2.39. When a VAP reaches a tip of the wedge, it splits into two separated excitations traveling along upper and lower sides of the triangle, preserving their shape [see Ref.[90] for a movie]. The analysis of the phase field around the upper excitations shown in the panel (e), allows to assert that they are neither individual vortices nor new VAPs. Indeed no phase singularity is visible but rather a local $\pi/2$ phase shift going through the density dip characteristic for a gray soliton or more precisely a rarefaction pulse[94].

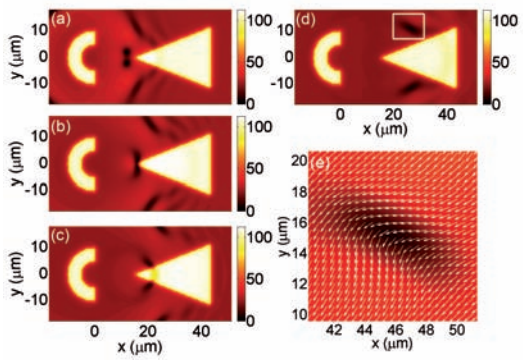

Figure 2.39: Scattering of a VAP induced by a metallic wedge. The panels (a)-(d) show the superfluid density at times : 10 ps, 13 ps, 15 ps and 20 ps after VAP creation respectively. The decomposition of a VAP into a pair of pseudo-topological excitations propagating along the upper and lower sides of the triangle is evidenced. The phase vector field of the upper topological excitation highlighted by the white square in (d) is shown in the panel (e). The phase of the condensate is roughly shifted by $\pi/2$ through the low density (dark) region which is characteristic for a gray soliton.

2.5.5 Single vortex generation

So far we have considered the nucleation of propagating vortex dipoles. Now we show, how single static vortices can be excited as well. We propose simply to use a single plate configuration as shown in the Fig.2.40. After the application of a short electric pulse to the plate a "lasso"-soliton is excited similarly to the one observed in Fig.2.35(a). It's shape is imposed by the rectangular geometry of the plate and is consequently strongly non-cylindrical. As a result the soliton is unstable and breaks into two types of excitations [see Fig.2.40(a)]. VAPs appear and are expelled towards the plate where they are merged, by the high density that reigns, generating phonon-like excitations. It reveals by the way another mean of destroying a VAP, if needed, inside a circuit for example. In addition, stable single noninteracting vortices are generated at each edge of the plate as it is shown in Fig.2.40(b) [see Ref.[90] for a movie]. They remain pinned at their nucleation position. In addition, dispersive shock waves induced by the local perturbation are excited in the system [see captions of Fig.2.40(b)].

2.5.6 Half-vortices and half-solitons nucleation

Now let us take the spinor nature of the polariton condensate into consideration separating the two spin components and including the TE-TM splitting. We keep in this part the parabolic approximation for the polariton dispersion. The dynamics

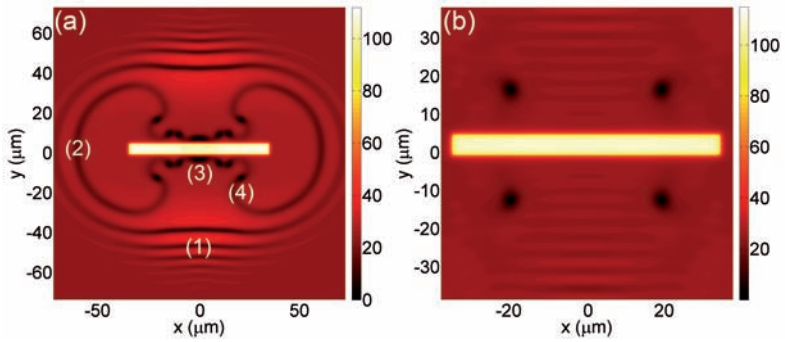

Figure 2.40: Generation of single vortices. (a) Superfluid density 30 ps after the arrival of the pulse which exhibit several features: (1) dispersive shock waves, (2) lasso-soliton broken into (3) VAPs and (4) single vortices. (b) Zoom on the plate region at 80 ps, the VAPs have vanished and 4 single vortices remain stable, locked at there initial positions.

of the system is therefore described by the set

$$\begin{aligned} i\hbar\frac{\partial\psi_+}{\partial t} &= -\frac{\hbar^2}{2m^*}\Delta\psi_+ + \left(\alpha_1|\psi_+|^2+\alpha_2|\psi_-|^2\right)\psi_+ \\ &+ \left[U_0\left(\mathbf{r},t\right)+U_V\left(\mathbf{r},t\right)\right]\psi_+ + \left(\frac{\partial}{\partial y}+i\frac{\partial}{\partial x}\right)^2\psi_- \qquad (2.85) \\ i\hbar\frac{\partial\psi_-}{\partial t} &= -\frac{\hbar^2}{2m^*}\Delta\psi_- + \left(\alpha_1|\psi_-|^2+\alpha_2|\psi_+|^2\right)\psi_- \\ &+ \left[U_0\left(\mathbf{r},t\right)+U_V\left(\mathbf{r},t\right)\right]\psi_- + \left(\frac{\partial}{\partial y}-i\frac{\partial}{\partial x}\right)^2\psi_+ \qquad (2.86) \end{aligned}$$

Here $\alpha_2 = -0.2\alpha_1$. Obviously it seems difficult to affect here *only one* of the two spin components, since the the potential U_0+U_V impacts equivalently on each spin components. We assume here that the condensate forms with a linear polarization e.g along the x axis ($\psi_+^0 = \psi_-^0$). We note that if the TE-TM splitting would be absent, the fluctuations of the linear polarization introducing a slightly elliptic component and therefore a density imbalance between the $\sigma_\pm$ components could be enough to break the polarization symmetry. But, in fact the presence of the TE-TM splitting makes things even simpler. If we remember the mechanism of formation of the oblique half-solitons, the situation will be here almost the same. Indeed, applying a voltage to the mesa induces currents, in the initially immobile condensate, in all the directions of the plane. As soon as the fluid is set in motion, it starts to feel the effective magnetic field induced by the TE-TM splitting and the situation is reminiscent to that of the optical spin-Hall effect. We are therefore able to break the symmetry of the flow with respect to both the phase of the condensate and the polarization. Consequently, if the TE-TM splitting is sufficiently strong, our device will naturally excite half-integer topological defects such as half-vortices and half-lasso solitons from the dissociation of integer topological defect within

the flow. One should furthermore keep in mind that the negative value of α_2 will further assist the separation as soon as it is triggered by the TE-TM splitting [see Sec.(2.3.1)], even if the latter is weak. We show in the Fig.2.41 the generation of propagating half-vortices dipoles and half-ring solitons using a horseshoe and circular mesa respectively. The situation would remain qualitatively the same modeling the nonresonant injection with a rate equation for e.g. an unpolarized reservoir connected to both spin components.

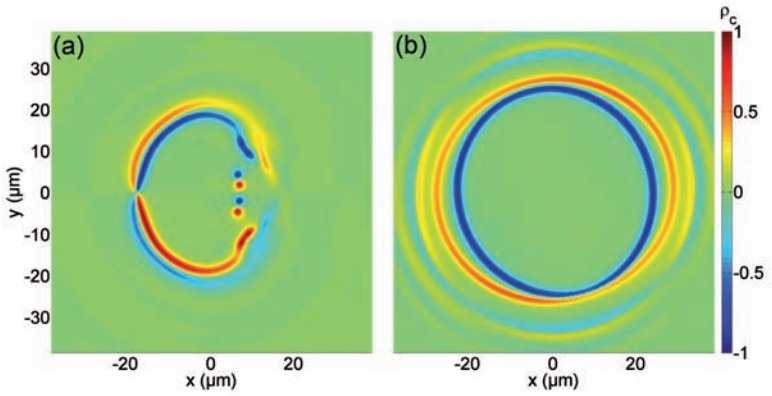

Figure 2.41: Generation of half-integer topological defects in the TE-TM splitting induced effective magnetic field. In both panel we plot the degree of circular polarization ρ_c to image both spin component in a single panel. (a) Generation of half-vortex dipoles by the horseshoe. (b) Generation of half-ring solitons by a circular mesa.

2.5.7 Conclusions

We have shown that vortices can be nucleated electrically in a microcavity with metallic contacts deposited on top of the Bragg mirrors. We have proposed a structure acting as a "vortex gun" allowing generation of propagating vortex-antivortex pairs on demand, analyzed their injection, deviation, oscillations, guiding, splitting into gray solitons. As well, we have shown the possibility to generate single vortices and half-vortices/half-solitons. The topological defects generated in the proposed system are stable and controllable excitations that can be easily guided. Moreover, the system we propose opens the way towards the analysis of nontrivial solitonic structures as well as dispersive shock waves inside a superfluid in an unprecedent manner. The main challenge for the experimental realization of the present proposal resides in the stabilization of the system under the action of frequencies in the ranges of 10 GHz accessible nowadays [95]. We believe that it could be achieved in a near future in view of the recent technological progresses.

2.6 Chapter conclusion

In this chapter we have discussed the incredible richness that offers the two component spinor polariton condensate. Its elementary topological excitations, half-solitons and half-vortices, can be artificially nucleated by several means with the current technology. We have seen that they can be manipulated as magnetic charges within the effective magnetic fields intrinsic to microcavities and embody extremely promising information carriers for the growing field of spin-optronics. The first observation of oblique half-solitons paves the way to the generation of "magnetricity" based on half-integer topological defects. We have proposed several realistic configurations to generate such objects: namely using phase imprinting technics, making the polariton fluid collide against a defect or using electric contacts on top of the microcavity.

Additionally, we have been able to explore the physics of black holes, proposing the polariton quantum fluid as an advantageous alternative for the creation of acoustic black holes allowing the investigation of the famous Hawking radiation. The half-soliton being a stable excitation in the condensate plays in this context the role of test signals allowing to verify the properties of the wormholes that can be organized thanks to the polariton features.

Bibliography

[1] M. Ueda and Y. Kawaguchi, Spinor Bose-Einstein condensates, *arXiv:1001.2072* (2010). (Cited on pages 70 and 76.)

[2] P. Ohberg and L. Santos, Dark Solitons in a Two-Component Bose-Einstein Condensate, *Phys. Rev. Lett.* **86**, 2918 (2001). (Cited on page 70.)

[3] P. G. Kevrekidis, H. E. Nistazakis, D. J. Frantzeskakis, B. A. Malomed and R. Carretero-Gonzalez, Families of matter-waves in two-component Bose-Einstein condensates, *Eur. Phys. J. D* **28**, 181 (2004). (Cited on page 70.)

[4] Y. G. Gladush, A. M. Kamchatnov, Z. Shi, P. G. Kevrekidis, D. J. Frantzeskakis, and B. A. Malomed, Wave patterns generated by a supersonic moving body in a binary Bose-Einstein condensate, *Phys. Rev. A* **79**, 033623 (2009). (Cited on pages 70 and 105.)

[5] M. M. Salomaa and G. E. Volovik, Half-solitons in superfluid ^{3}He-A: Novel $pi/2$-quanta of phase slippage, *J. Low Temp. Phys.* **74**, 3-4 (1989). (Cited on pages 70 and 82.)

[6] U. A. Khawaja and H. Stoof, Skyrmions in a ferromagnetic Bose-Einstein condensate, *Nature* **411**, 918 (2001). (Cited on pages 70 and 76.)

[7] K. Kasamatsu, M. Tsubota, and M. Ueda, Spin textures in rotating two-component Bose-Einstein condensates, *Phys. Rev. A* **71**, 043611 (2005). (Cited on pages 70 and 76.)

[8] G. E. Volovik, V. P. Mineev, Line and point singularities in superfluid ^{3}He, *JETP Lett.* **24**, 561 (1976). (Cited on page 70.)

[9] J. R. Kirtley, C. C. Tsuei, Martin Rupp, J. Z. Sun, Lock See Yu-Jahnes, A. Gupta, M. B. Ketchen, K. A. Moler, and M. Bhushan *Phys. Rev. Lett.* **76**, 1336 (1996). (Cited on page 70.)

[10] Yuri G. Rubo, Half Vortices in Exciton Polariton Condensates, *Phys. Rev. Lett.* **99**, 106401 (2007). (Cited on pages 70, 72, 76 and 77.)

[11] K. G. Lagoudakis, M. Wouters, M. Richard, A. Baas, I. Carusotto, R. André, Le Si Dang, and B. Deveaud-Plédran, Quantized vortices in an exciton-polariton condensate, *Nature Physic*, **4**, 706 (2008). (Cited on pages 70, 100 and 120.)

[12] K. G. Lagoudakis, F. Manni, B. Pietka, M. Wouters, T. C. H. Liew, V. Savona, A. V. Kavokin, and R. André, Probing the Dynamics of Spontaneous Quantum Vortices in Polariton Superfluids, *Phys. Rev. Lett.* **106**, 115301 (2011). (Cited on page 70.)

[13] K. G. Lagoudakis, T. Ostatnický, A. V. Kavokin, Y. G. Rubo, R. André, and B. Deveaud-Plédran, Observation of half-quantum vortices in an exciton-polariton condensate, *Science* **326**, 974 (2009). (Cited on page 100.)

[14] T. C. H. Liew, A. V. Kavokin, and I. A. Shelykh, Excitation of vortices in semiconductor microcavities, *Phys. Rev. B* **75**, 241301(R) (2007). (Cited on page 70.)

[15] T. C. H. Liew, Yuri G. Rubo, and A. V. Kavokin, Generation and Dynamics of Vortex Lattices in Coherent Exciton-Polariton Fields, *Phys. Rev. Lett.* **101**, 187401 (2008). (Cited on page 70.)

[16] J. Keeling and N. G. Berloff, Spontaneous Rotating Vortex Lattices in a Pumped Decaying Condensate, *Phys. Rev. Lett.* **100**, 250401 (2008). (Cited on page 70.)

[17] M. D. Fraser, G. Roumpos and Y. Yamamoto, Vortex-antivortex pair dynamics in an exciton-polariton condensate, *New J. Phys.* **11** (2009). (Cited on page 70.)

[18] M. O. Borgh, J. Keeling, and N. G. Berloff, Spatial pattern formation and polarization dynamics of a nonequilibrium spinor polariton condensate, *Phys. Rev. B* **81**, 235302 (2010). (Cited on page 70.)

[19] A. V. Gorbach, R. Hartley, and D. V. Skryabin, Vortex Lattices in Coherently Pumped Polariton Microcavities, *Phys. Rev. Lett.* 104, 213903 (2010). (Cited on page 70.)

[20] D. Sanvitto, F. M. Marchetti, M. H. Szymanska, G. Tosi, M. Baudisch, F. P. Laussy, D. N. Krizhanovskii, M. S. Skolnick, L. Marrucci, A. Lemaître, J. Bloch, C. Tejedor, and L. Vina, Persistent currents and quantized vortices in a polariton superfluid, *Nature Physics* **6**, 527 (2010). (Cited on pages 70, 94 and 100.)

[21] F. M. Marchetti, M. H. Szymanska, C. Tejedor, and D. M. Whittaker, Spontaneous and Triggered Vortices in Polariton Optical-Parametric-Oscillator Superfluids, *Phys. Rev. Lett.* **105**, 063902 (2010). (Cited on pages 70, 94, 100 and 107.)

[22] D. N. Krizhanovskii, D. M. Whittaker, R. A. Bradley, K. Guda, D. Sarkar, D. Sanvitto, L. Vina, E. Cerda, P. Santos, K. Biermann, R. Hey, and M. S. Skolnick, Effect of Interactions on Vortices in a Nonequilibrium Polariton Condensate, *Phys. Rev. Lett.* **104**, 126402 (2010). (Cited on page 70.)

[23] G. Roumpos, M. D. Fraser, A. Löffler, Sven Höfling, A Forchel, and Y. Yamamoto, Single vortex-antivortex pair in an exciton-polariton condensate, *Nature Physics* **7**, 129 (2011). (Cited on page 70.)

[24] G. Nardin, G. Grosso, Y. Léger, B. Pietka, F. Morier-Genoud, and B. Deveaud-Plédran, Hydrodynamic nucleation of quantized vortex pairs in a polariton quantum fluid, *Nature Phys.* **7**, 635 (2011). (Cited on page 70.)

[25] G. Tosi, F. M. Marchetti, D. Sanvitto, C. Anton, M. H. Szymanska, A. Berceanu, C. Tejedor, L. Marrucci, A. Lemaitre6, J. Bloch, and L. Vina, Onset and Dynamics of Vortex-Antivortex Pairs in Polariton Optical Parametric Oscillator Superfluids, *Phys. Rev. Lett.* **107**, 036401 (2011). (Cited on page 70.)

[26] D. Sanvitto, S. Pigeon, A. Amo, D. Ballarini, M. De Giorgi, I. Carusotto, R. Hivet, F. Pisanello, V. G. Sala, P. S. S. Guimaraes, R. Houdré, E. Giacobino, C. Ciuti, A. Bramati and G. Gigli, All-optical control of the quantum flow of a polariton condensate, *Nature Photonics* **5**, 610 (2011). (Cited on page 70.)

[27] G. Grosso, G. Nardin, F. Morier-Genoud, Y. Léger, and B. Deveaud-Plédran, Soliton Instabilities and Vortex Street Formation in a Polariton Quantum Fluid, *Phys. Rev. Lett.* **107**, 245301 (2011). (Cited on page 70.)

[28] H. Flayac, I. A. Shelykh, D. D. Solnyshkov, and G. Malpuech, Topological stability of the half-vortices in spinor exciton-polariton condensates, *Phys. Rev. B* **81**, 045318 (2010). (Cited on page 77.)

[29] J. Keeling and N. G. Berloff, Controllable half-vortex lattices in an incoherently pumped polariton condensate, *arXiv*:1102.5302 (2011). (Cited on page 70.)

[30] A. V. Larionov, V. D. Kulakovskii, S. Höfling, C. Schneider, L. Worschech, and A. Forchel, Polarized Nonequilibrium Bose-Einstein Condensates of Spinor Exciton Polaritons in a Magnetic Field, *Phys. Rev. Lett.* **105**, 256401 (2010). (Cited on page 72.)

[31] P. M. Chaikin and T. C. Lubensky, Principles of Condensed-Matter Physics, Cambridge University Press, Cambridge (2000). (Cited on pages 74 and 79.)

[32] M. Toledo Solano and Yuri G. Rubo, Comment on "Topological stability of the half-vortices in spinor exciton-polariton condensates", *Phys. Rev. B* **82**, 127301 (2010). (Cited on page 77.)

[33] H. Flayac, I. A. Shelykh, D. D. Solnyshkov, G. Malpuech, Reply to ŞComment on "Topological stability of the half-vortices in spinor exciton-polariton condensates"", *Phys. Rev. B* **82**, 127302 (2010). (Cited on page 77.)

[34] Th. Busch and J. R. Anglin, Wave-function monopoles in Bose-Einstein condensates, *Phys. Rev. A* **60**, R2669-R2672 (1999). (Cited on page 78.)

[35] P. G. Kevrekidis, D. J. Frantzeskakis, and R. Carretero-Gonzalez, Emergent Nonlinear Phenomena in Bose-Einstein Condensates, Springer, (2008). (Cited on page 82.)

[36] P. A. M. Dirac, Quantized Singularities in Electromagnetic Field, *P. R. Soc. A* **133**, 60 (1931). (Cited on page 82.)

[37] H. Flayac, D. D. Solnyshkov, and G. Malpuech, Oblique half-solitons and their generation in exciton-polariton condensates, *Phys. Rev. B* **83**, 193305 (2011). (Cited on pages 82, 105, 107 and 108.)

[38] D. D. Solnyshkov, H. Flayac, and G. Malpuech, Stable magnetic monopoles in spinor polariton condensates, *Phys. Rev. B* **85**, 073105 (2012). (Cited on pages 82, 102 and 103.)

[39] H. Flayac, D. D. Solnyshkov, and G. Malpuech, Separation and acceleration of analogues of magnetic monopoles in semiconductor microcavities, *arXiv*:1203.0885. (Cited on page 82.)

[40] R. Hivet, H. Flayac, D. D. Solnyshkov, D. Tanese, T. Boulier, D. Andreoli, E. Giacobino, J. Bloch, A. Bramati, G. Malpuech, A. Amo, Half-solitons in a polariton quantum fluid behave like magnetic monopoles, *arXiv*:1204.3564. (Cited on pages 82, 105 and 110.)

[41] G. Dasbach, C. Diederichs, J. Tignon, C. Ciuti, Ph. Roussignol, C. Delalande, M. Bayer, and A. Forchel, Polarization inversion via parametric scattering in quasi-one-dimensional microcavities, *Phys. Rev. B* **71**, 161308(R) (2005). (Cited on pages 84, 120 and 122.)

[42] G. E. Volovik, The Universe in a Helium Droplet, Clarendon Press, Oxford (2003). (Cited on pages 85 and 122.)

[43] G. A. Swartzlander, Jr., D. R. Andersen, J. J. Regan, H. Yin, and A. E. Kaplan, Spatial dark-soliton stripes and grids in self-defocusing materials, *Phys. Rev. Lett.* **66**, 1583 (1991). (Cited on page 88.)

[44] D. Tanese, D. D. Solnyshkov, A. Amo, L. Ferrier, E. Bernet-Rollande, E. Wertz, I. Sagnes, A. Lemaitre, P. Senellart, G. Malpuech, and J. Bloch, Backscattering Suppression in Supersonic 1D Polariton Condensates, *Phys. Rev. Lett.* **108**, 036405 (2012). (Cited on page 96.)

[45] M. Toledo Solano and Yuri G. Rubo, Vortices in exciton-polariton condensates with polarization splitting, *J. Phys.: Conf. Ser.* **210**, 012024 (2010). (Cited on pages 93 and 102.)

[46] A. J. Leggett, *Quantum Liquids*, Oxford University Press (Oxford, 2008). (Cited on page 94.)

[47] M. R. Matthews, B. P. Anderson, P. C. Haljan, D. S. Hall, M. J. Holland, J. E. Williams, C. E. Wieman, and E. A. Cornell, Watching a Superfluid Untwist Itself: Recurrence of Rabi Oscillations in a Bose-Einstein Condensate, *Phys. Rev. Lett.* **83**, 3358 (1999). (Cited on page 94.)

[48] N. A. Gippius, I. A. Shelykh, D. D. Solnyshkov, S. S. Gavrilov, Yuri G. Rubo, A. V. Kavokin, S. G. Tikhodeev, and G. Malpuech, Polarization Multistability of Cavity Polaritons, *Phys. Rev. Lett.* **98**, 236401 (2007). (Cited on page 95.)

[49] S. T. Bramwell, S. R. Giblin, S. Calder, R. Aldus, D. Prabhakaran, and T. Fennell, Measurement of the charge and current of magnetic monopoles in spin ice, *Nature* **461**, 956 (2009). (Cited on page 113.)

[50] A. Amo, S. Pigeon, D. Sanvitto, V. G. Sala, R. Hivet, I. Carusotto, F. Pisanello, G. Leménager, R. Houdré, E Giacobino, C. Ciuti, and A. Bramati, Polariton Superfluids Reveal Quantum Hydrodynamic Solitons, *Science* **3**, 1167 (2011). (Cited on pages 104, 105, 106, 114, 119 and 120.)

[51] S. Pigeon, I. Carusotto, and C. Ciuti, Hydrodynamic nucleation of vortices and solitons in a resonantly excited polariton superfluid, *Phys. Rev. B* **83**, 144513 (2011). (Cited on pages 104, 106 and 109.)

[52] E. Cancellieri, F. M. Marchetti, M. H. Szymanska, and C. Tejedor, Superflow of resonantly driven polaritons against a defect, *Phys. Rev. B* **82**, 224512 (2010). (Cited on pages 104 and 106.)

[53] A. M. Kamchatnov and L. P. Pitaevskii, Stabilization of Solitons Generated by a Supersonic Flow of Bose-Einstein Condensate Past an Obstacle, *Phys. Rev. Lett.* **100**, 160402 (2008). (Cited on pages 104 and 109.)

[54] A. M. Kamchatnov, S. V. Korneev, Condition for convective instability of dark solitons, *Phys. Lett. A* **375** 26, 2577 (2011). (Cited on page 104.)

[55] A. M. Kamchatnov and Y. V. Kartashov, Quasi-one-dimensional flow of polariton condensate past an obstacle, *Eur. Phys. Lett.* **97**, 10006 (2012). (Cited on page 104.)

[56] T. Frisch, Y. Pomeau, and S. Rica, Transition to dissipation in a model of superflow, *Phys. Rev. Lett.* **69**, 1644 (1992). (Cited on page 104.)

[57] A. Amo, J. Lefrère, S. Pigeon, C. Adrados, C. Ciuti, I. Carusotto, R. Houdré, E. Giacobino, and A. Bramati, Superfluidity of polaritons in semiconductor microcavities, *Nat. Phys.* **5**, 805 (2009). (Cited on page 105.)

[58] A. Amo, S. Pigeon, C. Adrados, R. Houdre, E. Giacobino, C. Ciuti, and A. Bramati, Light engineering of the polariton landscape in semiconductor microcavities, *Phys. Rev. B* **82**, 081301(R) (2010). (Cited on page 107.)

[59] D. D. Solnyshkov, H. Flayac, and G. Malpuech, Black Holes and Wormholes in spinor polariton condensates, *Phys. Rev. B* **84**, 233405 (2012). (Cited on page 116.)

[60] A. Einstein and N. Rosen, The Particle Problem in the General Theory of Relativity, *Phys. Rev.* **48**, 73-77 (1935). (Cited on page 116.)

[61] A. F. Young and P. Kim, Quantum interference and Klein tunnelling in graphene heterojunctions, *Nature Physics* **5**, 222 (2009). (Cited on page 117.)

[62] Muse, Black Holes and Revelations, Helium 3 (2006). (Cited on page 117.)

[63] L. J. Garay, J. R. Anglin, J. I. Cirac, and P. Zoller, Sonic Analog of Gravitational Black Holes in Bose-Einstein Condensates, *Phys. Rev. Lett.* **85**, 4643 (2000). (Cited on pages 117, 118 and 119.)

[64] O. Lahav, A. Itah, A. Blumkin, C. Gordon, S. Rinott, A. Zayats, and J. Steinhauer, Realization of a Sonic Black Hole Analog in a Bose-Einstein Condensate, *Phys. Rev. Lett.* **105**, 240401 (2010). (Cited on pages 117 and 120.)

[65] K. Muamer, D. Guillaume, T. M. Chang, S. Guenneau, S. Enoch, Curved trajectories on transformed metal surfaces: Beam-splitter, invisibility carpet and black hole for surface plasmon polaritons, *Photonics and Nanostructures - Fundamentals and Applications* **9** 4, 302-307(2011). (Cited on page 117.)

[66] H. Chen, R. X. Miao, M. Li, Transformation optics that mimics the system outside a Schwarzschild black hole, *Opt. Express* **18** 14, 15183 (2010). (Cited on page 117.)

[67] A. Greenleaf, Y. Kurylev, M. Lassas, and G. Uhlmann, Electromagnetic Wormholes and Virtual Magnetic Monopoles from Metamaterials, *Phys. Rev. Lett.* **99**, 183901 (2007). (Cited on page 117.)

[68] W. G. Unruh, Experimental Black-Hole Evaporation?, *Phys. Rev. Lett.* **46**, 1351 (1981). (Cited on pages 117 and 119.)

[69] S. Weinfurtner, E. W. Tedford, M. C. J. Penrice, W. G. Unruh, and G. A. Lawrence, Measurement of Stimulated Hawking Emission in an Analogue System, *Phys. Rev. Lett.* **106**, 021302 (2011). (Cited on page 117.)

[70] S. W. Hawking, Black hole explosions?, Nature **248**, 30-31 (1974). (Cited on page 119.)

[71] M. Visser et al., Artificial Black Holes, World Scientific Publishing, New Jersey (2002). (Cited on page 119.)

[72] R. Schutzhold, and W. G. Unruh, Origin of the particles in black hole evaporation, *Phys. Rev. D* **78**, 041504(R) (2008). (Cited on page 119.)

[73] E. Wertz, L. Ferrier, D. D. Solnyshkov, R. Johne, D. Sanvitto, A. Lemaître, I. Sagnes, R. Grousson, A. V. Kavokin, P. Senellart, G. Malpuech, and J. Bloch, Spontaneous formation and optical manipulation of extended polariton condensates, *Nature Physics* **6**, 860 (2010). (Cited on pages 119, 120 and 122.)

[74] R. Balbinot et al., Nonlocal density correlations as a signature of Hawking radiation from acoustic black holes, Phys. Rev. A **78**, 021603(R) (2008). (Cited on pages 120 and 122.)

[75] R. Balbinot, A. Fabbri, S. Fagnocchi, A. Recati, and I. Carusotto, Numerical observation of Hawking radiation from acoustic black holes in atomic Bose-Einstein condensates, *New J. Phys.* **10**, 103001 (2008). (Cited on page 120.)

[76] C. Mayoral, A. Recati, A. Fabbri, R. Parentani, R. Balbinot, and I. Carusotto, *New J. Phys.* **13**, 025007 (2011). (Cited on page 122.)

[77] J. A. Wheeler, Geometrodynamics, Academic, New York (1962). (Cited on page 121.)

[78] M. S. Morris, K. S. Thorne, and U. Yurtsever, Michael S. Morris, K. S. Thorne, and U. Yurtsever, Wormholes Time Machines and the Weak Energy Condition, *Phys. Rev. Lett.* **61**, 1446 (1988). (Cited on page 122.)

[79] G. Malpuech, M. M. Glazov, I. A. Shelykh, P. Bigenwald, and K. V. Kavokin, Electronic control of the polarization of light emitted by polariton lasers, *Appl. Phys. Lett.* **88**, 111118 (2006). (Cited on page 122.)

[80] L. Pitaevskii and S. Stringari, Bose-Einstein Condensation, *Oxford Science Publications - International Series of Monographs on Physics 116* (2002). (Not cited.)

[81] H. Flayac, G. Pavlovic, M. A. Kaliteevski, and I. A. Shelykh, Electric generation of vortices in polariton superfluids, *Phys. Rev. B* **85**, 075312 (2012). (Cited on page 125.)

[82] M. Kaliteevski, I. Iorsh, S. Brand, R. A. Abram, J. M. Chamberlain, A. V. Kavokin, and I. A. Shelykh, Tamm plasmon-polaritons: Possible electromagnetic states at the interface of a metal and a dielectric Bragg mirror, *Phys. Rev. B* **76**, 165415 (2007). (Cited on page 126.)

[83] C. Symonds, A. Lemaitre, E. Homeyer, J. C. Plenet, and J. Bellessa, Emission of Tamm plasmon/exciton polaritons, *Appl. Phys. Lett.* **95**, 151114 (2009). (Cited on page 126.)

[84] C. W. Lai, N. Y. Kim, S. Utsunomiya, G. Roumpos, H. Deng, M. D. Fraser, T. Byrnes, P. Recher, N. Kumada, T. Fujisawa, Y. Yamamoto, Coherent zero-state and π-state in an exciton-polariton condensate array, *Nature* **450**, 529-532 (2007). (Cited on page 126.)

[85] H. Flayac, D. D. Solnyshkov, and G. Malpuech, Bloch oscillations of an exciton-polariton Bose-Einstein condensate, *Phys. Rev. B* **83**, 045412 (2011). (Cited on page 126.)

[86] M. Kaliteevski, S. Brand, R. A. Abram, I. Iorsh, A. V. Kavokin, and I. A. Shelykh, Hybrid states of Tamm plasmons and exciton polaritons, *Appl. Phys. Lett.* **95**, 251108 (2009). (Cited on page 126.)

[87] T. C. H. Liew, A. V. Kavokin, T. Ostatnicky, M. Kaliteevski, I. A. Shelykh, and R. A. Abram, Exciton-polariton integrated circuits, *Phys. Rev. B* **82**, 033302 (2010). (Cited on page 126.)

[88] G. Theocharis, D. J. Frantzeskakis, P. G. Kevrekidis, B. A. Malomed, and Y. S. Kivshar, Ring Dark Solitons and Vortex Necklaces in Bose-Einstein Condensates, *Phys. Rev. Lett.* **90**, 120403 (2003). (Cited on page 126.)

[89] M. A. Hoefer, M. J. Ablowitz, I. Coddington, E. A. Cornell, P. Engels, and V. Schweikhard, Dispersive and classical shock waves in Bose-Einstein condensates and gas dynamics, *Phys. Rev. A* **74**, 023623 (2006). (Cited on page 126.)

[90] See supplemental material at http://link.aps.org/supplemental/10.1103/PhysRevB.85.075312 for a movie. (Cited on pages 131 and 132.)

[91] M. Wouters and I. Carusotto, Excitations in a Nonequilibrium Bose-Einstein Condensate of Exciton Polaritons, *Phys. Rev. Lett.* **99**, 140402 (2007). (Not cited.)

[92] T. Aioi, T. Kadokura, T. Kishimoto, and H. Saito, Controlled Generation and Manipulation of Vortex Dipoles in a Bose-Einstein Condensate, *Phys. Rev. X* 1, 021003 (2011). (Cited on page 130.)

[93] H. Smith and C. J. Pethick, Bose-Einstein Condensation in Dilute Gases, Cambridge University Press, Cambridge (2002). (Cited on page 130.)

[94] C. A. Jones and P. H. Roberts, Motions in a Bose condensate - Axisymmetric solitary waves, *J. Phys. A: Math. Gen.* **15**, 2599 (1982). (Cited on page 131.)

[95] M. Tonouchi, Cutting-edge terahertz technology, *Nature Photonics* **1**, 97-105 (2007). (Cited on page 134.)

Chapter 3

Polariton condensates in low dimensional structures

Contents

While the original planar microcavity that gave birth to the first polariton condensate [1] seems to have still much to offer, today's technological progresses allow to broaden the perspectives. Indeed, the modern lithography processes push the boundaries away, and now almost any sample design seems possible to implement. These perspective open the way to the polariton physics in dimensions lower than two. One remarkable recent result is the observation of the polariton condensation

in a very high quality factor quasi-one dimensional microwires by Wertz et al. [2]. In this work, the *coherent* propagation of the condensate over the whole sample was an outstanding result. More recently, the condensation was obtained in single or pairs of micropillars (or "molecules"), where the polaritons were even more confined [3, 4]. The connections between such elements could lead in a near future to the fabrication of a real polariton-based optical circuit or even a complete optical computer operating at THz frequencies.

Capitalizing on these results, we discuss here the polariton physics within low dimensional structures. After an introductory paragraph [Sec.3.1], we will present first the recent observation of polariton gap states [Sec.3.2] within periodically patterned microwire [5]. Second, we shall discuss our prediction of the Bloch oscillations of an exciton-polaritons condensate [6, 7]. Finally, we will analyze the Josephson oscillations of a polariton condensate [Sec.3.3] within the density matrix formalism (suitable for indirect excitons as well) [Sec.3.4]. This effect could be observed experimentally within pairs of micropillars [8].

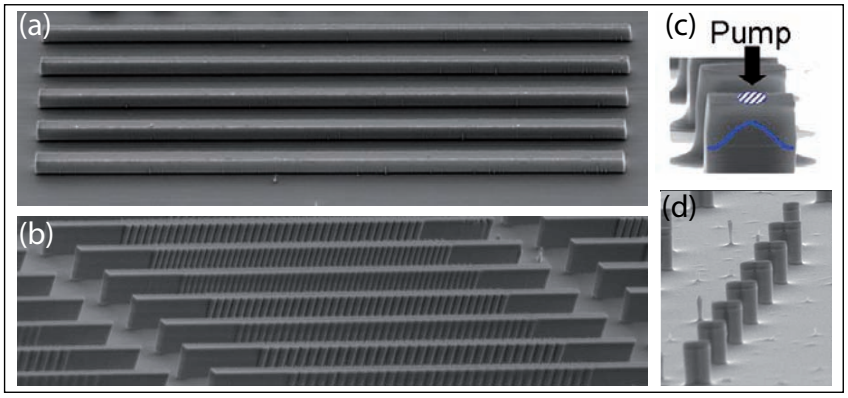

Figure 3.1: Low dimensional microcavities. (a) Microwires from Ref.[2], (b) periodically modulated wires from Ref.[5], (c) single micropillars from Ref.[3] and (d) pairs of micropillars from Ref.[4].

3.1 Bose-Einstein condensate in a periodic potential

3.1.1 Linear waves in periodic potentials

Let us start here with a reminder on the textbook theory [see e.g. [9]] of linear waves in a periodic potential. We shall consider here that the particles experience a cosine potential

$$U(x) = A\cos(k_0 x)^2 \tag{3.1}$$

where $k_0 = \pi/d$ d, being the period of the potential. Assuming that in the absence of U the dispersion is parabolic, the stationary Schödinger equation for the field $\psi(x)$ reads

$$E\psi(x) = -\frac{\hbar^2}{2m^*}\frac{\partial^2\psi(x)}{\partial x^2} + A\cos(k_0 x)^2\psi(x) \tag{3.2}$$

Applying Bloch's theorem, we look for eigenfunctions in the form

$$\psi_{p,q}(x) = u_{p,q}(x)\, e^{iqx} \tag{3.3}$$

where q is the so-called quasimomentum and p is the band index. The function $u_{p,q}$ is d-periodic. We are therefore allowed to rewrite $\psi(x)$ and $U(x)$ in terms of Fourier Series

$$\psi_{p,q}(x) = e^{iqx}\sum_m c_m^n e^{2imk_0 x} \tag{3.4}$$

$$U(x) = \sum_m U_m e^{2imk_0 x} \tag{3.5}$$

Injecting this Anzatz into Eq.(3.2) considering $2N+1$ modes which means truncating the sums to $|m| = N$ leads to the set of $2(2N+1)$ linear equations

$$\left[\frac{\hbar^2}{2m^*}(q-2mk_0)^2 + V_0\right] c_{q-mG} + U_{+2k_0}c_{q-2(m+1)k_0} + U_{-G}c_{q-2(m-1)k_0} = Ec_{q-2mk_0} \tag{3.6}$$

The choice of our periodic potential imposes $U_{\pm}2k_0 = A/4$ and $U_{m=0} = A/2$. For a given quasimomentum q, we obtain $2N+1$ eigenenergies forming the so-called energy bands separated by forbidden energy gaps. To each eigenvalue E_p corresponds a eigenfunction defined by the Fourier component c_{q-2mk_0}. The total dispersion relation obviously strongly depends on both the amplitude A of the potential and the quasimomentum q. The recoil energy $E_R = \hbar^2 k_0^2/2m^*$ is the characteristic scale in the system and we can consider two opposite limits depending on the ratio A/E_R.

In the case $A \simeq E_R$ the potential is said to be shallow and the eigenenergies crucially depend on q. Since the gaps width E_g^p scale like A^{p+1} its magnitude is only significant between the first and second band. Therefore particles having an energy larger than E_g^1 are well described as free particles. The band structure can be estimated as [10]

$$\frac{E(\widetilde{q})}{E_R} = \widetilde{q}^2 \mp \sqrt{4\widetilde{q}^2 + \frac{A^2}{16E_R^2}} \tag{3.7}$$

where $\widetilde{q} = q/k - 1$ and $s = A/E_R$. This approximation gives here the first (minus sign) and second band (plus sign). In Fig.3.2, the energies in real space are shown. In the same graph are shown the real space probability distributions of the eigenfunctions. The eigenfunctions at the lowest and highest energy are almost constant, which implies that the wave function is mainly given by a plane wave corresponding to an almost free particle. It is important to note that for energies near the upper band edge of the lowest band, the probability distribution is periodic and its maxima coincide with the potential minima. For this energy we additionally depict the wave function, which reveals that the relative phase in the adjacent potential minima is π. This is the well-known sinusoidal *Bloch state* at the band edge defining the Brillouin zone. From this graph one can also see that the Bloch state in the first excited band is also sinusoidal but it is in-phase with the periodic potential. Thus the energy of this state is higher due to the bigger overlap with the periodic potential.

In the opposite limit, where $A \gg E_R$, we enter the well known tight binding treatment. In that case, the eigenenergies of the first bands are only weakly dependent on q and the energy gaps are large. The first band can be found analytically [11] to be

$$\frac{E(q)}{E_R} = \sqrt{\frac{A}{E_R}} - 2J\cos(qd) \tag{3.8}$$

where J is the coupling energy between adjacent wells (Josephson coupling constant) which can be found as

$$J = \frac{4}{\sqrt{\pi}}\left(\frac{A}{E_R}\right)^{3/4} e^{-2\sqrt{A/E_R}} \tag{3.9}$$

The expression (3.8), is plotted in Fig.3.2(c) as a dotted line and reveals the good agreement with the numerically calculated eigenenergies. The corresponding eigenfunctions are depicted on the right-hand side. Although the absolute value of the eigenfunctions for the lowest band shows no significant dependence on the quasimomentum, the wave functions at $q = 0$ and at $q = \pi/d$ differ by the relative phase between adjacent potential minima [solid lines in Fig.3.2(d)]. As in the weak periodic potential limit, the wave function at the upper band edge of the lowest band is staggered, i.e., there is a π phase jump between different sites. Phenomena studied in this regime only involve the lowest band, which is well described by localized wave functions at each site. Therefore, in this limit the dynamics can be described using the localized Wannier functions, which are superpositions of the Bloch functions

$$\psi_p(R,x) = \frac{1}{d}\int \psi_{p,q}(x) e^{-iRq} dq \tag{3.10}$$

where R is the center of the function. The dynamics is simply described via inter-well tunneling. The characteristic energy scale of tunneling coupling between two sites is given by the width of the band, which is $4J$.

We have seen that the linear properties of the periodic potential are defined by the potential amplitude A. The transition between weak and strong potential

is continuous and thus no well-defined boundary can be given. A characteristic potential modulation for this transition may be found by equating the bandwidth and the gap energy, which have the same magnitude at a potential modulation depth of $A = 1.4E_R$.

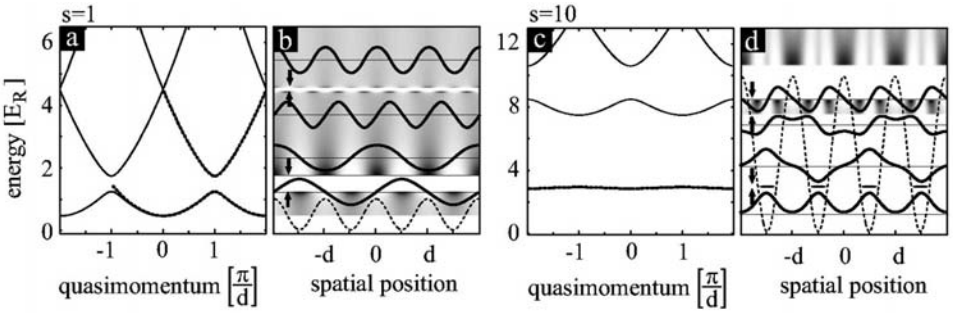

Figure 3.2: Band structure for two different potential depths: (a) weak potential $A = E_R$, (b) deep potential with $A = 10E_R$ ($s = A/E_R$). In both cases, the analytical expressions (3.7) and (3.8) are depicted with dotted lines. In (b) and (d) we show the spatial dependence of the corresponding Bloch states. The periodic potentials are represented by the dashed lines. For each energy, the absolute square value of the corresponding Bloch states is depicted in the gray scale plot, where high probabilities are darker. Additionally, the wave functions are shown for the energies at the gaps indicated with the arrows. One clearly sees that the wave functions at the first gap change their sign from well to well, i.e., there is a phase slip of π. These modes are also known as staggered modes.

3.1.1.1 Bloch oscillations and Landau-Zener Tunneling

In the presence of an accelerating force, the linear theory predicts the occurrence of Bloch oscillations [13] and possibly Landau-Zener tunneling [14] (for shallow lattices) that will be under the scope of this chapter [see Sec.(3.3)]. The wavepacket dynamics of a particle in a periodic potential in the presence of an additional external potential, i.e., with an external force F, is generally not easy to solve. The problem becomes relatively simple, though, as soon as the width of the wave packet in quasimomentum space is small and thus the wave packet can be characterized by a single mean quasimomentum $q(t)$ at the time t. An external force then leads to a time dependence of q via

$$\hbar \frac{\partial q\,(t)}{\partial t} = F \tag{3.11}$$

The force F can be imposed by an electric field for electrons, a gravitational field for atoms or a gradient of confinement potential for photons or polaritons. From above, we easily obtain

$$q\,(t) = \frac{F}{m^*} t + q\,(0) \tag{3.12}$$

We can deduce the group velocity of the wavepacket lying in the band number p

$$v_p(q) = \frac{1}{\hbar}\frac{\partial E_p(q)}{\partial q} \tag{3.13}$$

The equations (3.12,3.13) determine that the rate of change of the quasimomentum is governed by the external force, but the rate of change of the wavepacket's momentum is given by the total force including the influence of the periodic potential included in the dispersion shape. The velocity at the time t is

$$v_p(q) = \frac{F}{m^*}t + v_p(q(0)) \tag{3.14}$$

Since v_q is periodic in the reciprocal lattice, the velocity is a bounded and oscillatory function of time. Therefore the result of the force is not a simple acceleration of the wave packet, and instead the wavepacket demonstrates an oscillatory behavior in real space [see Fig.3.3(a),(b)]. This counterintuitive phenomenon is known as Bloch oscillations [12]. The period of these oscillations is

$$T_{BO} = \frac{2\pi\hbar}{Fd} \tag{3.15}$$

In the case of a strong external force F or a shallow lattice (reducing the gap), interband transitions are allowed to occur. In the context of electrons in solids, it is known as the Landau-Zener tunneling, occurring if the applied electric field is strong enough for the acceleration of the electrons to overcome the gap energy separating the valence and conduction bands. It was shown by Zener [14] that for a given acceleration corresponding to a constant force, one can deduce a tunneling probability P_{LZT} across the first band gap in the adiabatic limit

$$P_{LZT} = e^{-\frac{\pi^2 A}{32F_0}} \tag{3.16}$$

where $F_0 = Fd/E_R$ is a dimensionless force. This phenomenon results in the splitting of the oscillating wave packet at the first Brillouin zone edges where the separation with the second band is the smallest [see Fig.3.3](c),(d).

3.1.2 Effect of nonlinearities

Bose-Einstein condensates inside periodic lattices share many features with electrons in solids, but also with light waves in nonlinear materials and other nonlinear systems. However, the experimental control over the parameters of BEC and of the periodic potential make it possible to enter regimes inaccessible in other systems. However, an important difference between electrons in a crystal lattice and a Bose condensate inside the periodic potential is the strength of the self-interactions and hence the magnitude of the nonlinearity of the system. Electrons are almost noninteracting (all the interactions are already taken into account in their effective mass), whereas atoms inside a Bose-Einstein condensate interact strongly. A perturbation approach is appropriate in the former case while in the latter the full nonlinearity

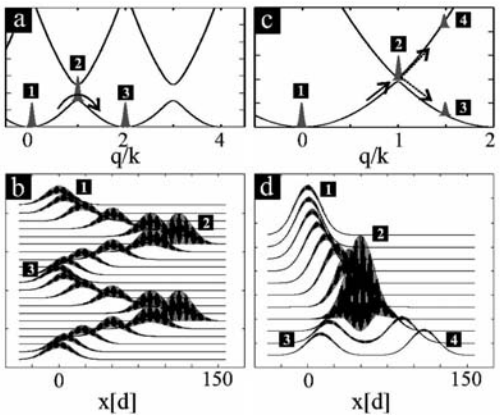

Figure 3.3: Wave-packet dynamics in a periodic potential in the presence of a constant force F. (a), (b) An external force leads to a variation of the central quasimomentum $q = 0$. Since the group velocity changes sign when q exceeds the Brillouin zone, the wavepacket exhibits an oscillatory behavior in real space [panel (b)]. The Bloch oscillations are an example of intraband dynamics. (c), (d) For strong external forces or small band gaps, nonadiabatic transitions to the first excited band can occur at the first Brillouin zone edges [panel (c)]. The Landau-Zener tunneling leads to a splitting of the wave packet in real space [panel (d)]. All plots reveal the Bloch state structure. Indeed, near $q = 0$, the wave packet is only weakly modulated with the period of the periodic potential, while at the band edge it is fully modulated revealing the sinusoidal Bloch state at the Brillouin zone edge.

must be taken into account. Generally, atom-atom interactions in Bose-Einstein condensates lead to rich and interesting nonlinear effects. Most experiments to date have been carried out in the regime of shallow lattice depth, for which the system is well described by the Gross-Pitaevskii equation. Moreover, the nonlinearity induced by the mean-field of the condensate has been shown both theoretically and experimentally to give rise to instabilities in certain regions of the Brillouin zone. The so-called Landau and dynamical instabilities [15] are not present in the corresponding linear system, i.e. the electron system. Such instabilities can be described within the Bogoliubov theory considering low amplitude perturbations on top of the periodically modulated condensate [see e.g. pages 255-257 of Ref.[16]]. While the latter is stable when it forms at zero quasimomentum demonstrating a linear excitation spectrum similar to that of the unmodulated condensate (for low momentum excitations), instability can develop for the propagating condensate around the top of the first band.

Considering the interactions between the particles introduces the interaction energy as new scale in the system. In this framework the situation becomes less straightforward than the previous linear case. Under the mean field approximation for the macroscopic wave function $\psi(x)$, the interaction energy of a condensate is

defined by

$$E_{int} = \frac{\alpha}{2}\int |\psi(x)|^4 dx \tag{3.17}$$

In the framework of periodic potential it would be more relevant to evaluate this interaction energy on a single site integrating the expression (3.17) over one period of the potential. Several regimes have been analyzed depending on the relative values of the energies of the system that are: the width of the first band, the width of the first gap and the on site interaction energy [17]. In the presence of a periodic potential $U(x)$, the 1D Gross-Pitaevskii equation for the mean field $\psi(x,t)$ reads

$$i\hbar\frac{\partial\psi}{\partial t} = -\frac{\hbar^2}{2m^*}\Delta\psi + \alpha|\psi|^2\psi + U\psi \tag{3.18}$$

When the nonlinearities are weak which corresponds to a diluted condensate ($|\psi|^2$ is small) and assuming a shallow lattice, a simplified description can be found starting from the linear description of matter wave packets. Indeed, wave packets with a small momentum distribution, centered around q_0 e.g in the first band ($p = 0$), are well described by a slowly varying amplitude $A(x,t)$, (on the scale of the periodicity) multiplied by the Bloch state corresponding to the central quasimomentum q_0

$$\psi(x,t) = A(x,t)\, u_{0,q_0}(x)\, e^{-i\hbar E(q_0)t/\hbar} \tag{3.19}$$

In this framework, it has been shown in different works [18, 19, 20] that in the case of weakly interacting matter waves, a nonlinear Schrödinger equation for the envelope $A(x,t)$, can be derived by means of the so-called multiple scales analysis [21]. The resulting differential equation for the envelope has the same form as the Gross-Pitaevskii equation but with a modified linear dispersion and interaction energy.

$$i\hbar\left(\frac{\partial A}{\partial t} + v_g\frac{\partial A}{\partial x}\right) = -\frac{\hbar^2}{2m^*}\frac{\partial^2 A}{\partial x^2} + U(x,t)\,A + g_{1D}\alpha_{nl}|A|^2 A \tag{3.20}$$

Here α_{nl} describes the renormalization of the interaction energy which increases due to the stronger localization in the periodic potential. Even though the stationary solutions of Eq.(3.20) do not differ significantly from the linear case, the dynamics of this system is totally different. Especially noteworthy is the formation of *bright* solitons, i.e., nonspreading wave packets that appear despite the repulsive atom-atom interaction provided that the central quasimomentum is in the regime of negative effective mass close to the first Brillouin zone edges. In the work by Steel and Zhang [22], such localized solution were named "gap-solitons". Indeed, a local density increase leads to a local interaction-induced blueshift that allows a state to form within the band gap. Such localized states are stabilized thanks to the negative effective mass that makes the effective time evolution to run backward preventing the dispersion to occur. The appearance of a new class of solitons called out-of-gap solitons was predicted by Yulin and Skryabin [23], who applied the coupled mode description developed in the field of nonlinear optics to the case of Bose-Einstein condensates in periodic potentials. Gap solitons were first observed within an accelerated optical lattice using the so-called dispersion management [24]. Employing

the multiple scale analysis, it is possible to show that in general, two types of gap solitons bifurcate from both band edges [25]. These are bright solitons centered on the maximum (off-site) and minimum (on-site) of the lattice potential respectively.

We have described here only a few samples of the incredibly rich physics that emerges from the condensation in periodic lattices and we refer the interested reader e.g. to the recent review [17] and book [16]. In the following, we will see how polaritons in patterned semiconductor microcavities allow to investigate the formation of gap solitons, Bloch oscillations, and Josephson oscillations.

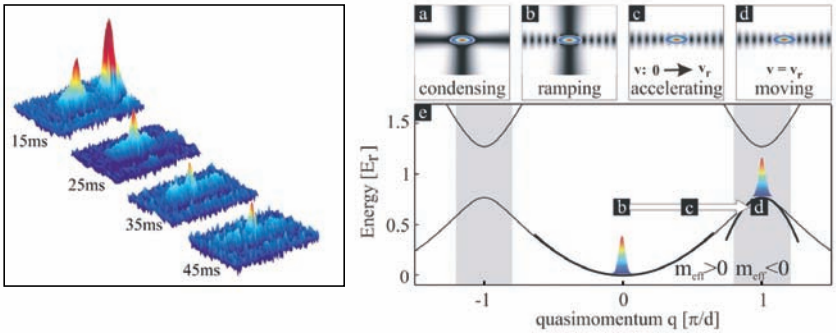

Figure 3.4: Experimental observation of gap solitons in an optical lattice from Ref.[24]. Left panel: Absorption images revealing the in situ density distribution in a one-dimensional wave guide for different evolution times. Clearly, a nonspreading wave packet is formed after 25 ms. Right panels: Principle of the creation of the gap soliton using the so-called dispersion management technique.

3.2 Polariton condensation in solitonic gap states

3.2.1 Introduction

Non-linear wave propagation in a periodic medium is fundamentally different from the propagation in a homogeneous medium. These non-linear waves can be photons propagating in a medium with a Kerr non-linearity (χ^3), or the macroscopic wave-function of an interacting Bose-Einstein condensate. In this last case, inter-particle interactions provide the equivalent of the χ^3 nonlinearity. Different localization phenomena can occur in a periodic medium due to the interplay between the band structure and inter-particle interactions. In the absence of interactions, a cavity state appears when the periodic lattice is locally perturbed, for instance, by removing one or several layers forming the lattice [26], or by slightly changing the periodicity [27] or the material refractive index [28]. In the case of stronger interactions or stronger non-linearities, gap solitons can be generated even without any local perturbation of the periodic potential. Gap solitons being bright solitons possess the characteristic hyperbolic secant density profile, slowly varying in the core region and recovering an exponential decay on the edges. In non-linear photonic crystal fibres such solitary waves have demonstrated propagation without any distortion [29, 30]. Remarkably, none of these various localized states can correspond to the ground state of the system. Thus, their observation with matter waves, for instance, requires setting atomic condensates out of equilibrium [16]. In the case of non-linear photonic crystal fibers, the generation of gap solitons involves exciting the system quasi-resonantly to the forbidden energy gap, and thus high excitation powers are required [29].

Cavity polaritons are quite unique from this point of view. The quantum state in which condensation occurs is not necessarily the ground state and strongly depends on the relative relaxation efficiency towards the different available states [4]. In the present section, we show that in a 1D periodic potential, polaritons spontaneously condense in highly localized interaction-induced gap states. These experiments were performed using non resonant excitation and thus highlight the potentiality of this strongly non-linear photonic system to generate gap solitons or reconfigurable gap states.

We have already seen that the polariton condensate characterized by repulsive interactions supports grey solitons in both 1D [Sec.(1.2.5.1)] and 2D [Sec.(1.2.5.4)]. Additionally, bright solitons were predicted [31] and observed [32] in a planar microcavity. While repulsive interactions and bright solitons seem at odd (especially in the absence of periodic potential), these objects are allowed to occur thanks to the nonparabolic shape of the lower polariton branch. Indeed, polaritons having a momentum larger than that of the inflection point of the dispersion possess an effective mass $m^* = \hbar^2(\partial^2 E/\partial k^2)^{-1}$ which is negative. In nonlinear optical media, described by the nonlinear Schödinger equation, the formation of temporal or spatial bright solitons naturally occurs from the self-focusing Kerr nonlinearity acting as an effective attractive interaction between photons [33]. Recently, matter wave

solitons were observed in an atomic Bose-Einstein condensate, and optical lattices were required in order to engineer the dispersion of the particles to provide the required negative effective mass [34, 35]. Here we propose to use a similar strategy for the polaritonic system. Currently, several works have already been devoted to the behavior of polariton condensates in periodic lattices, [36, 37, 38, 39, 40] and this topic has started now to attract a lot of attention.

Theoretically, the complete polariton dispersion in the presence of a quasi-1D periodic potential can be evidenced e.g. solving numerically the linear set of Schödinger equations for the coupled photonic $\phi(x,y,t)$ and excitonic fields $\chi(x,y,t)$.

$$i\hbar\frac{\partial\phi}{\partial t} = -\frac{\hbar^2}{2m_\phi}\Delta\phi + U_\phi\phi + \frac{\hbar\Omega_R}{2}\chi + P - \frac{i\hbar}{2\tau_\phi} \tag{3.21}$$

$$i\hbar\frac{\partial\chi}{\partial t} = -\frac{\hbar^2}{2m_\chi}\Delta\chi + U_\chi\chi + \frac{\hbar\Omega_R}{2}\phi - \frac{i\hbar}{2\tau_\phi} \tag{3.22}$$

Here $U_\phi(x,y)$ is a periodic potential of period d and amplitude A and the excitonic potential $U_\chi(x,y)$ is zero. The result is shown in the figure 3.5 for a potential of amplitude $A = 1$ meV and period $d = 2$ μm. We obtain the typical band structured dispersion with the occurrence of gaps in both the upper and lower branches. Interestingly, the first gap has a width which obviously dependent on the potential amplitude but here it depends as well on the period of the potential due to the nonparabolicity of the lower polariton branch. Different options can be envisaged to form this potential, it could be obtained either by depositing a metallic pattern along the wire [37] that would potentially form Tamm polariton states [41], by excitation of a surface acoustic wave [39] or by a square-wave-like lateral etching [5].

3.2.2 Surface states in the *cw* regime

In this direction and in the framework of our collaboration with the LPN in Paris, an original cavity microstructure with a periodic lateral etching has been designed in order to confine polaritons in a one dimensional periodic potential. Here we make use of the mixed nature of the polariton states, acting on their photonic part to create a periodic potential, and on their excitonic part to induce interactions. As evidenced by far field emission measurements in the low density regime [see Fig.3.6(b-d)], this periodic potential results in the formation of polariton mini-bands separated by mini-gaps. The width of the folded Brillouin zones is π/P, P being here the lattice periodicity, and the width of the mini-gaps is determined by the amplitude of the modulation. The real space distribution of the polariton emission can also be imaged: it is delocalized, demonstrating the propagative nature of the polariton states in the different sub-bands [Fig.3.7(b)]. We note that, differently from previously reported techniques used to spatially modulate the polariton energy [37, 42, 39], the resulting effective amplitude of the modulated potential can be as large as 2 meV.

Polaritons were generated under non-resonant optical excitation, with a focused single mode *cw* laser beam. Increasing the excitation power, we observe

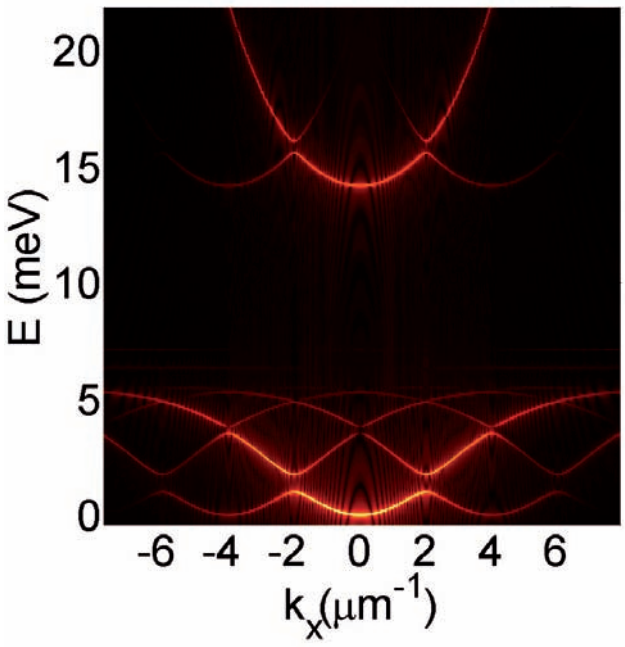

Figure 3.5: Band structured polariton dispersion in the presence of a periodic potential. Found from solving Eqs.(3.21,3.22) with a short and narrow probe pulse.

an abrupt threshold in the emission intensity, signature of polariton condensation [see Fig.3.7(a)]. Real space imaging above threshold reveals that the macroscopically occupied quantum state is strongly localized around the excitation region. Its energy lies inside the first forbidden energy gap. This behavior can be explained by taking into account the repulsive interaction with the cloud of uncondensed excitons, which are continuously injected in the system. This interaction results in a local blueshift of the polariton states in the excitation area. This repulsive potential was previously shown to induce a macroscopic expansion of polariton condensates in non-modulated 1D cavities. Here, in the presence of a periodic potential, the effect of the exciton cloud is the exact opposite. Indeed, the induced repulsive potential locally perturbs the periodic potential, and thus creates a cavity-like state in the minigap, characterized by an exponential decay of the probability density on both sides of the excitation area [Fig.3.7(b,c,h)]. Condensation is triggered on this excited state rather than on lower energy states of the first allowed band, because this localized state has the largest spatial overlap with the excitonic reservoir, providing efficient relaxation kinetics. As a result and counter-intuitively, repulsive interactions lead to the condensate localization. Of course, if one takes into account the negative mass at the edge of the Brillouin zone, the inversion of repulsion into attraction becomes quite natural.

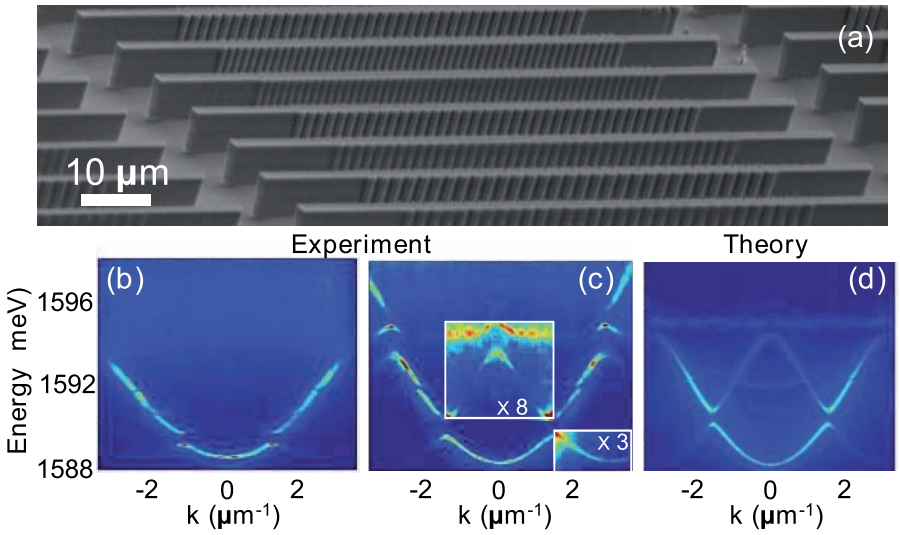

Figure 3.6: (a) Scanning electron micrograph of a set of laterally modulated wires. (b) Angle resolved emission measured on a single modulated wire in the low density regime. The modulation period is $P = 2.7$ μm and the wire width is modulated between $W_{min} = 1.9$ μm and $W_{max} = 2.8$ μm inducing a periodic potential of amplitude $V_{opt} = 1.6$ meV on the cavity mode, the detuning is $\delta = -1$ meV. (c) same as (b) with $P = 2.1$ μm, $W_{min} = 1.8$ μm and $W_{max} = 3.5$ μm inducing a periodic potential $V_{opt} = 2.4$ meV. The signal inside the rectangles has been amplified to better show the band folding. (d) Theoretical polariton dispersion of the wire shown in (c).

3.2.3 Theoretical model

We calculate theoretically the polariton states using Eqs.(3.21,3.22). $U_\phi(x, y)$ is fully reproducing the experimental photonic square-wave confinement potential imposed by the periodic structure. Besides $U_\chi(x, y)$ materializes the 2 μm large Gaussian potential imposed by the nonresonant injection-induced excitonic reservoir. This very simple model is sufficient to identify the accessible states in the system (and here we actually don't need more) but obviously does not reproduce the relaxation kinetics giving the population of each states. The numerical calculations show that depending on the height of the potential, two orthogonal localized states can appear in the band gap [labeled as $S1$ and $S2$ in Fig.3.7] which correspond to off-site and on-site states. Experimentally, condensation in one or the other of these two states is observed. At the threshold, condensation is first favored in the localized mode of the lower half of the gap ($S1$). As the population of this state increases, its blueshift results in a stronger localization, amplifying the transfer of reservoir excitons and thus providing a positive feed-back mechanism. Next, as the energy of the condensate rises and exceeds the middle of the gap, the state spatially broadens, thus reducing the efficiency of the particles transfer into this state. The condensation switches to the second localized state in the gap ($S2$), which becomes kinetically

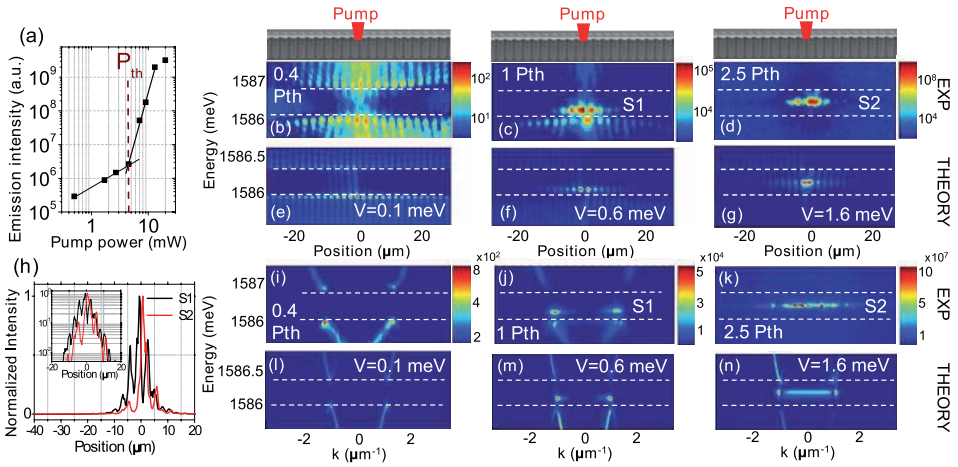

Figure 3.7: Polariton condensation inside the band-gap. (a) Total emission intensity measured from a single modulated wire as a function of the excitation power. (b-d) Spectrally and spatially resolved emission for 3 increasing excitation powers. (i-k) Spectrally resolved far field emission measured on the same wire for the same excitation powers; the first mini-gap induced by the periodicity is indicated with dashed lines. (e-g) and (l-m) Calculated emission distribution in real space and in k-space solving a Schrödinger equation in the presence of both a periodic potential and a Gaussian potential at $y = 0$. Three increasing values of the Gaussian potential accurately reproduce the experimental results. (h) Spatial profile of the $S1$ and $S2$ gap states observed in the panels (c) and (d). A characteristic size (width at half maximum) of 5 μm and 2.5 μm is observed for the $S1$ and $S2$ states respectively. In the inset, the same profiles are shown in logarithmic scale highlighting an exponential decay length of 2.5 μm. Parameters of the wire: Period 2.7 μm, $W_{min} = 1.9$ μm and $W_{max} = 2.8$ μm, $V_{opt} = 1.6$ meV, $\delta = -5.5$ meV.

favored [see Fig.3.7(c-d)].

We note that when the condensate occupancy becomes very large, repulsive self-interactions in the condensate should become significant and induce the formation of a gap soliton bound to the reservoir potential, similar to a surface gap soliton [43]. Nevertheless, the localization length is found to be close to one period, so that the soliton shape is hardly distinguishable from the single particle cavity state. We will therefore rather evidence the formation of gap solitons driven by self-interactions under *pulsed* excitation conditions. Indeed, in such a non-stationary case, a fast transfer of excitons from the reservoir into condensed polaritons is driven by bosonic stimulation. For long enough time delays, it becomes possible to strongly deplete the reservoir and to achieve a freely decaying polariton condensate [see below]. In the following, the wires will be non-resonantly excited by picosecond laser pulses and polariton relaxation across the minibands will be time resolved.

Let us first show how the pulsed excitation scheme allows complete transfer of the reservoir excitons into the polariton condensate, so that a free polariton condensate

can be generated. We use a simplified version of a model recently published in Ref.[4]. We consider an excitonic reservoir maintained at thermal equilibrium (by its interplay with the phonon bath) coupled to a single polariton state. The relaxation mechanism we take into account is the scattering of two reservoir excitons toward a polariton state and a third reservoir state. The temperature of the lattice is assumed to be low enough in order to be able to neglect scattering from polariton state back to the excitonic reservoir. The time evolution of the excitonic reservoir population N_R and of the polariton state N_0 is described by the following simple set of rate equations

$$\frac{dN_R}{dt} = -\frac{N_R}{\tau_R} - WN_R^2(N_0+1) \tag{3.23}$$

$$\frac{dN_0}{dt} = -\frac{N_0}{\tau_R} + WN_R^2(N_0+1) \tag{3.24}$$

Here the scattering rate between the reservoir and the condensate is taken as $W = 10^4$ s^{-1}. $\tau_R = 400$ ps and $\tau_0 = 30$ ps are the lifetimes of the reservoir and the polaritons respectively. This system of equations is solved by considering a non-zero initial reservoir population N_R^0. The figures 3.8(a,b) show the calculated and measured intensity of the emission versus pumping power. One can see that despite the assumptions and simplifications made by the model, the general agreement with the experiment is quite satisfactory. Fig.3.8(c,d) show the calculated and measured time resolved emission intensity for different pumping powers. Below $2P_{th}$ (P_{th} defining the condensation threshold), a long rise time of the emission is observed. The decay time (not shown) is of the order of hundreds of ps and is governed by the exciton reservoir life time. The situation radically changes at 3-4 P_{th}. The rise time shortens and becomes a few tens of ps and is followed by a monoexponential decay time of 40 ps given by the polariton lifetime. In this regime, we expect the excitonic reservoir to be quickly transferred to the condensate, which then decays with its lifetime. This is confirmed by Fig.3.8(e) which shows, for 4 different pumping rates, the calculated dynamics of both ground state and reservoir populations. These results have been obtained with simplified semiclassical Boltzmann equations. At threshold, the condensate population is completely negligible and all decay times are given by the reservoir decay time (400 ps). The situation radically changes at higher pumping. One can see that the rise of the condensate is accompanied by a depletion of the reservoir. The condensate population becomes completely dominant in a very large time window, where the decay time of the emission is of the order of 30 ps. This pumping range and time window is favorable to observe inter-particle interactions within the condensate, which can lead to the formation of gap solitons as we will see now.

3.2.4 Formation of gap solitons in the pulsed regime

The experimentally measured spatial distribution of the emission is presented in Fig.3.9(a). In order to properly identify which polariton state is emitting for each

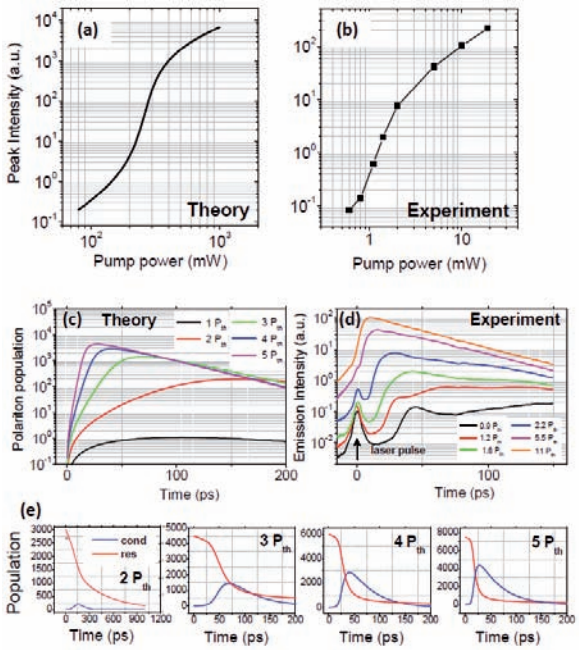

Figure 3.8: (a,b) Emission peak intensity versus pump power: (a) theory, (b) experiment. (c) Calculated polariton population as a function of time for several pump powers. (d) Measured total emission intensity as a function of time for different excitation powers. (e) Time evolution of the population of the reservoir (red) and of the condensate (blue).

time interval, we show the spectrally resolved emission for different time delays in Fig.3.9(b-e). Right after the laser pulse arrival, the excitonic reservoir gets populated and the relaxation and condensation toward low energy polariton state is triggered. First, the emission mainly arises from high energy polariton states, close to the excitonic reservoir and from the second polariton sub-band. Since polaritons in the second band have high group velocity, they can propagate rapidly outside the excitation region. This is why for short time delays, an exponential decay is observed in the spatial intensity profiles [reported in Fig.3.9(f,g)]. At longer times, the emission energy decreases due to both energy relaxation and the decay of the overall exciton and polariton population. Interestingly, in the time-window (50-80 ps), the emission is dominated by a state lying inside the energy gap [see Fig. 3.9(d)]. States at higher energy show almost no emission [Fig.3.9(d)] indicating strong depletion of the reservoir at this moment. An abrupt change in the spatial profile of the emission is observed [see Fig.3.9(g-h)]: starting from an exponentially decaying profile given by the propagation, the condensate wavefunction becomes focused, and well fitted using the characteristic hyperbolic secant density profile of a gap soliton:

$$n\left(x\right)=\left|\psi\left(x\right)\right|^{2}=\left|\psi\left(0\right)\right|^{2}\mathrm{sech}\left(\frac{\mathrm{x}}{\xi\sqrt{2}}\right)^{2} \tag{3.25}$$

Here n_0 is the soliton peak density. The figures 3.9(g-h) show fits of the emission using Eq.(3.25), and the good qualitative agreement gives strong support to the interpretation of the gap states as gap solitons. As the energy further decreases, the condensate reaches the first polariton miniband [Fig.3.9(e)]. The self-focused wave is strongly enlarged again, transforming into a spreading wavepacket [Fig.3.9(i)].

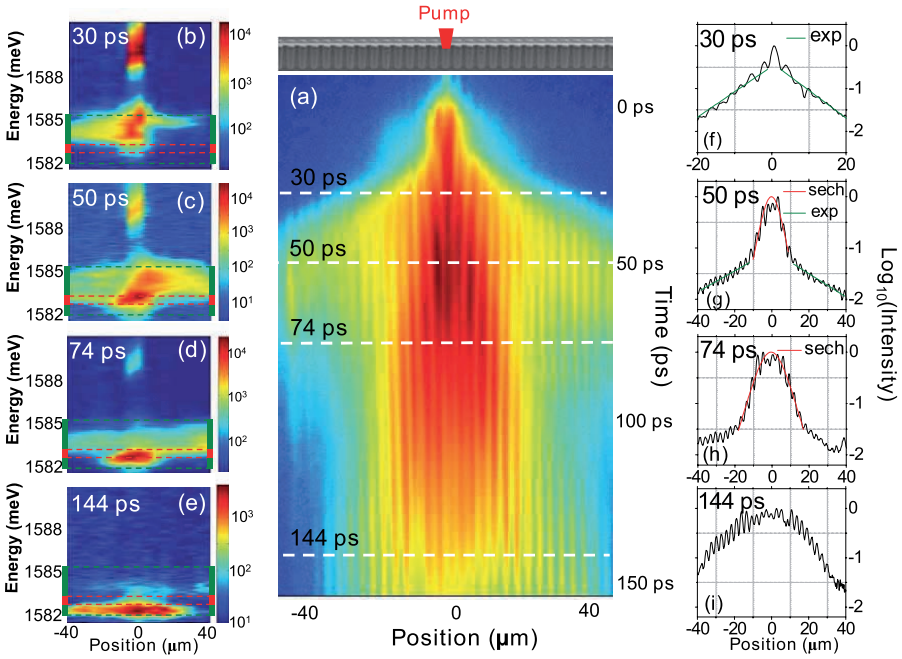

Figure 3.9: Condensation dynamics under pulsed excitation. (a) Spatially resolved emission as a function of time measured on a single modulated wire for an excitation $P = 3P_{th}$, P_{th} being the threshold power. The 2 μm radius and 1.6 ps pulse excites the sample at $y = 0$ μm and $t = 0$ ps. (b-e) Spectrally resolved spatial distribution of the emission for different time delays after the arrival of the laser pulse. The chosen times are indicated as horizontal dashed lines in (a). The first and second allowed energy mini-bands are indicated as green rectangles while red ones highlight the first band-gap. (Parameters of the wire: same as in Fig.3.8 except for $\delta = -3$ meV). (f-h) Normalized spatial profile of the emission extracted from (a) for the same time delays of panels (b-e). The green lines correspond to exponential decays and fits using the gap soliton wavefunction given by the expression (3.25) are shown with red lines.

These measurements demonstrate the successive switching from propagating to a localized gap soliton regime. Then, the passage from the gap state into the first miniband propagating regime is evidenced, when looking at the time evolution of the emission energy. Fig.3.10(a) shows a step-like jump in the energy decrease occurring exactly at the moment corresponding to the transition from the gap soliton regime to the propagating regime in the first mini-band. This is caused by the abrupt decrease in the density when the strongly self-interacting soliton reaches the first

miniband, and rapidly spreads, losing all its interaction energy.

This step-like behavior has been reproduced theoretically [see inset of Fig.3.10(a) and Fig.3.11]. To do so we have included exciton-exciton interactions adding the usual term $\alpha|\chi|^2\chi$ to Eq.(3.22) completely neglecting the strongly depleted reservoir. In such a configuration, the only energy relaxation mechanism involves the lifetime of the particles that makes the interaction-induce decay with time. Here it is difficult to start from an initial condition e.g. from a state lying at the bottom of the second energy band since in this place the particles would decay diffusively without relaxing their energy. Therefore we have resorted to the following trick: We use a *quasi-resonant* pulsed pump detuned by +0.2 meV from the top of the first energy band, the spot width is taken to be small in order to have a sufficient extension in momentum space to excite equally both edges of the first Brillouin zone. Then we use a sufficient pump power to benefit from the bistability effect setting the localized macroscopically occupied state at the top of the gap. We then monitor the lifetime-induced relaxation dynamics shown in the figure 3.11(a-c). The panel (a) shows the energy of the wave-packet versus time. A strongly nonlinear and discontinuous relaxation is obtained: indeed, in the lower half of the gap, one can observe a discontinuous jump before the ground state is reached. In the panel (b) we show the real space dynamics, demonstrating an initial propagative behavior, because of the pulsed pump-induced linewidth, which allows an overlap with the bottom of the second energy band to occur, then a localization of the wave-packet while the gap is crossed (from 20 to 100 ps), and finally, the propagation is recovered entering in the first band. In the panel (c) we analyze the density profile (black line) of the localized wave-packet within the gap at energy and instant marked by the dashed white lines in the panels (a) and (b) respectively. The red curve is a fit of the profile using the function (3.25) where $\xi = 3$ μm. This simulation not only reproduces well the experimental behavior, but also suggests another efficient means of creating gap solitons in semiconductor microcavities using resonant pumping. We have by the way checked that this technique allows to form *propagating* gap solitons, which could be crucial to use such solitonic states as information carrier analogically to slow light in optical fibers.

We have as well theoretically considered the opposite regime, which corresponds to lower excitation power. The excitonic reservoir is still populated and induces a blueshift of the polariton condensate energy due to repulsive interactions. In this case the simulation is based, at first, on the analysis of the dispersions at different reservoir densities, in order to find the conditions required to have the defect state at the top of the gap. When such state is found, it is used as an initial condition for a simulation, where the reservoir density is progressively decreased over time. The time-dependent equation which is solved is essentially the same as above, except that polariton-polariton interactions are neglected ($\alpha = 0$). Now, the energy evolution [Fig.3.11(d)] is governed by the decrease of the reservoir population. In this case, polaritons are found to be localized in a defect state in the pump region. The energy of this state decreases reflecting the decay of the reservoir population. Once it reaches the conduction band, polaritons start propagating [Fig.3.11(d-e)].

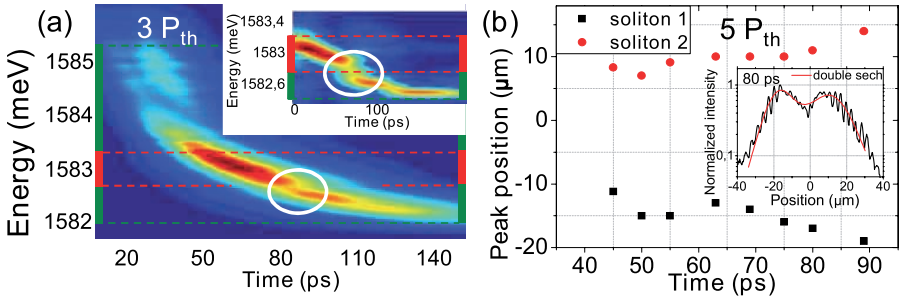

Figure 3.10: Formation of gap solitons. (a) Emission energy as a function of time measured at the center of the wire for $P = 3P_{th}$. The energy gap is shown with a red rectangle while the green one corresponds to the first mini-band. The white arrows point the time delays chosen in (a). The inset shows the time evolution of the emission energy simulated using a time-dependent Gross-Pitaevskii equation [see Fig.3.11]. (b) Positions of the two solitons observed in the case of $P = 5P_{th}$ as a function of time. The inset shows the spatial profile of the emission measured at 80 ps and a fit using a double gap soliton function.

The localized state presents the spatial exponential decay typical for defect state [Fig.3.11(f)], being clearly different from the profile of the gap soliton.

Finally, we show that pumping at higher power we were able to nucleate two gap solitons propagating away from the excitation area. Again, right after the pulse arrival, polaritons are formed in the second minigap and spread from the excitation region further than in the previous case. When the decaying condensate reaches the gap, it is significantly wider than the soliton characteristic width subsequently leading to the nucleation of two distinct gap solitons symmetrically positioned on each side of the excitation spot. The corresponding spatial emission profiles are shown in Fig.3.10(b), where the pump power is 1.7 time larger than in Fig.3.9. These gap solitons repel and move away from each other. Both the self-organization of a spatially wide condensate into several solitons, and the mutual repulsive interaction are the expected properties of bright gap solitons[16].

3.2.5 Conclusion

The time resolved experiments under non-resonant excitation provide a very effective and simple way to create gap solitons in a polariton condensate. This is in strong contrast with standard photonic systems, where the excitation of gap solitons requires complex strategies using resonant beams. Moreover, contrary to the atomic system in optical lattices which requires numerous lasers to trap the condensate and form the lattice, here we only need one laser. The polaritonic gap solitons could be further manipulated, for instance, by using several control beams in fully reconfigurable polaritonic circuits. In such a way, the information could be stored in polaritonic gap solitons, then released, and eventually transmitted in an ultrafast way. We have not considered in that work the spin degree of freedom of polaritons

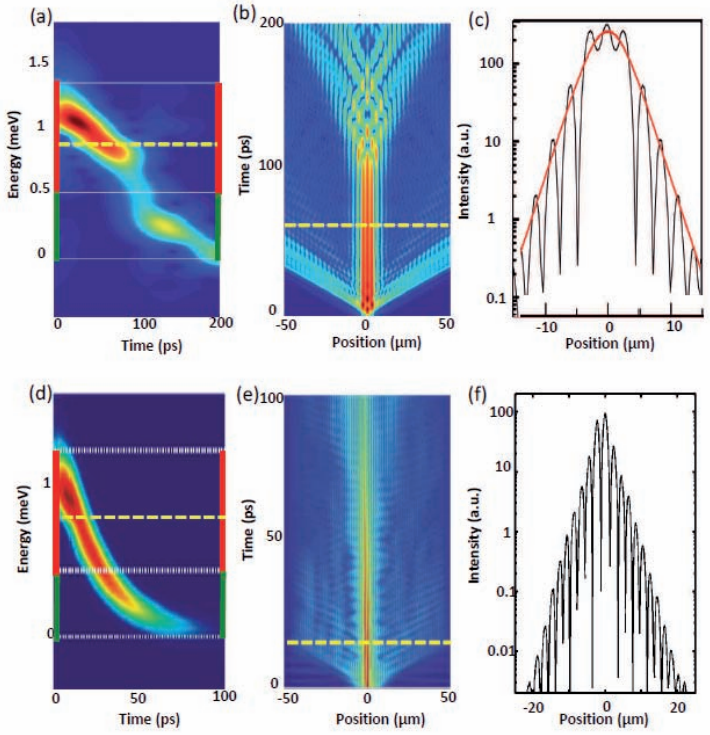

Figure 3.11: (a-c): Simulated emission dynamics in the case where only polariton-polariton interaction is taken into account. (a) Energy of the polariton condensate as a function of time. The red and green rectangles represent the energy gap and the first mini-band respectively. (b) Time resolved spatial distribution of the polariton condensate. (c) Density profile of the condensate at a time delay indicated by the dashed yellow lines in (b). The red line is a fit with the gap soliton function (3.25) introduced in the main text. (d-e) Same as (a-c) in the case where only polariton interaction with the exciton reservoir is included.

that could allow to form propagating polarized gap states.

3.3 Bloch oscillations of exciton-polaritons

In this section, we will first study theoretically spinless Bloch oscillations of exciton-polaritons both in linear and in condensed regimes [6]. We propose an original structure for the observation of this phenomenon despite the constraints imposed by the relatively short lifetime of the particles. First, we focus on the linear regime in a perfect lattice where regular oscillations are obtained. Second, we take into account a realistic structural disorder known to localize non-interacting particles, which is quite dramatic for propagation-related phenomena. In the non-linear condensed regime, the renormalization of the energy provided by interactions between particles allows us to screen efficiently the disorder and to recover oscillations. This effect is useful only in a precise range of parameters outside of which the system becomes dynamically unstable. For a large chemical potential of the order of the potential's amplitude, a strong Landau-Zener tunneling tends to completely delocalize particles.

In a second part, we shall discuss the spin dynamics of polaritons during their Bloch oscillations in the presence of the effective field present in the structure [7]. We show that the periods of the Bloch oscillations and of the pseudospin precession can become commensurate. Under such conditions, linearly polarized exciting pulses can be transformed in a THz alternating spin current. The structure acts as a spin-optronic device, which converts the polarization and emits spin-polarized pulses. Finally, we propose two different schemes which allows to maintain the intensity of the spin signal during times much larger than polaritons lifetime.

3.3.1 Spinless Bloch oscillations in a disordered microcavity

In 1929, F. Bloch predicted that an electron in the atomic periodic potential would oscillate in time rather than simply accelerate under the action of a constant electric field[12]. This pure quantum phenomenon is the consequence of Bragg reflections on the first Brillouin zone (FBZ) [see Sec.(3.1.1.1)]. Although widely discussed during the last century, Bloch Oscillations (BOs) were only observed in the 90s in artificial crystals (superlattices) [44, 45, 46].

BOs have been described and observed in three alternative systems showing extended spatial and long temporal coherence, namely, coherent light waves propagating in photonic crystals [47, 48], ultracold atoms [49], and atomic Bose-Einstein condensates (BECs) in optical lattices [50, 51] [see Fig.3.12]. In the linear regime, the electronic, photonic, and atomic systems show very similar single-particle behavior. However, they differ strongly in their specific non-linear response. In electronic systems, dephasing leads to the destruction of coherent BOs. On the other hand, photons are non-interacting particles, and of course, if they propagate in a linear media, no peculiar non-linear behavior is expected. The situation is radically different for atomic BECs in optical lattices, where the transport properties are strongly affected by the non-linear effects linked with the density of condensed particles. The latter topic is still widely under discussion, as rich physics emerges out of it [52, 53, 54]. Indeed, while an optical lattice constitutes a perfect periodic optical

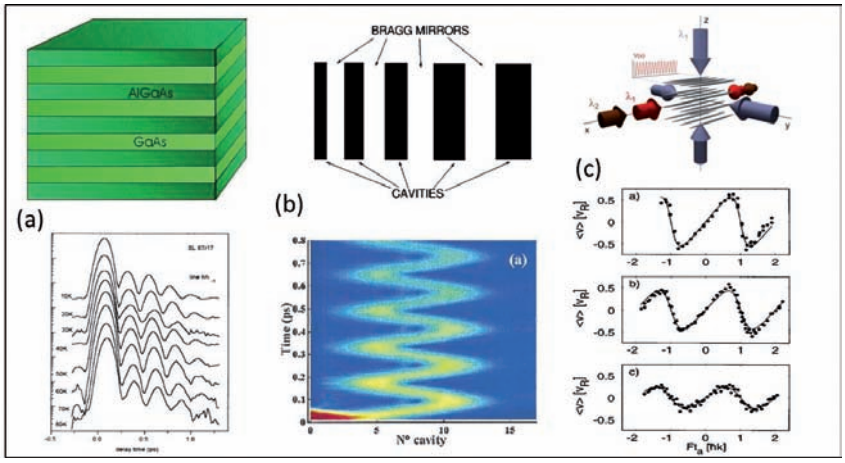

Figure 3.12: Experimental observation of Bloch oscillations of: (a) electrons in a superlattice from Ref.[44], (b) cavity photons in an array of semiconductor microcavities having varying thickness from Ref.[48] and (d) ultracold cold atoms in an optical lattice from Ref.[49].

crystal that can lead to long living BOs of dilute (ultra)cold atoms [55], a BEC can experience decoherence [56] and dynamical instabilities [15, 57] due to non negligible interactions. Moreover, the account of disorder leads to phenomena such as Anderson-like localization [58, 59] or the breakdown of superfluidity [60, 61]. The non-uniformity of the potential tends to prevent wave function's spreading, while interactions drive the system toward superfluidity. This interplay has serious consequences for the phase diagram of the system [62, 63] and most importantly, the disorder induces extra dephasing which is revealed by a damping of the matter wave BOs [64, 65]. Besides, new perspectives have recently been opened by works focused on spin related BOs [66, 67, 68].

In this section we theoretically describe BOs of polaritons in a patterned one-dimensional microwire. In both atomic and optical systems, it is possible to design a potential that allows short period oscillations (less than 1 ps for instance, in Ref.[47]). This short period cannot occur in polaritonic systems, where oscillations must take place in the strongly coupled part of the lower polariton branch. In total, the width of the first Brillouin zone has to be smaller than one fourth of the Rabi splitting. This gives values of the order of $1-5$ meV and implies some lower bound for the BOs period, that, at the same time, has to be be smaller than the polariton lifetime.

In the first part of this section devoted to Bloch oscillations, we propose a realistic structure in which polariton BOs could be observed, and show numerical simulations in the linear regime. In the second part of the paper, we study the effect of structural disorder on BOs of a polariton condensate. Indeed, an important peculiarity of the polariton system is that it is affected by intrinsic sample disorder which can be absent in atomic systems and which perturbs much less the propagation of pure

photons. As a result, polaritons are often found to be localized [1, 69, 70], which evidently can make the observation of propagation effects, like BOs, difficult. In the non-interacting regime, we can expect that the polaritons' motion will be blurred (dephased) with increasing disorder potential. So, strictly speaking, an uncondensed thermal gas of polaritons cannot undergo BOs, if the disorder is too important. Nevertheless, the formation of an interacting polariton BEC should permit us to recover an oscillatory behavior as a result of a partial screening of the disorder. The growth of interaction energy leads the polariton gas toward superfluidity at low velocities, where the influence of disorder is the strongest.

In general, the oscillations are found to be damped because of both the residual scattering by disorder when polaritons are moving at a supersonic velocity, and the occurrence of specific parametric instabilities, discussed in Ref.[71] and well known in the atomic BEC field, when polaritons are accelerated to the inflexion point in the first Bloch band of the dispersion [see Sec.1.3.2]. The most interesting result is that one of these effects can compensate the other: The interactions protect (at least partially) the BOs from the damping linked with disorder. The precise characterization of these non-linear scattering processes is not in the scope of the present discussion. However, we would like to point out a key specificity of the polariton system with respect to the atomic one: the possibility to perform resonant excitation experiments (with spatial and frequency resolution) that allows us to address specifically the various non-linear scattering processes that interacting particles accelerated in a disordered periodic potential can undergo.

3.3.1.1 Structure and linear Bloch oscillations

The structure proposed is schematically shown in Fig.3.13(a). It is based on a $L_x = 100$ μm long GaAs microcavity etched in the y-direction in order to realize a wire having a lateral size in the μm range. The confinement energy provided by the lateral etching is approximately $E_c = \hbar^2\pi^2/2m^*L_y^2$, where $m^* \sim 2m_\phi$ (at zero detuning) is the effective mass of the polariton. The linear potential ramp needed in order to mimic the electric field acting on electrons can be realized by changing the lateral size of the wire along its main axis x with a square root dependency $L_y(x) \sim L_0/\sqrt{x}$ in the region where BOs are expected. In principle, any type of accelerating potential can be designed thanks to modern lithography technics, but of course, there are some limitations due to the confinement energy dependence. It is also possible to make use of the wedge character of microcavities along the growth z-direction [72]. It should be noted that this potential ramp will be acting on the photonic part of the quasi-particle. In this work our proposal was to use periodic metallic deposition to form Schottky like junction (Tamm plasmon polariton states) that would locally blueshift (redshift) the polariton modes [37, 73]. We understood later on, in the framework of our collaboration with the LPN for the gap soliton observation, that the metal tends to reduce significantly the photon lifetime which can be strongly detrimental to propagation related effects. Therefore, the best option would actually be to use a squarewave lateral etching in addition to the

variation of the cavity width to form the required tilted periodic potential. Anyway, the following strictly 1D description does not favor any sample design apart from the fact that a lateral etching would act on the photonic component solely, which would definitely not change qualitatively the wavepacket behavior.

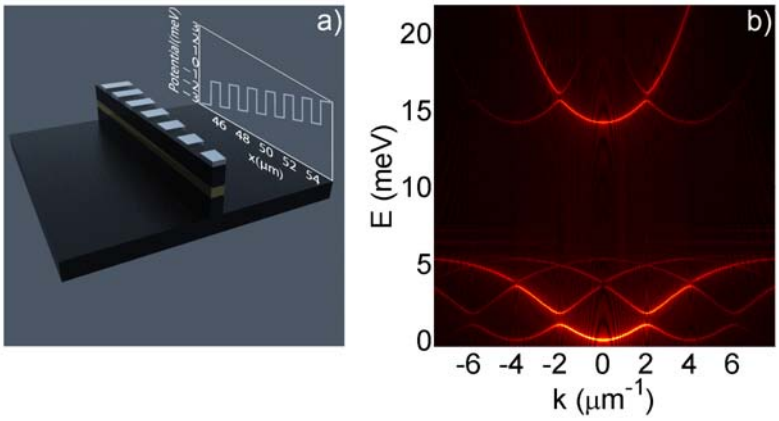

Figure 3.13: (a) The structure: laterally narrowed wire shaped microcavity with periodic metallic depositions and the resulting total potential (Only the central part where oscillations take place is represented for clarity). (b) The associated initial dispersion of the particles modified by the periodic potential $U_{ex}(x)$ created e.g. by the metal or a lateral etching.

To describe the linear dynamics of the system we use the 1D counterpart ($\mathbf{r} \to x$) of Eqs.(3.21,3.22) involving the resonant injection of a polariton wavepacket at $k_x = 0$. $U_\phi(x) = -Fx$ and $U_\chi(x)$ are here the accelerating ramp potential producing a constant force $F = 0.2\ meV/\mu$m [see Sec.(3.1.1.1)] and the squarewave potential of period $d = 1.56\ \mu$m and realistic amplitude $A = 2\ meV$, respectively. The corresponding recoil energy is $E_R \simeq 3$ meV and therefore the situation is that of a shallow lattice. Fig.3.13(b) shows the modified dispersion of exciton-polaritons with gaps both in the upper and lower polariton branches (LPB), opened by U_χ. In the following, we will concentrate on the LPB, where the condensation usually takes place. The gap and the first band where oscillations are expected, have width of $E_g = 0.75$ meV and $\Delta_1 = 1$ meV, respectively.

To begin our analysis and demonstrate the possibility of obtaining regular single-particle BOs in such a system, we show in Fig.3.14(a) the propagation of a 2-ps-long and 20-μm-large photonic Gaussian pulse tuned close to the energy of the LPB at $\mathbf{k} = \mathbf{0}$, with an amplitude low enough to assume a linear regime. Under the action of the constant force and for the parameters we use, our system exhibits BOs of amplitude $A_{BO} \approx 12\ \mu$m and period $T_{BO} \approx 25$ ps; the latter is close to lifetime of the particles. A further increase in F, would enhance the Landau-Zener tunneling (LZT) probability [slightly visible in Fig.3.14(a)] given by Eq.(3.16), and induce a significant splitting of the wave function at each period of oscillations. Fig.3.14(b) shows the time evolution of the wave vector k_x along the wire with the characteristic

reflections on the first Brillouin zone edges, which has an extension $Z_B = 2\pi/d = 4$ μm^{-1}, changing k_x into $-k_x$. We emphasize that the long polariton lifetime obtained in modern structures is crucial (larger than 30 ps in Ref.[74]) for the observation of polariton BOs. With the realistic limitations on the ramp potential, it is difficult to reduce the period of oscillations below 20 ps. Therefore, the polariton lifetime should exceed this value, for the phenomenon to be observable.

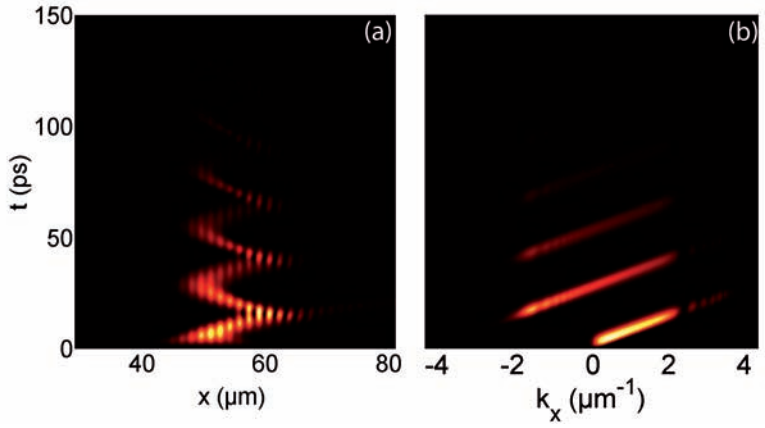

Figure 3.14: Propagation of a photonic Gaussian pulse in the biased square-wave potential. (a) The density probability versus time and space reveals clear BOs with a period of 25.3 ps and an amplitude of 11.7 μm, and (b) density vs time and momentum shows the characteristic reflections on the edges of the FBZ where the particles are localized. In both plots a LZT is visible as a fraction of the non-oscillating particles that escape at each period.

3.3.1.2 Bloch oscillations of the polariton condensate

In this second part, we consider the real specificity of the polariton condensate with respect to the coherent photonic wave, namely, the role played by interactions. This role is actually better revealed by considering the impact of a realistic structural disorder on polariton BOs. This disorder can have several origins, which could be the intrinsic sample imperfections, the non-ideal lateral etching, or some natural (artificial) fluctuations of the wells' depths and widths in the periodic potential. We assume that initially, before the potential ramp is applied, the resonantly created polariton condensate is at thermodynamic equilibrium at $T = 0$K, and is therefore in its lowest energy state. This situation corresponds to a nonresonant and homogeneous pumping over the whole sample. The ground state is found by minimizing at fixed chemical potential the free energy of the coupled exciton-photon system:

$$E = \int_0^{L_x} dx \sum_{\psi=\{\phi,\chi\}} \left(\frac{\hbar^2}{2m_\psi} |\nabla\psi|^2 + U_\psi |\psi|^2 \right) + \frac{\Omega_R}{2} \left(\phi\chi + \phi^*\chi \right) + \frac{\alpha}{2} |\chi|^4 \qquad (3.26)$$

Next we solve the time-dependent Eqs.(3.21,3.22) adding the interaction term $\alpha|\chi|^2\chi$ to Eq.(3.21), starting from the initial condition given by the ground state found previously, taking into account the action of the accelerating ramp potential for different chemical potentials μ (given by the energy of the ground state). To clarify, we first assume first an infinite lifetime of the particles. We show different accessible regimes (described in the next paragraph). Figures 3.15 and 3.16 display the probability density of the photonic wave function versus time and momentum and the associated average probability current of the condensate. The latter is given by

$$\langle j\,(t)\rangle = \frac{i\hbar}{2m^* N\,(t)} \int_0^{L_x} dx\,(\phi\nabla\phi^* - \phi^*\nabla\phi) \tag{3.27}$$

where $N(t)$ is the total density of particles and is time dependent to compensate for absorbing boundary conditions the lifetime of the particles (taken into account later on). Indeed, $\langle j(t)\rangle$ is relevant for imaging the global motion of the condensate, changing its sign $\langle j\,(t)\rangle > 0\ (< 0)$ when particles change their propagation direction.

The ground state of a non-interacting or, equivalently, a very dilute condensate in the presence of disorder is mainly localized in the lowest well of the sample. As a result, while the condensate is put into motion by the constant force, it is very sensitive to the disorder; the latter induces back-scattering [74], which leads to a dephasing and thus either to a damping of the oscillations or to their total destruction if the inhomogeneity is strong. In that latter case the system as a whole is insulating. In real systems we can expect the disorder induced by the sample imperfections to be weak with respect to the total periodic potential's amplitude. In order to introduce imperfections, we modulate the square-wave potential randomly in amplitude along the wire with a standard deviation $U_d = 0.1$ meV from the original potential. In Figs.3.15(a,b) we present this non-interacting case, which corresponds to a zero chemical potential ($N = 1$ particle). The dephasing is visible in Fig.3.15(a) where the creation of new harmonics blurs the oscillations, resulting in a damping and deformation of the motion in Fig.3.15(b). The solid blue curve corresponds to the parameters given here while the dotted-red curve is for a disorder that is twice stronger, showing the total suppression of the oscillations.

With the increase in the chemical potential, interactions drive the system toward superfluidity in the sense that was used in Ref.[69], that is, particles are no more affected by the presence of an in-plane potential so they can freely propagate in space without being scattered, and the interaction energy is able to efficiently screen the disorder. This phenomenon is called a "dynamical screening of disorder" in Ref.[64]. As a result, the damping is significantly reduced. Thus, owing to the interacting nature of the particles involved, BOs of exciton-polaritons are observable despite the presence of a structural disorder. Such a situation is depicted in Fig.3.15(c) and 3.15(d) for $\mu = 0.3$ meV.

Nevertheless, interactions are not sufficient to recover perfect oscillations obtained in linear homogeneous regimes, as one can see in Fig.3.15(d), and they also have drawbacks: Indeed, while the condensate is accelerated up to the first Brillouin

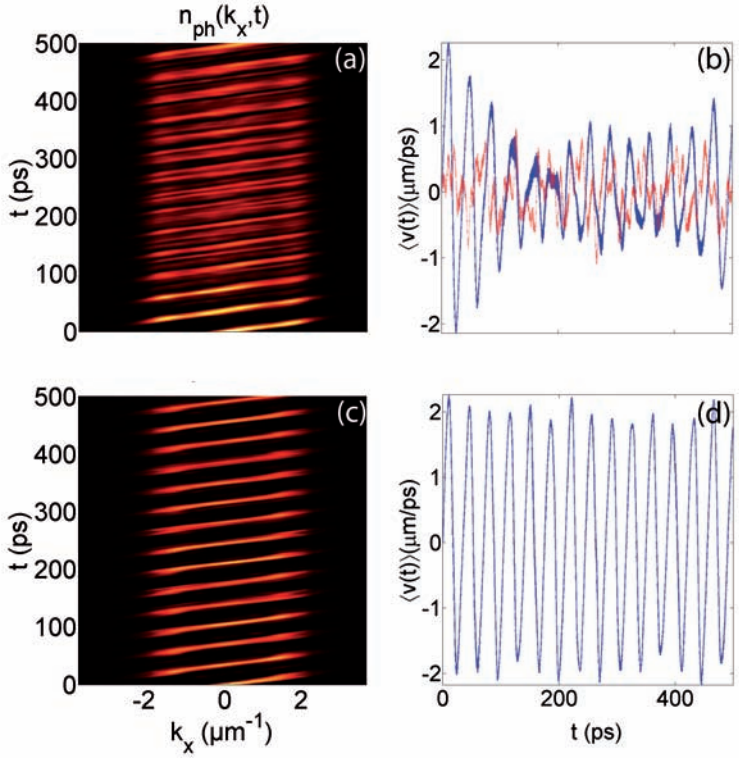

Figure 3.15: Bloch oscillations in the presence of structural disorder. (left panel) Probability density of the photonic wave function versus time and momentum. (right panel) Average velocity of the condensate versus time. (a) and (b) Non-interacting damped case ($\mu = 0$) for $U_d = 0.1$ meV (solid blue curve) and $U_d = 0.2$ meV (dotted red curve). (c) and (d) Interaction-induced revival of the oscillations for $\mu = 0.3$ meV.

zone, at a certain point, the velocity exceeds a critical value, and the particles enter a supersonic regime where they are no longer superfluid and are thus scattered on the disorder. Scattering results in a dephasing of the oscillations while approaching the FBZ's edges. Moreover, with a further increase in the density, parametric instability develops [15, 57, 71]. As already discussed in the Sec.(1.3.2), this kind of process is well known in the field of polaritons as the lower branch of their bare dispersion possesses an inflection point; thus above some density threshold, two polaritons can scatter at this point towards signal and idler states, conserving both momentum and energy. Here the same kind of phenomenon takes place, independently of the disorder, within the Bloch bands, which obviously possess their inflection points. We show in Fig.3.16(a) and 3.16(b) this kind of phenomenon appearing for $\mu = 0.5$ meV; oscillations are completely deformed and no more quantifiable. It is important to note that for stronger disorders, it is not possible at all to find a screened regime [Fig.3.15(a)-(b)], because the system enters the parametric instability region before recovering oscillations.

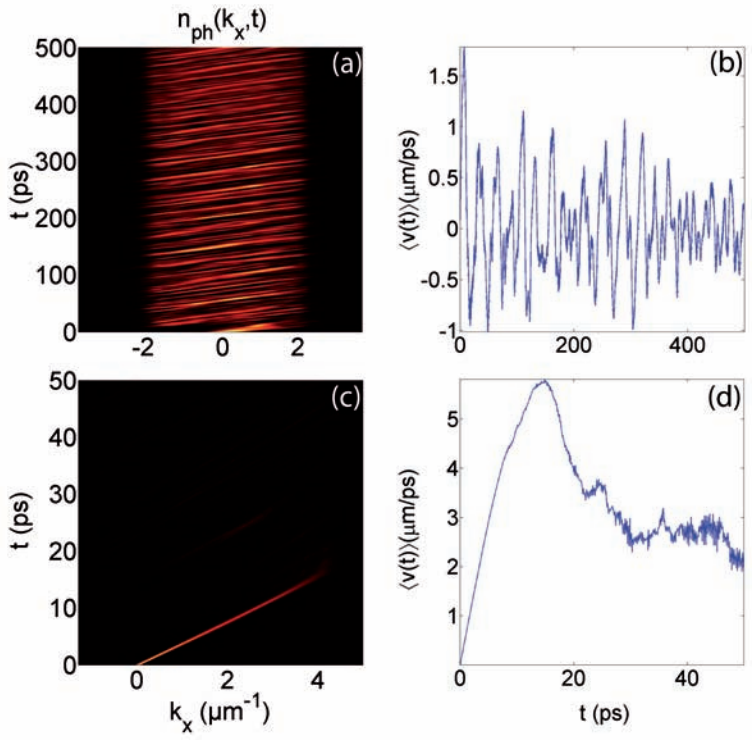

Figure 3.16: (a)-(b) Unstable and (c)-(d) strong LZT regimes. For $\mu = 0.5$ meV and 3 meV, respectively.

Finally, an even stronger density wipes out all the effects mentioned above and puts the Landau-Zener tunneling into play. The interactions renormalize the lowest Bloch band, almost closing the gap in the dispersion and increasing drastically the probability of the tunneling to the second band [75]. As a result, BOs vanish, and particles are almost uniformly accelerated. They practically no longer feel the lattice. This regime is illustrated in Figs.3.16(c) and 3.16(d) for a very strong, although probably not experimentally accessible, chemical potential of $\mu = 3\ meV$. The condensate is accelerated to the edge of the sample and disappears on the absorbing boundaries, as seen in 3.16(c). The particles are no longer reflected at the Brillouin zone edges. In Fig.3.16(d), the mean current keeps increasing until particles reach the boundary, and then decreases because of the remaining trapped particles.

Eventually, we will now take into account the finite lifetime of the particles to move to a realistic situation. In that case, the condensate will oscillate a few times and exponentially decay. Therefore we of course, expect the interaction energy to vanish with the particles; thus, a condensate prepared with a sufficient chemical potential to screen the disorder will suffer from growing localization with decreasing density, which will damp the oscillations. So here the ratio between lifetime and oscillation period becomes even more crucial. Fig.3.17 illustrates such a situation,

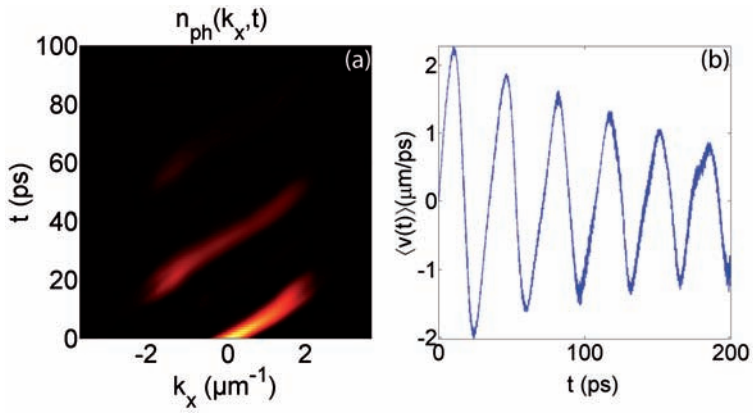

Figure 3.17: Taking into account the finite lifetime of the particles for $\mu = 0.35$ meV. (a) Oscillations remain visible, but (b) they are damped due to the decreasing interaction energy.

where $\mu = 0.35$ meV is taken slightly higher than in Figs.3.15(c) and 3.15(d) to compensate as much as possible for the localization for first oscillation periods. While the damping remains significant as seen in 3.17(b), several oscillations should be observable as shown in 3.17(a). Furthermore, in the next section we will see how the polariton BOs can be sustained to compensate for this natural decay.

3.3.1.3 Conclusions

In conclusion, we have proposed a realistic structure in which Bloch oscillations of exciton-polaritons, a phenomenon not previously reported, could be observed. We have analyzed both the linear and non-linear behavior and found a regime where oscillations are able to overcome the disorder expected in realistic systems as a result of to the interacting nature of the particles. At higher chemical potential, dynamical instability switches on and destroys oscillations, and at even higher density the massive Landau-Zener tunneling leads to a strong delocalization of the particles.

Regarding a real experimental investigation, we would like to point out some phenomena to be envisaged. First of all, metallic deposition will tend to reduce the cavity photon's lifetime; thus a lateral (along the x-axis) square-wave etching could be considered as a serious option. In a real two-dimensional system one should expect transverse excitations to modify the instability threshold [76]. Finally, in a configuration where Landau-Zener tunneling is significant (for a weak lattice or strong potential ramp) the wave function will split and the non-oscillating part could be backscattered at the wire's edges, which will slightly blur the motion. Nevertheless, the exceptional progresses in growth and technology leads to higher and higher quality sample characterized by lower and lower structural disorder therefore we can safely expect that the polaritons Bloch oscillations could be observed even in the linear regime.

3.3.2 Bloch oscillations of exciton-polaritons for the generation of an alternating THz spin current

The ultimate goal of spintronics is to replace electric currents by pure spin currents. Its optical counterpart, namely spin-optonics [77], has been proposed as a valuable alternative, since the characteristic decoherence times of optical excitations are orders of magnitude longer than those of electrons and holes. Consequently, many proposals of new types of optical spin-based microscopic components have been made in the past years. Non-exhaustively, one can mention: an optical gate[78], optical circuits based on polariton neurons[79], a Berry phase interferometer[80], a spin transistor[81], or a spin switch [82]. This field of research is extremely promising.

In the following, we shall extend the previous discussion on Bloch oscillations of polaritons, discussing the new phenomena to be expected from their spin dynamics. In this framework, we make a realistic proposal for device generating alternating THz spin currents which could be a key ingredient for a spin-optronic circuit. Noteworthy, regular BOs have been already proposed as a possible source of THz radiations [83] or as a tool to measure very sensitive atomic physical quantities [84, 85].

We will first mostly concentrate on the low-density linear regime, neglecting polariton-polariton interactions. In such a regime, low-momentum polaritons do not strongly differ from cavity photons, and most of the effects we find can perfectly be obtained for a purely photonic system as it was recently the case for the optical spin-Hall effect [86, 87]. However, in the very last part of this section we will discuss a polariton-specific nonlinear stimulation mechanism. The disadvantage of polaritons is mostly that they of course require low temperature operation, while their advantage in the linear regime lies in the possibility to finely tune the energy of the polarized polariton modes[88] with an electric field acting on the quantum well excitons. Similar modulation can of course be achieved in purely photonic systems with the Pockels or Kerr effects [89], but they require field intensities orders of magnitude larger than in the polariton systems. We will describe the polaritonic system as a reference and, when needed, comment on whether the description is also suitable for a photonic system.

3.3.2.1 LT splitting in microwires

We remind that, in quasi-one dimensional microcavities the TE and TM eigenmodes are linearly polarized perpendicular and parallel to the wire's axis (x-axis) respectively. The additional confinement lifts the degeneracy between the TE and TM modes even at $\mathbf{k} = \mathbf{0}$, like in usual photonic waveguides (leading to the monopole acceleration see Sec.(2.2). It provides an additional effective *static* (or k-independent) magnetic field along the x-axis. While this splitting is already present in planar structures as first demonstrated in Ref.[90], it is however much larger in wires. Mainly because of strain relaxation, the effective values can moreover be much larger than the one extracted from Maxwell's equations in isotropic media [91]. In what follows, we will consider the same patterned wires as in the section (3.3) sketched

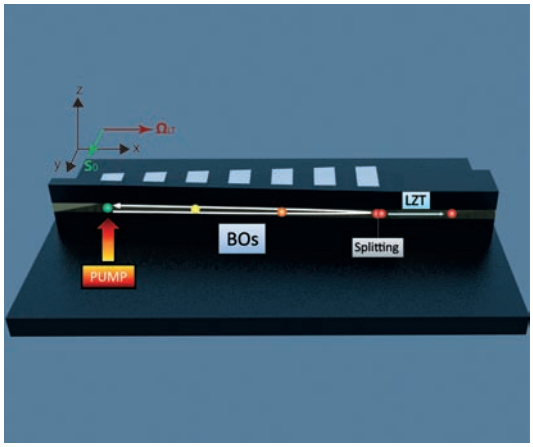

Figure 3.18: Scheme of the sample. Wire shaped microcavity with periodic metallic deposition. The situation described here corresponds to the results of Sec.3.3.3. The red arrow shows the direction of the effective magnetic field $\boldsymbol{\omega}_{LT}$, and the green arrow shows the initial pseudospin vector $\mathbf{S}_0$. The white curved arrow shows the trajectory of the particles during one period of BO. The light-blue arrow stands for the LZT-induced emission. The spheres mark the position of the Gaussian pulse during its first passage in the wire, and the (linear) color map indicates the degree of circular polarization: green is 0 (linear polarization) and red is ± 1 (circular polarization).

in Fig.3.18. In these samples, the total energy splitting is the strongest at $\mathbf{k} = \mathbf{0}$ and diminishes for increasing $\mathbf{k}$ since the excitonic fraction rises for larger k . Although the values of the splitting can be different for polaritons and photons, the general dependence is similar and therefore the discussion concerning the pseudospin dynamics remains valid for both.

The addition of a periodic pattern leads to a band-structured dispersion of the polaritons. The first TE and TM bands as well as their energy splitting gain a $2\pi/d$ periodicity. In what follows, we will see how it influences the spin dynamics (pseudospin precession) of the system. We show in Fig.3.19 the corresponding first TE and TM Bloch bands with their energy splitting. The parameters are those given in the numerical part of the next section.

3.3.2.2 Spin dynamics induced by the polarization splitting

Let us consider first a linear regime and neglect any gain and dissipation. We known that in the presence of an effective magnetic field, the pseudospin dynamics of the center of mass of a Gaussian pulse is given by the following vectorial equation

$$\partial_t \mathbf{S}(t) = \mathbf{S}(t) \times \boldsymbol{\Omega} \tag{3.28}$$

For analytical considerations we assume that our system is described by the tight binding approximation. This approximation is reasonable so far we are discussing

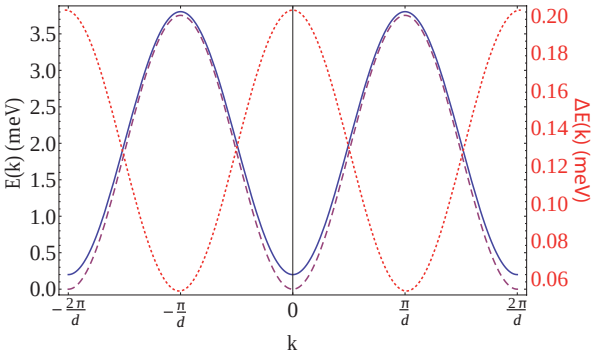

Figure 3.19: First TE (solid blue line and left scale) and TM (dashed purple line and left scale) Bloch bands and their energy splitting (dotted red line and right scale) for the parameters defined in the next section.

phenomena linked with the BOs period (which does not depend on the width of the band) and not with their amplitude. We therefore consider cosine-shaped bands and a strictly one dimensional system ($k_x \to k$). Under such conditions, the first Bloch bands [see Fig.3.19] for the TE (t index) and TM (l index) states are defined by $E_l(k) = J_l[1-\cos(kd)]$ and $E_t(k) = J_t[1-\cos(kd)] + H_x$, where H_x accounts for the energy splitting at $k = 0$ (static field) and $J_{t,l}$ are the coupling constants between adjacent wells. They can be approximated [17] by $J_{t,l} = 4\varepsilon_{t,l}(A/\varepsilon_{t,l})^{3/4}\exp(-2\sqrt{A/\varepsilon_{t,l}})$ with $\varepsilon_{t,l} = \hbar^2\pi^2/2m_{t,l}d^2$ the recoil energies and A the amplitude of the periodic potential. Then, the k-dependence of the effective field along the wire reads

$$\mathbf{\Omega}_{LT} = \Omega_x \mathbf{u}_x = \frac{H_x - \Delta J\left[1-\cos\left(kd\right)\right]}{\hbar}\mathbf{u}_x \tag{3.29}$$

with $\Delta J = J_l - J_t$. Eq.3.28 leads to the following coupled equations for the evolution of the pseudospin components:

$$\partial_t S_x\left(t\right) = 0 \tag{3.30}$$

$$\partial_t S_y\left(t\right) = +\frac{H_x - \Delta J\left[1-\cos\left(k\left(t\right)d\right)\right]}{\hbar}S_z\left(t\right) \tag{3.31}$$

$$\partial_t S_z\left(t\right) = -\frac{H_x - \Delta J\left[1-\cos\left(k\left(t\right)d\right)\right]}{\hbar}S_y\left(t\right) \tag{3.32}$$

Under the action of a constant force F, the particles exhibit BOs. Therefore, in the equations for the pseudospin, the wavevector is time dependent $k(t) = Ft/\hbar$. The period of oscillations depends on the splitting Fd between the so called Wannier-Stark states: $T_{BO} = 2\pi\hbar/Fd$. Putting for example Eq.(3.32) into Eq.(3.31) allows decoupling the equations. The pseudospin is then governed by the following dynam-

ics

$$S_x(t) = + S_{0x} \tag{3.33}$$

$$S_y(t) = + S_{0y}\cos\left[\frac{(H_x-\Delta J)}{\hbar}t + \frac{\Delta J}{\hbar}\frac{T_{BO}}{2\pi}\sin\left(\frac{2\pi}{T_{BO}}t\right)\right] + S_{0z}\sin\left[\frac{(H_x-\Delta J)}{\hbar}t + \frac{\Delta J}{\hbar}\frac{T_{BO}}{2\pi}\sin\left(\frac{2\pi}{T_{BO}}t\right)\right] \tag{3.34}$$

$$S_z(t) = - S_{0y}\sin\left[\frac{(H_x-\Delta J)}{\hbar}t + \frac{\Delta J}{\hbar}\frac{T_{BO}}{2\pi}\sin\left(\frac{2\pi}{T_{BO}}t\right)\right] + S_{0z}\cos\left[\frac{(H_x-\Delta J)}{\hbar}t + \frac{\Delta J}{\hbar}\frac{T_{BO}}{2\pi}\sin\left(\frac{2\pi}{T_{BO}}t\right)\right] \tag{3.35}$$

where $S_{0i} = S_i(0)$. This solution is deterministic with respect to the sample parameters: a given initial pseudospin vector $\mathbf{S}_0 = (S_{0x}, S_{0y}, S_{0z})^T$ (the polarization of the input pulse) completely defines the spin dynamics of the system. We are dealing with the evolution of a single particle (a center of mass) thus, the pseudospin vector $\mathbf{S}$ should be normalized to unity, it imposes: $S_{0x}^2 + S_{0y}^2 + S_{0z}^2 = 1$. The maximum precession amplitude given by Eq.(3.28) is obtained when $\mathbf{S} \perp \mathbf{\Omega}_{LT}$. For arbitrary parameters, the precession of $\mathbf{S}$ is expected to be independent of T_{BO} as we can see in the figure 3.20(a). However, we can impose a specific pseudospin state $\mathbf{S}_{BO} = \mathbf{S}(jT_{BO})$ with j an integer ($j = 1$ is sufficient), in order to obtain commensurate pseudospin and spatial oscillations. We show in Fig.3.21(b) an example of such a regime with a set of conditions $\mathbf{S}_0 = (0, +1, 0)$ (diagonal linear polarization) and $\mathbf{S}_{BO} = (0, -1, 0)$ (anti-diagonal). The corresponding synchronization criterion reads

$$T_{BO} = \frac{\pi\hbar(1+2\kappa)}{H_x - \Delta J} \Leftrightarrow F = \frac{2(H_x - \Delta J)}{(1+2\kappa)\,d} \tag{3.36}$$

where κ is an integer taken to be zero for the case of Fig.3.20(b). For example, using the typical parameters $H_x = 0.2$ meV and $\Delta J = 0.1$ meV we obtain $T_{BO} \simeq 20$ ps and $F \simeq 0.13$ meV/μm which enters perfectly in the range of accessible values for polaritonic or photonic systems.

Let us now turn to numerical modeling of the system. For this purpose, we use a set of spin-dependent Schrödinger equations and, for a first simple description, we start with neglecting the lifetime of the particles and assuming parabolic bare dispersions

$$i\hbar\frac{\partial}{\partial t}\begin{pmatrix}\psi_+\\ \psi_-\end{pmatrix} = \begin{pmatrix} -\frac{\hbar^2}{2m^*}\frac{\partial^2}{\partial x^2} + U & \beta\frac{\partial^2}{\partial x^2} + H_x \\ \beta\frac{\partial^2}{\partial x^2} + H_x & -\frac{\hbar^2}{2m^*}\frac{\partial^2}{\partial x^2} + U\end{pmatrix}\begin{pmatrix}\psi_+\\ \psi_-\end{pmatrix} + \begin{pmatrix}P_+\\ P_-\end{pmatrix} \tag{3.37}$$

This first description suits well a pure photonic system and is the common simplest approximation to the polaritonic system which will be extended in Sec.3.3.3.1. The initial Gaussian light pulse injected via $P_\pm(x)$ is right circularly polarized ($\mathbf{S} = (0, 0, +1)$), resonant with the lower polariton branch (LPB) at $k = 0$ and its amplitude is taken low enough to consider a linear regime. The effective mass is defined by $m^* = 2m_t m_l/(m_t + m_l)$ where $m_t = 5 \times 10^{-5} m_0$, $m_l = 0.95 m_t$ are

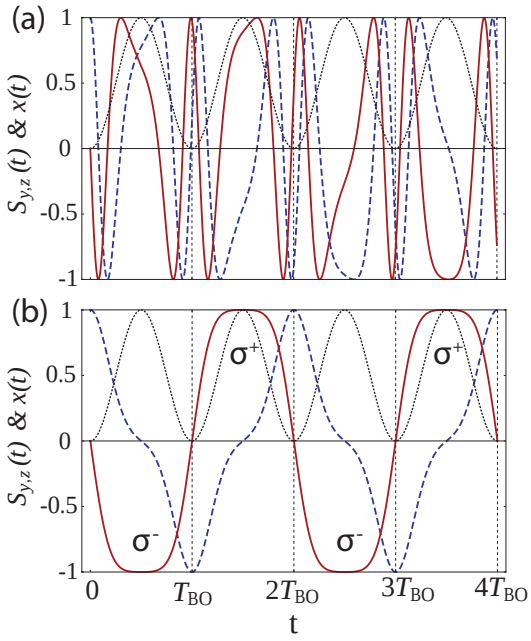

Figure 3.20: Pseudospin dynamics during BOs (a) for arbitrary parameters and (b) following the criterion (3.36). The solid red curves shows the S_z component of the pseudospin, the dashed blue curves shows the S_y component (S_x is always zero) and the dotted black line stands for the trajectory of the center of mass of the wave packet.

the masses of the transverse and longitudinal modes and m_0 is the free electron mass. We note that the mass of the polariton is usually of the order of twice the cavity photon mass. $U(x)$ is the total external potential: the sum of the square-wave periodic potential of amplitude $A = 5$ meV (large enough to stay close to the tight binding approximation) and period $d = 1.56$ μm and a ramp potential $-Fx$, $F = 0.1$ meV/μm^{-1} being a constant force. The off-diagonal terms account for the k-dependent LT splitting, where $\beta = \hbar^2/4(m_l - m_t)/(m_l m_t)$. We remind that the components of $\mathbf{S}$ are defined by the wave function components $\psi_\pm$ along

$$\begin{aligned} S_x &= \Re\left(\psi_+ \psi_-^*\right) \\ S_y &= \Im\left(\psi_- \psi_+^*\right) \\ S_z &= \left(|\psi_+|^2 - |\psi_-|^2\right)/2 \end{aligned} \tag{3.38}$$

The Figure 3.21 shows the probability density in real space of the σ^+ (a) and σ^- (b) components. In (c)-(d) we plot the degree of circular polarization, which is nothing but S_z because it is normalized to unity, in real and momentum space respectively. Remarkably, as described analytically in the previous section, every single spatial oscillation in the first Brillouin zone displays alternatively a right or left circular polarization. Because each spin component is present in the system only for a half-period, we will call this regime "Half-Bloch Oscillations" (HBOs). We note that

this effect requires no external magnetic field to be applied. Nevertheless, for a microcavity with sufficiently high exciton g-factor, an additional tuning could be provided by means of applied magnetic field.

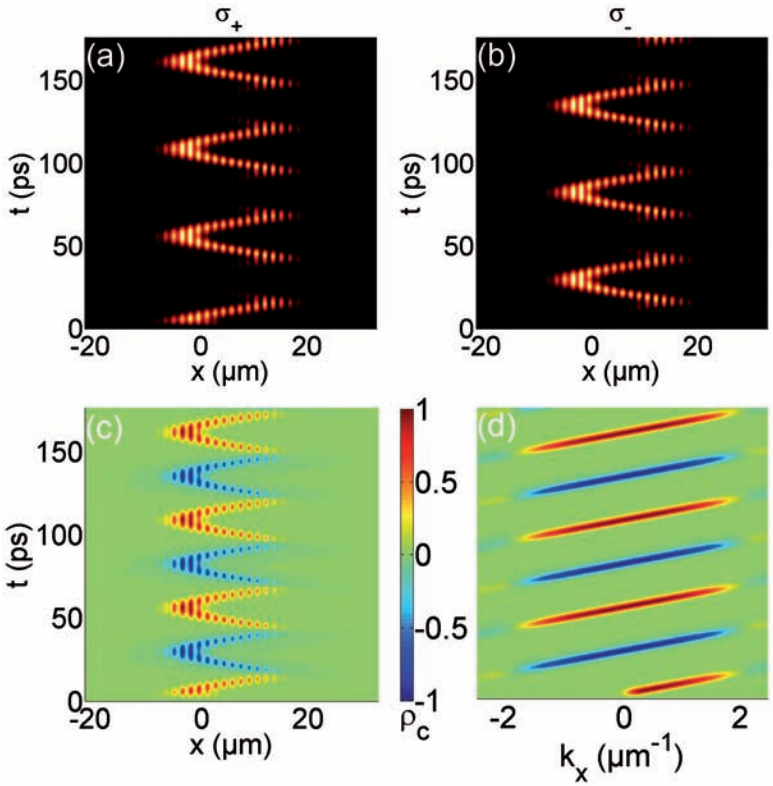

Figure 3.21: Half Bloch-Oscillations. The (a) and (b) panels show the emission intensity in real σ_+ and σ_- space respectively. (c) and (d) are the corresponding circular polarization degree in real and momentum space respectively.

3.3.3 Emission of a terahertz spin current

So far, we have been working with wide gaps between the minibands which is not realistic for the case of polaritons because of the limitations on the height of the periodic potential imposed by technological constraints discussed previously. For shallow potentials, the Landau-Zener tunneling [see Sec.(3.1.1.1)] can be significant and induces a signal loss every single oscillation, which is usually harmful for the observation of steady-state BOs. However, we are going here to take advantage of this effect in order to generate periodic polarized light beams at the FBZ edges. Indeed, reducing the value of the periodic potential's amplitude A to a more realistic value will tend to increase P_{LZT} (defined by Eq.(3.16)) and then induce a significant emission at every oscillation at the point where the band separation is the smallest. The peculiarity of our spin-dependent system is that the emitted pulses will have a specific circular polarization degree, controlled by the coupling between BOs and

the pseudospin precession. Indeed, the LZT occurs every $j^{th}+1/2$ oscillations and the corresponding emission has a circular polarization degree

$$\begin{aligned} S_z^{LZT} = & + S_{0y}\sin\left[(j+1)\frac{T_{BO}}{2}\frac{(H_x-\Delta J)}{\hbar}\right] \\ & - S_{0z}\cos\left[(j+1)\frac{T_{BO}}{2}\frac{(H_x-\Delta J)}{\hbar}\right] \end{aligned} \tag{3.39}$$

In particular, using the same conditions as in Fig.3.20(b), the circular polarization degree of the emitted signal is $S_z^{LZT}=(-1)^{j+\kappa}$. We show in Fig.3.22 a configuration showing a synchronized regime for $A=1$ meV, $\kappa=0$ and $H_x=0.2$ meV. The LZT-induced signal measured 40 μm away from the input pulse reveals a spin current, alternating between σ_+ and σ_-. We make the following remark: of course, if the effective magnetic field is present along the whole wire, the signal's pseudospin is expected to keep on rotating while it propagates, which can either be regarded as an issue or not. In such case the polarization of the output signal will crucially depend on the propagation distance. However, in the synchronized regime, the relative polarization between two consecutive pulses will not depend on the propagation distance. Anyway, since the effective field depends strongly on the lateral size of the wire, it can be reduced in the region of free propagation, so that it will not affect the polarization of the emitted signal significantly during its propagation time. In the figure 3.22, $\mathbf{\Omega}_{LT}$ is acting only in the BOs region in order to preserve the polarization of the signal outside of this region for the sake of simplicity.

3.3.3.1 Realistic polaritonic system

In this section we will focus on the polariton system with all its specificities. We should rewrite Eqs.(3.21,3.21) taking into account the two spin projections (indices $\pm$) and the TE-TM splitting

$$\begin{aligned} i\hbar\frac{\partial\phi_\pm}{\partial t} = & -\frac{\hbar^2}{2m_\phi}\frac{\partial^2\phi_\pm}{\partial x^2}+\frac{\Omega_R}{2}\psi_\pm-\frac{i\hbar}{2\tau_\phi}\phi_\pm+U_\phi\phi_\pm \\ & + \left(\beta\frac{\partial^2}{\partial x^2}+H_x\right)\phi_\pm+P_\pm \end{aligned} \tag{3.40}$$

$$i\hbar\frac{\partial\chi_\pm}{\partial t} = -\frac{\hbar^2}{2m_\chi}\frac{\partial^2\chi_\pm}{\partial x^2}+\frac{\Omega_R}{2}\phi_\pm-\frac{i\hbar}{2\tau_\chi}\chi_\pm+U_\chi\chi_\pm \tag{3.41}$$

The analytical description of the previous section appears of course a bit less accurate with respect to the full treatment. The dependence of $\mathbf{\Omega}_{LT}$ over k is slightly affected because of the modified shape of the first Bloch band, which mostly changes the amplitude of oscillations and the shape of the pseudospin oscillations, but is not detrimental for our effect. The period T_{BO} is not expected to strongly vary because it depends on the quantity Fd, and therefore our commensurability criterion remains valid. The design of a real sample would require of course a comprehensive description of the dispersion imposed by the structure which has to be predicted by full two-dimensional simulations.

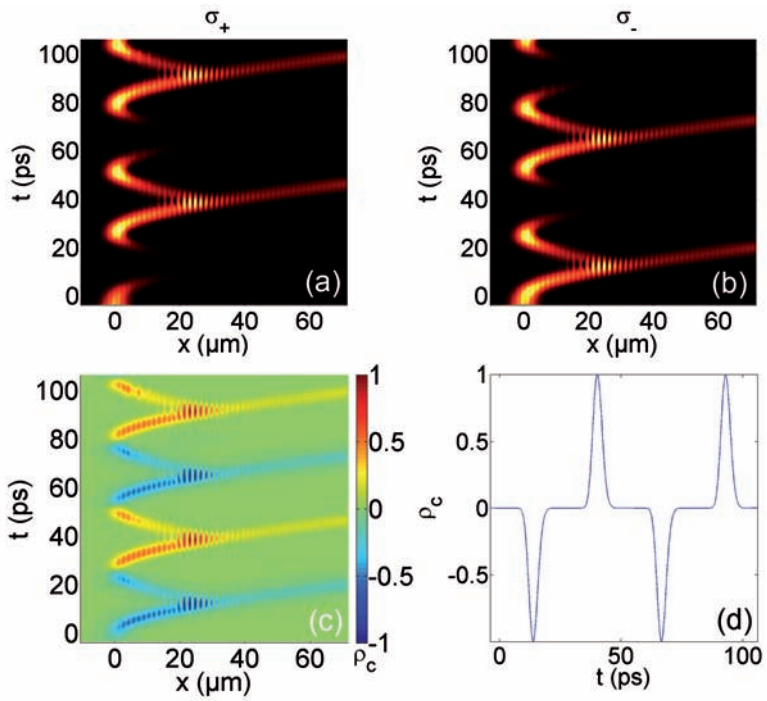

Figure 3.22: LZT emission regime. (a), (b) and (c) show the same representations as Fig.3.21 (in (a) and (b) the local density is normalized for clarity) while the (d) panel shows the normalized circular polarization degree of the emitted signal 40 μm away from the input pulse. The latter has been filtered so that very low density regions don't contribute to the normalized signal.

We aim now at reproducing the synchronized LZT-emitter regime of Fig.3.22. To do so, we need to compensate the particles losses by pumping. It can be done thanks to a pulsed input synchronized with T_{BO} as seen in Fig.3.23, where particles are injected every two oscillations periods ($2T_{BO} = 50$ ps) when the signal weakens too much due to both LZT and lifetime. The wire is therefore acting as an ultra fast spin emitter which converts a linearly polarized input into two oppositely circularly polarized outputs in that particular case. Many other configurations are also possible, depending on the parameters imposed by the sample and the polarization of the input, for example the conversion from circular to linear polarization.

Finally, let us consider a sample etched specifically to achieve the commensurable oscillation regime described above. A small controllable perturbation to the BOs period or to the LT splitting, produced by an electric contact [88] or even strain on the sample, would lead to a loss of this synchronization and to an arbitrary relative circular polarization degree between two consecutive LZT pulses. In the synchronized regime the average polarization difference of two consecutive pulses is $\Delta S_z = 2$ which can be assigned a logical **1**, whereas in any incommensurate configuration the polarization difference is smaller, which can be regarded as logical **0**. The switching between the two regimes is controlled by a gate (perturbations).

The device can therefore be used as a spin-optronic switch working at the frequency $1/T_{BO}$ in the range of tens of THz.

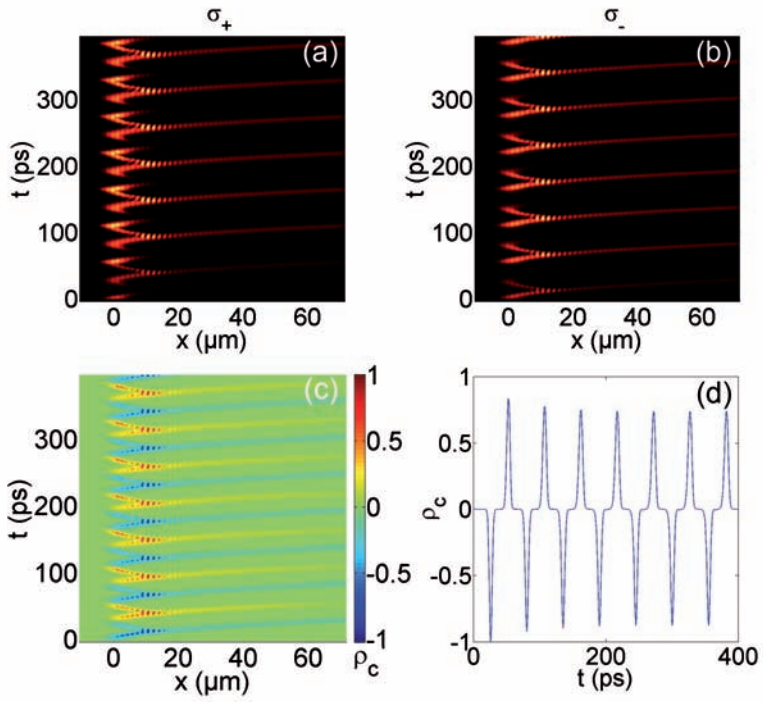

Figure 3.23: Accounting for the real non-parabolic dispersion and the lifetime of the particles. Input pulses with a period of $2T_{BO} \simeq 50$ ps are used to maintain the output signal intensity.

3.3.3.2 Driven half-Bloch oscillations and LZT emission

In this last section, we show that polaritons BOs and the alternating spin signal can be maintained thanks to a localized non-resonant pump. The latter is spatially located in the region of the LZT emission. The pump power is tuned just below the condensation threshold. It essentially generates an unpolarized excitonic reservoir localized within the pumping area [2]. BOs are then triggered by a single resonant, linearly polarized pulse as previously. The oscillations can then be sustained despite of the life time because the propagating wave packet is re-amplified (stimulated) each time it passes below the localized non-resonant pump. The clear advantage of this scheme is that it no more requires the use of THz synchronized input pulses. The modeling of such scheme is more challenging. It requires the description of the coupling between an incoherent excitonic reservoir and a coherent polariton condensate. Contrary to the previous sections, it is now essential to properly take into account the interactions between all types of particles. Here we are going to use the simplest description of this problem based on modified spin dependent Ginzburg-Landau equations. These equations have been introduced for the spinless case in

Sec.(2.5) [see Eqs.(2.81,2.82,2.82) and Ref.[92]] to describe the polaritonic system.

$$\begin{aligned} \hbar\frac{\partial\phi_\pm}{\partial t} = & - \frac{\hbar^2}{2m_\phi}\frac{\partial^2\phi_\pm}{\partial x^2} + \frac{\Omega_R}{2}\psi_\pm - \frac{i\hbar}{2\tau_\phi}\phi_\pm + U_\phi\phi_\pm \\ & + \left(\beta\frac{\partial^2}{\partial x^2} + H_x\right)\phi_\pm + P_\pm \end{aligned} \tag{3.42}$$

$$\begin{aligned} i\hbar\frac{\partial\chi_\pm}{\partial t} = & - \frac{\hbar^2}{2m_\chi}\frac{\partial^2\chi_\pm}{\partial x^2} + \frac{\Omega_R}{2}\phi_\pm - \frac{i\hbar}{2\tau_\chi}\chi_\pm + U_\chi\chi_\pm \\ & + \alpha_1\left(|\chi_\pm|^2 + n_R\right)\chi_\pm + \frac{i\hbar\Gamma_R}{2}n_R\chi_\pm \end{aligned} \tag{3.43}$$

$$\frac{\partial n_R}{\partial t} = + P_R - \frac{n_R}{\tau_R} - \Gamma_R\left(\left|\psi_+^{ex}\right|^2 + \left|\psi_-^{ex}\right|^2\right)n_R \tag{3.44}$$

This model has the advantage of being reasonably simple but does not take into account the interaction with surrounding phonons and therefore lacks any thermalization mechanisms. The latter could be treated using a master equation approach [8, 93]. We assume a localized exciton reservoir with a lifetime $\tau_R = 500$ ps. The reservoir population n_R is described by a rate equation, containing a non-resonant cw-pump $P_R(x) = A_R \exp[(x - x_R)^2/\sigma_R^2]/\tau_R$ with $x_R = 25$ μm and $\sigma_R = 2$ μm. $\Gamma_R = 200/\tau_R$ is the scattering rate towards the oscillating polariton condensate. The interactions between particles with parallel spins are introduced via the constant $\alpha = 6E_b a_B^2/S$, where $E_b = 10$ meV is the exciton binding energy, $a_B = 10^{-2}$ μm its Bohr radius, and S is the normalization area (we neglect here intercomponent interactions $\alpha_2 = 0$). For the pumping intensity we consider, the presence of the reservoir induces an effective localized potential barrier $\alpha n_R(x)$. The latter should not be too large, to perturb only weakly the oscillations of the pulse. We show in Fig.3.24 the numerical results obtained in this framework [see captions]. The resonant short pulse is amplified by stimulated scattering from the excitonic reservoir. The condensate population is roughly doubled each time it crosses the reservoir area. The lifetime and LZT emission-induced losses become strongly compensated upon a relevant reservoir density as we can see in Fig.3.24(a). This figure should be compared to Fig.3.24(b) where the free oscillations (non-resonant pumping is absent) are displayed. We note that in (a) there is still a weak global decay of the number of particles, because the density can not be increased too much to avoid parametric instability discussed in the spinless part.

We are therefore able to create persistent driven Bloch oscillations of polaritons as well as a maintained alternating spin emission with a single input pulse thanks to the bosonic and interacting nature of the particles. This mechanism based on stimulation is not only advantageous to compensate the polariton lifetime. Since the stimulated scattering is spin-selective, the spin component with a higher population is amplified more than the other component when the traveling wave packet crosses the reservoir region. Thus, it provides a necessary feedback, compensating any deviations from a perfect $\sigma_\pm$ emission and further improving the efficiency of the device. Another advantage of working in this nonlinear high density regime is that it allows to overcome the BOs damping due to the structural disorder of the

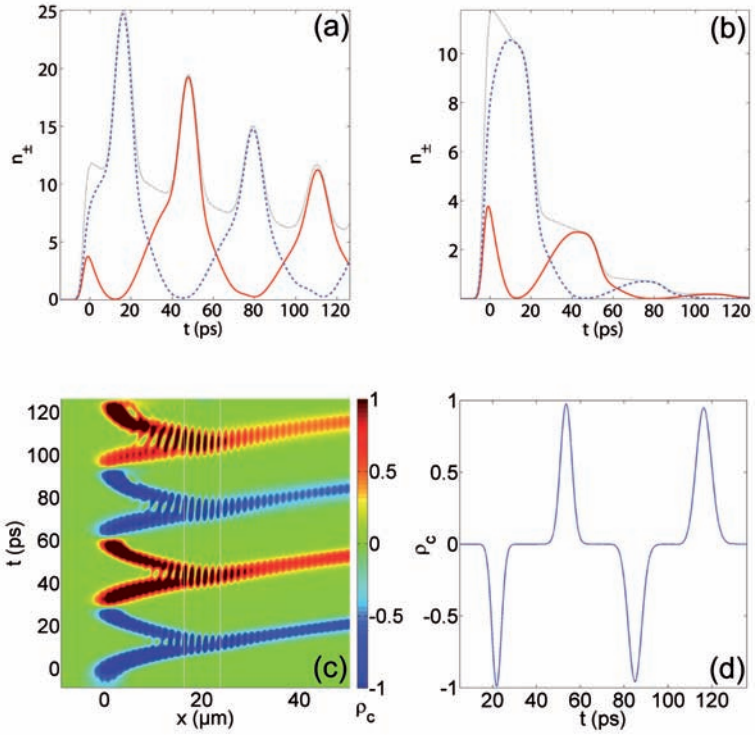

Figure 3.24: Half-Bloch oscillations and LZT emission stimulated by a local reservoir. Density of photonic particles for driven Bloch oscillations (a) compared to free oscillations (b) with a 50 ps lifetime. The solid-red and dashed-blue curve stand for the total density of σ_+ and σ_- particles respectively versus time and the dotted black curve shows the sum of the two. (c) Degree of circular polarization in real space, the solid white lines show the position of the reservoir. (d) LZT spin signal emitted.

microcavity. We would like to point out that this scheme is not specifically linked with spin dependent oscillations, but can be also used to achieve sustained spinless BOs.

We make the following final remark. A similar effect could also be achieved with a pure photonic system. The amplification of the propagating wave would however require to achieve the gain condition, which occurs only with pumping powers typically one or two orders of magnitude larger than the amplification condition in a polaritonic system[94, 95]. Also the repulsive excitonic reservoir tends to expel polaritons for the pumped area whereas in the weak coupling regime, gain confinement tends to localize photons below the non-resonant pumping laser, which can be highly detrimental for the BOs. From these points of view, the use of the strong coupling is advantageous, whereas, on the other hand, it requires low temperature operation, at least in arsenide-based systems.

3.3.3.3 Conclusions

Bloch-oscillations of exciton-polaritons reveal to be promising not only from the fundamental point of view, offering the possibility to observe the spatio-temporal oscillations but also offer interesting applied perspectives. Indeed, once again the polariton spin dynamics imposed by the effective magnetic field combined with the Landau-Zener tunneling broadens the perspectives towards an alternating spin current emitter working at THz frequencies. We have shown how such signal could be sustained despite the polariton lifetime simply thanks to a local *cw* and nonresonant pump.

3.4 The role of phonons in Josephson oscillations of a polariton and indirect exciton condensates

Collective phenomena lie beyond many remarkable effects in condensed matter physics. One of their famous manifestations is Josephson effect [96], which was first predicted to occur between superconductors separated by a thin dielectric layer. Due to the build-up of the macroscopic phase coherence resulting in the appearance of an order parameter (playing a role of macroscopic wavefunction of the Cooper pairs) $\psi(\mathbf{r},t) = \sqrt{n}e^{i\theta}$, a tunnel current appears between superconduction regions proportional to the sine of the phase difference between them [97]:

$$I = I_0 \sin \Delta\theta \tag{3.45}$$

where I_0 is a constant depending on the properties of the junction.

Later on, it was proposed that similar phenomena can be observed using liquid Helium [98] and cold atoms [99], where the appearance of a macroscopic wavefunction accompanies the transition towards superfluid and BEC states [100, 101, 102, 103] respectively. In this last case, the Josephson effect can take place between two spatially separated Bose-Einstein condensates of atoms, weakly coupled through a potential barrier. The situation there can demonstrate new physical phenomena with respect to the original junctions between superconductors, as interactions between the tunneling particles play a major role and can lead to remarkable nonlinear effects in the Josephson dynamics. These effects are the anharmonicity of the Josephson oscillations [104, 105] and macroscopic self-trapping in the case, when the initial imbalance between the two condensates exceeds some critical value [106, 107, 108]. The serious disadvantage of the cold atom systems is that the corresponding critical temperatures are extremely small (usually in the nano-Kelvin range) and thus any experimental investigations in the field become challenging. Besides, low critical temperatures rule out any possibility of using the system for practical applications.

On the other hand, in the field of condensed matter physics, various candidates were proposed for the realization of Bose-Einstein condensates with critical temperatures orders of magnitudes higher than those of cold atoms. The formation of exciton condensates in bulk semiconductors was theoretically predicted more than 40 years ago [109], but appeared to be difficult to realize experimentally. Since then, other solid- state systems were proposed for the achievement of high-temperature BEC, including Quantum Hall bilayers [110, 111], magnons [112], indirect excitons [113, 114] and exciton-polaritons. The latter two systems will be in the focus of the present section.

Spatially indirect excitons have been widely studied both experimentally and theoretically in recent years [see Ref.[114] for a review]. For such particles, electrons and holes are localized in parallel coupled 2D layers. Their wave functions show a very little overlap and consequently, indirect excitons have a very long lifetime (up to tens of milliseconds), and can be treated as metastable particles. Superfluid

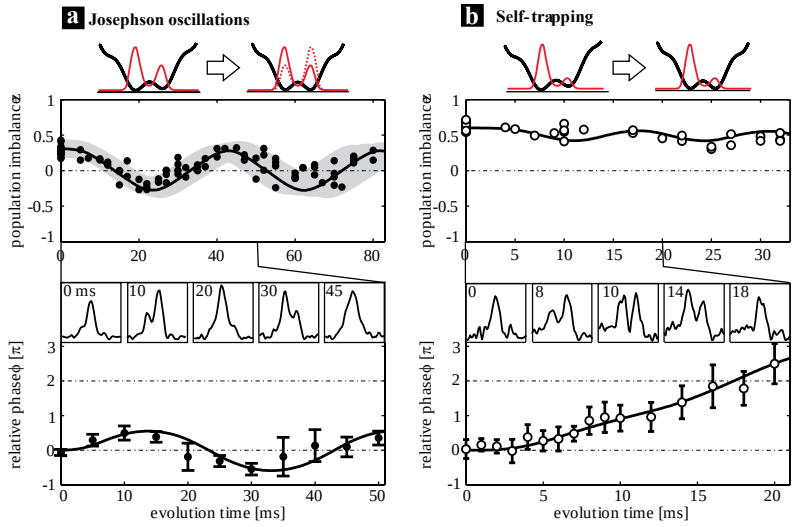

Figure 3.25: Observation of the nonlinear Josephson effect in a bosonic Josephson junction from Ref.[99].

behavior of a system of indirect excitons has been predicted by Lozovik and Yudson more than 30 years ago [115, 116, 117] and subsequent theoretical [118, 119, 120] and experimental [121, 122, 123, 124, 125] studies have suggested that this should be manifested in a series of remarkable effects, including persistent currents and Josephson- related phenomena.

The recently demonstrated possibilities of engineering of spatial confinement for excitons and exciton-polaritons [126, 127, 128, 129, 2, 4] open a way to the investigation of the Josephson effect based on the tunneling between two spatially separated condensates of these particles [130, 131, 132, 133] in the cleanest fashion. We note that coherent oscillations of a polariton condensate were observed recently but within natural traps in the disorder landscape of the microcavity [70], which is not the ideal situation.

The Josephson effect for excitons and cavity polaritons has several important differences from those for superconductors and cold atomic BECs: First, the interparticle interactions play by far a more important role here, leading to the anharmonicity of the Josephson oscillations and to the self-trapping effect [104, 106]. Second, the presence of the polarization (spin) degree of freedom, combined with spin-anisotropy of polariton-polariton interactions gives rise to a much richer and original phenomenology, including spontaneous polarization separation in the real space[131, 133]. Third, due to their short lifetime, cavity polaritons (not indirect excitons) cannot be considered as stable particles, and effects of pump and decay should be accounted for, while considering Josephson- related phenomena. Due to the strong polariton- polariton interactions one can expect that effects of bistability and multistability can play an important role. Fourth, indirect excitons and cavity polaritons efficiently interact with phonons, which play the role of a source of

decoherence and can also affect the tunneling rates [134].

3.4.1 The model

The system we analyze here is schematically represented on the Fig.3.26. We consider two spatially separated excitonic or polaritonic condensates located in a pair of coupled traps that could be formed by a merged pair of micropillars similarly to those of Ref.[4]. Each trap (indices L and R in the following) contains a *single* confined discrete level. These two localized states are weakly coupled the one to another by the tunneling constant J. This tunneling process can give rise to a coherent oscillation between the right and the left wells, which can be described as a bosonic Josephson effect (extrinsic Josephson effect in terms of Ref.[131]). The particles have two spin projections, corresponding to the right (σ_+ index $\uparrow$) and left-circular (σ_- index $\downarrow$) polarizations of the counterpart photons. Due to the structural asymmetry, one can have a coherent exchange of particles between the condensates with opposite polarizations [135, 90] (spin dynamics induced by an effective field), referred to as intrinsic Josephson effect [131]. Besides, the system contains excited delocalized levels, which are coupled with localized states in the traps via processes involving acoustic phonons which contribute to the exchange of the particles between the traps and introduce a source of decoherence to the system. An alternative process of transfer of particles from one well to another and based on polariton-polariton scattering could be envisaged. This will involve the simultaneous scattering of one condensed particle to a reservoir state and the scattering of a reservoir particle to the other condensed state. This type of mechanism can lead either to decoherence or to the enhancement of the Josephson coupling constant depending on the coherence degree of the reservoir state [136].

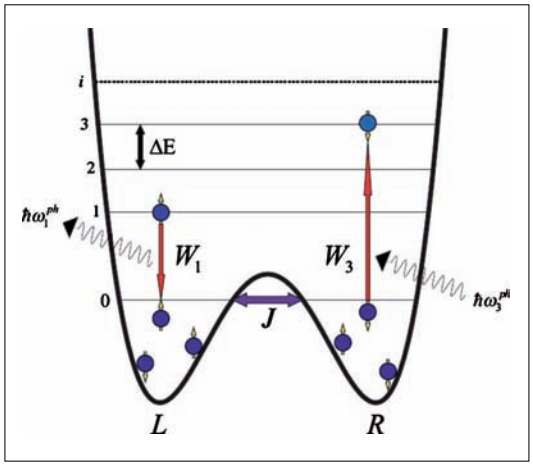

Figure 3.26: Geometry of the system. Spinor polaritons are confined in two traps coupled with each other by coherent tunneling and with delocalized excited states by energy-conserving phonon-assisted processes. Such coupled potential well could be experimentally obtained within pairs of micropillars.

Within the second quantization formalism, the model Hamiltonian is thus separated into two parts:

$$H = H_{co} + H_{deco} \tag{3.46}$$

The coherent part reads:

$$H_{co} = H_0 + H_J + H_\Omega + H_{pol-pol} \tag{3.47}$$

where:

$$H_0 = \varepsilon_0 \left(a^\dagger_{L\uparrow} a_{L\uparrow} + a^\dagger_{L\downarrow} a_{L\downarrow} + a^\dagger_{R\uparrow} a_{R\uparrow} + a^\dagger_{R\downarrow} a_{R\downarrow} \right) \tag{3.48}$$

$$H_J = J \left(a^\dagger_{L\uparrow} a_{R\uparrow} + a^\dagger_{R\uparrow} a_{L\uparrow} + a^\dagger_{L\downarrow} a_{R\downarrow} + a^\dagger_{R\downarrow} a_{L\downarrow} \right) \tag{3.49}$$

$$H_\Omega = \Omega \left(a^\dagger_{L\uparrow} a_{L\downarrow} + a^\dagger_{L\downarrow} a_{L\uparrow} + a^\dagger_{R\uparrow} a_{R\downarrow} + a^\dagger_{R\downarrow} a_{R\uparrow} \right) \tag{3.50}$$

$$H_{pol-pol} = H_{\uparrow\uparrow} + H_{\uparrow\downarrow} \tag{3.51}$$

$$H_{\uparrow\uparrow} = \frac{\alpha_1}{2} \left(\begin{array}{l} a^\dagger_{L\uparrow} a^\dagger_{L\uparrow} a_{L\uparrow} a_{L\uparrow} + a^\dagger_{R\uparrow} a^\dagger_{R\uparrow} a_{R\uparrow} a_{R\uparrow} \\ + a^\dagger_{L\downarrow} a^\dagger_{L\downarrow} a_{L\downarrow} a_{L\downarrow} + a^\dagger_{R\downarrow} a^\dagger_{R\downarrow} a_{R\downarrow} a_{R\downarrow} \end{array} \right) \tag{3.52}$$

$$H_{\uparrow\downarrow} = \alpha_2 \left(a^\dagger_{L\uparrow} a^\dagger_{L\downarrow} a_{L\uparrow} a_{L\downarrow} + a^\dagger_{R\uparrow} a^\dagger_{R\downarrow} a_{R\uparrow} a_{R\downarrow} \right) \tag{3.53}$$

$a^\dagger$ and a are respectively the bosonic creation and annihilation operators for the polariton or exciton field, the subscripts L, R and $\uparrow, \downarrow$ refer respectively to condensed particles in the left or right trap with σ_+ or σ_- polarization. H_0 is the free particles Hamiltonian, H_J stands for the spin conservative Josephson tunneling, H_Ω models the spin flip process induced by the structural anisotropy and $H_{pol-pol}$ is the condensed particles interaction term which contains respectively parallel ($H_{\uparrow\uparrow}$) and antiparallel ($H_{\uparrow\downarrow}$) spin-dependent scattering processes.

And the decoherent part:

$$H_{deco} = H_+ + H_- \tag{3.54}$$

where:

$$H_+ = D \sum_{i=1}^{N} \left(\begin{array}{l} a^\dagger_{L\uparrow} a_{i\uparrow} b^\dagger_i + a^\dagger_{L\downarrow} a_{i\downarrow} b^\dagger_i \\ + a^\dagger_{R\uparrow} a_{i\uparrow} b^\dagger_i + a^\dagger_{R\downarrow} a_{i\downarrow} b^\dagger_i \end{array} \right) \tag{3.55}$$

$$H_- = D \sum_{i=1}^{N} \left(\begin{array}{l} a_{L\uparrow} a^\dagger_{i\uparrow} b_i + a_{L\downarrow} a^\dagger_{i\downarrow} b_i \\ + a_{R\uparrow} a^\dagger_{i\uparrow} b_i + a_{R\downarrow} a^\dagger_{i\downarrow} b_i \end{array} \right) \tag{3.56}$$

which contains the spin conserving interactions between condensed particles and the acoustic phonons reservoir described by $b^\dagger_i$ and b_i operators. The decoherent Hamiltonian is split the following way: H_- models the excitation of a L or R condensed particle toward the i^{th} of the N trapped state ($a^\dagger_i$ operator) via the absorbtion of a phonon with energy $\hbar\omega_i$ and H_+ represents the opposite relaxation scheme.

We shall describe the dynamic of the system by means of the density matrix formalism that allows to merge the previous coherent and dissipative processes. The time evolution of the condensed part is treated by the usual Liouville-von Neumann equation:

$$(\partial_t \rho)_{co} = \frac{i}{\hbar}\left[\rho; H_{co}\right] \tag{3.57}$$

under the assumption that any scattering act is conserving the coherence. For any operator $\widehat{A}$, one has: $\langle \widehat{A} \rangle = Tr(\rho \widehat{A})$ and thus:

$$\partial_t \left\langle \widehat{A} \right\rangle_{co} = \frac{i}{\hbar} Tr\left(\left[\rho, H_{co}\right] \widehat{A} \right) = \frac{i}{\hbar} \left\langle \left[H_{co}, \widehat{A} \right] \right\rangle \tag{3.58}$$

Applying this formula to the observables $n_{\{L,R\}\{\uparrow,\downarrow\}} = a^{\dagger}_{\{L,R\}\{\uparrow,\downarrow\}} a_{\{L,R\}\{\uparrow,\downarrow\}}$ and to correlators that follow, namely: $a^{\dagger}_{\{R,L\}\uparrow} a_{\{R,L\}\downarrow}$, $a^{\dagger}_{\{R,L\}\uparrow} a_{\{L,R\}\downarrow}$ and $a^{\dagger}_{\{R,L\}\uparrow} a_{\{L,R\}\uparrow}$ and using mean field approximation for truncation of the fourth- order correlators one can get a closed set of ten evolution equations. We write here only write one sample of each type of equation, the remaining complementary ones are straightforwardly obtained by permutations of L, R and $\uparrow, \downarrow$ indexes. We also compact the notation for mean values of correlators i.e. for example $\left\langle a^{\dagger}_{R\downarrow} a_{L\uparrow} \right\rangle$ becomes $\alpha^{\downarrow\uparrow}_{RL}$:

$$\begin{aligned}
\hbar\left(\partial_t \alpha^{\downarrow\uparrow}_{LL}\right)_{co} &= iJ\left[\alpha^{\downarrow\uparrow}_{RL} - \alpha^{\uparrow\downarrow *}_{RL}\right] + i\Omega\left[n_{L\uparrow} - n_{L\downarrow}\right] \\
&+ i\left[\alpha_1\left(n_{L\downarrow} - n_{L\uparrow} - 1\right) + \alpha_2\left(n_{L\uparrow} - n_{L\downarrow} - 1\right)\right]\alpha^{\downarrow\uparrow}_{LL} \qquad (3.59) \\
\hbar\left(\partial_t \alpha^{\uparrow\uparrow}_{RL}\right)_{co} &= iJ\left[n_{L\uparrow} - n_{R\uparrow}\right] + i\Omega\left[\alpha^{\downarrow\uparrow}_{RL} - \alpha^{\uparrow\downarrow}_{RL}\right] \\
&+ i\left[\alpha_1\left(n_{R\uparrow} - n_{L\uparrow} - 1\right) + \alpha_2\left(n_{R\downarrow} - n_{L\downarrow}\right)\right]\alpha^{\uparrow\uparrow}_{RL} \qquad (3.60) \\
\hbar\left(\partial_t \alpha^{\downarrow\uparrow}_{RL}\right)_{co} &= iJ\left[\alpha^{\downarrow\uparrow}_{LL} - \alpha^{\downarrow\uparrow}_{RR}\right] + i\Omega\left[\alpha^{\uparrow\uparrow}_{RL} - \alpha^{\downarrow\downarrow}_{RL}\right] \\
&+ i\left[\alpha_1\left(n_{R\downarrow} - n_{L\uparrow} - 1\right) + \alpha_2\left(n_{R\uparrow} - n_{L\downarrow}\right)\right]\alpha^{\downarrow\uparrow}_{RL} \qquad (3.61)
\end{aligned}$$

The dynamics of the decoherent part involving phonons is dissipative, and should be treated in the following way. Liouville- von Neumann equation can be rewritten in the following integro-differential form:

$$(\partial_t \rho)_{deco} = -\frac{1}{\hbar^2} \int_{-\infty}^{t} \left[H_{deco}(t) ; \left[H_{deco}\left(t'\right) ; \rho\left(t'\right) \right] \right] dt' \tag{3.62}$$

where $H_{deco}(t)$ is the time- dependent Hamiltonian of the polariton- phonon interaction [Eq.(3.54)] written in a Dirac picture. To account for the decoherent nature of the evolution with phonons, Born-Markov approximation should be applied while treating Eq.(3.62). It consists in replacing t' by t which will give after integration only energy-conservative terms [137]. The time evolution of the density matrix considering Eq.(3.54) is thus given by the following master equation:

$$\begin{aligned}
\delta^{-1}(\Delta E)\hbar\partial_t \rho &= 2\left(H_+ \rho H_- + H_- \rho H_+\right) - \left(H_+ H_- + H_- H_+\right)\rho \\
&- \rho\left(H_+ H_- + H_- H_+\right) \qquad (3.63)
\end{aligned}$$

where the factor $\delta^{-1}(\Delta E)$ denotes the conservation of energy. For time evolution of the mean value of any arbitrary operator $\widehat{A}$, with still $\langle\widehat{A}\rangle = Tr(\rho\widehat{A})$ one has:

$$\delta^{-1}(\Delta E)\hbar\partial_t\langle\widehat{A}\rangle = Tr\left(\rho[H_-,[\widehat{A},H_+]]\right) + Tr\left(\rho[H_+;[\widehat{A};H_-]]\right) \quad (3.64)$$

We now apply Eq.(3.64) to the previous densities and correlators with Eqs.(3.55,3.56) to obtain the set of equations for the decoherent part, and once again we only write the six foretype equations:

$$\begin{aligned}
(\partial_t n_{L\uparrow})_{deco} &= 2W\sum_{i=1}^{N}\mathrm{Re}\{(n_i^{ph}+1)[n_{i\uparrow}(n_{L\uparrow}+1+\alpha_{RL}^{\uparrow\uparrow *}) \\
&+ \alpha_{ii}^{\downarrow\uparrow}(\alpha_{LL}^{\downarrow\uparrow *}+\alpha_{RL}^{\downarrow\uparrow *})] - n_i^{ph}[(n_{i\uparrow}+1)(n_{L\uparrow}+\alpha_{RL}^{\uparrow\uparrow *}) \\
&+ \alpha_{ii}^{\downarrow\uparrow}(\alpha_{LL}^{\downarrow\uparrow *}+\alpha_{RL}^{\downarrow\uparrow *})]\} \quad (3.65)\\
(\partial_t \alpha_{LL}^{\downarrow\uparrow})_{deco} &= W\sum_{i=1}^{N}\{(n_i^{ph}+1)[(n_{i\downarrow}+n_{i\uparrow})\alpha_{LL}^{\downarrow\uparrow} + n_{i\downarrow}\alpha_{RL}^{\downarrow\uparrow} + n_{i\uparrow}\alpha_{RL}^{\uparrow\downarrow *} \\
&+ \alpha_{ii}^{\downarrow\uparrow}(n_{L\downarrow}+n_{L\uparrow}+2+\alpha_{RL}^{\uparrow\uparrow}+\alpha_{RL}^{\downarrow\downarrow *})] \\
&- n_i^{ph}[(n_{i\downarrow}+n_{i\uparrow}+2)\alpha_{LL}^{\downarrow\uparrow} + (n_{i\downarrow}+1)\alpha_{RL}^{\downarrow\uparrow} \\
&+ (n_{i\uparrow}+1)\alpha_{RL}^{\uparrow\downarrow *} + \alpha_{ii}^{\downarrow\uparrow}(n_{L\downarrow}+n_{L\uparrow}+\alpha_{RL}^{\uparrow\uparrow}+\alpha_{RL}^{\downarrow\downarrow *})]\} \quad (3.66)\\
(\partial_t \alpha_{RL}^{\uparrow\uparrow})_{deco} &= W\sum_{i=1}^{N}\{(n_i^{ph}+1)[n_{i\uparrow}(n_{L\uparrow}+n_{R\uparrow}+2+2\alpha_{RL}^{\uparrow\uparrow}) \\
&+ \alpha_{ii}^{\downarrow\uparrow}(\alpha_{RL}^{\uparrow\downarrow}+\alpha_{RR}^{\downarrow\uparrow *}) + \alpha_{ii}^{\downarrow\uparrow *}(\alpha_{RL}^{\downarrow\uparrow}+\alpha_{LL}^{\downarrow\uparrow})] \\
&- n_i^{ph}[(n_{i\uparrow}+1)(n_{L\uparrow}+n_{R\uparrow}+2\alpha_{RL}^{\uparrow\uparrow}) \\
&+ \alpha_{ii}^{\downarrow\uparrow}(\alpha_{RL}^{\uparrow\downarrow}+\alpha_{RR}^{\downarrow\uparrow *}) + \alpha_{ii}^{\downarrow\uparrow *}(\alpha_{RL}^{\downarrow\uparrow}+\alpha_{LL}^{\downarrow\uparrow})]\} \quad (3.67)\\
(\partial_t \alpha_{RL}^{\downarrow\uparrow})_{deco} &= W\sum_{i=1}^{N}\{(n_i^{ph}+1)[n_{i\downarrow}(\alpha_{LL}^{\downarrow\uparrow}+\alpha_{RL}^{\downarrow\uparrow}) + n_{i\uparrow}(\alpha_{RR}^{\downarrow\uparrow}+\alpha_{RL}^{\downarrow\uparrow}) \\
&+ \alpha_{ii}^{\downarrow\uparrow}(n_{R\downarrow}+n_{L\uparrow}+2+\alpha_{RL}^{\uparrow\uparrow}+\alpha_{RL}^{\downarrow\downarrow})] \\
&- n_i^{ph}[(n_{i\downarrow}+1)(\alpha_{LL}^{\downarrow\uparrow}+\alpha_{RL}^{\downarrow\uparrow}) + (n_{i\uparrow}+1)(\alpha_{RR}^{\downarrow\uparrow}+\alpha_{RL}^{\downarrow\uparrow}) \\
&+ \alpha_{ii}^{\downarrow\uparrow}(n_{R\downarrow}+n_{L\uparrow}+\alpha_{RL}^{\uparrow\uparrow}+\alpha_{RL}^{\downarrow\downarrow})]\} \quad (3.68)\\
(\partial_t n_{i\uparrow})_{deco} &= 2W\sum_{i=1}^{N}\mathrm{Re}\{n_i^{ph}[(n_{i\uparrow}+1)(n_{L\uparrow}+n_{R\uparrow}+2\mathrm{Re}(\alpha_{RL}^{\uparrow\uparrow})) \\
&+ \alpha_{ii}^{\downarrow\uparrow}(\alpha_{LL}^{\downarrow\uparrow *}+\alpha_{RR}^{\downarrow\uparrow *}+\alpha_{RL}^{\downarrow\uparrow *}+\alpha_{RL}^{\uparrow\downarrow})] \\
&- (n_i^{ph}+1)[n_{i\uparrow}(n_{L\uparrow}+n_{R\uparrow}+2+2\mathrm{Re}(\alpha_{RL}^{\uparrow\uparrow})) \\
&+ \alpha_{ii}^{\downarrow\uparrow}(\alpha_{LL}^{\downarrow\uparrow *}+\alpha_{RR}^{\downarrow\uparrow *}+\alpha_{RL}^{\downarrow\uparrow *}+\alpha_{RL}^{\uparrow\downarrow})]\} \quad (3.69)
\end{aligned}$$

$$
\begin{aligned}
(\partial_t \alpha_{ii}^{\downarrow\uparrow})_{deco} &= W \sum_{i=1}^{N} \{ n_i^{ph} [(n_{i\downarrow} + n_{i\uparrow} + 2)(\alpha_{LL}^{\downarrow\uparrow} + \alpha_{RR}^{\downarrow\uparrow} + \alpha_{RL}^{\uparrow\downarrow *} + \alpha_{RL}^{\downarrow\uparrow}) \\
&+ \alpha_{ii}^{\downarrow\uparrow} (n_{L\uparrow} + n_{L\downarrow} + n_{R\uparrow} + n_{R\downarrow})] \\
&- (n_i^{ph} + 1)[(n_{i\downarrow} + n_{i\uparrow})(\alpha_{LL}^{\downarrow\uparrow} + \alpha_{RR}^{\downarrow\uparrow} + \alpha_{RL}^{\uparrow\downarrow *} + \alpha_{RL}^{\downarrow\uparrow}) \\
&+ \alpha_{ii}^{\downarrow\uparrow} (n_{L\uparrow} + n_{L\downarrow} + n_{R\uparrow} + n_{R\downarrow} + 4 + 2\mathrm{Re}(\alpha_{RL}^{\uparrow\uparrow} + \alpha_{RL}^{\downarrow\downarrow}))]\}
\end{aligned} \tag{3.70}
$$

We get $2N$ extra equations for the excited levels populations $n_{i\uparrow}$ and $n_{i\downarrow}$ plus N more for the new associated correlators $\alpha_{ii}^{\downarrow\uparrow}$ so a total of $(10+3N)$ equations which can be solved numerically. The scattering rates can be estimated as $W = D^2/\Gamma\hbar$, with Γ being a characteristic broadening of the level, $n_i^{ph} = b_i^\dagger b_i$ is the distribution of phonons with energy $E_i = \hbar\omega_i$ at the temperature T given by the Bose-Einstein distribution.

In order to get closer to a realistic situation, one can include in the model the inter-excited levels transitions processes by adding to the decoherent Hamiltonian (Eq.3.54) the extra term:

$$
H_{int-ex} = D \left\{ \sum_{i<j}^{N} \left(a_{i\uparrow} a_{j\uparrow}^\dagger b_{j-i} + a_{i\downarrow} a_{j\downarrow}^\dagger b_{j-i} \right) + \sum_{i>j}^{N} \left(a_{j\uparrow}^\dagger a_{i\uparrow} b_{i-j}^\dagger + a_{j\downarrow}^\dagger a_{i\downarrow} b_{i-j}^\dagger \right) \right\} \tag{3.71}
$$

which participates to time dependent equations the following way (the 2 spin down equations are obviously the same):

$$
\begin{aligned}
(\partial_t n_{i\uparrow})_{deco}^{int-ex} &= W \sum_{i>j}^{N} \left\{ +n_{i-j}^{ph} n_{j\uparrow} - \left(1 + n_{i-j}^{ph} + n_{j\uparrow}\right) n_{i\uparrow} \right\} \\
&+ W \sum_{i<j}^{N} \left\{ -n_{j-i}^{ph} n_{i\uparrow} + \left(1 + n_{j-i}^{ph} + n_{i\uparrow}\right) n_{j\uparrow} \right\}
\end{aligned} \tag{3.72}
$$

The full set of equations for the dynamics of the system is finally obtained by:

$$
\partial_t \left\langle \widehat{A} \right\rangle = \partial_t \left\langle \widehat{A} \right\rangle_{co} + \partial_t \left\langle \widehat{A} \right\rangle_{deco} + \partial_t \left\langle \widehat{A} \right\rangle_{deco}^{int-ex} \tag{3.73}
$$

We are then able to describe the long living indirect excitonic system. Now, to study properly the behavior of the decaying polaritonic condensate as well, one also has to include pumping and lifetime to the Hamiltonian. The last results of the numerical experiment described in the next section involve non-resonant pumping of the excited levels, which can be easily introduced in the master equation [137] and give standard pump and decay terms in dynamic equations for the occupancies. The addition to all equations due to finite lifetime is

$$
\partial_t \left\langle \widehat{A} \right\rangle_{lt} = - \left\langle \widehat{A} \right\rangle / \tau \tag{3.74}
$$

where τ is the particle lifetime. For the pumping, a constant source term is added only to the equations for the populations

$$
\partial_t \left(n_\nu \right)_{pump} = P_\nu \tag{3.75}
$$

In the following we present the results of numerical simulations of the system of the kinetic equations derived in the previous section. In all calculations, the values chosen for the parameters when they are not taken to be zero are $J = 50$ μeV, $\Omega = 60$ μeV, $\alpha_1 = 3$ μeV,$\alpha_2 = \quad 0.1\alpha_1$, $W = 2.23 \cdot 10^{15} s^{\ 1}$ μeV and $T = 20$ K.

3.4.2 Josephson oscillations and self-trapping

We start considering the case of particles of infinite lifetime, corresponding to indirect excitons in coupled quantum wells. Therefore, here no decay or pumping terms included and we start from some hypothetical initial population of the ground states, the excited states being initially unpopulated. In the third subsection of the results, finite particle lifetime is introduced along with pumping, corresponding to the polariton system.

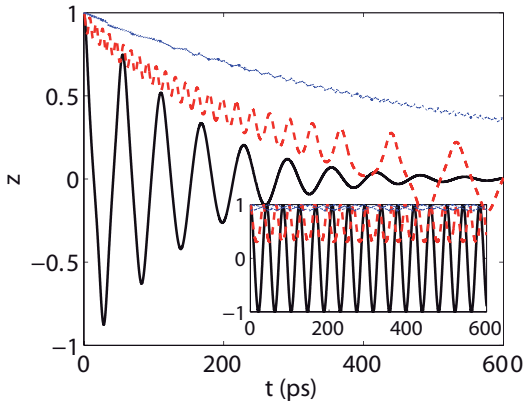

Figure 3.27: Josephson oscillations for the case $\tau = 0$. Spin degree of freedom is neglected to emphasize effects of polariton-polariton and polariton-phonon interactions. Curves show population imbalance at different occupation numbers.(Solid/black: $N_L = 100$, dashed/red: $N_L = 200$, dotted/blue: $N_L = 500$) Inset: the oscillations for the case when interaction with phonons are absent.(Solid/black: $N_L = 10$, dashed/red: $N_L = 70$, dotted/blue: $N_L = 150$) One sees that polariton-polariton interactions lead to self- trapping effect, shortened period and anharmonicity, while interaction with phonons lead to the damping of the Josephson oscillations and increased population needed to reach self-trapping.

Fig.3.27 shows the Josephson oscillations, when all particles are initially in the left well. We have neglected here the spin degree of freedom ($\Omega = \alpha_2 = 0$) for simplicity and to emphasize the effect of exciton-exciton and exciton-phonon interactions. The figure shows the time evolution of the population imbalance, defined as

$$z = \frac{n_L \quad n_R}{n_L + n_R} \tag{3.76}$$

The inset shows the oscillations in the absence of phonons. The main plot shows that the phonon interactions induce a damping of the oscillations as compared to

the inset plot. The effect of increasing the population and therefore exciton-exciton scattering, is the self-trapping of the particles, characterized by a shortened period of oscillations and their anharmonicity, which is especially obvious in the time interval $400 - 600$ ps for the dashed-red curve. The population imbalance creates a strong interaction-induced blueshift in the well having the largest population so that the L, R condensed states are strongly out of resonance reducing significantly their coupling. Another observation is that the phonon damping lowers the effect of exciton-exciton scattering in the sense that a much higher population is needed to get back to the self-trapping.

3.4.3 Spatial separation of polarization

Accounting now for the spin degree of freedom, one can observe interesting phenomena in the polarization domain. We keep $\Omega = 0$ (no spin flips) for the moment to clarify. In that case, the spin up component behaves quite independently of the spin down component. They do affect each other slightly through the weak exciton-exciton scattering. We can thus have three situations, where both spin components are self-trapped, only one of them which corresponds, or neither. Fig.3.28 shows the behavior of the polarization degree in both traps for two different population numbers but same initial polarization degree. Initially all particles are in the left trap. The solid/black and the dashed/red curves are the circular polarization degrees in the left and right traps, respectively, for $N = 100$. Neither spin component is self-trapped, so the oscillations of the polarizations are quite similar. For $N = 200$ (dash-dot/blue: L, dotted/green: R) the spin-up component is self-trapped, and we get a spatial separation of polarization. The oscillations are damped by the phonon interaction, and for large times the polarizations equalize. The inset shows the case $N = 200$ without phonon interaction. There is a visible separation of the polarizations, but without damping, the spin-down component makes full oscillations between the two traps and thus the polarization degree periodically reaches 1. The short oscillations in the right trap polarization (dashed/red) are due to the oscillations of the spin-up component, which are not visible in the left trap polarization.

3.4.4 Bistability and sustained oscillations

For a consistent description of the Josephson tunneling in polariton systems one needs to introduce pumping and decay terms into kinetic equations. In the case where decoherence in the system due to the interaction with acoustic phonons is neglected, the dynamics can be described by the driven dissipative Gross-Pitaevskii equation, which in some range of parameters can have several different stationary solutions. The system thus demonstrates multistability [138] as recently observed experimentally [82]. We remind that in the case of the quasi-resonant pumping, the bi(multi)-stability occurs when the pumping laser lies above the energy of the interacting polariton state. An increase of the pumping results in a larger population of the state which becomes closer in energy to the one of the laser, increasing the

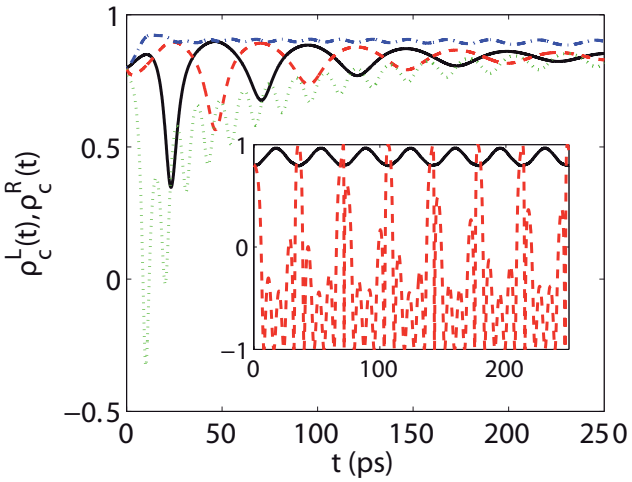

Figure 3.28: Temporal dependence of circular polarization degree in both traps. We let $\Omega = 0$ for simplicity. Initially there are no polaritons in the right trap, N_L in the left with initial circular polarization degree $\rho_c = 0.8$. ($N_L = 100$: Solid/black: L, dashed/red: R; $N_L = 200$: dash-dot/blue: L, dotted/green: R) For $N_L = 100$, no self-trapping occurs and the L/R polarizations oscillate in a similar way. For $N_L = 200$, the spin-up particles are self-trapped and the system shows a spatial separation of polarizations. Inset: $N_L = 200$, no phonons. One sees a similar separation of polarizations, but the polarization of the right trap goes to 1 periodically as the spin-down component is emptied.

absorption light absorption. Above some threshold, an avalanche effect takes place and the system jumps on a new stability point with a much larger population and an energy of the state lying above the one of the laser. Decreasing the pumping intensity from this higher stability branch the system will jump back to the the branch with a smaller population only for a pumping much below the one allowing to jump up, leading to the formation an hysteresis cycle. Although we use a different approach to be able to include polariton-phonon interaction, one can expect that a similar type of effect will appear in our results. In our model the low population stable branch corresponds to the case a balanced population in the two wells. The high population stable branch corresponds to the self trapping case.

Fig.3.29 shows the behavior of polaritons having a lifetime $\tau = 16$ ps. In both plots, the spin-down component of the first excited level is being pumped continuously at varying strengths. As the excited levels are delocalized, the nonresonant pumping is spatially homogeneous. The inset shows the case where only one spin component is considered. Up until $t = 250$ ps, the excited level is being pumped with a low power, and the equilibrium state is stable. At $t = 250$ ps the pumping strength is increased beyond some threshold which causes the populations to split and stabilize in a state where the occupancy of one of the traps is much higher than the other. In numerical calculations, this requires sending a very small asymmetric probe to get out of the unstable equilibrium.

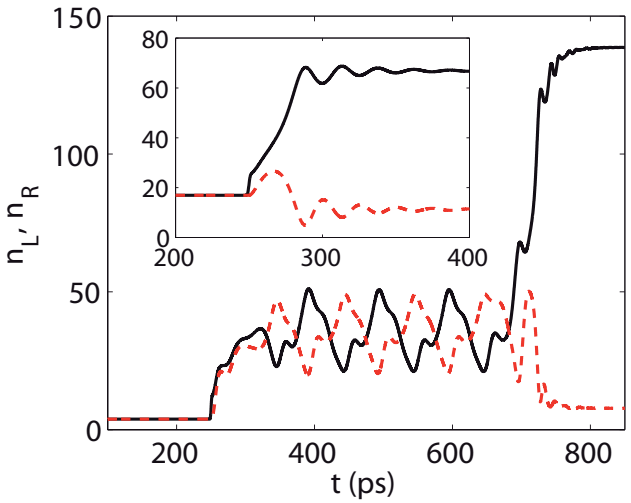

Figure 3.29: Bistability in polariton Josephson junction with pump and decay. Main plot: $\Omega = 60$ μeV. Initial conditions at $t = 0$ are $N_L = 5$, $\rho_{c,L} = 0.5$, $N_R = 0$ to break the symmetry. At $t = 250$ ps and $t = 650$ ps the amplitude of the constant pump increases in a step-like manner. In the intermediate regime of moderate pumping, the system reveals self- sustained oscillations. Inset: $\Omega = 0$, spin degree of freedom neglected. In this case, no self-sustained oscillations can be observed, but the bistability jump remains. A short probe is sent to the left trap at the moment of the pump jump.

The situation gets even more interesting when one considers both spins and introduces the coherent coupling between the two. In this case, there is also a stable state of split populations for high pumping strength and equal populations for low pumping strength but in between there is a regime where the populations do not reach stationary values but reveals self-sustained oscillations resulting from the interplay between intrinsic and extrinsic Josephson effects as is shown in the main plot of Fig.3.29 (Only the spin-down particles are shown for readability). This can be explained in terms of a Hopf bifurcation appearing in our system, where for a certain range of parameters the equilibrium point becomes unstable and instead a stable limit cycle is created. Another interesting effect is that the oscillations are not necessarily periodic and become chaotic for a certain range of parameters [132], which means that a strange attractor instead of a limit cycle is formed in the system. Figure3.30 shows an illustration of the concepts of attractors and limit cycles in the phase space with the left and right trap populations on the axes. The paths show the trajectory of the populations over time for the nonoscillating, periodically oscillating, and chaotically oscillating regimes.

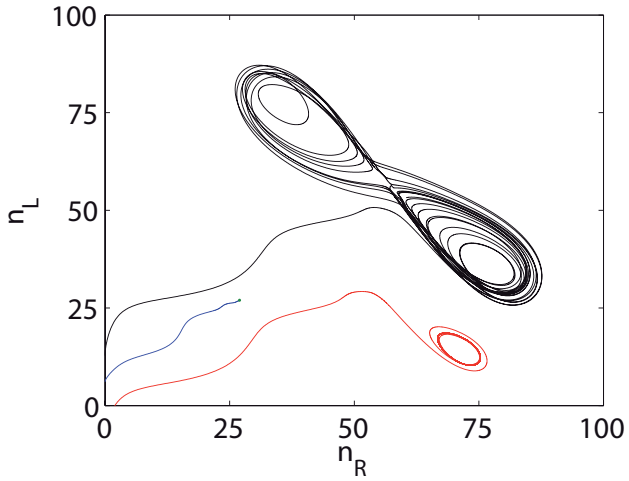

Figure 3.30: Illustration of the concepts of attractors and limit cycles. The middle trajectory (blue line) is for low pumping and has an attractor point with equal populations. The lower trajectory (red line) is for pumping in the oscillatory regime as shown by the appearance of a limit cycle. The upper trajectory (black line) is for pumping in the chaotic regime, resulting in a strange attractor with chaotic behavior. Note that it was necessary to make a phase shift of 10 ps between the populations to make the cycles visible since in reality the populations oscillate more or less in phase, creating a trajectory that goes back and forth in the same track.

The oscillations and their Fourier spectra are shown for two cases in Fig.3.31. They are for $\Omega = 55, 90\ \mu$eV and pumping strengths $P = 10, 13$ ps ^{1}, respectively. In the first case, the oscillations are periodic, as characterized by their Fourier spectrum with sharp peaks. The second case shows chaotic oscillations with a broadband Fourier spectrum. These periodic and chaotic oscillations have previously been

predicted for a polaritonic system [131, 132].

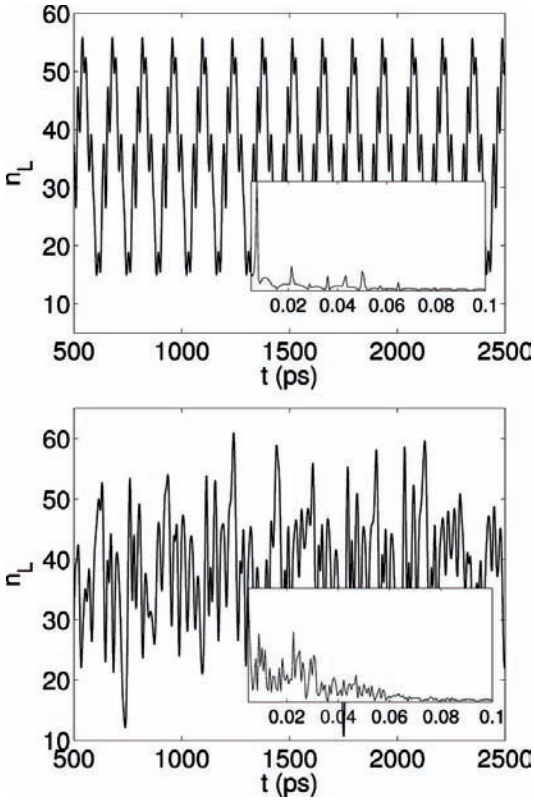

Figure 3.31: Two plots showing the differences between chaotic and regular oscillations in the system. In the upper plot, $\omega = 55$ μeV and P=10 ps^{-}1, and the oscillations are non-chaotic, characterized by a a Fourier spectrum with sharp peaks. The inset shows the Fourier spectrum in arbitrary amplitude units as a function of the frequency (ps^{-}1). In the lower plot, $\omega = 90$ μeV and P=13 ps^{-}1. In that case, the oscillations become chaotic.

The figure 3.32 shows a phase diagram of the system in axes of pumping strength P versus the polarization splitting Ω. The pump is still applied to the spin-down component of the first delocalized excited level. The area A corresponds to low pumping, where the only population splitting is the one between the spin up and spin down. In B, both spin components get split equally. C is the range of parameters which give rise to sustained oscillations, and in D there is a massive split-off of one of the spin-down populations while spin-up populations remain low. The shaded part of C is where chaotic oscillations can be observed.

3.4.5 Conclusions

In conclusion, we analyzed the Josephson-related phenomena in coupled condensates of indirect excitons and cavity polaritons taking into account their peculiar spin structure, particle-particle interactions, scattering with phonons and pump and

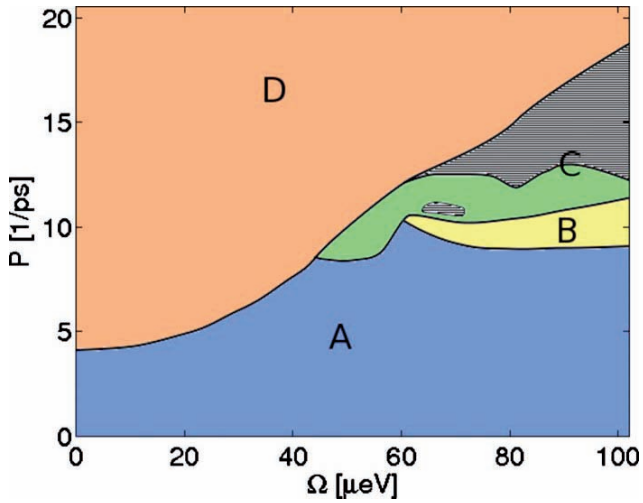

Figure 3.32: Phase diagram for polariton system with constant non- resonant circularly polarized pumping of one of the excited levels. A: No obvious splitting pattern of populations. B: Spin-up and spin-down particles enter bistable states separately. C: Self-sustained oscillations. D: Massive splitting where one of the populations with same polarization as the pump reaches a high value while the others have a low value.

decay terms. For long living indirect excitons, we have shown that exciton-exciton interactions lead to anharmonicity of Josephson oscillations, self trapping effect and spontaneous separation of the fractions with opposite circular polarizations in the real space. The main effect of the particle-phonon interaction is to dampen the oscillations and raise the population threshold for the self-trapping to appear. For cavity polaritons having short lifetimes we demonstrated the bistable behavior of the Josephson junction in the regime of the incoherent constant pump. We have shown that the account of the coupling between the polaritons with opposite circular polarizations can qualitatively change the bistability pattern and in some range of the parameters lead to self-sustained oscillations. These oscillations can then have periodic or chaotic behavior.

3.5 Chapter conclusion

The new class of samples that are accessible nowadays gives to both theoreticians and experimentalists the possibility to investigate the polariton physics within almost any geometry. We have seen that a polariton condensate in a periodic potential is able to form in a solitonic gap state naturally thanks to its off-equilibrium specificity. Such solitonic states could be turned into efficient information carriers. We have shown how the famous Bloch oscillations can be reproduced with our half-matter half-light quasiparticles. The quasi-one dimensional polaritonic system is foresighted as a serious candidate for building real spin-optronic polariton circuits. In this

direction, we have proposed the spin-dependent Bloch oscillations as an efficient source of THz spin currents. Besides we have analyzed in more details one single period of the previous lattice discussing the spin-dependent Josephson oscillations of a polariton (and exciton) condensate within a double well accounting for a finite temperature. Thanks to its bistable or multistable behavior, such a system could be crucial for the creation of ultrafast optical switches or triggers. Putting all these elements together could lead in a near future to the fabrication of an operational optical computer.

Bibliography

[1] J. Kasprzak, M. Richard, S. Kundermann, A. Baas, P. Jeambrun, J. M. J. Keeling, F. M. Marchetti, M. H. Szymaska, R. André, J. L. Staehli, V. Savona, P. B. Littlewood, B. Deveaud, and Le Si Dang, Bose-Einstein condensation of exciton polaritons, *Nature* **443**, 409 (2006). (Cited on pages 145 and 167.)

[2] E. Wertz, L. Ferrier, D. D. Solnyshkov, R. Johne, D. Sanvitto, A. Lemaître, I. Sagnes, R. Grousson, A. V. Kavokin, P. Senellart, G. Malpuech, and J. Bloch, Spontaneous formation and optical manipulation of extended polariton condensates, *Nature Physics* **6**, 860 (2010). (Cited on pages 146, 182 and 187.)

[3] L. Ferrier, E. Wertz, R. Johne, D. D. Solnyshkov, P. Senellart, I. Sagnes, A. Lemaitre, G. Malpuech, and J. Bloch, Interactions in Confined Polariton Condensates, *Phys. Rev. Lett.* **106**, 126401 (2011). (Cited on page 146.)

[4] M. Galbiati, L. Ferrier, D. D. Solnyshkov, D. Tanese, E. Wertz, A. Amo, M. Abbarchi, P. Senellart, I. Sagnes, A. Lemaître, E. Galopin, G. Malpuech, and J. Bloch, Polariton Condensation in Photonic Molecules, *Phys. Rev. Lett.* **108**, 126403 (2012). (Cited on pages 146, 154, 159, 187 and 188.)

[5] D. Tanese, H. Flayac, D.Solnyshkov, A. Amo, A. Lemaitre, E. Galopin, R. Braive, P. Senellart, I. Sagnes, G. Malpuech and J. Bloch, Polariton Condensation in Solitonic Gap States in a 1D periodic Potential, Submitted to *Nat. Commun.* (2012). (Cited on pages 146 and 155.)

[6] H. Flayac, D. D. Solnyshkov, and G. Malpuech, Bloch oscillations of an exciton-polariton Bose-Einstein condensate, *Phys. Rev. B* **83**, 045412 (2011). (Cited on pages 146 and 165.)

[7] H. Flayac, D. D. Solnyshkov, and G. Malpuech, Bloch oscillations of exciton-polaritons and photons for the generation of an alternating THz spin signal, *Phys. Rev. B* **84**, 125314 (2011). (Cited on pages 146 and 165.)

[8] E. B. Magnusson, H. Flayac, G. Malpuech, and I. A. Shelykh, Role of phonons in Josephson oscillations of excitonic and polaritonic condensate, *Phys. Rev. B* **82** *195312* (2010). (Cited on pages 146 and 183.)

[9] C. Kittel, Introduction to Solid State Physics, John Wiley and Sons, New York (1996). (Cited on page 147.)

[10] N. W. Ashcroft and N. David Mermin, Solid State Physics, Harcourt, Orlando (1976). (Cited on page 147.)

[11] W. Zwerger, Mott-Hubbard transition of cold atoms in optical lattices, *J. Opt. B: Quantum Semiclass. Opt.* **5** S9 (2003). (Cited on page 148.)

[12] F. Bloch, Uber die Quantenmechanik der Elektronen in Kristallgittern, *Z. Phys.* **52**, 555 (1929). (Cited on pages 150 and 165.)

[13] L. Landau, Zur Theorie der Energieubertragung, *Physics of the Soviet Union* **2**, 46-51 (1932). (Cited on page 149.)

[14] C. Zener, Non-adiabatic Crossing of Energy Levels, *Proceedings of the Royal Society of London A* **137** 6, 696-702 (1932). (Cited on pages 149 and 150.)

[15] , B. Wu and Q. Niu, Superfluidity of Bose-Einstein condensate in an optical lattice: Landau-Zener tunnelling and dynamical instability, *New J. Phys.* **5**, 104.1-104.24 (2003). (Cited on pages 151, 166 and 171.)

[16] P. G. Kevrekidis, D. J. Frantzeskakis, and R. Carretero-Gonzalez, Emergent Nonlinear Phenomena in Bose-Einstein Condensates, Springer, (2008). (Cited on pages 151, 153, 154 and 163.)

[17] O. Morsch and M. Oberthaler, Dynamics of Bose-Einstein condensates in optical lattices, *Rev. Mod. Phys.* **78**, 179 (2006). (Cited on pages 152, 153 and 176.)

[18] G. Lenz, P. Meystre, and E. M. Wright, Nonlinear atom optics: General formalism and atomic solitons, *Phys. Rev. A* **50**, 1681 (1994). (Cited on page 152.)

[19] V. V. Konotop and M. Salerno, Modulational instability in Bose-Einstein condensates in optical lattices, *Phys. Rev. A* **65**, 021602(R) (2002). (Cited on page 152.)

[20] H. Pu, L. O. Baksmaty, W. Zhang, N. P. Bigelow, and P. Meystre, Effective-mass analysis of Bose-Einstein condensates in optical lattices: Stabilization and levitation, *Phys. Rev. A* **67**, 043605 (2003). (Cited on page 152.)

[21] C. Bender and S. Orszag, Advanced Mathematical Methods for Scientists and Engineers: Asymptotic Methods and Perturbation Theory Springer, New York (1978). (Cited on page 152.)

[22] M. J. Steel and W. Zhang, Bloch function description of a Bose-Einstein condensate in a finite optical lattice, *arXiv*:9810284 (2008). (Cited on page 152.)

[23] A. V. Yulin and D. V. Skryabin, Out-of-gap Bose-Einstein solitons in optical lattices, *Phys. Rev. A* **67**, 023611 (2003). (Cited on page 152.)

[24] B. Eiermann, Th. Anker, M. Albiez, M. Taglieber, P. Treutlein, K.-P. Marzlin, and M. K. Oberthaler, Bright Bose-Einstein Gap Solitons of Atoms with Repulsive Interaction, *Phys. Rev. Lett.* **92** 230401 (2004). (Cited on pages 152 and 153.)

[25] D. E. Pelinovsky, A. A. Sukhorukov, and Y. S. Kivshar, Bifurcations and stability of gap solitons in periodic potentials, *Phys. Rev. E* **70**, 036618 (2004). (Cited on page 153.)

[26] O. Painter, R. K. Lee, A. Scherer, A. Yariv, J. D. O'Brien, P. D. Dapkus, I. I. Kim, Two-Dimensional Photonic Band-Gap Defect Mode Laser, *Science* **284**, 5421 (1999). (Cited on page 154.)

[27] Y. Akahane, T. Asano, B.-S. Song, and Susumu Noda, High-Q photonic nanocavity in a twodimensional photonic crystal, *Nature* **425**, 944 (2003). (Cited on page 154.)

[28] M. Notomi, H. Taniyama, On-demand ultrahigh-Q cavity formation and photon pinning via dynamic waveguide tuning, *Optics Express* **16**, 18657 (2008). (Cited on page 154.)

[29] B. J. Eggleton, R. E. Slusher, C. M. De Sterke, P. A. Krug, J. E. Sipe, Bragg Grating Solitons, *Phys. Rev. Lett.* **76**, 1627 (1996). (Cited on page 154.)

[30] A. B. Aceves, S. Wabnitz, Self-induced transparency solitons in nonlinear refractive periodic media, *Phys. Lett. A* **141**, 37 (1989). (Cited on page 154.)

[31] O. A. Egorov, D. V. Skryabin, and F. Lederer, Parametric polariton solitons in coherently pumped semiconductor microcavities, *Phys. Rev. B* **84**, 165305 (2011). (Cited on page 154.)

[32] M. Sich, D. N. Krizhanovskii, M. S. Skolnick, A. V. Gorbach, R. Hartley, D. V. Skryabin, E. A. Cerda-Méndez, K. Biermann, R. Hey, and P. V. Santos, Observation of bright polariton solitons in a semiconductor microcavity, *Nature Photonics* **6**, 50 (2012). (Cited on page 154.)

[33] Y. Kivshar, G. Agrawal, Optical Solitons: From Fibers to Photonic Crystals Academic Press (2001). (Cited on page 154.)

[34] L. Khaykovich, F. Schreck, G. Ferrari, T. Bourdel, J. Cubizolles, L. D. Carr, Y. Castin and C. Salomon, Formation of a matter-wave bright soliton, *Science* **296**, 1290-1293 (2002). (Cited on page 155.)

[35] Strecker, K. E., Partridge, G. B. Truscott, A. G. Hulet, R. G. Formation and propagation of matter-wave soliton trains, *Nature* **417**, 150-153 (2002). (Cited on page 155.)

[36] K. Cho, K. Okumoto, N. I. Nikolaev, and A. L. Ivanov, Bragg Diffraction of Microcavity Polaritons by a Surface Acoustic Wave, *Phys. Rev. Lett.* **94**, 226406 (2005). (Cited on page 155.)

[37] C. W. Lai, N. Y. Kim, S. Utsunomiya, G. Roumpos, H. Deng, M. D. Fraser, T. Byrnes, P. Recher, N. Kumada, T. Fujisawa, Y. Yamamoto, Coherent zero-state and π-state in an exciton-polariton condensate array, *Nature* (London) **450**, 529 (2007). (Cited on pages 155 and 167.)

[38] T. Byrnes, P. Recher, Y. Yamamoto, Mott transitions of exciton polaritons and indirect excitons in a periodic potential, *Phys. Rev. B* **81**, 205312 (2010). (Cited on page 155.)

[39] E. A. Cerda-Mendez, D. N. Krizhanovskii, M. Wouters, R. Bradley, K. Biermann, K. Guda, R. Hey, P. V. Santos, D. Sarkar, and M. S. Skolnick, Polariton Condensation in Dynamic Acoustic Lattices, *Phys. Rev. Lett.* **105**, 116402 (2010). (Cited on page 155.)

[40] A. V. Gorbach, and D. V. Skryabin, Parametric instabilities of microcavity polaritons in a periodic potential, *Phys. Rev. B* **82**, 125313 (2010). (Cited on page 155.)

[41] M. Kaliteevski, I. Iorsh, S. Brand, R. A. Abram, J. M. Chamberlain, A. V. Kavokin, and I. A. Shelykh, Tamm plasmon-polaritons: Possible electromagnetic states at the interface of a metal and a dielectric Bragg mirror, *Phys. Rev. B* **76**, 165415 (2007). (Cited on page 155.)

[42] N. Y. Kim, K. Kusudo, C. Wu, N. Masumoto, A. Loffler, S. Hofling, N. Kumada, L. Worschech, A. Forchel, and Y. Yamamoto. Dynamical *d*-wave condensation of exciton-polaritons in a two-dimensional square-lattice potential. *Nature Physics* **7**, 681 (2011). (Cited on page 155.)

[43] Y. V. Kartashov, V. A. Vysloukh, and L. Torner, Surface Gap Solitons, *Phys. Rev. Lett.* **96**, 073901 (2006). (Cited on page 158.)

[44] K. Leo, P. Haring Bolivar, F. Bruggemann, and R. Schwedler, Observation of Bloch oscillations in a semiconductor superlattice, *Solid State Commun.* **84**, 10 (1992). (Cited on pages 165 and 166.)

[45] C. Waschke, H. G. Roskos, R. Schwedler, K. Leo, H. Kurz, and and K. Kohler, Coherent submillimeter-wave emission from Bloch oscillations in a semiconductor superlattice, *Phys. Rev. Lett.* **70**, 3319-3322 (1993). (Cited on page 165.)

[46] T. Dekorsy, R. Ott, H. Kurz, and K. Kohler, Bloch oscillations at room temperature, *Phys. Rev. B* **51**, 17275-17278 (1995). (Cited on page 165.)

[47] G. Malpuech, A. Kavokin, G. Panzarini, and A. Di Carlo, Theory of photon Bloch oscillations in photonic crystals, *Phys. Rev. B* **63**, 035108 (2001). (Cited on pages 165 and 166.)

[48] V. Agarwal, J. A. delRio, G. Malpuech, M. Zamfirescu, A. Kavokin, D. Coquillat, D. Scalbert, M. Vladimirova, and B. Gil, Photon Bloch Oscillations in Porous Silicon Optical Superlattices, *Phys. Rev. Lett.* **92**, 097401 (2004). (Cited on pages 165 and 166.)

[49] M. Ben Dahan, E. Peik, J. Reichel, Y. Castin, and C. Salomon, Bloch Oscillations of Atoms in an Optical Potential, *Phys. Rev. Lett.* **76**, 4508 (1996). (Cited on pages 165 and 166.)

[50] I. Choi and Q. Niu, Bose-Einstein Condensates in an Optical Lattice, *Phys. Rev. Lett.* **82**, 2022 (1999). (Cited on page 165.)

[51] O. Morsch, J. H. Muller, M. Cristiani, D. Ciampini, and E. Arimondo, Bloch Oscillations and Mean-Field Effects of Bose-Einstein Condensates in 1D Optical Lattices, *Phys Rev. Lett.* **87**, 140402 (2001). (Cited on page 165.)

[52] M. Cristiani, O. Morsch, J. H. Muller, D. Ciampini, and E. Arimondo, Experimental properties of Bose-Einstein condensates in one-dimensional optical lattices: Bloch oscillations, Landau-Zener tunneling, and mean-field effects, *Phys. Rev. A* **65**, 063612 (2002). (Cited on page 165.)

[53] C. Menotti, A. Smerzi, and A. Trombenotti, Superfluid dynamics of a Bose-Einstein condensate in a periodic potential, *New. J. Phys.* **5**, 112 (2003). (Cited on page 165.)

[54] B. Deissler, M. Zaccanti, G. Roati, C. D Errico, M. Fattori, M. Modugno, G. Modugno, and M. Inguscio, Delocalization of a disordered bosonic system by repulsive interactions, *Nature Physics* **6**, 354 (2010). (Cited on page 165.)

[55] G. Ferrari, N. Poli, F. Sorrentino, and G. M. Tino, Long-Lived Bloch Oscillations with Bosonic Sr Atoms and Application to Gravity Measurement at the Micrometer Scale, *Phys Rev. Lett.* **97**, 060402 (2006). (Cited on page 166.)

[56] A. Buchleitner and A. R. Kolovsky, Interaction-Induced Decoherence of Atomic Bloch Oscillations, *Phys. Rev. Lett.* **91**, 253002 (2003). (Cited on page 166.)

[57] A. R. Kolovsky, H. J. Korsch, and E.-M. Graefe, Interaction-Induced Decoherence of Atomic Bloch Oscillations *Phys Rev. A* **80**, 023617 (2009). (Cited on pages 166 and 171.)

[58] T. Schulte, S. Drenkelforth, J. Kruse, W. Ertmer, J. Arlt, K. Sacha, J. Zakrzewski, and M. Lewenstein, Routes Towards Anderson-Like Localization of Bose-Einstein Condensates in Disordered Optical Lattices, *Phys. Rev. Lett.* **95**, 170411 (2005). (Cited on page 166.)

[59] G. Modugno, M. Modugno, and M. Inguscio, Anderson localization of a non-interacting Bose-Einstein condensate, *Nature* **453**, 895 (2008). (Cited on page 166.)

[60] G. E. Astrakharchik, J. Boronat, J. Casulleras, and S. Giorgini, Superfluidity versus Bose-Einstein condensation in a Bose gas with disorder, *Phys. Rev. A* **66**, 023603 (2002). (Cited on page 166.)

[61] M. Albert, T. Paul, N. Pavloff, and P. Leboeuf, Breakdown of the superfluidity of a matter wave in a random environment, *Phys. Rev. A* **82**, 011602(R) (2010). (Cited on page 166.)

[62] R. Roth and K. Burnett, Ultracold bosonic atoms in two-colour superlattices, *J. Opt. B* **5**, S50 (2003). (Cited on page 166.)

[63] B. Damski, J. Zakrzewski, L. Santos, P. Zoller, and M. Lewenstein, Atomic Bose and Anderson Glasses in Optical Lattices, *Phys. Rev. Lett.* **91**, 080403 (2003). (Cited on page 166.)

[64] T. Schulte, S. Drenkelforth, G. K. Buning, W. Ertmer, J. Arlt, M. Lewenstein, and L. Santos, Dynamics of Bloch oscillations in disordered lattice potentials, *Phys. Rev. A* **77**, 023610 (2008). (Cited on pages 166 and 170.)

[65] S. Drenkelforth, G. K. Buning, J. Will, T. Schulte, N. Murray, W. Ertmer, L. Santos, and J. J. Arlt, Damped Bloch oscillations of Bose-Einstein condensates in disordered potential gradients, *New J. Phys.* **10**, 045027 (2008). (Cited on page 166.)

[66] D. M. Gangardt and A. Kamenev, Bloch Oscillations in a One-Dimensional Spinor Gas, *Phys. Rev. Lett.* **102**, 070402 (2009). (Cited on page 166.)

[67] J. Larson, J.-P. Martikainen, A. Collin, and E. Sjoqvist, Spin-orbit-coupled Bose-Einstein condensate in a tilted optical lattice, *Phys. Rev. A* **82**, 043620 (2010). (Cited on page 166.)

[68] B. J. Wu and J. M. Zhang, *arXiv*:1107.0609 (2011). (Cited on page 166.)

[69] G. Malpuech, D. D. Solnyshkov, H. Ouerdane, M. M. Glazov, and I. A. Shelykh, Bose Glass and Superfluid Phases of Cavity Polaritons, *Phys. Rev. Lett.*, **98**, 206402 (2007). (Cited on pages 167 and 170.)

[70] K. G. Lagoudakis, B. Pietka, M. Wouters, R. Andre, and B. Deveaud-Pledran, Coherent Oscillations in an Exciton-Polariton Josephson Junction, *Phys. Rev. Lett.* **105**, 120403 (2010). (Cited on pages 167 and 187.)

[71] A. V. Gorbach and D. V. Skryabin, Parametric instabilities of microcavity polaritons in a periodic potential, *Phys. Rev. B* **82**, 125313 (2010). (Cited on pages 167 and 171.)

[72] B. Sermage, G. Malpuech, A. V. Kavokin, and V. Thierry-Mieg, Polariton acceleration in a microcavity wedge, *Phys. Rev. B* **64**, 081303(R) (2001). (Cited on page 167.)

[73] H. Flayac, G. Pavlovic, M. A. Kaliteevski, and I. A. Shelykh, Electric generation of vortices in polariton superfluids, *Phys. Rev. B* **85**, 075312 (2012). (Cited on page 167.)

[74] D. Tanese, D. D. Solnyshkov, A. Amo, L. Ferrier, E. Bernet-Rollande, E. Wertz, I. Sagnes, A. Lemaitre, P. Senellart, G. Malpuech, and J. Bloch, Backscattering Suppression in Supersonic 1D Polariton Condensates, *Phys. Rev. Lett.* **108**, 036405 (2012). (Cited on pages 169 and 170.)

[75] M. Jona-Lasinio, O. Morsch, M. Cristiani, N.Malossi, J. H. Muller, E. Courtade, M. Anderlini, and E. Arimondo, *Phys. Rev. Lett.* **91**, 230406 (2003). (Cited on page 172.)

[76] M. Modugno, C. Tozzo, and F. Dalfovo, *Phys. Rev. A* **70**, 043625 (2004). (Cited on page 173.)

[77] I. Shelykh, K. V. Kavokin, A. V. Kavokin, G. Malpuech, P. Bigenwald, H. Deng, G. Weihs, and Y. Yamamoto, Semiconductor microcavity as a spin-dependent optoelectronic device, *Phys. Rev. B* **70**, 035320 (2004). (Cited on page 174.)

[78] C. Leyder, T. C. H. Liew, A. V. Kavokin, I. A. Shelykh, M. Romanelli, J. Ph. Karr, E. Giacobino, and A. Bramati, Interference of Coherent Polariton Beams in Microcavities: Polarization-Controlled Optical Gates, *Phys. Rev. Lett.* **99**, 196402 (2007). (Cited on page 174.)

[79] T. C. H. Liew, A. V. Kavokin, and I. A. Shelykh, Optical Circuits Based on Polariton Neurons in Semiconductor Microcavities, *Phys. Rev. Lett.* **101**, 016402 (2008). (Cited on page 174.)

[80] I. A. Shelykh, G. Pavlovic, D. D. Solnyshkov, and G. Malpuech, Proposal for a Mesoscopic Optical Berry-Phase Interferometer, *Phys. Rev. Lett.* **102**, 046407 (2009). (Cited on page 174.)

[81] I. A. Shelykh, R. Johne, D. D. Solnyshkov, and G. Malpuech, Optically and electrically controlled polariton spin transistor, *Phys Rev B* **82**, 153303 (2010). (Cited on page 174.)

[82] T. K. Paraiso, M. Wouters, Y. Leger, F. Mourier-Genoud, and B. Deveaud-Plédran, Multistability of a coherent spin ensemble in a semiconductor microcavity, *Nature Materials* **9**, 655-660 (2010). (Cited on pages 174 and 194.)

[83] T. Dekorsy, P. Leisching, C. Waschke, K. Kohler, K. Leo, H. G. Roskos and H. Kurz, Terahertz Bloch oscillations in semiconductor superlattices, Semicond. Sci. Technol. **9**, 1959 (1994). (Cited on page 174.)

[84] I. Carusotto, L. Pitaevskii, S. Stringari, G. Modugno3, and M. Inguscio, Sensitive Measurement of Forces at the Micron Scale Using Bloch Oscillations of Ultracold Atoms, *Phys. Rev. Lett.* **95**, 093202 (2005). (Cited on page 174.)

[85] G. Ferrari, N. Poli, F. Sorrentino, and G. M. Tino, Long-Lived Bloch Oscillations with Bosonic Sr Atoms and Application to Gravity Measurement at the Micrometer Scale, *Phys. Rev. Lett.* 97, 060402 (2006). (Cited on page 174.)

[86] C. Leyder, M. Romanelli, J. Ph. Karr, E. Giacobino, T. C. H. Liew, M. M. Glazov, A. V. Kavokin, G. Malpuech and A. Bramati, Observation of the optical spin Hall effect, *Nature Physics* **3**, 628-631 (2007). (Cited on page 174.)

[87] M. Maragkou, C. E. Richards, T. Ostatnicky, A. J. D. Grundy, J. Zajac, M. Hugues, W. Langbein, and P. G. Lagoudakis, Optical analogue of the spin Hall effect in a photonic cavity, *Opt. Lett.* **36**, 1095 (2011). (Cited on page 174.)

[88] G. Malpuech, M. M. Glazov, I. A. Shelykh, P. Bigenwald, and K. V. Kavokin, Electronic control of the polarization of light emitted by polariton lasers, *Appl. Phys. Lett.* **88**, 111118 (2006). (Cited on pages 174 and 181.)

[89] M. O. Scully and M. Suhail Zubairy, Quantum Optics, Cambridge University Press, Cambridge (1997). (Cited on page 174.)

[90] L. Klopotowski, M. D. Martin, A. Amo, L. Vina, I. A. Shelykh, M. M. Glazov, G. Malpuech, A. V. Kavokin, and R. Andre, Optical anisotropy and pinning of the linear polarization of light in semiconductor microcavities, *Solid State Commun.* **139**, 511 (2006). (Cited on pages 174 and 188.)

[91] G. Dasbach, C. Diederichs, J. Tignon, C. Ciuti, Ph. Roussignol, C. Delalande, M. Bayer, and A. Forchel, Polarization inversion via parametric scattering in quasi-one-dimensional microcavities, *Phys. Rev. B* **71**, 161308(R) (2005). (Cited on page 174.)

[92] M. Wouters and I. Carusotto, Excitations in a Nonequilibrium Bose-Einstein Condensate of Exciton Polaritons, *Phys. Rev. Lett.* **99**, 140402 (2007). (Cited on pages 128 and 183.)

[93] I. G. Savenko, E. B. Magnusson, and I. A. Shelykh, Density-matrix approach for an interacting polariton system, *Phys. Rev. B* **83**, 165316 (2011). (Cited on page 183.)

[94] H. Deng, G. Weihs, D. Snoke, J. Bloch, and Y. Yamamoto, Polariton lasing vs. photon lasing in a semiconductor microcavity, *Proc. Natl. Acad. Sci.* **26** vol.100, 15318-15323 (2003). (Cited on page 184.)

[95] L. Ferrier, E. Wertz, R. Johne, D. D. Solnyshkov, P. Senellart, I. Sagnes, A. Lemaitre, G. Malpuech, and J. Bloch, Interactions in Confined Polariton Condensates, *Phys. Rev. Lett.* **106**, 126401 (2011). (Cited on page 184.)

[96] B. D. Josephson, Possible new effects in superconductive tunnelling, *Phys. Lett.* **1**, 251 (1962). (Cited on page 186.)

[97] A. Legett, Quantum Liquids: Bose Condensation and Cooper Pairing in Condensed-Matter Systems, Oxford University Press, New York, (2006). (Cited on page 186.)

[98] S. V. Pereverzev, A. Loshak, S. Backhaus, J. C. Davis, and R. E. Packard, Quantum oscillations between two weakly coupled reservoirs of superfluid ^{3}He, *Nature* **388**, 449 (1997). (Cited on page 186.)

[99] M. Albiez, R. Gati, J. Folling, S. Hunsmann, M. Cristiani, and M. K. Oberthaler, Direct Observation of Tunneling and Nonlinear Self-Trapping in a Single Bosonic Josephson Junction, *Phys. Rev. Lett.* **95**, 010402 (2005). (Cited on pages 186 and 187.)

[100] M. H. Anderson, J. R. Ensher, M. R. Matthews, C. E. Wieman, and E. A. Cornell, Observation of Bose-Einstein Condensation in a Dilute Atomic Vapor, *Science* **269**, 198 (1995). (Cited on page 186.)

[101] K. B. Davis, M.-O. Mewes, M. R. Andrews, N. J. van Druten, D. S. Durfee, D. M. Kurn, and W. Ketterle, Bose-Einstein Condensation in a Gas of Sodium Atoms, *Phys. Rev. Lett.* **75**, 3969 (1995) (Cited on page 186.)

[102] C. C. Bradley, C. A. Sackett, J. J. Tollett, and R. G. Hulet, Evidence of Bose-Einstein Condensation in an Atomic Gas with Attractive Interactions, *ibid.* **75**, 1687 (1995). (Cited on page 186.)

[103] M. R. Andrews, C. G. Townsend, H.-J. Miesner, D. S. Durfee, D. M. Kurn, and W. Ketterle, Observation of Interference Between Two Bose Condensates, *Science* **275**, 637 (1997). (Cited on page 186.)

[104] M. W. Jack, M. J. Collett, and D. F. Walls, Coherent quantum tunneling between two Bose-Einstein condensates, *Phys. Rev. A* **54**, R4625 (1996). (Cited on pages 186 and 187.)

[105] I. Zapata, F. Sols, and A. J. Leggett, Josephson effect between trapped Bose-Einstein condensates, *ibid.* **57**, R28 (1998). (Cited on page 186.)

[106] A. Smerzi, S. Fantoni, S. Giovanazzi, and S. R. Shenoy, Quantum Coherent Atomic Tunneling between Two Trapped Bose-Einstein Condensates, *Phys. Rev. Lett.* **79**, 4950-4953 (1997). (Cited on pages 186 and 187.)

[107] G. J. Milburn, J. Corney, E. M. Wright, and D. F. Walls, Quantum dynamics of an atomic Bose-Einstein condensate in a double-well potential, *Phys. Rev. A* **55**, 4318 (1997). (Cited on page 186.)

[108] S. Raghavan, A. Smerzi, S. Fantoni, and S. R. Shenoy, Coherent oscillations between two weakly coupled Bose-Einstein condensates: Josephson effects, π oscillations, and macroscopic quantum self-trapping, *ibid.* **59**, 620 (1999). (Cited on page 186.)

[109] L. V. Keldysh and Yu. V. Kopaev, *Sov. Phys. Solid State* **6**, 2219, (1965). (Cited on page 186.)

[110] I. B. Spielman, J. P. Eisenstein, L. N. Pfeiffer, and K. W. West, Observation of a Linearly Dispersing Collective Mode in a Quantum Hall Ferromagnet, *Phys. Rev. Lett.* **87**, 036803 (2001). (Cited on page 186.)

[111] J. P. Eisenstein and A. H. MacDonald, Bose-Einstein condensation of excitons in bilayer electron systems, *Nature* **432**, 691-694, (2004). (Cited on page 186.)

[112] S. O. Demokritov, V. E. Demidov, O. Dzyapko, G. A. Melkov, A. A. Serga, B. Hillebrands and A. N. Slavin, Bose-Einstein condensation of quasi-equilibrium magnons at room temperature under pumping, *Nature* **443**, 430-433 (2006). (Cited on page 186.)

[113] V. B Timofeev, Collective exciton effects in spatially separated electron-hole layers in semiconductors, *Physics-Uspekhi* 48(3):295 (2005). (Cited on page 186.)

[114] L. V. Butov, Cold exciton gases in coupled quantum well structures, *J. Phys.: Condens. Matter* **19** 295202 (2007). (Cited on page 186.)

[115] Yu. E. Lozovik and V. I. Yudson, *JETP Lett.* **22**, 26 (1975). (Cited on page 187.)

[116] Yu. E. Lozovik and V. I. Yudson, *Sov. Phys. JETP* **44**, 389 (1976). (Cited on page 187.)

[117] Yu. E. Lozovik and V. I. Yudson, Electron-hole superconductivity. Influence of structure defects *Solid State Commun.* **18**, 628 (1976). (Cited on page 187.)

[118] S. I. Shevchenko, Phase diagram of systems with pairing of spatially separated electrons and holes, *Phys. Rev. Lett.* **72**, 3242-3245 (1994). (Cited on page 187.)

[119] X. Zhu, P. B. Littlewood, M. S. Hybertsen, and T. M. Rice, Exciton Condensate in Semiconductor Quantum Well Structures, *Phys. Rev. Lett.* **74**, 1633-1636 (1995). (Cited on page 187.)

[120] O. L. Berman, Y. E. Lozovik, D. W. Snoke, and R. D. Coalson, Collective properties of indirect excitons in coupled quantum wells in a random field, *Phys. Rev. B* **70**, 235310 (2004). (Cited on page 187.)

[121] A. V. Larionov, V. B. Timofeev, J. Hvam, and K. Soerensen, Interwell excitons in GaAs/AlGaAs double quantum wells and their collective properties, *Zh. Eksp. Teor. Fiz.* **117**, 1255 (2000). (Cited on page 187.)

[122] A. V. Larionov, and V. B. Timofeev, Condensation of interwell excitons in GaAs/AlGaAs double quantum wells, *PisŠma Zh. Eksp. Teor. Fiz.* **73**, 342 (2001). (Cited on page 187.)

[123] D. Snoke, S. Denev, Y. Liu, L. Pfeiffer, and K. West, Long-range transport in excitonic dark states in coupled quantum wells, *Nature* **418**, 754 (2002). (Cited on page 187.)

[124] L. V. Butov, C. W. Lai, A. L. Ivanov, A. C. Gossard, and D. S. Chemla, Towards Bose-Einstein condensation of excitons in potential traps, **Nature 417**, 47 (2002). (Cited on page 187.)

[125] L. V. Butov, A. C. Gossard, and D. S. Chemla, Macroscopically ordered state in an exciton system, *ibid.* **418**, 751 (2002). (Cited on page 187.)

[126] A. T. Hammack, M. Griswold, L. V. Butov, L. E. Smallwood, A. L. Ivanov, and A. C. Gossard, Trapping of Cold Excitons in Quantum Well Structures with Laser Light *Phys. Rev. Lett.* **96**, 227402 (2006). (Cited on page 187.)

[127] R. B. Balili1, D. W. Snoke, L. Pfeiffer2, and K. West, Actively tuned and spatially trapped polaritons, *Appl. Phys. Lett.* **88**, 031110 (2006). (Cited on page 187.)

[128] O. El Daif, A. Baas, T. Guillet, J.-P. Brantut, R. Idrissi Kaitouni, J. L. Staehli1, F. Morier-Genoud, and B. Deveaud, Polariton quantum boxes in semiconductor microcavities, *Appl. Phys. Lett.* **88**, 061105 (2006). (Cited on page 187.)

[129] R. I. Kaitouni, O. El Daif, A. Baas, M. Richard, T. Paraiso, P. Lugan, T. Guillet, F. Morier-Genoud, J. D. Ganiere, J. L. Staehli, V. Savona, and B. Deveaud, Engineering the spatial confinement of exciton polaritons in semiconductors, *Phys. Rev. B* **74**, 155311 (2006). (Cited on page 187.)

[130] D. Sarchi, I. Carusotto, M. Wouters, and V. Savona, Coherent dynamics and parametric instabilities of microcavity polaritons in double-well systems, *Phys. Rev. B* **77**, 125324 (2008). (Cited on page 187.)

[131] I. A. Shelykh, D. D. Solnyshkov, G. Pavlovic, G. Malpuech, Josephson effects in condensates of excitons and exciton polaritons, *Phys. Rev. B* **78**, 041302R (2008). (Cited on pages 187, 188 and 198.)

[132] D. D. Solnyshkov, R. Johne, I. A. Shelykh, and G. Malpuech, Chaotic Josephson oscillations of exciton-polaritons and their applications, *Phys. Rev. B* **80**, 235303 (2009). (Cited on pages 187, 197 and 198.)

[133] D. Read, Yu. G. Rubo, and A. V. Kavokin, Josephson coupling of Bose-Einstein condensates of exciton-polaritons in semiconductor microcavities, *Phys. Rev. B* **81**, 235315 (2010). (Cited on page 187.)

[134] A. O. Caldeira and A. J. Leggett, Influence of Dissipation on Quantum Tunneling in Macroscopic Systems, *Phys. Rev. Lett.* **46**, 211 (1981). (Cited on page 188.)

[135] I. L. Aleiner and E. L. Ivchenko, The nature of anisotropic exchange splitting in type II GaAs/AlAs superlattices *JETP Lett.* **55**, 692 (1992). (Cited on page 188.)

[136] M. Trujillo-Martinez, A. Posazhennikova, and J. Kroha, *Phys. Rev. Lett.* **103**, 105302 (2009). (Cited on page 188.)

[137] H. Carmichael, Quantum Optics 1: Master Equations And Fokker-Planck Equations, Springer, New York (2007). (Cited on pages 190 and 192.)

[138] N. A. Gippius, I. A. Shelykh, D. D. Solnyshkov, S. S. Gavrilov, Yuri G. Rubo, A. V. Kavokin, S. G. Tikhodeev, and G. Malpuech, Polarization Multistability of Cavity Polaritons, *Phys. Rev. Lett.* **98**, 236401 (2007). (Cited on page 194.)

Publications

1. H. Flayac, D. D. Solnyshkov, G. Malpuech and I. A. Shelykh, Topological stability of the half-vortices in spinor exciton-polariton-condensates, *Phys. Rev. B*, **81** 045318 (2010).

2. E. B. Magnusson, H. Flayac, G. Malpuech and I. A. Shelykh, Role of phonons in Josephson oscillations of excitonic and polaritonic condensates, *Phys. Rev. B.* **82**, 195312 (2010).

3. H. Flayac, D. D. Solnyshkov and G. Malpuech, Bloch oscillations of an exciton-polariton Bose-Einstein condensate, *Phys. Rev. B* **83**, 045412 (2011).

4. H. Flayac, D. D. Solnyshkov and G. Malpuech, Oblique half-solitons and their generation in exciton-polariton condensates, *Phys. Rev. B* **83**, 193305 (2011).

5. H. Flayac, D. D. Solnyshkov and G. Malpuech, Bloch-oscillations of exciton-polaritons and photons for the generation of an alternating THz spin signal, *Phys. Rev. B* **84**, 125314 (2011).

6. D. D. Solnyshkov, H. Flayac and G. Malpuech, Black holes and wormholes in spinor polariton condensates, *Phys. Rev. B* **84**, 233405 (2011).

7. H. Flayac, G. Pavlovic, M. A. Kaliteevski, and I. A. Shelykh, Electric generation of vortices in polariton superfluids, *Phys. Rev. B* **85**, 075312 (2012).

8. D. D. Solnyshkov, H. Flayac and G. Malpuech, Stable magnetic monopoles in spinor polariton condensates, *Phys. Rev. B* **85**, 073105 (2012).

9. R. Hivet, H. Flayac, D. D. Solnyshkov, D. Tanese, T. Boulier, D. Andreoli, E. Giacobino, J. Bloch, A. Bramati, G. Malpuech, and A. Amo, Half-solitons in a polariton quantum fluid behave like magnetic monopoles, *Nature Physics* **8**, 724-728 (2012).

10. H. Flayac, D. D. Solnyshkov and G. Malpuech, Separation and propagation of magnetic monopole analogs in semiconductor microcavities, *New J. Phys.* **14**, 085018.

11. H. Flayac, D. D. Solnyshkov and G. Malpuech, Quantum fluids - Hot topics and new Trends: "Spin effects in polariton condensates: From half-Solitons to wormholes (Review Book Chapter), to appear - *Springer Verlag* - Berlin (2012).

12. D. Tanese, H. Flayac, D. D. Solnyshkov, A. Amo, A. Lemaître, E. Galopin, R. Braive, P. Senellart, I. Sagnes, G. Malpuech and J. Bloch, Polariton condensation in solitonic gap states in a 1D periodic potential, submitted to *Nat. Commun.* (2012).

13. H. Flayac, D. D. Solnyshkov and G. Malpuech, Transmutation of skyrmions into half-solitons driven by the nonlinear optical spin-Hall effect, to appear in *Phys. Rev. Lett.* (2013), (preprint) *arXiv*:1207.3533.

14. H. Flayac, D. D. Solnyshkov, G. Malpuech and I. A. Shelykh, Parametric Inversion of Spin Currents in Semiconductor Microcavities, to appear in *Phys. Rev. B* (2013), (preprint) *arXiv*:1211.5100.

Conferences

Oral Contributions

1. 6^{th} International Conference on Spontaneous Coherence in Excitonic Systems (ICSCE-6 2012) - Stanford, United-States.

2. 2^{nd} International School on SpinOptronics (ISSO2 2012) - Saint-Petersburg, Russia.

3. 12^{th} International Conference on Physics of Light-Matter Coupling in Nanostructures (PLMCN-12 2012) - Hangzhou, China.

4. 1^{st} International School on Relativistic Phenomena in Solids (RPS-1 2012) - Le Mont Dore, France.

5. 12^{th} International Conference on Optics of Excitons in Confined Systems (OECS-12 2011) - Paris, France.

6. 11^{th} International Conference on Physics of Light-Matter Coupling in Nanostructures (PLMCN-11 2011) - Berlin, Germany.

7. Workshop on Solitons and Polaritons in Cavities (2010) - Valbonne, France.

Poster Contributions

1. 12^{th} International Conference on Physics of Light-Matter Coupling in Nanostructures (PLMCN-12 2012) - Hangzhou, China.

2. 11^{th} International Conference on Physics of Light-Matter Coupling in Nanostructures (PLMCN-11 2011) - Berlin, Germany.

3. International Workshop on New Trends in the Physics of Quantum Vacuum - Trento, Italy (2011).

4. 5^{th} International Conference on Spontaneous Coherence in Excitonic Systems (ICSCE-5 2011) - Lausanne, Swizerland.

New trends in the physics of spinor exciton-polaritons condensates

Abstract: Along this thesis manuscript I shall present some emergent nonlinear phenomena in spinor exciton polariton-condensates. After an introductory chapter bringing the necessary background, I will in a first part focus on half-integer topological defects discussing their stability, acceleration and nucleation in the presence of effective magnetic fields. We will see that these objects behave as magnetic charges being fascinating dirac's monopole analogues. Remarkably we will see as well how they can be used as stable signals allowing to seed the physics acoustic black holes analogues.

In a second part I will concentrate on low dimensional structures. Especially, I'll describe the formation of gap solitons and the Bloch oscillations of exciton-polaritons in periodically patterned microwires, and besides, the room temperature Josephson oscillations within pairs of coupled micropillars.

Résumé: Au long de ce manuscrit de thèse je présenterais des effets non-linéaires émergents dans les condensats d'exciton-polariton spineurs. Après un chapitre d'introduction amenant les notions de bases nécessaires, je me concentrerais dans une première partie sur les défauts topologiques quantifiés par des nombres demi-entiers et discuterais leur stabilité, accélération et nucléation en présence de champs magnétiques effectifs. Nous verrons que ces objets se comportent comme des charges magnétiques manipulables démontrant une analogie fascinante avec les monopoles de Dirac. De manière remarquable nous verrons également que ces objets peuvent être utilisés comme des signaux stable pour sonder la physique d'analogues acoustiques de trous noirs.

Dans une seconde partie j'étudierais des structure de basse dimensions. Plus particlièrement, je décrirais la formation de solitons de bande interdite et les oscillations de Bloch des exciton-polaritons dans des microfils comportant des structures périodiques et d'autre part les oscillations Josephson à température ambiante dans des paires de micropilliers couplés.

Keywords: Exciton-polaritons, nonlinear optics, Bose-Einstein condensation, spin dynamics, topological defects, vortex, solitons, analogue gravity, black-holes, magnetic monopoles, Bloch oscillations, Josephson effect.

Mots clés: Exciton-polaritons, optique nonlinéaire, condensation de Bose-Einstein, dynamique de spin, défauts topologiques, vortex, solitons, systèmes gravitationnels analogues, trous noirs, monopoles magnétiques, oscillations de Bloch, effet Josephson.